# Developing a Framework for the Design of Hydrogen Fuel Cell Supply Architectures

Noah Tarbah

Technische Universiteit Delft


TU Delft Delft University of Technology

Challenge the future

# Developing a Framework for the Design of Hydrogen Fuel Cell Supply Architectures

by

**Noah Tarbah**

in partial fulfilment of the requirements for the degree of

**Master of Science**
in Aerospace Engineering

at the Delft University of Technology,
to be defended publicly on Friday June 14, 2024 at 9:00 AM.

| | | |
|---|---|---|
| Supervisors: | Dr. F. Oliviero | TU Delft |
| | Dr. S. de Graaf | DLR Institute of Electrified Aero Engines |
| | D. Dimos | DLR Institute of Electrified Aero Engines |
| Thesis committee: | Prof. dr. ir. L. L. M. Veldhuis | TU Delft |
| | Dr.-Ing. S. G. P. Castro | TU Delft |



An electronic version of this thesis is available at `http://repository.tudelft.nl/`.

TU Delft Delft University of Technology

# PREFACE

This report presents results of the master thesis project performed at the DLR Institute of Electrified Aero Engines in Cottbus over the course of around 10 months. I would like to thank my supervisors Dr. Fabrizio Oliviero and Dr. Stefanie de Graaf for their invaluable support, guidance, and feedback throughout the entire thesis. Special thanks go to Dimitrios Dimos for letting me pester him day to day with my questions and helping me on every step of the way, and also for being a good friend. I also appreciate the help from Sahil Bhapkar and Pundeep Hundal with implementing some of the models in my work.

This also marks the end of six years of studies in Cottbus and Delft, and I am grateful for all the friends I have made during this time and for the good times shared together.

Last but not least, I am extremely thankful for the unwavering love and support from my family, which guided me through every obstacle faced along the way.

*Noah Tarbah*
*Delft, June 2024*

# ABSTRACT

One of the solutions for reducing emissions from the aviation industry is the implementation of electric or hybrid-electric propulsion systems in the aircraft. The German Aerospace Center (DLR) Institute of Electrified Aero Engines is investigating the feasibility of using fuel cells in hybrid-electric propulsion systems to power regional aircraft. The aim of the thesis is to develop a framework for the design, optimisation, and assessment of hydrogen fuel cell supply architectures for an Solid Oxide Fuel Cell (SOFC) powered aircraft. In addition to this, the implementation of waste reduction methods using a turbine is examined by modelling the air supply system.

Key components for a hydrogen fuel cell supply architecture include cryogenic storage tanks, vaporisers, pipes, heat exchangers, pumps, turbines and compressors. Three architectures were defined using these components. Two of them utilised the tank self-pressurisation as the driving force behind the hydrogen flow in the system, with the one extracting gaseous and the other extracting the liquid hydrogen from the tank. The final architecture employed liquid hydrogen extraction using piston pumps.

Analytical models for sizing each of these components and modelling the fluid flow through them were implemented in Python scripts. These were integrated in an optimisation loop utilising a local simplex-based algorithm within the RCE integration environment. Each architecture was optimised for two objective functions, the first being for system mass, and the second for both system mass and net power recovered. The optimisation parameters are the geometrical parameters of the components. Its constraints were related to dimensional limitations set by the aircraft and the fluid properties, such as pressure drops and fluid phases, throughout the system. Preliminary component sizings from previous project phases set the intialisation point.

Results indicated that the choice of objective function greatly impacts the converged system. For the mass optimisation, the optimiser minimised the mass of all the air side components. On the hydrogen side, a compromise is found between the mass of the component responsible for maintaining the pressure difference for the desired mass flowrate and the mass of the remaining components. When optimising for mass and power, the optimiser reduced air side pressure drops in order to maximise turbine power recovery and minimise compressor power, resulting in a heavier but more power-efficient system.

The different architecture layouts primarily affected the system's parasitic power, which includes additional power required to maintain tank and vaporiser storage pressure, as well as pump power. The implementation of a vaporiser in the liquid extraction architectures reduces this value, as less hydrogen needs to be vaporised in the tank and the mass of hydrogen in the vaporiser is less. Similarly, using a pump allowed for lower tank pressure, reducing both tank mass and power, leading to further reductions in parasitic power.

These findings led to the selection of the pump-fed liquid hydrogen extraction architecture as the most suitable for the mission. Post-optimisation analyses included a sensitivity analysis to identify parameters with the largest impact on the converged system. The heat exchanger geometrical parameters had the largest impact due to their significant contribution to overall system mass and pressure losses, which affected other components like tanks and pipes. The analysis also shows that components related to the pressure drop, such as the pipes, become more important when optimising for mass and power. A mission analysis for tank self-pressurisation in the gaseous extraction architecture revealed substantial additional energy required for tank operation, corresponding to a 14.7% system mass increase if stored in lithium-ion batteries. Finally, two additional sets of optimisations were performed with different initialisation points to examine its effect on the results. Although the converged systems differed from baseline optimisations, similar trends were observed.

# Contents

# NOMENCLATURE

| Symbol | Definition | Unit |
|---|---|---|
| $c_p$ | Specific heat capacity at constant pressure | $[J/(kgK)]$ |
| $d$ | Diameter | $[m]$ |
| $e$ | Emissivity | [-] |
| $e_w$ | Weld efficiency | [-] |
| $f$ | Friction coefficient | [-] |
| $g$ | Gravitational acceleration | $[m/s^2]$ |
| $h$ | Heat transfer coefficient | $[W/(m^2K)]$ |
| $h_f$ | Fin height | $[m]$ |
| $h_v$ | Gaseous hydrogen specific enthalpy | $[J/kg]$ |
| $h_l$ | Liquid hydrogen specific enthalpy | $[J/kg]$ |
| $k$ | Thermal conductivity | $[W/(mK)]$ |
| $k_f$ | Fitting k factor | $[W/(mK)]$ |
| $l$ | Length | $[m]$ |
| $m$ | Mass | $[kg]$ |
| $\dot{m}$ | Mass flowrate | $[kg/s]$ |
| $n$ | Number of elements | [-] |
| $n_q$ | Pump specific speed | [-] |
| $n_{ss}$ | Suction specific speed | [-] |
| $p$ | Pressure | $[Pa]$ |
| $p_f$ | Fin pitch | $[m]$ |
| $r$ | Radius | $[m]$ |
| $s$ | Stroke length | $[m]$ |
| $t$ | Thickness | $[m]$ |
| $t$ | Time | $[s]$ |
| $v$ | Velocity | $[m/s]$ |
| $z$ | Pipe Elevation | $[m]$ |
| $A$ | Area | $[m^2]$ |
| $AU$ | Air utilisation | [-] |
| $C$ | Pump crank length to radius ratio | [-] |
| $E$ | E-modulus | $[Pa]$ |
| $E_{thermo}$ | Ideal voltage | $[V]$ |
| $F$ | Faraday constant | $[A/mol]$ |
| $FU$ | Fuel utilisation | [-] |
| $G$ | Heat exchanger core mass velocity | $[m/s]$ |
| $H$ | Enthalpy | $[J]$ |
| $H_P$ | Pump head | $[m]$ |
| $H_S$ | Heat exchanger stack height | $[m]$ |
| $I$ | Current | $[A]$ |
| $K_1$ | Tank Ellipiticity Factor | $[Pa]$ |
| $L$ | Heat exchanger side length | $[m]$ |
| $Lp$ | Pump rod length | $[m]$ |
| $L_{cyl}$ | Unsupported Tank Cylinder Length | $[m]$ |
| $LHV$ | Latent Heat of Vaporisation | $[J/kg]$ |
| $M$ | Mach number | [-] |
| $M_{H_2}$ | Hydrogen molar mass | $[kg/kmol]$ |
| $Nu$ | Nusselt number | [-] |

| Symbol | Definition | Unit |
|---|---|---|
| $P$ | Power | $[W]$ |
| $Pr$ | Prandtl number | [-] |
| $\dot{Q}$ | Heat Transfer Rate | $[W]$ |
| $R$ | Thermal Resistance | $[K/W]$ |
| $\bar{R}$ | Universal gas constant 287 $J/(kgK)$ or $8314.41 J/(kmol \cdot K)$ | |
| $Ra$ | Rayleigh number | [-] |
| $Re$ | Reynold's number | [-] |
| $T$ | Temperature | $[K]$ |
| $U$ | Overall heat transfer coefficient | $[W/(m^2K)]$ |
| $V$ | Volume | $[m^3]$ |
| $\dot{V}$ | Volumetric flowrate | $[m^3/s]$ |
| $V_{FC}$ | Voltage | $[V]$ |
| $Z$ | Compressibility | [-] |
| $\alpha_d$ | Diffusivity | $[m^2/s]$ |
| $\alpha_f l$ | Fluid heat transfer coefficient | $[W/(m^2K)]$ |
| $\beta$ | Thermal expansion coefficient | $[K^{-1}]$ |
| $\delta_{max}$ | Maximum deflection | $[rad]$ |
| $\epsilon$ | Pipe roughness | $[m]$ |
| $\epsilon_r$ | Pump cylinder radial strain | [-] |
| $\eta$ | Efficiency | [-] |
| $\varepsilon$ | Heat exchanger effectiveness | [-] |
| $\gamma$ | Ratio of specific heats | [-] |
| $\lambda$ | Fuel cell voltage losses | $[V]$ |
| $\chi$ | Composition | [-] |
| $\rho$ | Gravimetric Density | $[kg/m^3]$ |
| $\rho_{P,m}$ | Gravimetric Power Density | $[W/kg]$ |
| $\rho_{V,m}$ | Volumetric Power Density | $[W/m^3]$ |
| $\sigma$ | Stress | $[Pa]$ |
| $\sigma_{bolt}$ | Stefan-Boltzmann constant | $[W/(m^2K^4)]$ |
| $\theta$ | Angle | $[rad]$ |
| $\mu$ | Dynamic Viscocity | $[Pa \cdot s]$ |
| $\mu_{JT}$ | Joule-Thomson coefficient | $[K/Pa]$ |
| $\nu$ | Poisson's Ratio | $[kg/m^3]$ |
| $\nu_v$ | Kinematic Viscocity | $[m^2/s]$ |
| $\omega$ | Rotational Speed | $[rad/s]$ |
| $\zeta$ | Power recovery effectiveness | [-] |

# List of Acronyms

| Abbreviation | Definition |
|---|---|
| **CFD** | Computational Fluid Dynamics |
| **COBYLA** | Constrained Optimization BY Linear Approximations |
| **DLR** | German Aerospace Center |
| **$GH_2$ SP** | gaseous hydrogen extraction with self-pressurisation |
| **HEX** | heat exchanger |
| **$LH_2$ Pump** | liquid hydrogen extraction with pumps |
| **$LH_2$ SP** | liquid hydrogen extraction with self-pressurisation |
| **MDO** | Multidisciplinary Optimisation |
| **$NPSH_A$** | Net Positive Section Head Available |
| **$NPSH_R$** | Net Positive Section Head Required |
| **NTU** | number of transfer units |
| **PEMFC** | Polymer Electrolyte Membrane Fuel Cell |
| **PEMFCs** | Polymer Electrolyte Membrane Fuel Cells |
| **SOFC** | Solid Oxide Fuel Cell |
| **SOFCs** | Solid Oxide Fuel Cells |
| **XDSM** | Extended Design Structure Matrix |

# List of Figures

# List of Tables

# 1

# INTRODUCTION

## 1.1. MOTIVATION

The aviation industry is experiencing exponential growth year after year, with Airbus and Boeing both projecting annual growth figures of 4.4% and 4.6% respectively [1]. With this growth comes a corresponding increase in global emissions. As of 2018, approximately 2.4% of anthropogenic carbon dioxide ($CO_2$) emissions could be attributed to aviation, with the total $CO_2$ emissions increasing 5% every year from 2013 to 2018 [2]. Additional byproducts from air transport that have an effect on the climate include water vapour, nitrogen oxides ($NO_x$), unburnt hydrocarbons, and soot [1]. Lee et al. [2] find that non-$CO_2$ impacts correspond to two-thirds of the net radiative forcing due to aviation.

Therefore, the reduction of the environmental impacts of aviation becomes ever more important. The European Commission introduced its goals and vision for the aviation sector by the year 2050 called 'Flightpath 2050' [3], where the goals for the environmental impact are as follows. The $CO_2$ and $NO_x$ emissions should be reduced by 75% and 90% respectively compared to that of a new aircraft produced in the year 2000, as well as a 65% noise reduction [3]. Additionally, taxiing should be emission free and the aircraft should be as recyclable as possible [3].

One possible solution for achieving the emission goals is the utilisation of electric propulsion systems in the aircraft. Different systems can be defined based on the ratio of the electric energy to the total energy stored in the system. These include turbo-electric, where a turboshaft generator produces all the electric energy required, all electric, with the total energy stored in a battery, and fuel cell based propulsion systems. Additionally, hybrid-electric systems can be defined that use a combination of the previously mentioned energy storage systems [4]. The German Aerospace Center (DLR) Institute of Electrified Aero Engines is investigating the feasibility of using fuel cells in hybrid-electric propulsion systems to power regional aircraft in the $H_2$EAT project [5].

The top level mission requirements for the aircraft concept developed for the $H_2$EAT project are displayed in Table 1.1. The project will examine two different propulsion system architectures for the aircraft. The first is a nacelle integrated fuel cell architecture where the majority of the components, including the fuel cell and thermal management systems are placed in the nacelles attached to the wings. The second is a fuselage integrated architecture, where the fuel cell related components are placed mostly in the aircraft fuselage, and only the electrical propulsion components in the nacelle. A cryogenic liquid hydrogen storage system is implemented for both topologies. The topics investigated in the project include the following.

- Environmental Impacts and Aviation Requirements
- Overall Aircraft Design and Modifications
- Design of Propulsion System Components and Architecture
- Design of System Control Algorithms
- Component Development

Table 1.1: Top level mission requirements for $H_2$EAT project [5].

| Parameter | Value | Unit |
|---|---|---|
| Cruise Mach Number | 0.45 | - |
| Cruise Altitude | 7315 | m |
| Range | 1850 | km |
| Payload | 6650 | kg |
| Number of Passengers | 50 | - |

The thesis will focus on the propulsion system architectures and in particular the storage and delivery of hydrogen to the fuel cell. This includes modelling the effect of each of the architecture components on the hydrogen flow, as well as the implementation of some waste energy reduction methods utilising the air flow and its respective components.

## 1.2. RESEARCH FOCUS, OBJECTIVE, AND QUESTIONS

Multiple aspects of the implementation of a hydrogen fuel cell propulsion architecture in aviation have been investigated in research. Onorato and Vonhoff of the TU Delft both investigate the conceptual design of hydrogen-powered aircraft [6, 7]. However, their work did not focus on the effect of the hydrogen supply architecture, excluding the tank, on the design of the aircraft.

Millis et al. investigated hydrogen propulsion architectures utilising Solid Oxide Fuel Cells (SOFCs), Polymer Electrolyte Membrane Fuel Cells (PEMFCs), and the internal combustion of hydrogen to provide power for the propulsion system of a hydrogen-powered aircraft.[8]. Some of the main components of the architecture were identified in this work. These are hydrogen storage tanks, vaporisers, pumps, valves, and fuel transfer lines. The systems examined utilised liquid extraction by implementing a hybrid transportation method of pressurising the tank and pumping the fuel. For this report, however, pressure losses in the system as well as energy recovery from the SOFC were not investigated. In order to determine the energy recovery of the system, the power required to compress the air coming into and the power recovered from the exhaust stream need to be computed. Therefore, a compressor and turbine model are also required.

By examining the research performed previously, there is a clear gap visible in the modelling of complete fuel cell supply architectures, specifically the variation in fluid properties through the system and power utilisation and recovery. Additionally, the comparison of the liquid and gaseous extraction of hydrogen from the storage tank can be investigated. This lead to the formulation of the following main research objective.

*The research objective is to develop a framework for the design, optimisation, and assessment of hydrogen fuel cell supply architectures for an SOFC powered aircraft by modelling the architecture components, the flow of hydrogen through them, and their effect on the propulsion system level.*

The aim is to be able to use this framework to perform preliminary analyses of different architectures for a wide variety of applications and provide insight into the effect of certain design choices on the propulsion system level. It is intended to be as general as possible to quickly accommodate for different mission definitions and requirements. Additionally, the components are designed to be modular so that they can be combined in any logical order. Subsequently, the following main research question and a set of subquestions were defined.

*What are the most impactful design parameters and decisions of the hydrogen storage and distribution system and how can they be derived and evaluated?*

- What extraction method is most suitable for SOFC powered aircraft?
- What is the effect of different architectures on weight and power required?
- What additional modifications could be implemented to increase its efficiency?
- What is the effect of the mission operation on the system sizing?

## 1.3. REPORT STRUCTURE

The report is structured as follows. First, Chapter 2 explains the background theory and analytical models, either found in literature or provided by the DLR and expanded upon for this work, needed to model the individual components of the hydrogen architecture, which were determined in Section 1.2. Subsequently, in Chapter 3, the framework methodology is defined based on the theoretical knowledge gained, and the implementation of the analytical models in the architectures is described. Furthermore, the set up of the architecture optimisations is explained. Next, Chapter 4 provides the results and discussions regarding to the sizings and optimisations of the architectures. It also contains, the post-optimisation analyses related to the effect of the preliminary mission analysis and the derivation of the most impactful optimisation parameters. Last but not least, Chapter 5 summarises the conclusions of the thesis and discusses the limitations of the research and recommendations for further research.

# 2

# Background Knowledge

The theoretical knowledge required before constructing the hydrogen supply architectures is presented in this chapter. An overview of the working principle of an SOFC is provided in Section 2.1. Subsequently, Section 2.2 describes the analytical models for the modelling of the components defined in Section 1.2.

## 2.1. Solid Oxide Fuel Cells

Fuel cells are devices consisting of an anode, cathode, and electrolyte that make use of an electrochemical reaction to generate electricity. The electricity generated can then be utilised to power, in this case, the aircraft. An oxidation and reduction reaction occurs at the anode and cathode respectively, which allows for a transfer of ions through the electrolyte and electrons through an electric circuit connecting both sides of the fuel cell. These reactions require a fuel and an oxidising agent to be provided at the fuel cell inlet. In the fuel cells examined in this work, the reactions are with the hydrogen fuel and the oxygen in the atmosphere. The exhaust fluids have a larger temperature than those entering due to the exothermic reactions, leading to some heat losses in addition to the electrical energy produced [9].

A fuel cell is typically one of two main types, which are Polymer Electrolyte Membrane Fuel Cells (PEMFCs) and Solid Oxide Fuel Cells (SOFCs). The main difference between the different types is the electrolyte utilised to transfer the ions between the anode and the cathode. PEMFCs implement a thin polymer membrane as the electrolyte while SOFCs use a ceramic one. The operating temperature of a PEMFC is around 80 °C for a low temperature variant. The SOFC operates at much higher temperatures, typically 600-1000 °C [9, 10]. The general chemical reaction implemented for the SOFC can be seen in Equation 2.1 and Equation 2.2. The hydrogen reaction occurs at the anode while the oxygen reaction occurs at the cathode [9]. A schematic for a SOFC is displayed in Figure 2.1 [10].

$$H_2 + O^{2-} \rightleftharpoons H_2O + 2e^- \tag{2.1}$$

$$\frac{1}{2}O_2 + 2e^- \rightleftharpoons O^{2-} \tag{2.2}$$

The voltage of the fuel cell $V_{FC}$ is obtained for different current densities by implementing the Nernst equation to obtain the ideal thermodynamic voltage of the cell $E_{thermo}$ and subtracting the different losses $\lambda$ experienced by the fuel cell, which are activation, ohmic, and concentration losses, as can be seen in Equation 2.3 [9]. The losses are all functions of the current density ($A/m^2$), which leads to the example voltage-current plot seen in Figure 2.2.

$$V_{FC} = E_{thermo} - \lambda_{act} - \lambda_{ohmic} - \lambda_{conc} \tag{2.3}$$

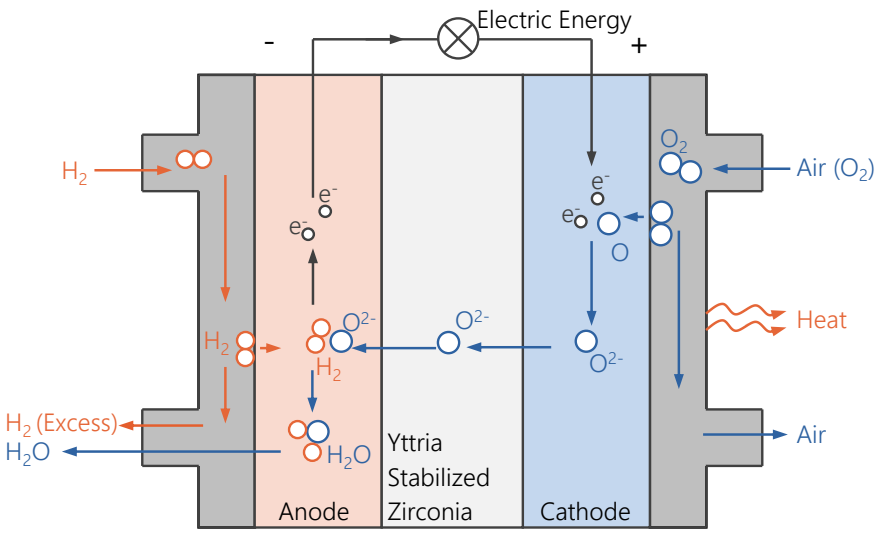


Figure 2.1: Schematic of a Solid Oxide Fuel Cell (SOFC) [10].

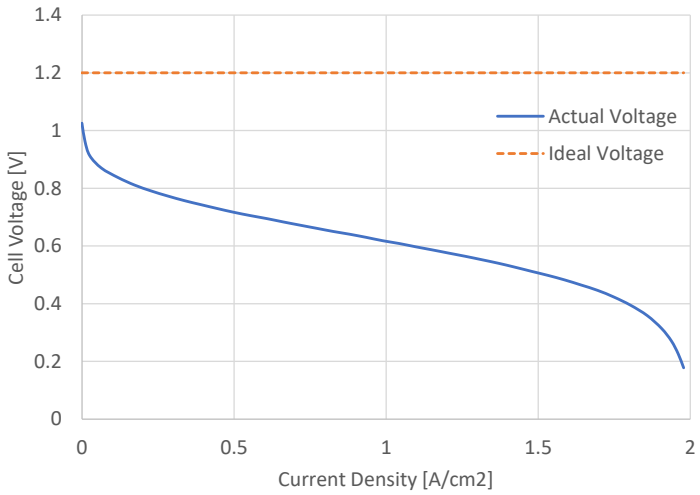


Figure 2.2: An example of a voltage-current plot for a fuel cell.

The power-current plot can be obtained by implementing the reaction area of the fuel cell and multiplying the voltage equation by the current. Subsequently, it is possible to determine the required current for a given power requirement during a mission phase. From the current, the required hydrogen mass flow rate for the fuel cell can be calculated using Equation 2.4-2.9. In these equations, $\dot{m}$ is the mass flow rate of the hydrogen, $I$ is the current, $n_{cells}$ is the number of cells in the fuel cell stack, $M$ is the molar mass of the gas, and $F$ is the Faraday constant [11].

$$\dot{m}_{H_2} = \frac{I n_{cells} M_{H_2}}{2F} \cdot 10^{-2} \tag{2.4}$$

The fuel utilisation and air utilisation factors, $FU$ and $AU$ respectively, are parameters of the fuel cell that determine what ratio of the inlet flow is utilised in the SOFC reaction. With the overall reaction in Equation 2.5, it is possible to determine the mass flow rates for both sides of the fuel cell at the inlet and outlet. These are detailed from Equation 2.6 to Equation 2.9, where subscipts *an* and *cat* refer to the anode and cathode respectively, and the subcripts *in* and *out* refer to the inlet and outlet of each anode and cathode. The cath-

ode inlet fluid is assumed to be air with 23% of its mass being oxygen ($\chi = 0.23$). These mass flow rates can subsequently be utilised to size all the components of the hydrogen supply architecture.

$$H_2 + \frac{1}{2}O_2 \rightleftharpoons H_2O \tag{2.5}$$

$$\dot{m}_{an,in} = \frac{\dot{m}_{H_2}}{FU} \tag{2.6}$$

$$\dot{m}_{cat,in} = 8\frac{FU}{AU} \cdot \frac{1}{\chi} \cdot \dot{m}_{an,in} \tag{2.7}$$

$$\dot{m}_{an,out} = (1 + 8FU) \cdot \dot{m}_{an,in} \tag{2.8}$$

$$\dot{m}_{cat,out} = \dot{m}_{cat,in} - 8FU \cdot \dot{m}_{an,in} \tag{2.9}$$

## 2.2. COMPONENT MODELS

The analytical models used to size the components defined in Table 1.1 and model the fluid flow through them are collected in this section. These components are the tank, pipe, pump, heat exchanger, compressor and turbine. The temperatures and pressures implemented in the models are the static values.

### 2.2.1. TANK SIZING

The liquid hydrogen storage tank modelled for the hydrogen supply architectures consists of a cylindrical body with hemispherical end-caps. The structure of the tank includes an inner vessel to withstand the design internal pressure, a layer of insulating material to regulate the environmental heat entering the tank, and an outer vessel which is subjected to external pressures. This model was implemented for both the main hydrogen storage tank and for the vaporiser, where the latter does not have an insulating layer. A cross-sectional view of the hydrogen storage tank can be seen in Figure 2.3.

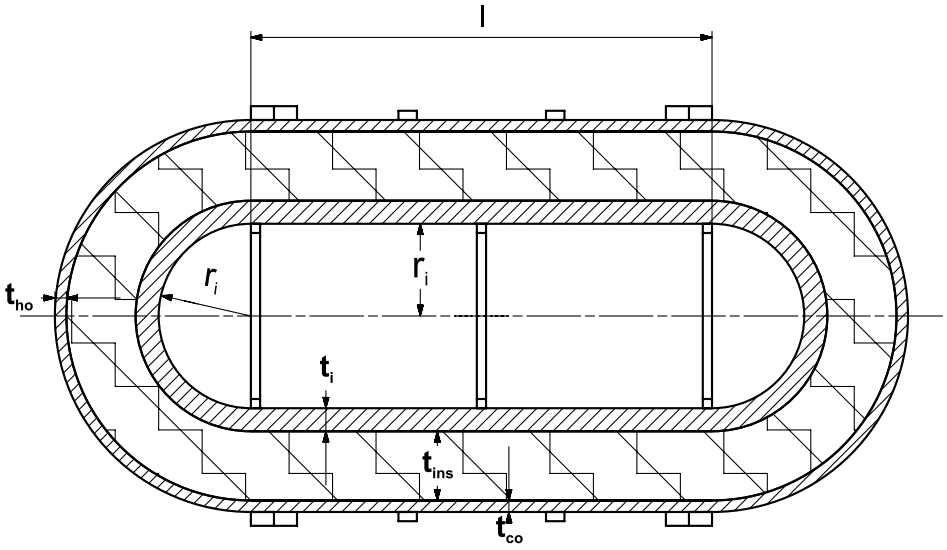


Figure 2.3: Cross-sectional view of storage tank

The iterative design process used to size the tank and the main parameters required for the tank sizing module are presented in Section 3.2.1. In addition, this section contains the methodology used for the sizing of the inner, outer, and insulation layers. The self-pressurisation model is subsequently described in Section 2.2.2. It is used to simulate the heating requirements for the tank to maintain its operational pressure throughout the mission.

### INNER VESSEL SIZING

The sizing of the inner vessel is performed using the methods presented by Barron and Colozza [12, 13]. Given the total mass and volume of hydrogen required ($m_{H_2}$ and $V_{H_2}$ respectively) and the inner radius $r_i$, the length of the cylindrical section of the tank $l$ can be derived from the tank shape using the following equation.

$$l = \frac{V_{H_2} - \frac{4}{3}\pi r_i^2}{\pi r_i^3} \tag{2.10}$$

The minimum required thickness of the cylindrical and hemispherical sections of the tank ($t_{cyl}$ and $t_{sph}$ respectively) can then be computed using the ASME Code equations presented by Barron [12] shown in Equation 2.11 and Equation 2.12. In these equations, $p$ is the tank design internal pressure (maximum operational pressure) and $r_i$ is the internal radius of the tank. The allowable stress and the weld efficiency ($\sigma_a$ and $e_w$ respectively) are material properties of the tank provided by the user.

$$t_{cyl} = \frac{2pr_i}{2\sigma_a e_w - 1.2p} \tag{2.11}$$

$$t_{sph} = \frac{pr_i}{2\sigma_a e_w - 0.2p} \tag{2.12}$$

In order to limit stress concentrations due to the step imposed by the different thicknesses, a constant thickness $t_i$ is implemented, which is the equal to the larger of the two calculated for the inner vessel. With all the dimensions of the inner vessel specified, its mass can be computed simply using its density $\rho_i$ and its volume as in Equation 2.13.

$$m_i = \rho_i \cdot \left(\frac{4}{3}\pi(r_i + t_i)^3 + \pi(r_i + t_i)^2 l - V_{H_2}\right) \tag{2.13}$$

### OUTER VESSEL SIZING

The sizing of the outer vessel thickness is done similarly to that of the inner vessel by using the ASME Code equations presented by Barron [12]. The thickness of the cylindrical part of the tank depends on if the tank can be classified as a "long" or "short" cylinder. The condition for classifying a cylinder as "long" can be seen in Equation 2.14. In this equation, $L_{cyl}$ is the unsupported length of the cylindrical section (which is equal to its length in this case). $d_{co}$ and $t_{co}$ are the diameter and thickness of the cylindrical section of the outer vessel. Finally, $\nu$ is the Poisson's ratio of the material.

$$\frac{L_{cyl}}{d_{co}} > 1.14\left(1-\nu^2\right)^{\frac{1}{4}}\left(\frac{d_{co}}{t}\right)^{\frac{1}{2}} \tag{2.14}$$

The main sizing parameter is the collapsing pressure of the cylinder $p_c$, which is 4 times the allowable external pressure (i.e. atmospheric pressure) $p_a$ according to the ASME Code, where the factor 4 is the safety factor [12]. For a "long" cylinder, this collapsing pressure is implemented alongside the tank material properties (Young's modulus $E$ and the Poisson's ratio $\nu$) and the outer diameter of the tank to obtain the thickness as can be seen in Equation 2.15 [12]. The equation for sizing a "short" cylinder uses the same parameters and is displayed in Equation 2.16 [12].

$$\text{Long Cylinder:} \quad p_c = \frac{2E\left(\frac{t_{co}}{d_o}\right)^3}{1-\nu^2} \tag{2.15}$$

$$\text{Short Cylinder:} \quad p_c = \frac{2.42E\left(\frac{t_{co}}{d_o}\right)^{\frac{5}{2}}}{(1-\nu^2)^{\frac{3}{4}}\left(\left(\frac{L_{cyl}}{d_o}\right) - 0.45\left(\frac{t_{co}}{d_o}\right)^{\frac{1}{2}}\right)} \tag{2.16}$$

The thickness of the spherical part of the tank (head) is calculated similarly to the long cylinder thickness as is displayed in Equation 2.17, where $K_1$ is a factor related to how elliptical the tank head is. For a spherical head, the factor is equal to 0.5 [12].

$$p_c = \frac{0.5E\left(\frac{t_{ho}}{K_1 d_{ho}}\right)^2}{(3(1-\nu^2))^{0.5}} \tag{2.17}$$

The initial thickness of the outer vessel is assumed to be equal to that of the inner vessel, while that of the insulation is first set to zero. These assumptions influence the outer diameter and thickness used in the computations. These thicknesses converge during the iterative design process presented in Section 3.2.1.

### INSULATION SIZING

The purpose of the insulation is to reduce the amount of heat entering the tank from the environment to maintain a desired liquid hydrogen boiloff rate while the aircraft is at standstill.

The method used to perform the sizing of the insulation layer involves calculating the thermal resistance of the individual layers of the tank. A figure of the thermal model of the tank can be seen in Figure 2.4 . At the design condition, the ambient temperature of the fuselage and the temperature of the hydrogen inside the tank are given. The thermal resistance of each layer of the tank is dependant on its thickness. The thickness of the inner and outer vessel are dependant are functions of the pressure requirements of the tank, while that of the insulating layer mainly depends on the standstill boiloff rate requirements. This thickness can be obtained as follows. The temperatures on either side of the insulation layer are computed using the heat transfer rate from the environment required to maintain the boiloff rate and the ambient and liquid hydrogen temperatures. Once these temperatures are known, they are used in combination with the heat transfer rate to obtain the required thermal resistance of the insulating layer, and subsequently its thickness.

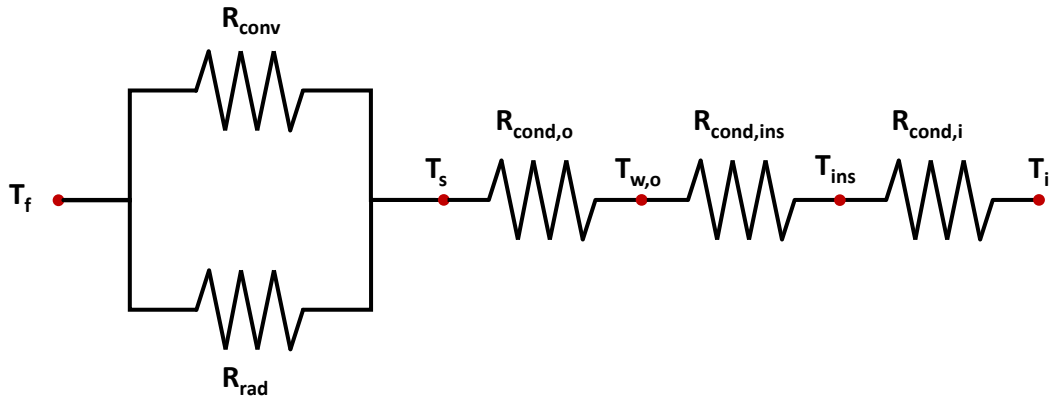


Figure 2.4: Thermal resistance figure for the tank layers.

The function relating the temperature difference between the two sides of a layer $\Delta T$, heat transfer rate $\dot{Q}$, and the thermal resistance of the layer $R$ can be seen below.

$$\dot{Q} \cdot R = \Delta T \tag{2.18}$$

The first step in the sizing of the insulation layer is determining the heat transfer rate $\dot{Q}$ required to maintain the desired boiloff rate. This can be computed with the latent heat of vaporisation ($LHV$) at the storage conditions as can be seen in Equation 2.19 [13].

$$\dot{Q} = \dot{m}_{bo} \cdot LHV_{H_2} \tag{2.19}$$

Next, the thermal resistance of each layer needs to be computed. The heat transfer methods that are used by the model include radiation, convection, and conduction.

First, the thermal resistance between the surrounding environment and the outer surface of the tank needs to be computed to determine the surface temperature of the tank due to radiation and convection. The radiation heat transfer coefficient $h_{rad}$ is computed using the following equation, where $\sigma_{bolt}$ is the Stefan-Boltzmann constant for radiation ($5.67 \cdot 10^{-8}\ W/(m^2K^4)$), $e_o$ is the emissivity of the outer surface, and $T_s$ and $T_f$ are the temperatures of the tank surface and the fuselage respectively.

$$h_{rad} = \sigma_{bolt} e_o \left(T_s^2 + T_f^2\right)(T_s + T_f) \tag{2.20}$$

The convection heat transfer coefficient is related to the Nusselt number $Nu$, the outer diameter of the tank $d_s$, and the thermal conductivity of the air around the tank $k_{air}$.

$$h_{conv} = \frac{k_{air} Nu}{d_s} \tag{2.21}$$

The Nusselt number for the tank is computed as follows. Equation 2.22 and Equation 2.23 display the Nusselt number for a sphere and cylinder respectively. They both use the Rayleigh $Ra$ and Prandtl $Pr$ numbers in the computation, which are obtained using Equation 2.24 and Equation 2.25 respectively [13].

$$Nu_{sph} = 2 + \frac{0.589 Ra^{0.25}}{\left(1 + \left(\frac{0.469}{Pr}\right)^{\frac{9}{16}}\right)^{\frac{4}{9}}} \tag{2.22}$$

$$Nu_{cyl} = \left(0.6 + \frac{0.387 Ra^{\frac{1}{6}}}{\left(1 + \left(\frac{0.559}{Pr}\right)^{\frac{9}{16}}\right)^{\frac{8}{27}}}\right)^2 \tag{2.23}$$

$$Ra = \frac{g\beta(T_f - T_s)d_s^3}{\nu_v \alpha_d} \tag{2.24}$$

$$Pr = \frac{\nu_v}{\alpha_d} \tag{2.25}$$

The main parameters implemented in these equations are the gravitational acceleration $g$, the volumetric thermal expansion coefficient $\beta$, the temperatures of the fuselage $T_f$ and tank surface $T_s$, the diameter of the object $d_s$, the air diffusivity $\alpha_d$, and the air kinematic viscosity $\nu_v$. For an ideal gas, the volumetric thermal expansion coefficient $\beta$ is equal to the inverse of the temperature as shown in Equation 2.26 [13]. Approximations for the diffusivity and kinematic viscosity of air depending on the temperature are used as in Equation 2.27 and Equation 2.28 [13].

$$\beta = \frac{1}{T_f} \tag{2.26}$$

$$\alpha_d = -3.119 \cdot 10^{-6} + 3.541 \cdot 10^{-8} T_f + 1.679 \cdot 10^{-10} T_f^2 \tag{2.27}$$

$$\nu_v = -2.079 \cdot 10^{-6} + 2.777 \cdot 10^{-8} T_f + 1.077 \cdot 10^{-10} T_f^2 \tag{2.28}$$

The total Nusselt number for the tank is assumed to be a weighted average of the individual geometries that make up the tank as can be seen in Equation 2.29.

$$Nu = \frac{l \cdot Nu_{cyl} + d_o \cdot Nu_{sph}}{l + d_o} \tag{2.29}$$

The thermal resistance between the environment and the tank is then computed given that the heat transfer due to convection and radiation occur in parallel. Similarly to electrical resistance, the total thermal resistance is then equal to the inverse of the sum of the inverse of the two individual thermal resistances. This can be seen in Equation 2.30.

$$R_{air} = \left(R_{rad}^{-1} + R_{conv}^{-1}\right)^{-1} = \frac{1}{A} \cdot \frac{1}{h_{rad} + h_{conv}} = \frac{1}{2\pi r_{s,cyl} l + 4\pi r_{s,sph}^2} \cdot \frac{1}{h_{rad} + h_{conv}} \tag{2.30}$$

It should be noted that the thermal resistance of the air is a function of the surface temperature of the tank, which is the desired value from these computations. Therefore, the value is solved for by initially assuming the temperature of the tank surface to be equal to the fuselage temperature, and iterating the computations until the surface temperature converges.

The process continues with the conductive heat transfer through the outer and inner vessel of the tank due to the temperature of the outer surface and the temperature of the stored hydrogen. The temperature of

the inner surface of the inner vessel is assumed to be equal to the temperature of the hydrogen stored inside.

A general method for computing the conduction thermal resistance through a layer is based on the conduction through a hollow sphere and cylinder occurring in parallel, which are presented in Equation 2.31 and Equation 2.32 respectively. In these equations, $r_i$ and $r_o$ are the radial positions of the inner and outer surface of the layer respectively, l is the length of the cylindrical section, and k is the thermal conductivity of the layer investigated. The total conduction thermal resistance is obtained with Equation 2.33.

$$R_{cond,sph} = \frac{1}{4\pi k}\left(\frac{1}{r_i} - \frac{1}{r_o}\right) \tag{2.31}$$

$$R_{cond,cyl} = \frac{\ln \frac{r_o}{r_i}}{2\pi l k} \tag{2.32}$$

$$R_{cond} = \left(R^{-1}_{cond,sph} + R^{-1}_{cond,cyl}\right)^{-1} \tag{2.33}$$

This method can then be used to determine the temperatures on the inner and outer surface of the insulation layer. Given these temperatures, the relation between the heat transfer rate, temperature difference, and thermal resistance shown in Equation 2.18 can be used to compute the required insulation thickness that fulfils the relation. The thermal resistance of the insulation layer is obtained using the equations for conductive heat transfer resistance shown above. The design process is then iterated until the thicknesses of the outer layer and insulation converge.

Finally, the overall thermal resistance of the tank can be calculated by adding the resistances of each layer in series as can be seen in Equation 2.34, where the subscripts *ins*, *o*, *i* and *env* refer to the resistances of the insulation, outer vessel, inner vessel, and environment. This value is utilised in the self-pressurisation computations to determine the heat entering the tank from the atmosphere at different altitudes.

$$R_{tank} = R_{ins} + R_o + R_i + R_{env} \tag{2.34}$$

### 2.2.2. TANK SELF-PRESSURISATION

Throughout the duration of the mission, the pressure of the tank needs to be maintained at a desired value to ensure that the required pressure at the Solid Oxide Fuel Cell (SOFC) is met given that either liquid or gaseous hydrogen is extracted from the tank for a given architecture. This is performed by heating the liquid hydrogen in the tank and causing it to boil of, leading to isochoric expansion and an increase in pressure for the same tank volume due to the lower average density in the tank. In order to compute the heat required for the condition to be met, a general methodology is constructed which is applicable for hydrogen supply architectures utilising either liquid or gaseous extraction. This methodology is based on the conservation of energy in the tank and is derived from the superheated vapour method presented by Al Ghafri et al [14]. The general equations for the energy balance in the tank for the liquid and gaseous hydrogen are presented below [14].

$$\dot{Q}_H + \dot{Q}_{VL} + \dot{Q}_L = \frac{dH_L}{dt} + \dot{m}_{LV} h_{LV} + \dot{m}_L h_L \tag{2.35}$$

$$\dot{Q}_V - \dot{Q}_{VL} = \frac{dH_V}{dt} - \dot{m}_{LV} h_{LV} + \dot{m}_V h_V + \dot{m}_{vent} h_V \tag{2.36}$$

In these equations, $\dot{Q}$ is the heat transfer rate entering the fluid, $\dot{m}$ is the mass flow rate of hydrogen, $H$ is the enthalpy, and $h$ is the specific enthalpy of the fluid. The subscripts $L$ and $V$ represent the mass flow rates of the liquid and vapour phases of hydrogen leaving the vessel respectively, and the subscript $LV$ indicates transfer from the liquid to vapour phase. $h_{LV}$ is the difference is specific enthalpy of the two phases. For the gaseous hydrogen extraction architecture, the liquid mass flow rate is set to 0 and the gaseous mass flow rate is equal to the system mass flow rate, while the opposite is true for the liquid hydrogen extraction architectures. The heat transfer rate due to a heating system is indicated by the variable $\dot{Q}_H$. The venting mass flow rate $\dot{m}_{vent}$ is either zero when the pressure of the tank is less than or equal to the allowable pressure set by the user and is larger than zero when the allowable pressure is exceeded.

In order to simplify calculations, some assumptions are made with regards to the system. First, it is assumed that both phases of hydrogen are homogeneous and all heat transferred is spread evenly throughout the individual phases. Next, the liquid hydrogen in the tank is assumed to be saturated, as its storage temperature is close to its boiling point. These assumptions are made by Al Ghafri et al and Colloza [13, 14]. Finally, it is assumed that all heat transferred to the vapour phase from the environment is transferred to the liquid phase of hydrogen ($\dot{Q}_V = \dot{Q}_{VL}$) [13]. Since the total heat entering the tank from the environment is the sum of the heat entering the individual phases, this leads to the following equations for the energy balance.

$$\dot{Q}_H + \dot{Q}_{env} = \frac{dH_L}{dt} + \dot{m}_{LV} h_{LV} + \dot{m}_L h_L \tag{2.37}$$

$$\frac{dH_V}{dt} - \dot{m}_{LV} h_{LV} + \dot{m}_V h_V + \dot{m}_{vent} h_V = 0 \tag{2.38}$$

Given a tank design and the surrounding environment, the heat entering the tank from the environment is computed using Equation 2.18. Additionally, the mass flow rate of gaseous or liquid hydrogen flowing from the tank to the supply system is known throughout the mission. The enthalpies and specific enthalpies are derived via the fluid properties of each phase, as the pressure and density are set initially via the tank operational pressure and the initial fill level of the tank. During the mission, the density varies by computing the change in mass, and subsequently the volume, of liquid and gaseous hydrogen due to flow of hydrogen through the system and the evaporation of liquid hydrogen. The pressure is kept constant at a certain operational point which accounts for the pressure losses of the system. The enthalpy of each phase is obtained by multiplying the specific enthalpy by the total mass of each phase. Finally, the venting mass flow rate is initially set to zero.

Once the hydrogen supply architecture and aircraft mission details are defined, an analysis of the pressure control of the tank throughout the mission can be performed. The system is solved as follows. First an initial guess of the mass flow rate of the hydrogen changing phases from liquid to vapour is provided. This initial guess is set to be equal to the mass flow rate of hydrogen required by the hydrogen supply architecture. Subsequently, the change in mass of the liquid and gaseous hydrogen in the tank is computed for a chosen time step $dt$ in Equation 2.39 and Equation 2.40. In these equations, the subscripts 1 and 2 refer to the values before and after the time step respectively.

$$m_{L,2} = m_{L,1} - \dot{m}_L dt - \dot{m}_{LV} dt \tag{2.39}$$

$$m_{V,2} = m_{V,1} - \dot{m}_V dt + \dot{m}_{LV} dt \tag{2.40}$$

The change in volume for the liquid hydrogen is calculated simply with the density at the saturation point, while the new volume of the gaseous hydrogen is obtained by subtracting the volume of liquid hydrogen from the tank volume. Subsequently, the new density of the gaseous hydrogen can be computed.

$$V_{L,2} = \frac{m_{L,2}}{\rho_L} \tag{2.41}$$

$$V_{V,2} = V_{Tank} - V_{L,2} \tag{2.42}$$

$$\rho_{V,2} = \frac{m_{V,2}}{V_{V,2}} \tag{2.43}$$

The operational pressure of the tank at different phases of the mission can either be set by the user or computed via the pressure losses in the system and the SOFC requirements. Additionally, for the former, the pressure gradient with respect to time can be decided by the user. When the change in pressure for a timestep is defined, the pressure and density of the gaseous and liquid hydrogen after the timestep are used to determine the complete properties. The changes in enthalpy for each phase over the timestep can then be calculated, which are then substituted in Equation 2.37 and Equation 2.38 to recalculate the mass flow rate from the liquid to vapour phase $\dot{m}_{LV}$. This process is iterated until this value is converged. As such, the heat transfer rate $\dot{Q}_H$ required to achieve the desire pressure change can be obtained.

If the heat transfer rate calculated is negative, the heat from the environment exceeds the heat required to keep the pressure constant, which means that the tank would need to be cooled. The other option is to keep the heat transfer rate due to the heating system zero and observe the self-pressurisation of the tank due to

the environmental heat. In that case, the same equations can be utilised to solve for the pressure change in the tank. However, in this scenario, $\dot{Q}_H$ is set to zero, and the estimate of the mass flow rate from the liquid to vapour phase $\dot{m}_{LV}$ is used to compute the change in specific enthalpy for the liquid phase over the timestep. Next, the new specific enthalpy and density of the liquid phase can be used to derive its saturation pressure at the new time step. This pressure is combined with the density of the vapour phase to obtain the change in enthalpy of the vapour phase and recalculate the liquid to vapour mass flow rate. This is iterated until the mass flow rate converges, at which point the pressure change over the timestep is determined.

Lastly, if the pressure exceeds a predetermined allowable pressure for the tank, the pressure change and heat transfer rate are both set to zero, and the venting mass flow rate required to maintain the maximum allowable pressure is computed using the same methodology.

This method for calculating the power required for heating the tank can be utilised to determine the maximum additional heating power required during a mission phase, for example when the largest mass flow rate is required by the fuel cell, and implement it in the overall system optimisation process. Additionally, it can be extended for the entire mission duration, where each timestep can have a different extraction mass flow rate leaving the tank, as required by the fuel cell. Subsequently, the total additional energy required by the system to heat up the tank over the duration of the mission can be computed. This additional energy requirement could be compensated via additional hydrogen mass flow rate through the fuel cell, which in turn affects the sizing of the system, or via waste energy reduction methods, such as energy extraction from the fuel cell exhaust gases using a turbine, or any other synergy within the system based on its topology and components.

When considering the power required for the vaporiser, the same method can also be used. For a preliminary power estimation, it is assumed that the liquid mass flow rate entering the vaporiser is equal to the gaseous mass flow rate exiting towards the SOFC, and are related to each other as in Equation 2.44.

$$\dot{m}_L = -\dot{m}_V \tag{2.44}$$

### 2.2.3. PIPE MODELLING

Pipes are required inside the aircraft to transport the hydrogen fuel and air between components and towards the Solid Oxide Fuel Cell (SOFC). However, during the fluid transport, pressure and temperature losses are incurred due to factors such as frictional pressure losses and environmental heat transfer. They also depend on the fluid state in the flowfield inside the pipes. For example, gaseous hydrogen is compressible while liquid hydrogen is not, leading to different pressure losses. An insulating layer is added to the pipe in order to ensure that the desired behaviour with respect to the pressure, temperature and velocity of the fluid is achieved. This layer also helps in achieving single-phase flow through the system (i.e. no change in phase from liquid to gaseous), as the modelling of two-phase flow requires higher fidelity simulation. Hence, the analytical models implemented in this work are not sufficient for such cases. A cross-sectional view of the pipe along its length is illustrated Figure 2.5.

#### MASS COMPUTATION

The minimum thickness $t$ of the pipes is obtained using the "ASA Code for Pressure Piping" for pipes subjected to internal pressure, which can be seen in Equation 2.45 [12]. In this equation, $p$ is the maximum pressure experienced by the pipe, $d_o$ is the outer diameter of the pipe, and $\sigma_a$ is the allowable stress of the pipe material.

$$t = \frac{p d_o}{2\sigma_a + 0.8p} \tag{2.45}$$

On top of the thickness requirement due to the pressure of the fluid flowing through the pipe, there are manufacturability restrictions imposed upon its construction, such as a minimum thickness required to weld two pipes together or apply fittings. A set of predefined pipe schedules is provided by the ASME for stainless steel pipes for which the actual thickness of the pipes is obtained using the inner radius and calculated thickness to find the nearest schedule which satisfies the pressure requirements [12]. Given a combination of the inner radius and calculated thickness, the nearest combination of outer diameter (O.D.) and thickness are

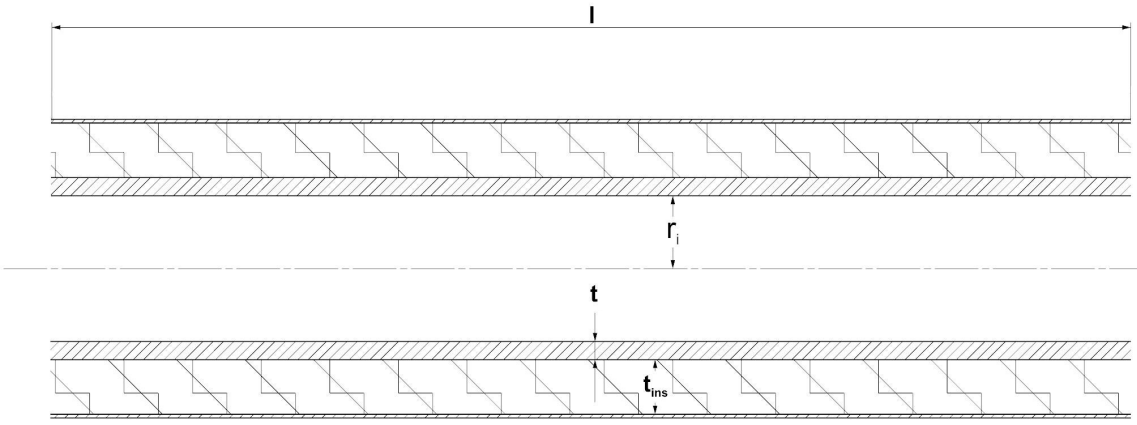


Figure 2.5: Cross-sectional view of the pipe.

selected that correspond to the desired inner radius [15]. The thicknesses can be seen in Appendix A.

### PRESSURE LOSSES ALONG STRAIGHT PIPES

The pressure drop through a straight pipe for an incompressible fluid (liquid hydrogen) can be determined using the Darcy-Weisbach equation shown in Equation 2.46. In this equation, $l$ is the length of the pipe, $d$ is the inner diameter, and $v$ is the speed of the flow inside the pipe. and. $f_D$ is the Darcy friction factor calculated using Equation 2.47 for turbulent flow [16]. The fluid properties are assumed to be constant along the pipe segments in this equation.

$$\Delta p = \frac{f_D l \rho v^2}{2d} \tag{2.46}$$

In order to compute the friction factor, the roughness of the pipe $\epsilon$ is required, which can be obtained from the material properties. The Reynold's number is computed in Equation 2.49, where $\mu$ is the dynamic viscosity , $v$ is the velocity, and $\rho$ is the density of the fluid. These parameters are combined in the implicit Colebrook-White formula seen in Equation 2.47 for calculating the friction coefficient [17]. An initial estimate for the implicit solving is provided using the less precise Moody's approximation shown in Equation 2.48 [16].

$$\frac{1}{f_D} = -2\log\left(\frac{\epsilon}{3.7d} + \frac{2.51}{Re\sqrt{f_D}}\right) \tag{2.47}$$

$$f_D = 0.0055\left[1 + \left(2\cdot 10^4 \frac{\epsilon}{d} + \frac{10^6}{Re}\right)^{\frac{1}{3}}\right] \tag{2.48}$$

$$Re = \frac{\rho v d}{\mu} \tag{2.49}$$

For laminar flow ($Re < 2300$), the frictional coefficient is calculated as follows [12].

$$f_D = \frac{64}{Re} \tag{2.50}$$

As gaseous hydrogen is a compressible fluid, the pressure change is computed using the formula in Equation 2.51 derived by Coelho et al. from the general equation for steady state flow [18]. This formula assumes a constant velocity for the fluid along the pipe segment. Additionally, values for the average pressure $p$, temperature $T$, and compressibility $Z$ of the fluid between the inlet and outlet of the segment are utilised. In the equation, $\rho$ and $v$ are the fluid density and velocity, $\bar{R}$ is the universal gas constant and equal to 8314.41 $J/(kmol \cdot K)$ and $\Delta z$ is the pipe elevation change.

$$\frac{M_{H_2}}{Z_{avg}\bar{R}T_{avg}}\frac{p_2^2-p_1^2}{2}+\frac{gp_{avg}^2M_{H_2}^2}{\left(Z_{avg}\bar{R}T_{avg}\right)^2}\Delta z+f_D\frac{l}{d}\frac{\rho^2v^2}{2}=0 \tag{2.51}$$

As the average values can not be known beforehand, this can be counteracted by splitting the pipe into multiple segments and utilising the inlet values instead. The output fluid properties of a preceding segment are passed along as an input for the next segment. This is also performed for the pressure losses of the incompressible fluids. While this increases the accuracy of the implementation, a tradeoff exists between the accuracy, the number of segments, and the computational cost. A study regarding the effect of the number of segments is presented in Section 4.6.

For the incompressible fluid, when there is a change in the elevation $\Delta z$ of the pipes, the additional pressure change is computed as follows [19].

$$\Delta p=-\rho g\Delta z \tag{2.52}$$

#### PRESSURE LOSSES DUE TO FITTINGS

Pressure losses along a pipe also occur due to the fittings applied to the pipe length. These include valves, bends, and tees. The k-method is used to obtain the headloss (pressure loss) $h_f$ in meters water gauge (mwg) in the equation below using the flow velocity $v$, the gravitational acceleration $g$ (9.81 m/s$^2$) and the $k_f$ factor of the fittings on the line. Table 2.1 displays values for $k_f$ for a few different fitting types. The $k_f$ factor method is applicable for both fluid phases [20, 21].

$$\Delta p_{fittings}=-\frac{k_f\rho v^2}{2} \tag{2.53}$$

Table 2.1: $k_f$ factor values for different fitting types [20, 21].

| **Fitting Type** | $k_f$ **Value** |
|---|---|
| Open Isolation Valve | 0.4 |
| Open Control Valve | 10.8 |
| Short Radius Bend (for every bend of 22.5deg) | 0.2 |
| Long Radius Bend (for every bend of 22.5deg) | 0.1 |
| Standard Tees used as elbows | 0.7 |
| Standard Tees Run Through | 0.1 |

#### TEMPERATURE CHANGE ALONG PIPE

In addition to the pressure drop over the length of the pipe, the temperature change needs to be calculated to discern the effect of the environmental heat transfer on the hydrogen fluid properties. This is done by computing the heat transfer coefficient $U$ of the pipe and the Joule-Thomson coefficient $\mu_{JT}$ of the hydrogen fluid. The latter influences the Joule-Thomson effect which describes the temperature change of a fluid when a change in pressure is applied at constant enthalpy.

The heat transfer coefficient of the fluid flowing through the pipes is obtained using the Reynolds and Prandtl numbers ($Re$ and $Pr$ respectively) [22]. The Prandtl number is computed using the specific heat capacity $c_p$, the dynamic viscosity $\mu$ and the thermal conductivity $k$ of the fluid as in Equation 2.54. This is then combined with the Reynolds number to obtain the Nusselt number $Nu$ in Equation 2.55.

$$Pr=\frac{c_p\mu}{k} \tag{2.54}$$

$$Nu=0.023Re^{0.8}Pr^{0.3} \tag{2.55}$$

Subsequently, the heat transfer coefficient of the fluid $\alpha_{fl}$ is determined using the following equation [22].

$$\alpha_{fl}=\frac{Nu\cdot k}{d} \tag{2.56}$$

In order to obtain the overall heat transfer coefficient $U$ of the entire pipe, the effect of the wall material and insulation also need to be taken into account. It is calculated as a function of the heat transfer coefficient of the fluid $\alpha_{fl}$, the thermal conductivity of the pipe and insulation materials ($k_{pipe}$ and $k_{ins}$ respectively), and their corresponding dimensions as can be seen in Equation 2.57 [22, 23]. The outer radius $r_o$ is the sum of the inner radius $r_i$ and the thickness $t$, and the insulation radius $r_{ins}$ adds the insulation thickness $t_{ins}$ to that. Additionally, the radiation heat transfer occurring in parallel $h_{rad}$ is obtained using Equation 2.20, where, due to the thin walls of the pipe, it is assumed that the surface temperature of the pipes is equal to the inlet temperature.

$$U = \frac{1}{\alpha_{fl}^{-1} + \frac{r_i}{k_{pipe}} \ln\left(\frac{r_o}{r_i}\right) + \frac{r_i}{k_{ins}} \ln\left(\frac{r_{ins}}{r_o}\right)} + h_{rad} \tag{2.57}$$

The Joule-Thomson coefficient is described using Equation 2.58, where $c_p$ is the specific heat capacity at constant pressure, $T$ is the temperature of the fluid, $v$ is the specific volume and is equal to the inverse of the density ($\frac{1}{\rho}$), and $\left(\frac{\partial v}{\partial T}\right)_p$ is its derivative with respect to temperature at a constant pressure.

$$\mu_{JT} = \frac{1}{c_p}\left(T\left(\frac{\partial v}{\partial T}\right)_p - v\right) \tag{2.58}$$

Finally, the temperature change over the length of the pipe is obtained with the following equation [23], which is a function of the pressure drop over the segment length $\frac{dp}{dl}$.

$$T_2 = T_{atm} + (T_1 - T_{atm})e^{\frac{-lU\pi d}{\dot{m}c_p}} + \frac{\dot{m}}{\pi U d}\left(\mu_{JT} c_p \frac{dp}{dl}\right)\left(1 - e^{\frac{-lU\pi d}{\dot{m}c_p}}\right) \tag{2.59}$$

Similarly to the pressure change computations, constant fluid properties are assumed along the segment length. Therefore, this method is applied by splitting the pipe into multiple segments and passing the intermediate output values from one pipe segment to the next.

### 2.2.4. PUMP MODELLING

In order to develop architectures that implement pumps to overcome the pressure drop over the hydrogen supply architecture and ensure the required pressure at the SOFC inlet, an analytical model for the preliminary sizing of the pumps as well as the simulation of the pressure rise over them is developed. As the temperatures of the fluid in the architecture are typically near cryogenic conditions, suitable pumps are required. Information on the low/medium fidelity design of cryogenic pumps and modelling of their effects on the flow of hydrogen through the architecture is not widely available, therefore their sizing is performed by assuming a similar process to regular pumps. The types of pumps considered for the model are positive displacement or centrifugal. The former is utilised when constant flow rates are required, while the latter allows for a variation in the flow rate and outlet pressure [20].

The pump specific speed $n_q$ is an important parameter used to determine the required pump type. It can be obtained from the flow conditions and gives the pump speed that would generate similar flow characteristics (i.e. pressure increase and flow rate) in geometrically similar pumps [24, 25]. Two pumps are geometrically similar if the ratio of the fluid velocities at the tip, inlet and outlet of the impeller are the same [25], regardless of the impeller diameter or rotational speed. Therefore, the pump specific speed can be used to compare different geometrically dissimilar centrifugal pumps and see which would be suitable for a certain application. Radial, semi-axial, and axial pumps are built in a range of $7 < \eta_q < 400$. If the specific speed for a certain application is determined to be below that range, positive displacement pumps should be considered [25].

The specific speed $n_q$ of a pump can be computed using Equation 2.60, where $\dot{V}$ is the volumetric flowrate required by the pump, $\omega$ is the pump rotational speed, $\rho$ is the fluid density, and $\delta H$ is the required pump head rise and is related to the pressure rise with Equation 2.61 [25].

$$n_q = 52.9\omega \frac{\sqrt{\dot{V}}}{(g\delta H_p)^{0.75}} \tag{2.60}$$

$$\delta H_p = \frac{\delta p}{\rho g} \tag{2.61}$$

The pump speed required for a centrifugal pump can be estimated with Equation 2.62. Here $n_{ss}$ is the suction specific speed, which is a similarity ratio that is used to determine safe operating speed for a specific type of pump when operated at the design point. For standard pumps with low flow velocities, a value of 160 can be used [25]. The Net Positive Section Head Available ($NPSH_A$) is the available head above a fluid's vapour pressure $p_{vap}$ and is an indication of how close the fluid is to cavitation (formation of vapour bubbles in the pump), which leads to increased wear in the pump [25]. The Net Positive Section Head Required ($NPSH_R$) is then the minimum suction head that must be exceeded to avoid cavitation and is computed using Equation 2.63 [25]. Note that since the tank is saturated during operation, the inlet pressure of the pump can be extremely close to the vapour pressure. Therefore, this scenario is also taken into account for the pump selection process.

$$\omega = n_{ss} \frac{NPSH_R^{0.75}}{\sqrt{\dot{V}}} \tag{2.62}$$

$$NPSH_R = 0.878 \cdot NPSH_A^{0.877} = \frac{p_{in} - p_{vap}}{\rho g} + \frac{v_{in}^2}{g} \tag{2.63}$$

With these equations, the specific speed of the pump can be calculated and used to decide on the most applicable pump type for the desired performance, as described by Gülich [25]. For the mission analysed in this report, a maximum specific speed of around 5 is calculated at the maximum mass flow rate, and a minimum of around 1 for the minimum mass flow rate and inlet pressure equal to the vapour pressure of hydrogen. This puts it near the limits of the centrifugal pump design space (and outside the range of radial or axial types) and more towards positive-displacement pumps. In addition to this pumps that are implemented in hydrogen supply architectures typically experience low mass and volumetric flow rates (maximum values in the order of 50 $g/s$ and 0.0005 $m^3/s$ respectively for the SOFC analysed in this report), which are much lower than those typically experienced by centrifugal pumps (typical volumetric flow rates between 0.001 $m^3/s$ and 60 $m^3/s$) [25]. A piston pump was selected for this work due to the following reasons. It displays high efficiency near the minimum calculated specific speed. Additionally, in the context of low flow rate for a low-density fluid, the utilisation of piston-cylinder type pumps has previously shown to present a compelling solution [26]. The volume envelope of a piston pump can be varied without changing the flow rate by either increasing the stroke length and decreasing the piston diameter, or vice-versa, thus offering greater packaging solutions. Furthermore, the number of cylinders can be increased to allow for a similar flow rate in smaller sized pistons. Finally, preliminary sizing methods for a piston pump are widely available.

A simplified piston pump model was utilised for the implementation in the pump driven hydrogen supply architectures consisting of a set of piston-cylinder devices, as portrayed in Figure 2.6, along with a corresponding motor. This model was based on the methods presented by Miller [26]. The operation of the piston-cylinder device involves the linear movement of the piston along the cylinder due to the rotation of the piston crank with length $r$. As the crank rotates from 0 to $\pi$ radians, the pump is in the discharge stroke, where the fluid leaves the cylinder through the outlet, while from $\pi$ to $2\pi$ radians, the pump is in the suction stroke and fluid is entering the cylinder. A connecting rod of length $L_p$ transfers the rotational motion of the crank to the linear motion of the piston. The length of the piston and cylinder are set to be equal to the stroke length $s$, which is equal to two times the crank radius. The piston pump may contain multiple cylinder devices connected to the same crank, spread evenly across the rotation.

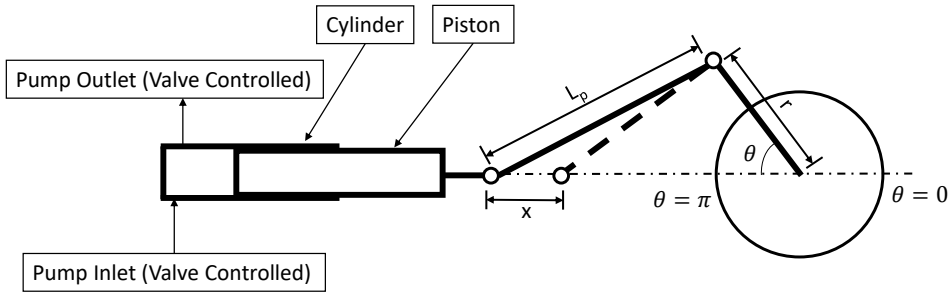


Figure 2.6: Simplified piston pump model.

The relationship between the crank angle $\theta$ and the piston position $x$ is given with Equation 2.64. This equation is critical in the computation of the dynamic characteristics of the pump such as the flowrate and pressure variations along a complete crank revolution.

$$x = r\left(1 - \cos\theta + \frac{L_p}{r} - \sqrt{\frac{L_p^2}{r^2} - \sin^2\theta}\right) \tag{2.64}$$

### FLOWRATE MODELLING

First the fluid flowrate through the pump is analysed. The mean volumetric flowrate of the pump $\dot{V}$ is obtained from the mass flowrate $\dot{m}$ and the fluid density $\rho$ required by the SOFC as in Equation 2.65. However, due to the motion of the piston, the flowrate will fluctuate around the mean, which has an effect on the outlet pressure and the stresses experienced by the cylinder, and the sizing of the pump.

$$\dot{V} = \frac{\dot{m}}{\rho} \tag{2.65}$$

The time derivative of the piston position function shown in Equation 2.64 results in the velocity of the piston in the cylinder as can be seen in the equation below, where $C$ is equal to $\frac{L_p}{r}$, and the pump rotational speed $\omega$ is the time derivative of the crank angle $\theta$ ($\theta = \omega t$). Larger efficiencies for the piston pumps are achieved when $C$ is set between 4 and 7 [26]. Therefore, $C$ is considered to be much larger than $\sin^2\theta$, leading to the simplification in Equation 2.67 [26].

$$v = r\left(\sin\theta + \frac{\sin 2\theta}{2\sqrt{C^2 - \sin^2\theta}}\right)\omega \tag{2.66}$$

$$v = r\left(\sin\theta + \frac{\sin 2\theta}{2C}\right)\omega \tag{2.67}$$

The instantaneous volumetric flowrate $\dot{V}$ in a piston-cylinder device with cross sectional area $A$ is then derived as in Equation 2.68.

$$\dot{V} = A \cdot v = A \cdot r\left(\sin\theta + \frac{\sin 2\theta}{2C}\right)\omega \tag{2.68}$$

This can be extended to encompass a system of $n$ cylinders distributed evenly over a complete rotation of the crank. For this system, the $i$-th cylinder is $\frac{2\pi}{i}$ radians ahead in phase compared to the first. Given that $\theta$ is equal to $\omega t$, the instantaneous flowrate for the fluid in the cylinder $\dot{V}$ is obtained with Equation 2.69 at any time $t$.

$$\dot{V} = A \cdot v = A \cdot r\left(\sin\left(\omega t + (i-1)\frac{2\pi}{n}\right) + \frac{\sin 2\left(\omega t + (i-1)\frac{2\pi}{n}\right)}{2C}\right)\omega \tag{2.69}$$

An example of the variation in the volumetric flow rate through a cylinder along one rotation of the crank can be seen in Figure 2.7, where a negative flowrate means that fluid is entering the cylinder. Due to this sinusoidal variation in the flowrate, the pump is only able to meet the upstream flow and pressure requirements

during the discharge stroke. Therefore, it is crucial to employ either multiple cylinders with controlled valve action within the pump or incorporate a surge tank upstream to guarantee the system's adherence to constant flow rate specifications. A surge tank contains a gas on top of the liquid that can react quickly to absorb much of the flow pulsation [26].

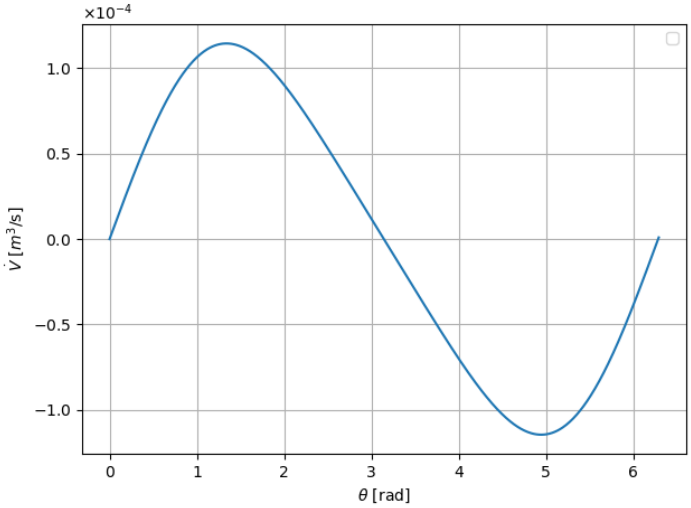


Figure 2.7: Variation in volumetric flow rate through a cylinder along one rotation of the crank

If multiple piston-cylinder devices are implemented, the difference in phase of the individual pistons allows for the discharge stroke of the individual pistons to compensate for the other pistons. This can be seen in the plot of a three cylinder pump as shown in Figure 2.8, where the discharge flows of the individual pistons and the total pump are represented by the dotted lines and the solid line respectively. In order to prevent back flow, the piston valve is closed at the end of the discharge stroke of the piston. Similarly, at the beginning of the stroke, the corresponding valve is opened. Through this opening and closing of valves, the flow rate fluctuations can be minimised [26].

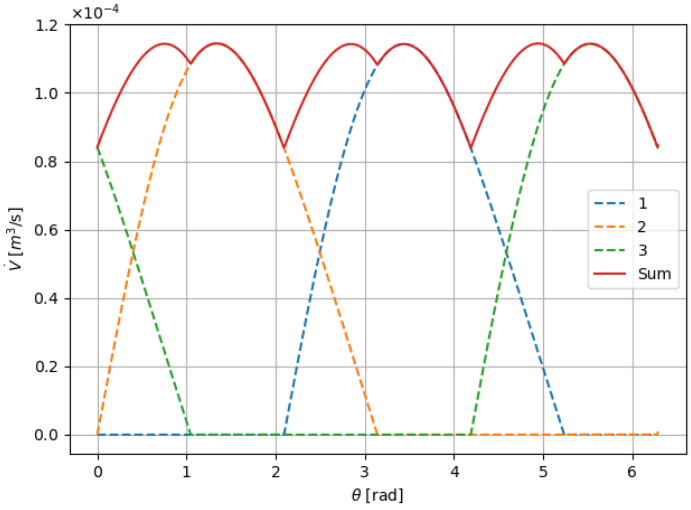


Figure 2.8: Individual and total flowrate through a pump with 3 piston-cylinder devices

### PRESSURE MODELLING

Next, the variation of the pressure of the fluid inside the cylinder during the suction and discharge stroke is examined, which required to compute the stresses in the cylinder walls. At the inlet, the pump is submerged

to ensure a constant inlet pressure equivalent to the tank fluid pressure [26]. At the outlet, the static pressure is equal to the required pressure to be produced by the pump determined by taking into account the losses in the remainder of the hydrogen supply system. As displayed in Figure 2.9, the inlet and outlet valves are closed during the discharge and suction strokes of the piston respectively. The pressure can be evaluated by considering the energy balance (Bernoulli's equation) between the fluid at the piston (location 2) and the fluid at the suction or discharge line (location 1). The pressure of the fluid at the piston is equal to the pressure applied by it at that point. This results in Equation 2.70 and Equation 2.71

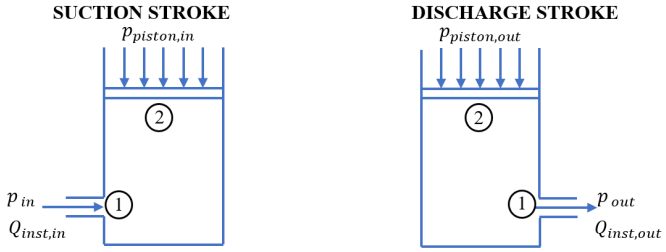


Figure 2.9: Simplified model of suction and discharge stroke inside the pump.

$$p_{piston,in} + \frac{1}{2}\rho\left(\frac{\dot{V}_{in}}{A}\right)^2 = p_{in} + \frac{1}{2}\rho\left(\frac{\dot{V}_{in}}{A_{pipe,in}}\right)^2 + \rho l_{suction}\frac{A}{A_{pipe,in}}\dot{v}_{piston,in} \tag{2.70}$$

$$p_{piston,out} + \frac{1}{2}\rho\left(\frac{\dot{V}_{out}}{A}\right)^2 + \rho l_{discharge}\frac{A}{A_{pipe,out}}\dot{v}_{piston,out} = p_{out} + \frac{1}{2}\rho\left(\frac{\dot{V}_{out}}{A_{pipe,out}}\right)^2 \tag{2.71}$$

Assuming that the pump is submerged and that the length of the suction line is small, and hence the flowrate into the pump is negligible, Equation 2.70 can be simplified to the following.

$$p_{piston,in} = p_{in} \tag{2.72}$$

Similarly, the length of the outlet pipe is assumed to be small enough that the pressure due to the accelerating fluid can be considered negligible, leading to the simplification in Equation 2.73.

$$p_{piston,out} = p_{out} + \frac{1}{2}\rho\left(\left(\frac{\dot{V}_{out}}{A_{pipe,out}}\right)^2 - \left(\frac{\dot{V}_{out}}{A}\right)^2\right) \tag{2.73}$$

Subsequently, by substituting the values for the instantaneous discharge flowrate obtained from Equation 2.69, the pressure in the piston-cylinder device during the discharge stroke can be obtained. Note that this includes only the positive values for the flowrates. As the pump transitions from the discharge to the suction stroke, the outlet valve closes and the inlet valve opens for each piston, and a discontinuity in pressure occurs in the cylinder. The pressure in the cylinder will change from the value during the discharge stroke to the inlet pressure from the tank $p_{in}$. The changing pressure between the suction and discharge stroke will cause a dynamic load on the piston and cylinder, and thus the thickness of the cylinder can be determined by designing the assembly based on this load.

### THICKNESS COMPUTATION

The pressure of the fluid in the piston cylinder causes stresses on the cylinder walls acting along the axial, radial, and tangential directions (with subscripts $a$, $r$, and $t$ respectively), as is presented in Figure 2.10. These stresses can be obtained using Equation 2.74 to Equation 2.76. These stresses depend on the inner and outer radius of the cylinder ($r_i$ and $r_o$ respectively), and the internal and external pressure acting on it ($p$ and $p_o$ respectively) [27]. The external pressure is equal to the ambient pressure and the outer radius is the sum of the inner radius and the thickness.

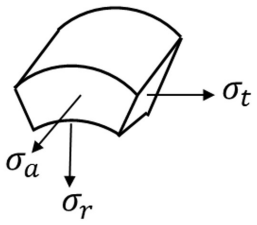


Figure 2.10: Stresses acting on a thick-walled cylinder

$$\sigma_a = \frac{r_i^2 p - r_o^2 p_o}{r_o^2 - r_i^2} \tag{2.74}$$

$$\sigma_r = \frac{r_i^2 p - r_o^2 p_o}{r_o^2 - r_i^2} - \frac{r_i^2 r_o^2 (p - p_o)}{(r_o^2 - r_i^2) r_i^2} \tag{2.75}$$

$$\sigma_t = \frac{r_i^2 p - r_o^2 p_o}{r_o^2 - r_i^2} + \frac{r_i^2 r_o^2 (p - p_o)}{(r_o^2 - r_i^2) r_i^2} \tag{2.76}$$

The cylinder will experience an oscillating pressure that causes fluctuating stresses along the three principal directions. The maximum value for these stresses $\sigma_{max}$ correspond to the maximum pressure $p$, which occurs during the middle of its discharge stroke and is equal to the maximum value of $p_{piston,out}$ calculated using Equation 2.73. As the pump goes through its discharge stroke, the connecting rod side of the pump will be evacuated. Assuming that this region is evacuated to ambient atmosphere, the minimum pressure $p$ experienced by the cylinder will be equal to the ambient pressure $p_{atm}$, which can then be used to obtained the minimum values for the stress in each direction $\sigma_{min}$.

In order to perform an analysis of the effects of fatigue on the cylinder thickness, the equivalent mean and alternating stresses need to be evaluated. The equivalent stress combines the stresses acting in each of the three principal directions into a single value. The mean and alternating stresses in each principal direction are obtained using the following equations [27].

$$\sigma_{mean} = 0.5\,(\sigma_{max} - \sigma_{min}) \tag{2.77}$$

$$\sigma_{alt} = 0.5\,(\sigma_{max} + \sigma_{min}) \tag{2.78}$$

Subsequently, the equivalent mean and alternating stresses are given by Equation 2.79 and Equation 2.80 [27].

$$\sigma_{mean,eq} = \sqrt{0.5\left((\sigma_{a,mean} - \sigma_{r,mean})^2 + (\sigma_{r,mean} - \sigma_{t,mean})^2 + (\sigma_{t,mean} - \sigma_{a,mean})^2\right)} \tag{2.79}$$

$$\sigma_{alt,eq} = \sqrt{0.5\left((\sigma_{a,alt} - \sigma_{r,alt})^2 + (\sigma_{r,alt} - \sigma_{t,alt})^2 + (\sigma_{t,alt} - \sigma_{a,alt})^2\right)} \tag{2.80}$$

Once the equivalent stresses are known, two main criteria are utilised to determined the thickness of the piston cylinders. The first criterion analyses fatigue failure through the use of a modified Goodman criterion as can be seen in Equation 2.81 [27]. This equation implements the critical fatigue stress $\sigma_{cr}$ of the material, which is the critical stress corresponding to $N$ cycles of fluctuating lead at which the material will fail. Additionally, the equation utilises the yield strength of the material $\sigma_{yield}$, and the equivalent alternating and mean stresses experienced by the cylinder. As the stresses experienced by the cylinder depend on its inner and outer radius, the thickness required for a given inner radius can be determined.

$$\frac{\sigma_{alt,eq}}{\sigma_{cr}} + \frac{\sigma_{mean,eq}}{\sigma_{yield}} = 1 \tag{2.81}$$

The second criterion involves limiting the maximum allowable change in diameter of the cylinder due to the pressure variations in order to prevent excessive friction losses between the piston and the cylinder, or volumetric losses to the connecting rod side of the cylinder. The strain in the radial direction can be calculated as in Equation 2.82 using the principal stresses, as well as the cylinder material's E-modulus $E$ and Poisson's ratio $\nu$. The radial strain $\epsilon_r$ is the ratio of the allowable change in diameter to the initial diameter as in Equation 2.83. By setting a maximum value for the strain, the minimum thickness required can be solved for via the principal stresses.

$$\epsilon_r = \frac{1}{E}\left(\sigma_{t,max} + \nu\left(\sigma_{r,max} - \sigma_{a,max}\right)\right) \tag{2.82}$$

$$\epsilon_r = \frac{\Delta d}{d} \tag{2.83}$$

After obtaining a minimum cylinder thickness required to satisfy each individual criterion, the final value is taken to be the larger of the two.

#### POWER COMPUTATION

The power needed to achieve the required fluid properties at the outlet of the pump is calculated using Equation 2.84, where $\dot{V}_{mean}$ is the mean volumetric flowrate required by the system, $\Delta p$ is the pressure increase required by the pump, and $\eta_{pump}$ is the component's total efficiency (set to 0.7 if no efficiency is specified) [20, 26].

$$P_{pump} = \frac{\dot{V}_{mean}\Delta p}{\eta_{pump}} \tag{2.84}$$

#### VOLUME AND MASS COMPUTATIONS

The pump consists of three main components which are the pistons, cylinders, and the motor required to achieve the desired pressure increase and flowrate. As can be seen in Equation 2.85, the total theoretical volumetric flowrate flowing through a pump $\dot{V}$ is obtained using the piston cross sectional area $A$, the pump rotational speed $\omega$, the number of pistons $n_{pistons}$, and the stroke length $s$ ($s = 2r$). As the mass flow rate, the inner radius of the cylinder, and the number of pistons are defined at the beginning of the design process, these can be used to determine the volumetric flowrate and the cross-sectional area, and subsequently the stroke length and lengths of the cylinders and pistons.

$$\dot{V} = \frac{A\omega s n_{pistons}}{2\pi} \tag{2.85}$$

Once the thickness of the cylinders is determined using the methods described earlier, the mass and volumes of the cylinder and pistons can be determined using the dimensions and material density of the pump.

$$m_{piston} = \rho\pi r_i^2 l n_{pistons} \tag{2.86}$$

$$m_{cylinder} = \rho\pi\left(r_o^2 - r_i^2\right) l n_{pistons} \tag{2.87}$$

Finally, the mass and volume of the pump motor are estimated from given gravimetric and volumetric energy densities. For this work, the corresponding values of 3 $kW/kg$ and 66.6 $kW/m^3$ are utilised as presented by Bahrs et al [28].

$$m_{motor} = \frac{P_{pump}}{\rho_{P,m}} \tag{2.88}$$

$$V_{motor} = \frac{P_{pump}}{\rho_{P,V}} \tag{2.89}$$

### 2.2.5. HEAT EXCHANGER MODELLING

Heat exchangers are required to heat up the hydrogen before the SOFC to ensure that it meets the required inlet temperature conditions. The heat exchanger model directly implemented in this work is the heat exchanger rating model of Bhapkar et al. [29], which is based on the $\varepsilon$-NTU method presented by Shah et al. in the book "Fundamentals of Heat Exchanger Design" [30]. Two types of heat exchangers models are speficied, one for a hydrogen-steam heat exchanger, and the other for an air-air heat exchanger.

### HEAT EXCHANGER TYPE AND MATERIAL

In order to select the heat exchanger type most applicable for implementation in the field of aviation, two main aspects of the heat exchangers have to be considered. First, it is important be as compact as possible, in order to minimise its weight and volume. A compact heat exchanger incorporates a large ratio of heat transfer surface area per unit volume of the heat exchanger [30]. The second aspect corresponds to minimising the pressure drop across the heat exchanger, as a larger pressure drop means that the rest of the remaining components need to compensate for it, leading to additional power, mass, and volume of the system. In addition to these points, the lifetime, reliability, and safety aspects of the heat exchanger must be accounted for in the selection. Bhapkar et al. [29] investigate different types of heat exchangers and concluded that for aerospace applications a cross-flow plate-fin heat exchanger is the most suitable, due to its compactness and the heat transfer coefficient enhancement through the use of fins. In particular, offset strip fins are implemented due to their superior heat transfer efficiency and reduced drag [29]. An isometric view of the hydrogen-steam heat exchanger can be seen in Figure 2.11, with the cross-section shown in Figure 2.12. The flow of the cold hydrogen is through the coolant plates, while that of the hot steam is through the fin channels. This arises from the fact that hydrogen has a sufficiently large heat transfer coefficient while steam does not. For the air-air heat exchange, both fluids flow through offset-strip fin channels due to air's low heat transfer coefficient.

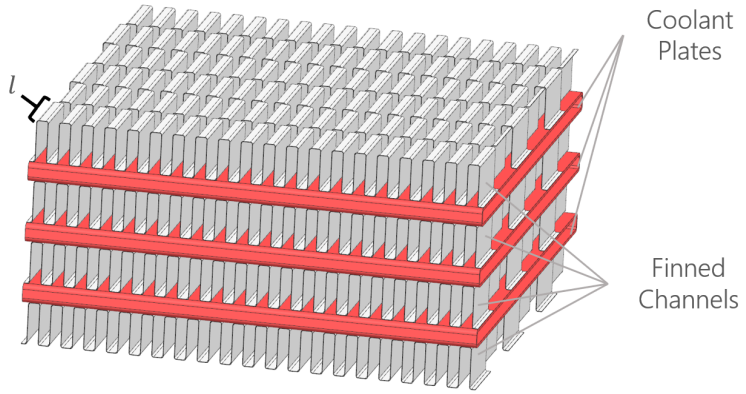


Figure 2.11: Cross-flow plate-fin heat exchanger with offset strip fins [29]

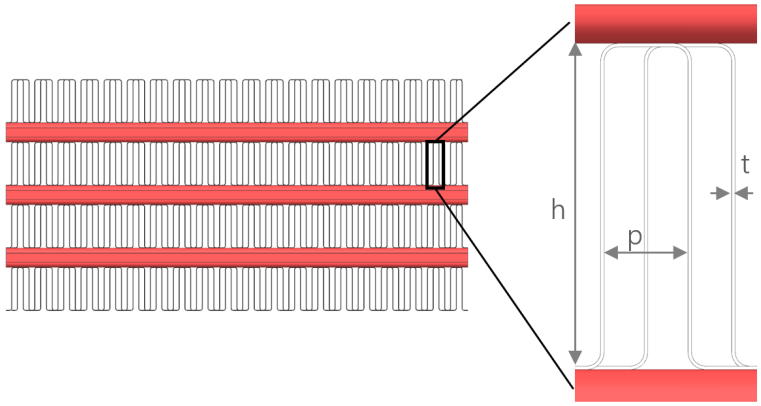


Figure 2.12: Heat exchanger cross-section perpendicular to flow direction [29]

In addition to the type of heat exchanger, the material selection is also of great importance. Heat exchangers implemented in a SOFC based hydrogen supply architecture can experience extremely high temperatures of around 1000K for inlet fluid conditioning. Therefore, the materials need to be capable of maintaining structural rigidity at these temperatures to prevent degradation and failure [29]. Metals are preferred for high

temperature applications due to their thermomechanical properties and ease of manufacturing. Iron-based alloys are preferred for temperatures up to 600°C, after which corrosion is a limiting factor. For higher temperatures, nickel-based super-alloys such as Inconel 625 provide better strength and corrosion resistance properties, however the cost of the materials is much higher [31]. Ceramics also offer great strength and corrosion resistance at high temperatures, however their brittleness causes challenges in manufacturing and mechanical joining [29].

### HEAT EXCHANGER SIZING

The first step in the rating model is to define the dimensions of the heat exchanger. This includes the length of the cold fluid and hot fluid side ($L_c$ and $L_h$ respectively), the height of the stack $H$, plate thickness $t_p$ and hydraulic diameter $d_{h,p}$, as well as the fin geometry (height $h_f$, length $l_f$, thickness $t_f$ and pitch $p_f$). For the hydrogen heat exchanger, the hydrogen flows through the coolant plate channels, which have a height $h_p$ of 2 mm. Once these are given, the different heat transfer and free flow areas of the hydrogen heat exchanger can be computed [29].

The primary heat transfer area of offset strip fins $A_p$ is the surface area directly in contact with the fluid or medium from which heat is being transferred. The secondary heat transfer area refers to the additional surface area created by the offset arrangement of the fins, which enhances heat transfer and increases the convective heat transfer coefficient [29]. These are calculated in the following equations.

$$A_p = 2(p_f - t_f)l \tag{2.90}$$

$$A_s = 2(h_f - t_f)l + 2(h_f - t_f)t_f + (p_f - t_f)t_f \tag{2.91}$$

The total heat transfer area of the hot side of the heat exchanger is the sum of the two areas multiplied by the total number of fins. This total number is a product of the number of fins per passage and the number of passages in the heat exchanger. The former is calculated from the total length on the cold and hot fluid sides of the heat exchanger ($L_c$ and $L_h$ respectively) given the pitch and length of the fins ($n_f = \frac{L_c}{p_f}\frac{L_h}{l_f}$). The total number of passages $N_p$ is a function of the stack height $H_s$, the fin height, and the plate thickness [29].

$$N_p = \frac{H_s - h_f}{h_f + h_p + 2t_p} \tag{2.92}$$

$$A_{ht,h} = n_f N_p (A_p + A_s) \tag{2.93}$$

The heat transfer area of the cold side is simply the area of the plates multiplied by the number of plates ($N_p - 1$).

$$A_{ht,c} = L_h L_c (N_p - 1) \tag{2.94}$$

The hydraulic diameter of the fins is required for the computation of the temperature and pressure changes along the heat exchanger, and can be determined using Equation 2.95 [29].

$$d_{h,f} = \frac{4l_f(p_f - t_f)(h_f - t_f)}{2(l(p_f - t_f) + (h_f - t_f)(l_f + t_f)) + (p_f - t_f)t_f} \tag{2.95}$$

Next, the volume and mass of the heat exchanger are determined as done by Bhapkar et al. [29]. The volume of the heat exchanger can be easily obtained using the length of the cold fluid and hot fluid sides and the stack height as in Equation 2.96.

$$V_{HEX} = L_h L_c H_s \tag{2.96}$$

The mass of the heat exchanger is the sum of the mass of the fins and the plates. For this, the volume of each needs to first be determined using their dimensions. The volume of a single fin is given by Equation 2.97 using the length, thickness, pitch and height of the fins[29]. The total mass of all the fins is then calculated via Equation 2.98

$$V_f = l_f t_f (p_f + h_f - t_f) \tag{2.97}$$

$$m_f = \rho V_f n_f N_p \tag{2.98}$$

The mass of the plates is determined with the lengths of the heat exchanger in the direction of the cold fluid side and hot fluid side, the thickness of the plates and the number of passages as follows [29].

$$m_p = \rho L_c L_h t_p (2N_p - 1) \tag{2.99}$$

The total mass of the heat exchanger is then the sum of masses of the fins and the plates.

$$m_{HEX} = m_f + m_p \tag{2.100}$$

For the air heat exchanger, the same computations are performed, with the difference being each passage contains an additional layer of fins. The two fin layers are for the cold and hot air while the plates are between each fin layer for structural support. However, the plates are not included for the heat transfer area.

### TEMPERATURE CHANGE

The temperature change for a single-phase heat exchanger can be computed using the $\varepsilon$-NTU method presented by Shah et al. in the book "Fundamentals of Heat Exchanger Design" [30]. This method utilises the heat exchanger effectiveness $\varepsilon$ to estimate the heat transfer rate $\dot{Q}$ from the thermodynamically maximum heat transfer rate of a heat exchanger of infinite surface area $q_{max}$ as can be seen in Equation 2.101. In order to simplify the computations, an important assumption taken in the calculations is that the fluid properties, like the density and heat capacity, are taken to be at the inlet pressure and the mean temperature conditions [29].

$$\varepsilon = \frac{\dot{Q}}{\dot{Q}_{max}} \tag{2.101}$$

The heat transfer rate $\dot{Q}$ can be determined with the temperature change of the hot or cold fluid using Equation 2.102. In this equation, $C$ is the heat capacity and $T$ is the temperature. The subscripts h and c indicate the hot fluid and cold fluid respectively, and i and o indicate the inlet and outlet of the heat exchanger respectively [30].

$$\dot{Q} = C_h (T_{h,i} - T_{h,o}) = C_c (T_{c,i} - T_{c,o}) \tag{2.102}$$

$\dot{Q}_{max}$ is obtained using the equation below. $C_{min}$ is the minimum heat capacity of the cold and hot fluid and is equal to the product of the mass flow of the fluid and its specific heat coefficient.

$$\dot{Q}_{max} = C_{min} (T_{h,i} - T_{c,i}) \tag{2.103}$$

The effectiveness $\varepsilon$ is a function of the number of transfer units (NTU) of the heat exchanger and the heat capacity ratio ($C^* = \frac{C_{min}}{C_{max}}$). There are multiple relations between the effectiveness and the NTU based on the flow arrangement of the heat exchanger. For a cross-flow heat exchanger, the empirical correlation in Equation 2.104 can be utilised [29].

$$\varepsilon = 1 - e^{\frac{e^{-C^* \cdot NTU^{0.78}} - 1}{C^* \cdot NTU^{-0.22}}} \tag{2.104}$$

The NTU is computed using Equation 2.105, where U is the heat transfer coefficient of the heat exchanger and A is the total heat transfer surface area [30]. The heat transfer coefficient of the hydrogen heat exchanger is obtained from the heat transfer area $A_h$ and coefficient $h_h$ and the fin efficiency $\eta_h$ of the fins on the hot side of the heat exchanger, as well as the heat transfer area $A_c$ and coefficient $h_c$ of the cold plates.

$$NTU = \frac{UA}{C_{min}} \tag{2.105}$$

$$\frac{1}{UA} = \frac{1}{\eta_h A_h h_h} + \frac{1}{A_c h_c} \tag{2.106}$$

An important parameter in the computation of the temperature and pressure changes is the core mass velocity $G$, which is the ratio of the mass flow rate $\dot{m}$ to the free flow area of the heat exchanger $A_o$. Once the dimensions of the fins and heat exchanger are given, the free flow area of one side of the heat exchanger can easily be calculated using the hydraulic diameter and the total heat transfer area of one side $A_{ht}$ as in Equation 2.108, where $L$ is the length of the investigated side. In turn the core mass velocity of each side can be obtained.

$$G = \frac{\dot{m}}{A_o} \tag{2.107}$$

$$A_o = \frac{d_h A_{ht}}{4L} \tag{2.108}$$

The heat transfer coefficient of the fins (hot fluid side) is then determined using Equation 2.109, where $Pr$ is the Prandtl number of the fluid and is dependant on its temperature and pressure, $c_p$ is the mean specific heat capacity of the fluid through the heat exchanger, and j is the Colburn factor determined with Equation 2.110. In the latter equation, $s$ and $h'$ are equal to the fin pitch $p_f$ and height $h_f$ each subtracted by the thickness $t_f$ respectively [29]. The Reynolds number is simply given by Equation 2.111.

$$h = \frac{jGc_p}{Pr^{\frac{2}{3}}} \tag{2.109}$$

$$j = 0.65Re^{-0.54}\left(\frac{s}{h'}\right)^{-0.15}\left(\frac{t_f}{l_f}\right)^{0.15}\left(\frac{t_f}{s}\right)^{-0.07}\cdot\left(1+5.27\cdot10^{-5}Re^{1.3}\left(\frac{s}{h'}\right)^{-0.5}\left(\frac{t_f}{l_f}\right)^{0.46}\left(\frac{t_f}{s}\right)^{-1.05}\right)^{0.1} \tag{2.110}$$

$$Re = \frac{Gd_h}{\mu} \tag{2.111}$$

The heat transfer coefficient of the coolant plates (cold fluid side) is a factor of the Nusselt number of the cold fluid flow through the coolant plates. For laminar conditions (Re<2300), the Nusselt number is determined using the aspect ratio of the plate $\left(\tau = \frac{h_p}{L_h}\right)$ with the following equation [30].

$$Nu_{laminar} = 8.235\left(1-2.0421\tau+3.0853\tau^2-2.4765\tau^3+1.0578\tau^4-0.1861\tau^5\right) \tag{2.112}$$

For turbulent flows, the Nusselt number is a function of the friction factor of the plates as follows [32].

$$f = \left(1.58\ln Re - 3.28\right)^{-2} \tag{2.113}$$

$$Nu_{turbulent} = \frac{0.5f\cdot Re\cdot Pr}{1.07+12.7\sqrt{0.5f}\left(Pr^{\frac{2}{3}}-1\right)} \tag{2.114}$$

Finally, the heat transfer coefficient is obtained using Equation 2.115 by implementing the Nusselt number $Nu$, the thermal conductivity $k$ and the hydraulic diameter $d_h$.

$$h = \frac{k\cdot Nu}{d_h} \tag{2.115}$$

With the dimensions of the heat exchanger given, it is possible to work backwards from the core mass velocity to obtain the maximum heat transfer rate of the heat exchanger to heat up the cold fluid via the effectiveness $\varepsilon$ and the number of transfer units (NTU). This can then be compared to the required heat transfer rate given the inlet temperature and a required outlet temperature set by the SOFC requirements. The dimensions of the heat exchanger can then be changed from an initial guess to more closely match the required rate.

$$\dot{Q}_{req} = \dot{m}c_p(\Delta T_{req}) \tag{2.116}$$

In order to calculate the NTU of the air heat exchanger, the same method is used, except taking into account that both fluids flow through fin layers. This leads to the following equation implemented to calculate the NTU in Equation 2.105.

$$\frac{1}{UA} = \frac{1}{\eta_h A_h h_h} + \frac{1}{\eta_c A_c h_c} \tag{2.117}$$

The core velocity of both fin layers is also computed via Equation 2.109.

### PRESSURE DROP

The total pressure drop over one side of a single-phase plate-fin heat exchanger can be obtained by computing the sum of the pressure loss over the core, the pressure drop over the entrance, and the pressure rise at the core exit. Additionally, there is a term due to the momentum effect. The full equation can be seen in Equation 2.118. In this equation, G is the fluid mass velocity based on the minimum free area. In order to obtain the entrance and exit effects, more details on the geometry are required such as the ratio of free flow to frontal area $\sigma$, and the contraction and expansion loss coefficients $K_c$ and $K_e$ [30].

$$\frac{\Delta p}{p_i} = \frac{G^2}{2\rho_i p_i}\left[\underbrace{1-\sigma^2+K_c}_{\text{entrance effect}} + \underbrace{2\left(\frac{\rho_i}{\rho_o}-1\right)}_{\text{momentum effect}} + \underbrace{f\frac{L}{r_h}\rho_i\left(\frac{1}{\rho}\right)_m}_{\text{core friction}} - \underbrace{(1-\sigma^2-K_e)\frac{\rho_i}{\rho_o}}_{\text{exit effect}}\right] \tag{2.118}$$

Since the frictional pressure drop is the major source for the total core pressure drop, the total pressure drop can be approximated using the Equation 2.119 for one side of the heat exchanger[30]. Here, $G$ is the core velocity, $L$ is the length of either the hot or the cold side, $d_h$ is the hydraulic diameter, $\rho$ is the fluid density, and $f$ is the friction factor. In order to calculate the pressure drop on the hot side of the hydrogen heat exchanger, the friction factor of the fins is required as shown in Equation 2.120, while for the pressure drop on the cold side, the plate friction factor in Equation 2.113 is required. For the air heat exchangers, the fluid on both sides flows through a layer of fins and therefore Equation 2.120 is used for both.

$$\Delta p \approx \frac{4fLG^2}{2d_h\rho} \tag{2.119}$$

$$f = 9.62Re^{-0.74}\left(\frac{s}{h'}\right)^{-0.19}\left(\frac{t_f}{l_f}\right)^{0.31}\left(\frac{t_f}{s}\right)^{-0.27}\cdot\left(1+7.67\cdot10^{-8}Re^{4.43}\left(\frac{s}{h'}\right)^{-0.92}\left(\frac{t_f}{l_f}\right)^{3.78}\left(\frac{t_f}{s}\right)^{0.24}\right)^{0.1} \tag{2.120}$$

### 2.2.6. COMPRESSOR AND TURBINE MODELLING

In order to model the power requirement and recovery of the Solid Oxide Fuel Cell supply architecture, the air side of the architecture also needs to be considered. In particular, the power required to compress the SOFC inlet air to the required pressure and the power that can be recovered from the SOFC exhaust gas need to be computed. Therefore, simple compressor and turbine models are implemented in this work that utilise a given isentropic efficiency to model the pressure changes [33].

#### COMPRESSOR MODELLING

The method used to model the change in the fluid properties through the compressor is presented below. In these equations, the input and output properties use the subscripts 1 and 2 respectively. First, given the dimensions of the pipe and the properties of the fluid before the compressor, the total pressure and temperature of the fluid before the compressor can be obtained using Equation 2.121 and Equation 2.122. $\gamma$ is the ratio of specific heats of the fluid and is equal to 1.4 for air. The mach number $M$ can be determined as in Equation 2.123 using the mass flow rate $\dot{m}$, the fluid density $\rho_1$, the cross-sectional area of the pipe $A_1$, and the temperature $T_1$. In these equations, $\bar{R}$ is the universal gas constant and equal to 287 $J/(kgK)$

$$p_{t1} = p_1\left(1+\frac{\gamma-1}{2}\cdot M_1^2\right)^{\frac{\gamma}{\gamma-1}} \tag{2.121}$$

$$T_{t1} = T_1\left(1+\frac{\gamma-1}{2}\cdot M_1^2\right) \tag{2.122}$$

$$M_1 = \frac{v_1}{\sqrt{\gamma\bar{R}T_1}} = \frac{\dot{m}}{\rho_1 A_1\sqrt{\gamma\bar{R}T_1}} \tag{2.123}$$

Subsequently, given a total pressure ratio $\Pi$ to be achieved by the compressor, the change in the total temperature is computed using Equation 2.124, where $\eta_{is}$ is the isentropic efficiency of the compressor.

$$T_{t2} = T_{t1}\left(1+\frac{1}{\eta_{is}}\left(\Pi^{\frac{\gamma-1}{\gamma}}-1\right)\right) \tag{2.124}$$

Next, to convert back to static conditions, the following system of five equations needs to be solved, where the variables to be determined are the outlet static pressure $p_2$, temperature $T_2$, density $\rho_2$ and Mach number $M_2$.

$$p_2 = \rho_2\bar{R}T_2 \tag{2.125}$$

$$\dot{m} = \rho_2 A_2 M_2\sqrt{\gamma\bar{R}T_2} \tag{2.126}$$

$$p_{t2} = p_2\left(1+\frac{\gamma-1}{2}\cdot M^2\right)^{\frac{\gamma}{\gamma-1}} \tag{2.127}$$

$$T_{t2} = T_2\left(1 + \frac{\gamma - 1}{2} \cdot M^2\right) \tag{2.128}$$

Finally, the power required by the compressor can be determined via the enthalpy $h$ difference between the inlet and outlet with the specific heat of the fluid $c_p$ and the difference in the total temperatures $T_t$ as follows.

$$P_{comp} = \dot{m}(h_2 - h_1) = \dot{m}c_p(T_{t2} - T_{t1}) \tag{2.129}$$

### TURBINE MODELLING

The modelling of the turbine is performed similarly to that of the compressor, with the main difference being that the outlet static pressure of the turbine is assumed to be equal to the atmospheric pressure. This is to investigate the maximum theoretical power recovery via a turbine. The inlet conditions at the turbine are once again determined using Equation 2.121 to Equation 2.123.

The fluid properties after the turbine can be computed by solving the same system of equations as for the shown from Equation 2.125 to Equation 2.128, with the addition of Equation 2.130. The unknown variables that need to be determined are the outlet static pressure $p_2$, static and total temperature ($T_2$ and $T_{t2}$ respectively), density $\rho_2$ and Mach number $M_2$.

$$T_{t2} = T_{t1}\left(1 - \eta_{is}\left(1 - \frac{p_{t2}}{p_{t1}}\right)^{\frac{\gamma-1}{\gamma}}\right) \tag{2.130}$$

The power produced by the turbine is then equal to the following.

$$P_{turb} = -\dot{m}(h_2 - h_1) = \dot{m}c_p(T_{t1} - T_{t2}) \tag{2.131}$$

# 3

# METHODOLOGY

The knowledge presented in Chapter 2 can be used to develop a framework for the design, optimisation, and assessment of hydrogen supply architectures for SOFC powered aircraft. The general process of the work in this thesis is presented in Figure 3.1. The architectures to be analysed are first defined in Section 3.1. The design process for each component is detailed in Section 3.2. These are implemented in an optimisation loop in the DLR work-flow integration environment RCE as described in Section 3.3.

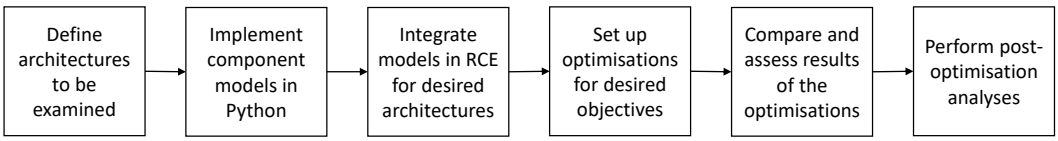


Figure 3.1: Hydrogen supply architecture utilising liquid hydrogen extraction and self-pressurisation.

## 3.1. FUEL CELL SUPPLY ARCHITECTURE DEFINITION AND REQUIREMENTS

The first step in the analysis is the definition of the hydrogen fuel cell supply architectures to be analysed. The functions that need to be fulfilled by the systems are listed below.

- Storage of hydrogen
- Transportation of hydrogen and air through the system
- Treatment of hydrogen and air before the fuel cell
- Recovery of waste heat and energy after the fuel cell

Three main fuel extraction methods were determined, which are the self-pressurisation with liquid extraction, self-pressurisation with gaseous extraction, and pumping of liquid hydrogen. The architectures derived from these fuel transportation methods can be seen in Figure 3.2, Figure 3.3, and Figure 3.4 respectively. The sizing of the systems is performed for the take-off phase which requires the most power from the SOFC, and therefore the largest mass flowrate.

The main components of the liquid hydrogen extraction with self-pressurisation ($LH_2$ SP) architecture are described below following the flow of hydrogen in Figure 3.2. For this system, the hydrogen is stored in an insulated, cryogenic storage tank at a pressure higher than that of the SOFC. This difference in pressure is the driving factor for the flow of hydrogen in the system. The maximum operating pressure required in the tank is dependant on the pressure losses in the system and the inlet conditions of the SOFC. As the hydrogen is extracted, the volume of the gaseous hydrogen in the tank increases and the density decreases, leading to a reduction in pressure. This can be counteracted by vaporising some of the liquid hydrogen, increasing the density, and in turn maintaining the desired storage pressure. The heat is provided through the use of an electric heater.

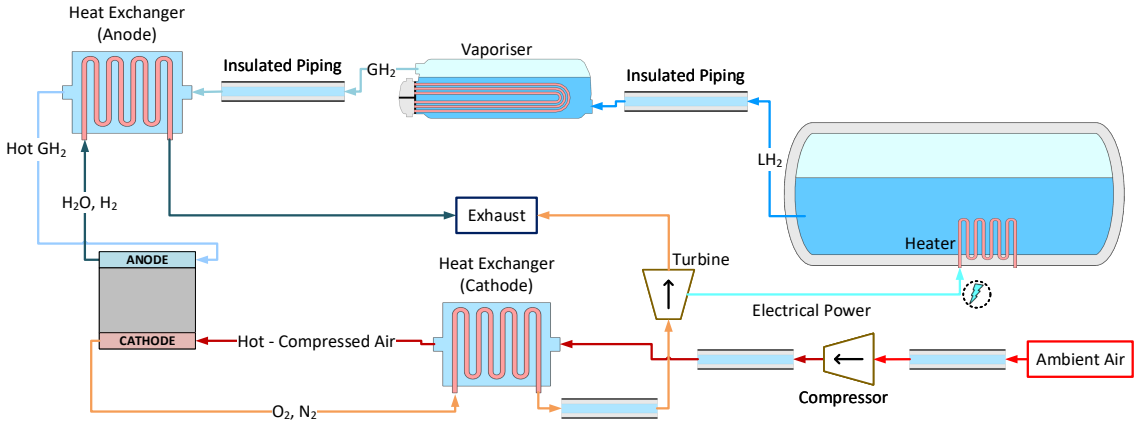


Figure 3.2: Hydrogen supply architecture utilising liquid hydrogen extraction and self-pressurisation.

After the fuel leaves the storage vessel, it passes through insulated pipes to a vaporiser. The modelling of the pipes is vital as it is a major source for pressure losses in the system which need to be accounted for to ensure that the SOFC required inlet pressure is achieved. The insulation is required to reduce the effect of environmental heating on the fluid and prevent transition from the liquid phase to the gaseous phase. Finally, the increase in temperature of the fluid can cause the density to reduce, increasing the fluid velocity for a given mass flow rate, which could be a constraint on the design.

The vaporiser is modelled as a storage tank with no insulation. It is assumed that liquid hydrogen flows in and gaseous hydrogen flows out of it at the same mass flow rate. The operating pressure and temperature of the hydrogen in the vaporiser is equal to the outlet pressure and temperature of the preceding pipe. A heater is utilised to provide the heat required for the vaporisation of hydrogen and maintain the pressure.

The last component modelled on the hydrogen side is the heat exchanger whose function is treating the cold hydrogen gas flowing in to ensure that the hydrogen enters the SOFC inlet at its operating temperature. The heating is provided via the anode exhaust gas, whose temperature is larger than the SOFC operating temperature. For these architectures, the two components are assumed to be placed close enough that the pressure and temperature drop of the hydrogen are negligible, and therefore the required hydrogen conditions at the heat exchanger outlet are the same as the inlet conditions to the SOFC.

In order to ensure the operation of the fuel cell at optimal conditions, the treatment of the air before the inlet is just as important as the treatment of hydrogen. On the air side, the air from the atmosphere passes through an inlet pipe to a compressor, which increases its pressure to ensure the SOFC inlet conditions are met while considering the system pressure losses. The pipe model implemented is the same as for the hydrogen side. The compressed air then passes through another pipe to a heat exchanger where it is treated to the SOFC inlet conditions using the fuel cell cathode's hot exhaust air. Subsequently, the exhaust air passes through another pipe to a turbine which expands the air to atmospheric pressures. All the pipes can utilise a small layer of insulation to influence the heat loss to the environment, and with it the pressure and temperature changes through them.

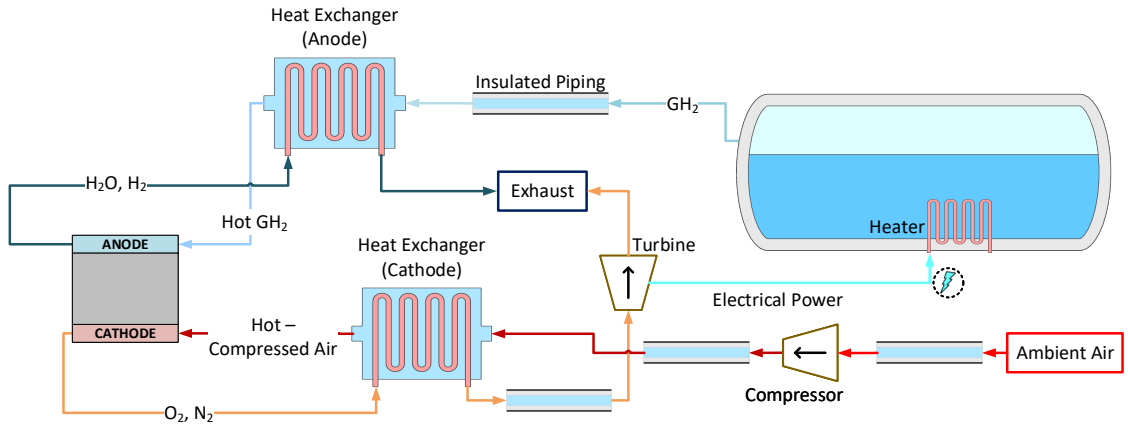


Figure 3.3: Hydrogen supply architecture utilising gaseous hydrogen extraction and self-pressurisation.

The gaseous hydrogen extraction with self-pressurisation ($GH_2$ SP) architecture in Figure 3.3 is similar to the previous one. The main difference arises from the fact that gaseous hydrogen does not need to be vaporised after leaving the storage tank, leading to the exclusion of the vaporiser from the system.

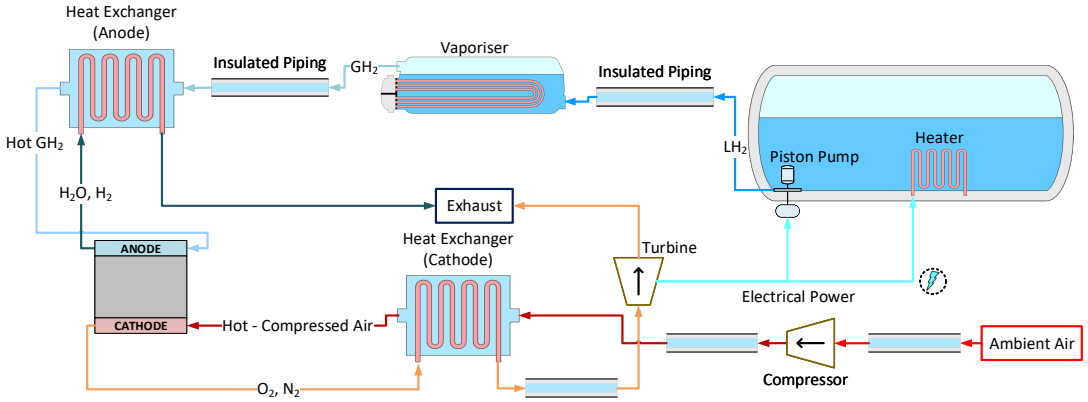


Figure 3.4: Hydrogen supply architecture utilising liquid hydrogen extraction and a piston pump.

Lastly, the liquid hydrogen extraction with pumps ($LH_2$ Pump) architecture shown in Figure 3.4 allows for a reduction in the storage pressure of hydrogen in the tank, as the pressure difference can be compensated by the pump.

The sizing of the hydrogen supply architecture is derived from the electric propulsion system requirements. A preliminary mission analysis for the concept aircraft in the $H_2$EAT project was performed at an earlier stage in the project. Given an SOFC concept, the power required for this mission can be converted to a required hydrogen fuel mass flowrate at the SOFC inlet. The flowrate along with the altitude variation throughout the mission are provided as the main input to the thesis, and are presented in Figure 3.5. The maximum mass flowrate required by the SOFC is the main sizing criterion for the hydrogen supply architecture and equal to 43.4 $g/s$. Its operational pressure and inlet temperature are set to 5 $bar$ and 1073 $K$. The SOFC user input implemented in the sizing can be seen in Table 3.3

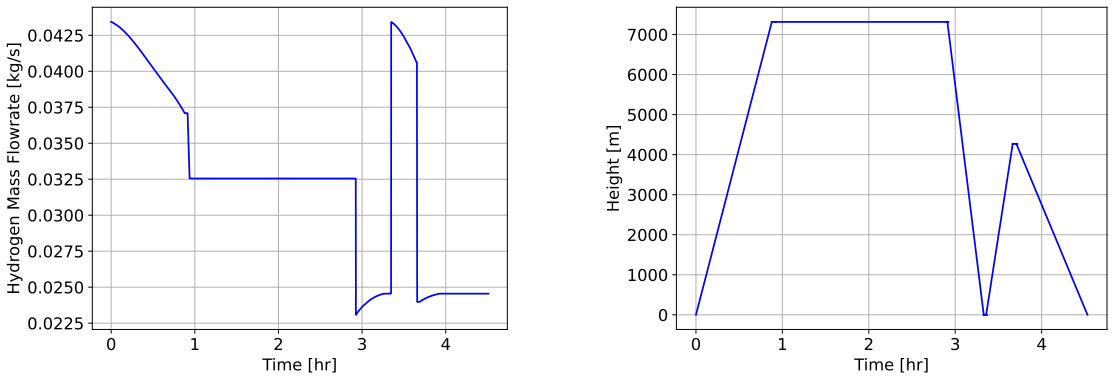


(a) Hydrogen mass flowrate at the SOFC inlet.

(b) Altitude variation throughout the mission.

Figure 3.5: Preliminary mission analysis of $H_2$EAT project provided as input.

## 3.2. COMPONENT DESIGN PROCESSES

This section describes the modelling of all the components implemented in the hydrogen supply architectures analysed in this report. In particular, these components are the tank (and vaporiser), pipe, pump, heat exchanger, compressor, and turbine. In these models, the fluid properties of the hydrogen or air are obtained using the Pyfluids wrapper of the Coolprop Python package [34]. This package allows for the determination of all properties of a fluid given two input properties (for example two from the temperature, pressure, density, enthalpy, and so on).

### 3.2.1. TANK DESIGN PROCESS

The general design process for sizing the tank is presented in Figure 3.6. The first step is defining the requirements of the hydrogen tank. The three main requirements that the tank design needs to fulfil are related to the maximum hydrogen mass derived from the mission, the maximum operational pressure of the tank, and a maximum allowable hydrogen boiloff rate at aircraft standstill to size the insulation thickness. The boiloff gas is defined as the hydrogen vaporised due to the heating of the liquid phase, either due to environmental or electrical heating. At standstill, this can increase the pressure in the tank beyond an maximum allowable value, leading to the venting of hydrogen.

Moreover, the material allocation for each layer of the tank is required to calculate their structural and thermal characteristics and determined corresponding thicknesses. The effect of the environmental heating can not be completely prevented and will result in the vaporisation of some liquid hydrogen, which increases the pressure inside the tank. Therefore, an additional tank volume needs to be defined to accommodate the boiloff gases (7.2% of the total tank volume for typical cryogenic storage tanks [13]). The maximum operational pressure of the tank is provided given the system pressure requirements. The liquid hydrogen in the tank is assumed to be saturated and homogeneous, indicating that given a pressure for the hydrogen, its temperature can also be obtained.

Once the user input is defined, the inner radius of the tank ($r_i$ in Figure 2.3) needs to be specified as a starting point for the sizing of the tank. This is the main geometrical design parameter defined at the beginning of the process, as with the radius defined, the remainder of the inner vessel dimensions can be calculated and its sizing can be completed.

As can be seen in Figure 3.6, the sizing of the insulation and outer layer are coupled. Since the inner radius of the outer vessel depends on the thickness of the insulation. Therefore, an initial guess of the insulation thickness needs to given be to calculate the thickness of the outer vessel. This then influences the thermal conductivity through the tank and in turn the required insulation to achieve a given maximum boiloff rate. These two processes are repeated until the thicknesses converge. The sizing method for each layer of the tank is described in detail in Section 2.2.1.

Subsequently, once all the dimensions are known, and the mass and volume of each layer and of the com-

plete tank can be derived. For the vaporiser, the insulation thickness is kept at zero, and therefore no iteration between the sizing of the layers is required.

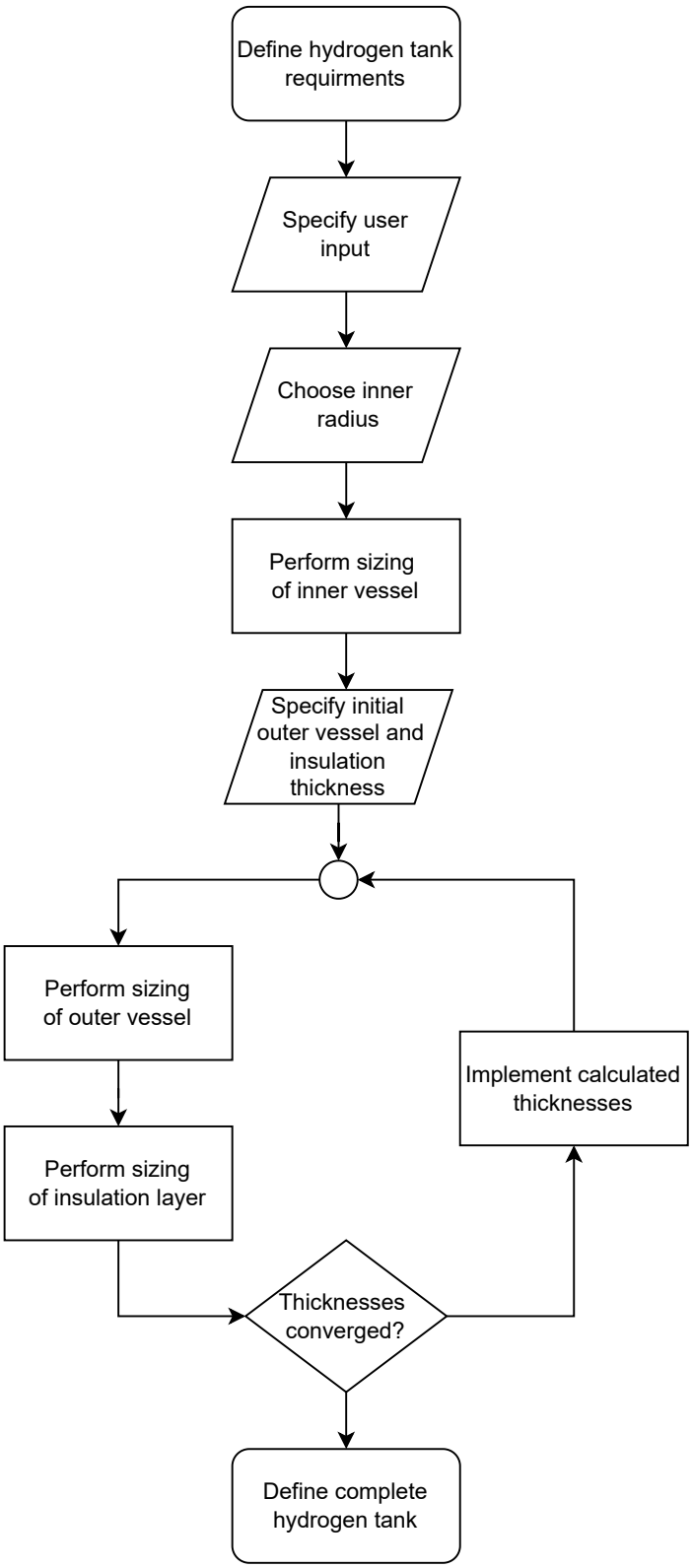


Figure 3.6: Flow chart of tank design process.

### 3.2.2. PIPE DESIGN PROCESS

The process for the pipe modelling is presented in Figure 3.7. The main design criterion is the maximum mass flow rate of fluid derived from the SOFC requirements. Next, some user input for the pipe needs to be defined including material selection for the walls (stainless steel in this work) and insulation, a list of coordinates of the main points connected by straight pipes from which the length and height change can be obtained, and the number and type of fittings attached to it.

The main geometrical design parameter defined at the beginning of the computations is the inner radius and insulation thickness of the pipe. Once these are given, all the pipe computations can be performed, including the pressure and temperature changes along its length. However, as discussed in Section 2.2.3, the methods to calculate the pressure and temperature variations utilise the inlet fluid properties through the entire pipe segment. Therefore, the pipe is split into multiple segments where the outlet values of the preceding segment are the inlet values to the succeeding segment. Finally, the mass of the pipe can be computed by determining the required thickness for the pipes.

### 3.2.3. PUMP DESIGN PROCESS

Figure 3.8 displays the general design process implemented for the sizing of a pump in this report. The main pump requirements defined at the start of the process are the pressure increase required for the pump and the mean volumetric flowrate. The former is computed given an initial tank pressure and the system pressure losses that the pump needs to overcome to achieve a required inlet pressure at the Solid Oxide Fuel Cell, while the latter depends on the mass flow rate required by the SOFC and the dimensions of the pipe after the pump. Next, the user can specify some aspects of the pump design, such as the number of pistons, the pump efficiency, the material used in the pump, and the gravimetric and volumetric energy densities of the motor driving the pump.

The main design parameters of the pump are the radius of the piston and the crank rotational speed. From these values, all other pump design variables can be derived. Additionally, the flowrate and pressure variations in the cylinder can be modelled. Subsequently, when the pressure variations are determined, a preliminary stress analysis of the pump cylinder can be performed to compute the required cylinder thickness. The power of the motor required can be derived from the mean volumetric flowrate of the fluid and the pressure rise over the pump. The analytical models used to perform these computations are presented in Section 2.2.4. Once all these calculations are performed, the total mass and volume of the pump can be obtained.

### 3.2.4. HEAT EXCHANGER DESIGN PROCESS

The design process of the heat exchanger (HEX) model developed by Bhapkar et al. [29] and implemented in this work is presented in Figure 3.9. The purpose of the heat exchanger is to condition the fluid to meet the inlet temperature requirements of the Solid Oxide Fuel Cell. Therefore, the heat exchanger input temperature, pressure, and mass flow rates of both the hot and cold fluid must be defined, which can be derived from the remaining system. Additionally, the target output temperature of the cold fluid needs to be specified.

The model developed by Bhapkar et al. [29] is a rating model, which means that instead of obtaining heat exchanger dimensions for a given application, the dimensions are given to the model and its performance is obtained. The performance can then be compared to the application requirements to determine if the heat exchanger is suitable. This model type is preferable for the heat exchanger sizing the sizing problem is much more complex and open ended due to the large number of dimensions that needs to be specified [30]. In this work, with the help of DLR colleagues, some of the dimensions have been specified beforehand. These are the fin dimensions and plate thicknesses.

The main design parameters of the rating model are the total lengths of the heat exchanger on the cold fluid and hot fluid sides, as well as the stack height. With these parameters, the model calculates the maximum heat transfer rate of the heat exchanger by determining the core velocities of either heat exchanger side and implementing the $\varepsilon$-NTU method as described in Section 2.2.5. The core velocities can also be used to obtain the pressure drops over the heat exchanger. The maximum heat transfer rate is then compared to the required heat transfer rate to achieve the required temperature change. If it is not sufficient, the process can be repeated with different values for the design parameters, until the requirements are met.

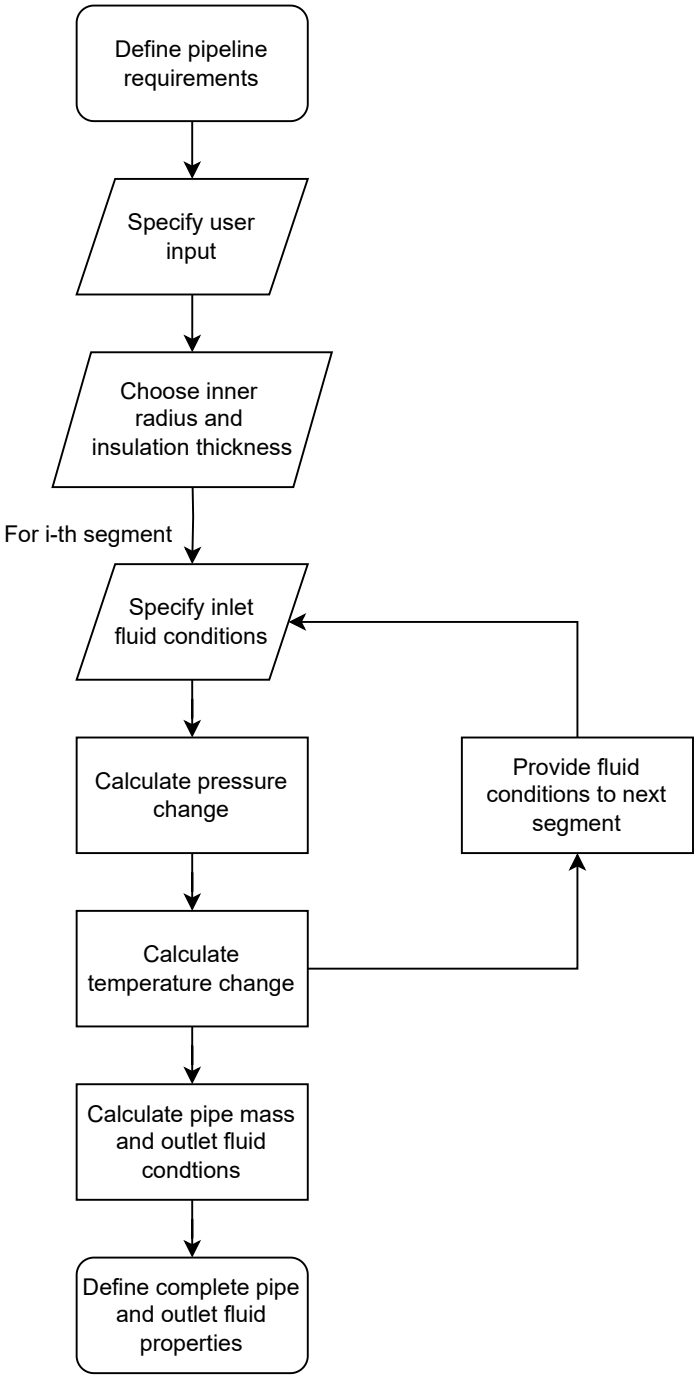


Figure 3.7: Flow chart of pipe design process.

## 3.3. RCE IMPLEMENTATION AND OPTIMISATION

Once the models of each of the components was implemented in Python, RCE was used to generate the desired architectures. RCE is an open source, workflow-driven integration environment developed by the DLR to allows for integrating of design tools in complex design processes and passing variables between them [35]. In addition to being able to implement external tools into the workflow environment, RCE contains built-in workflow tools such as input providers, output writers, convergers and optimisers [35]. These tools are utilised in parallel with the external models to generate the architectures presented in Chapter 2. The implementation of the architectures in RCE is described in Section 3.3.1 and the set up for the optimisation of the architectures in Section 3.3.2.

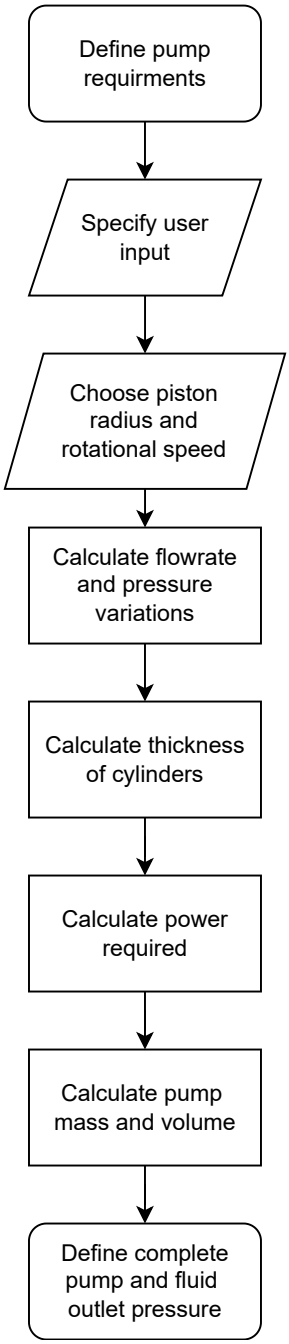


Figure 3.8: Flow chart of pump design process.

### 3.3.1. ARCHITECTURE IMPLEMENTATION

In this work, the architectures of Chapter 2 are optimised and the final results are used to perform their comparison. Two different cost functions are defined. The first is with respect to the mass of the system, and the second with respect both the mass and power. These are displayed in Equation 3.1 and Equation 3.3 respectively. In addition to the optimisation objective, constraints need to be set to specify the design space. These constraints are based on restrictions due to the fluid properties through the system and the geometry of the components. As the optimisations are performed on the system level, the user needs to define aspects of the components related to material selection and mission requirements, among others. A detailed description of the optimisation parameters is presented in Section 3.3.2.

The implementation of the optimisation and the component models described in Section 3.2 in RCE can

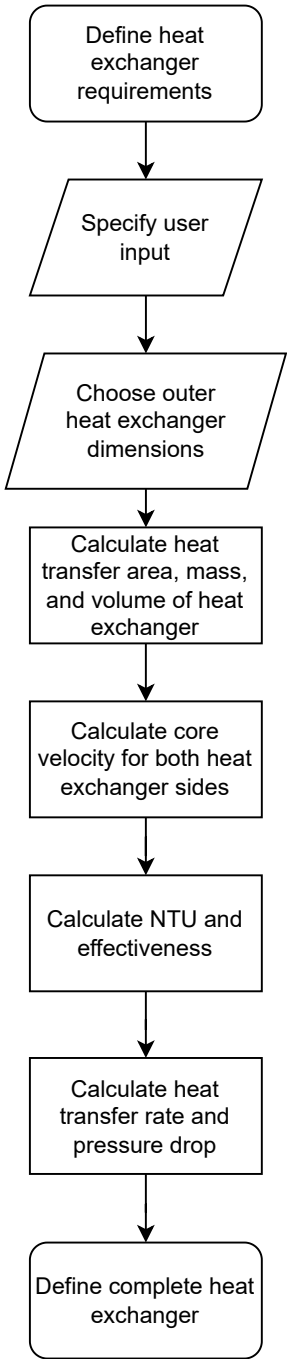


Figure 3.9: Flow chart of pipe design process.

be explained using an Extended Design Structure Matrix (XDSM) diagram. An XDSM diagram is a diagram that can be utilised to visualise Multidisciplinary Optimisation (MDO) processes by showing the data transfer between components and the flow of the process in one diagram [36]. In the diagrams, the boxes along the diagonal show the models or processes utilised in the optimisation loop. With the components as the origin, their input are on the vertical axis passing through them, while the outputs are on the horizontal one. The thick grey lines connecting two components with a list of variables shows how these variables are passed along between them, where the output of one component is the input to the other. The black lines follow the order in which the components are initiated.

The XDSM diagram describing the overall structure of the implementation can be seen in Figure 3.10. The

process begins at the optimiser, which defines the optimisation parameters passed along to the components. The input box above optimiser is a list containing the initial guesses for the optimisation parameters, while the output box on the left contains the final optimised values. Next, the SOFC characteristics are utilised to calculate all the inlet and outlet mass flow rates and pass those along to the calculations on both the hydrogen and air side of the architectures. The hydrogen and air supply subsystems are then modelled using the output from the SOFC computations and the optimiser. The results of the modelling are passed along to the objective function and the optimisation constraint computations, and, in turn, back to the optimiser. This general loop repeats until the convergence criterion or the maximum iteration limit is reached, whichever comes first.

Figure 3.11 illustrates an XDSM diagram of the hydrogen side modelling process. In particular this diagram shows the process used to size the hydrogen side of the liquid hydrogen extraction with pumps ($LH_2$ Pump) architecture displayed in Figure 3.4. The input boxes in the top row are all the input obtained from the SOFC computations and the optimiser, while the output boxes in the left column contain the variables that are passed back to the objective and constraint computations for the optimiser. Each of the components pass along the main fluid parameters to the next component, which are the mass flow rate, pressure, and temperature.

The first step is the sizing of the tank given the optimiser and user input. Next, a convergence loop is initiated to determine the required pump pressure increase. This is due to the fact that the pressure losses through the system are dependant on the initial pressure, which makes calculating the pressure rise of the pump an intrinsic problem. An initial guess for the pressure rise is given to the converger and is equal to the pressure difference of the tank and the SOFC. The outlet fluid properties of the pump are passes along to the pipe connecting the pump and vaporiser. As the pump is flooded, its outlet temperature is assumed to be equal to the fuel storage temperature. The pressure and temperature drop over the pipeline are then calculated and passed to the vaporiser. The purpose of the vaporiser is changing the phase of the fluid, which is assumed to be saturated at its inlet pressure values. The fluid properties are then passed along to the next pipe that leads to the hydrogen heat exchanger, which is sized based on the SOFC inlet temperature requirements. The pressure drop over the system is then computed based on the pressure drop over each component. Subsequently, the required pressure rise in the pump to overcome this pressure drop is taken into account and passed back to the converger. The process is repeated until the pressure rise converges. Finally, all the sizing parameters are passed to the outer optimisation loop for the computation of the objective and constraint functions.

The sizing of the air side is performed in a similar way. The process is displayed in Figure 3.12. The input and output of this inner loop can be seen in the first row and column of the diagram respectively. The process begins by specifying the atmospheric conditions and the required SOFC cathode (air) inlet mass flow rate. These are used as input to the first duct. The air is then passed through a compressor to increase its pressure enough to meet the SOFC inlet requirements. However, as the pressure losses in the remainder of the system depend on the initial pressure after the compressor, a convergence loop is initiated once again. The converger passes the ratio of total pressure increase to the compressor, whose initial value is defined the ratio of the SOFC inlet pressure to the atmospheric pressure. The increase in static pressure and temperature over the pressure can be computed, as well as the power required by the compressor. The compressed air is then passed through a pipe and the air heat exchanger, similar to the hydrogen side. Once these are modelled, the pressure losses between the compressor and the SOFC and the inlet pressure requirement is used to calculate a new required pressure ratio for the compressor. Subsequently, the process is repeated until the pressure losses converge. Next, the SOFC cathode exhaust stream is investigated. The hot exhaust air is passed through the heat exchanger to heat up the cold air. Subsequently, it flows through another pipe to a turbine, where it is expanded to atmospheric conditions to investigate the maximum theoretical power recovery possible.

The XDSM diagrams of the two other architectures presented in Section 3.1, which are the self-pressurisation architectures with either liquid or gaseous hydrogen extraction, are presented in Figure 3.13 and Figure 3.14 respectively. The main difference is on the hydrogen side modelling as the pressure in the tank drives the transportation of hydrogen. Hence, the convergence loop includes the sizing of the tank and the variable that is being converged is the its storage pressure.

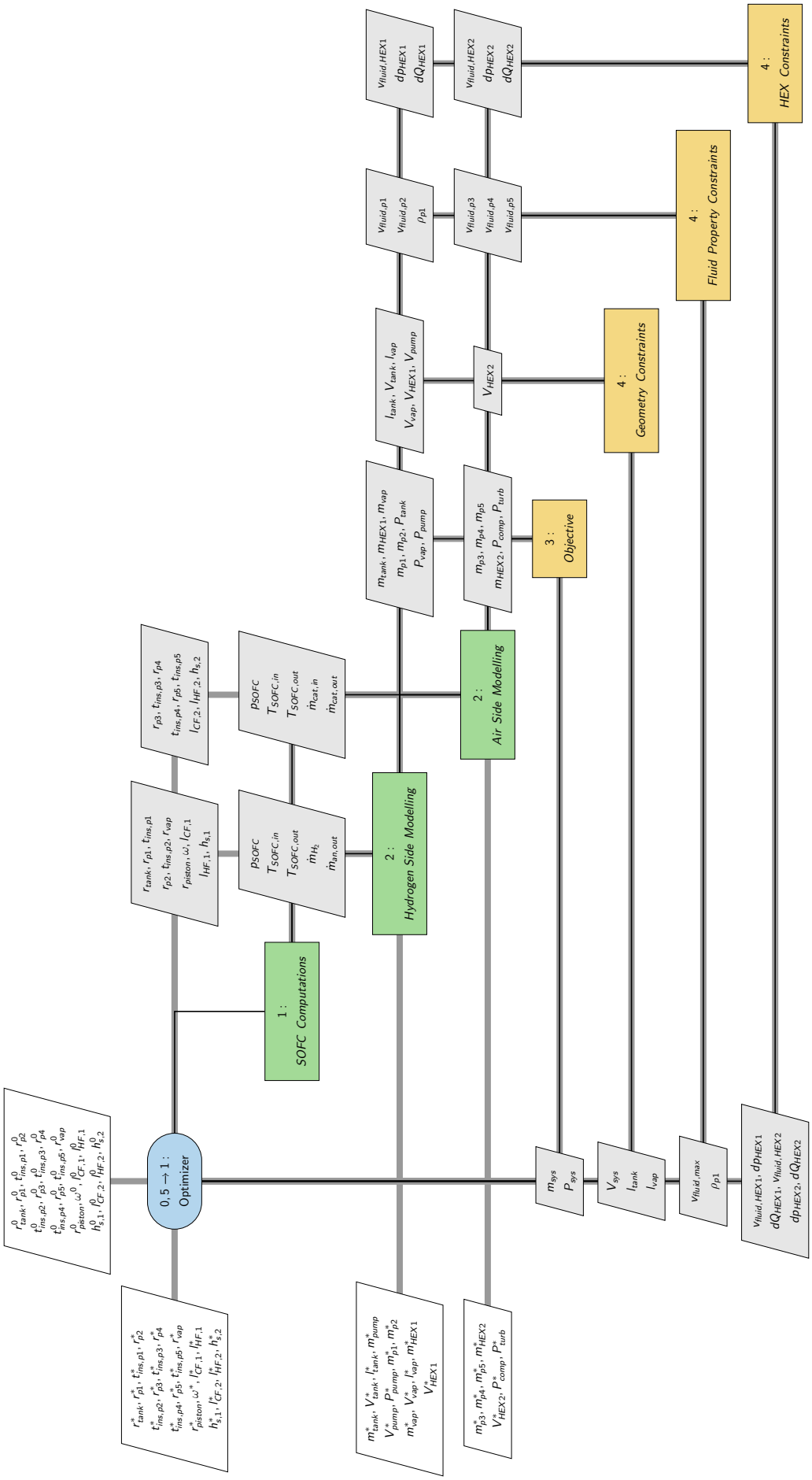


Figure 3.10: XDSM diagram with overall structure of optimisation

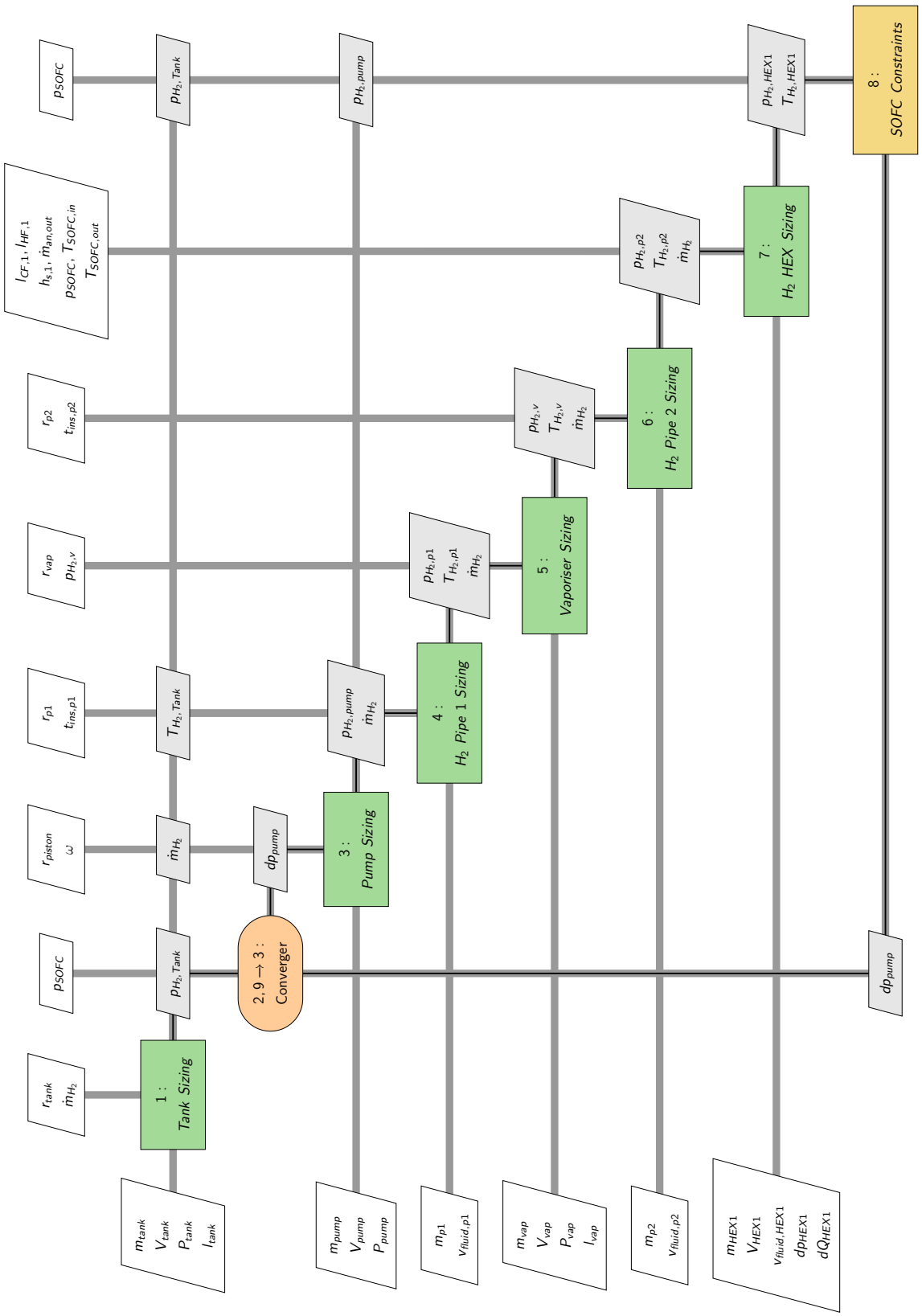


Figure 3.11: XDSM diagram of the hydrogen side modelling for the $LH_2$ Pump architecture.

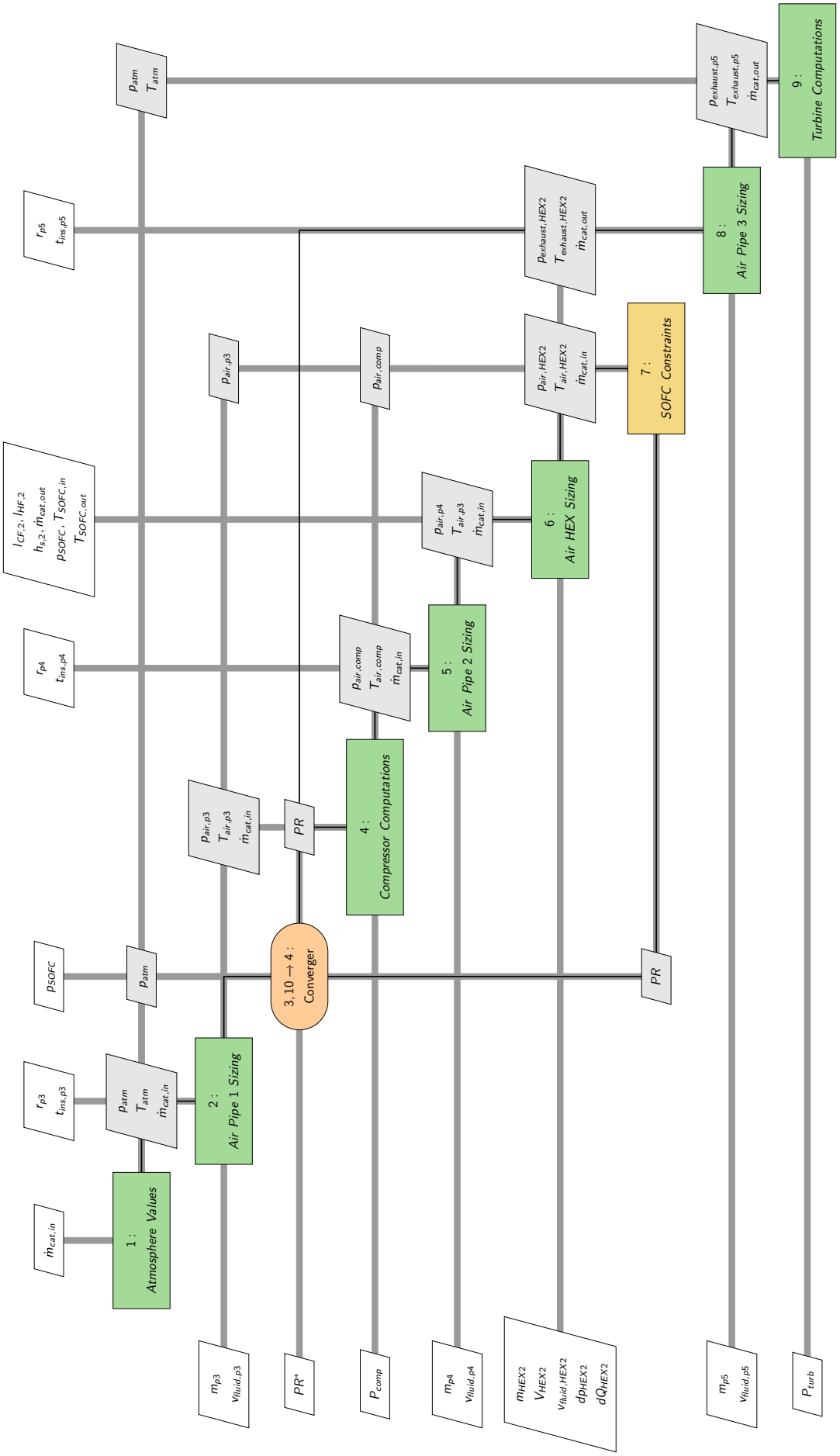


Figure 3.12: XDSM diagram of the air side modelling.

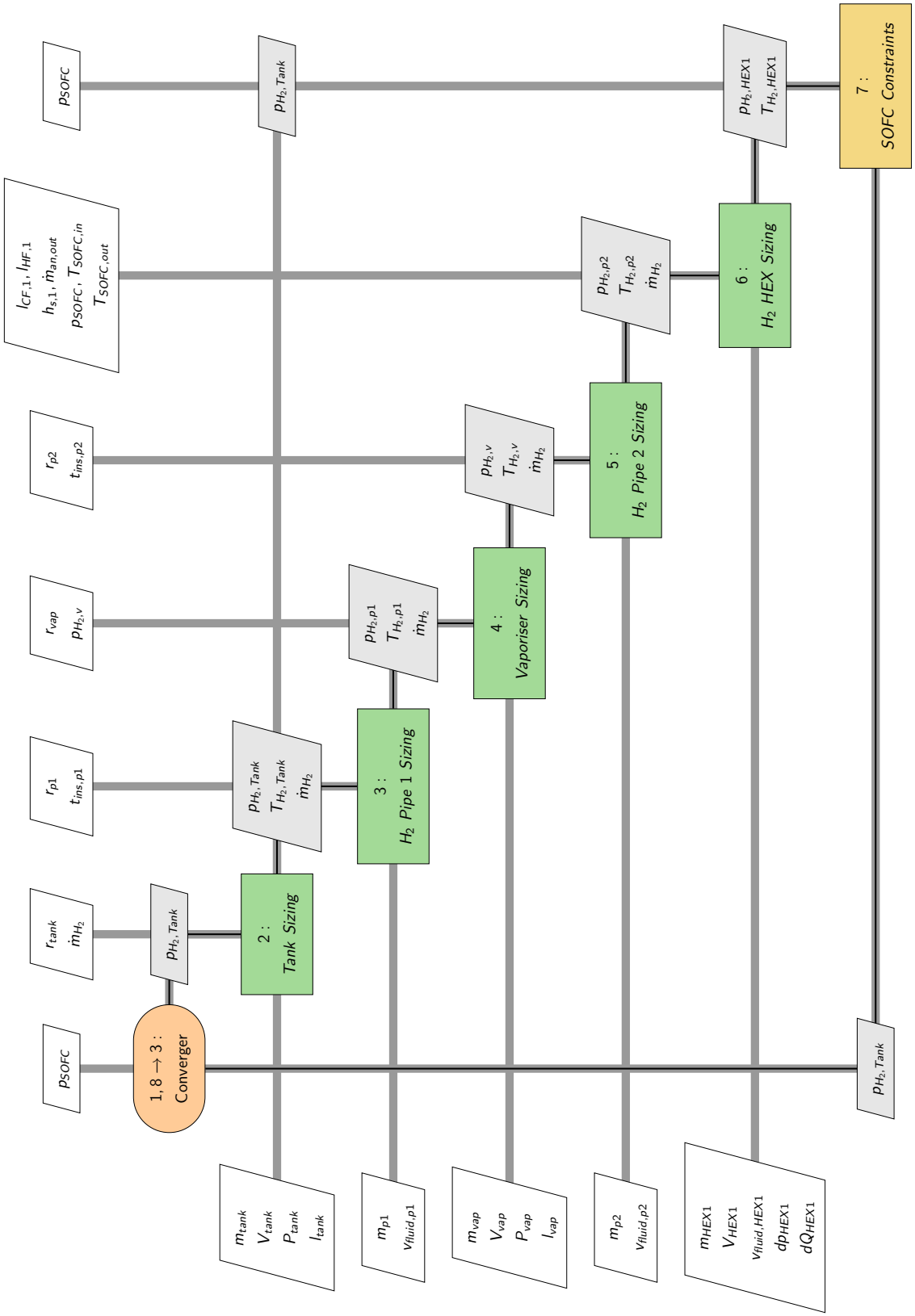


Figure 3.13: XDSM diagram of the hydrogen side modelling for the $LH_2$ SP architecture.

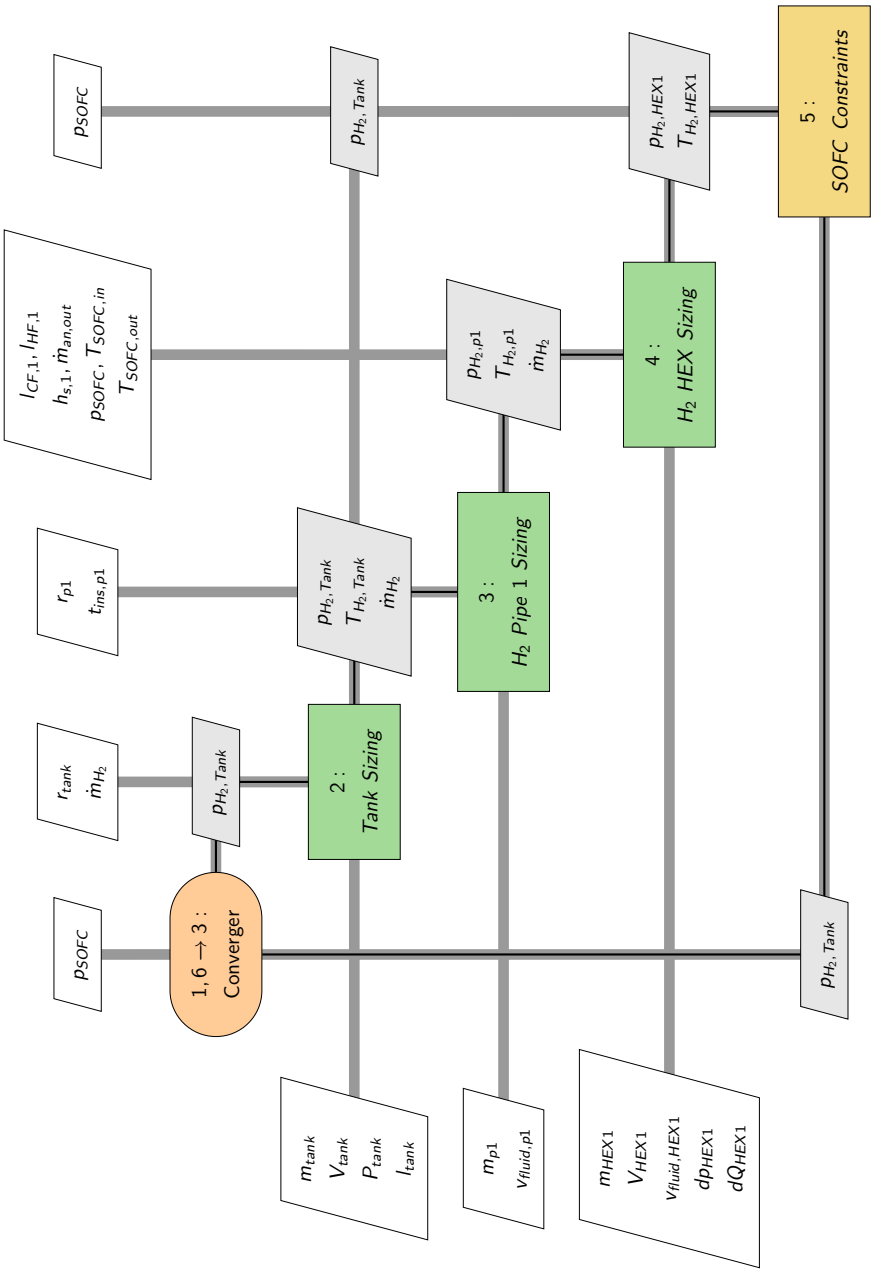


Figure 3.14: XDSM diagram of the hydrogen side modelling for the $GH_2$ SP architecture.

### 3.3.2. OPTIMISATION PARAMETERS AND USER DEFINED INPUT

Before the optimisations, presented in Section 3.3.1, can be performed, parameters related to the optimisation and the design of the components need to be defined. The built-in optimiser tool in RCE is used, which imports optimisation methods from the DAKOTA toolbox [35, 37]. Local gradient-based methods are implemented for the optimisations as their speed allows for the quick comparison of multiple architectures and the effect of certain design choices. If a complete architecture was already chosen for a definite mission, a global optimisation method, or a combination of the two types, is recommended to avoid falling into local minima. From the algorithms included in RCE, the Constrained Optimization BY Linear Approximations (COBYLA) local simplex method is selected for this work, as it was shown to be highly efficient with quicker convergence speeds compared to the other methods. It is an extension to the Nelder-Mead simplex algorithm and utilises the derivative of the objective function with respect to each parameter to determine the quickest path to minimising it [37–39].

Two main objectives are analysed for the optimisations performed in this work. The first objective is minimising the mass of the system and can be implemented directly in RCE as the output from the objective analysis to the optimiser tool. The cost function is presented in Equation 3.1.

$$f_1 = \frac{m_{system}}{m_{system,0}} \tag{3.1}$$

The other objective is to minimise a cost function related to minimising the mass of the system and maximising the net power recovered by the system. It is defined in Equation 3.2 as the power recovered by the turbine subtracted by the power required by the compressor and the system. The latter includes the power required by the tank, vaporiser, and pump. For calculating the power required to heat the tank and vaporiser, a critical mission phase is identified, and it is calculated using the method described in Section 2.2.2. This critical mission phase is chosen to be the take-off phase, due to the SOFC requiring the largest mass flow rate at this point.

$$P_{net} = P_{turb} - P_{comp} - P_{sys} \tag{3.2}$$

In order to define a cost function to minimise both variables, the inverse of the net power is utilised, as minimising this value is equivalent to maximising the net power. Additionally, as both variables have a different order of magnitude, both are scaled with respect to the values obtained from the initial guess.

$$f_2 = f_{mass} + f_{power} = \frac{m_{system}}{m_{system,0}} + \frac{P_{net}^{-1}}{P_{net,0}^{-1}} \tag{3.3}$$

The main optimisation parameters passed along to the components from the optimiser are shown in Table 3.1. These are all the geometrical parameters that will be varied by the optimiser between iterations and are all non-dimensionalised with respect to the maximum value for each. This is due to the fact that the optimiser in RCE takes the same step size for each variable, however they are within different order of magnitudes. Therefore, the optimisation parameters vary between a chosen lower bound and 1, where the value implemented in the modelling is the parameter multiplied by the maximum value. The lower bounds in this optimisation are typically chosen either by limitations in the model, as some of the components lead to non-physical values for the components (for example choosing too low of a tank radius can lead to a negative length for the cylindrical part for a given hydrogen volume, or too small of a radius leads to a very large pressure drop exceeding the initial pressure), or via expert interviews within the DLR. The latter is used in particular for the sizing of the heat exchanger, where Bhapkar assisted in determining the bounds and constraints of the design. The maximum values of the design are estimated based on the size available in the reference aircraft of the $H_2$EAT project, but can be varied by the user when more details about the concept aircraft are known. The starting points of the optimisations were chosen from initial sizing procedures on the individual components already performed in the $H_2$EAT project. These variables were kept constant between all optimisation initiations of the different architectures to fairly compare their outcomes.

Table 3.1: Table of Optimisation Parameters

| Optimisation Parameter | Range | Starting Value | Maximum Value | Architectures* |
|---|---|---|---|---|
| Tank Inner Radius | (0.1, 1) | 0.688916 | 1.5 $m$ | All |
| Stack Height Hydrogen HEX | (0.02,1) | 0.032156 | 5 $m$ | All |
| Stack Height Air HEX | (0.02,1) | 0.114831 | 5 m | All |
| Cold Side Length Hydrogen HEX | (0.0833,1) | 0.28605 | 0.6 $m$ | All |
| Cold Side Length Air HEX | (0.1,1) | 0.41406 | 0.6 $m$ | All |
| Hot Side Length Hydrogen HEX | (0.05,1) | 0.775914 | 1 $m$ | All |
| Hot Side Length Air HEX | (0.05,1) | 0.264929 | 1 $m$ | All |
| Pipe 1 Radius | (0.02,1) | 0.05 | 0.25 $m$ | All |
| Pipe 1 Insulation Thickness | (0.01,1) | 0.8 | 0.01 $m$ | All |
| Pipe 2 Radius | (0.04,1) | 0.05 | 0.25 $m$ | 2, 3 |
| Pipe 2 Insulation Thickness | (0.01,1) | 0.3 | 0.01 $m$ | 2, 3 |
| Pipe 3 Radius | (0.02,1) | 0.9 | 0.25 $m$ | All |
| Pipe 3 Insulation Thickness | (0.01,1) | 0.3 | 0.01 $m$ | All |
| Pipe 4 Radius | (0.02,1) | 0.8 | 0.25 $m$ | All |
| Pipe 4 Insulation Thickness | (0.01,1) | 0.3 | 0.01 $m$ | All |
| Pipe 5 Radius | (0.01,1) | 0.8 | 0.25 $m$ | All |
| Pipe 5 Insulation Thickness | (0.01,1) | 0.3 | 0.01 $m$ | All |
| Vaporiser Inner Radius | (0.01,1) | 0.81309 | 0.5 $m$ | 2, 3 |
| Pump Rotational Speed | (0.01,1) | 0.33 | 60 $rad/s$ | 3 |
| Piston Inner Radius | (0.01,1) | 0.723 | 0.3 $m$ | 3 |

* The self-pressurisation architecture with gaseous and liquid hydrogen extraction are numbered 1 and 2 respectively, and the pump-fed architecture with liquid hydrogen extraction is numbered 3.

In addition to these parameters, a set of constraints were applied to the optimisations to limit the design space of the systems, which are presented in Table 3.2. As can be seen in Figure 3.10, the constraints implemented in these optimisations are related to the fluid properties, the system geometry, and the heat exchanger (HEX). In RCE, these constraints can be given an upper and a lower bound. The fluid property constraints are mostly related to the maximum fluid velocity in all the pipes, where a maximum allowable fluid velocity can be defined by the user to avoid pipe degradation. The maximum fluid velocity could possibly be defined using the erosional velocity of the pipe, which is a value utilised in the gas pipeline industry to define the maximum fluid velocity after which the pipe begins to degrade due to erosion. For fluids that are not significantly corrosive and don't have a large amount of solid particles, Equation 3.4 can be used to estimate the erosional velocity [40]. This value is determined to be around 35 $m/s$ for liquid hydrogen, therefore a constraint of 30 $m/s$ was chosen for these optimisations. Another fluid property constraint is related to maintaining single-phase flow in the pipe connecting the liquid hydrogen storage tank and the vaporiser by utilising the insulation to ensure that the liquid hydrogen does not vaporise due to heating from the environment. While the script is able to model both types of flow (liquid or gaseous), the effect of transition between the phases was not modelled. Therefore, given a certain initial temperature and pressure, it is desired to maintain the corresponding phase. Note that for the architecture utilising gaseous extraction, this constraint is not required. The final constraint on the fluid parameters is that the pressure should decrease over the length of the pipeline. This constraint is set to ensure that there is no backflow in the pipeline.

$$v_e = \frac{300}{\sqrt{\rho}} \tag{3.4}$$

The constraints on the geometry of the architecture are related to the implementation of the system in the aircraft given the available space inside. This includes the total volume of the system in relation to the maximum value of the constraint, and the lengths of the components such as the tank and vaporiser.

The remaining constraints are related to the heat exchanger (HEX) performance on both sides of the system and were decided based on expert interviews from DLR colleagues. The main requirement is that the possible heat transfer rate through the both heat exchangers exceeds the heat transfer rate required by the fluid to achieve the SOFC inlet temperatures. A maximum value for the hot fluid pressure drop ratio over the

heat exchanger and the fluid velocity in the component are also specified by the user. These were chosen to be a 10% pressure drop and 50 $m/s$ based on DLR internal preliminary project results. Last but not least, a constraint on the maximum difference in the inlet pressures on the hot and cold side of the heat exchanger can be defined and is set to 20%.

Table 3.2: List of constraints implemented in the optimisations

| Component | Constraint | Lower Bound | Upper Bound |
|---|---|---|---|
| HEX | Fluid Velocity Constraint [m/s] | 0 | 50 |
| HEX | Difference in Heat Transfer Rate | 0 | - |
| HEX | Hot Fluid Pressure Drop Ratio | 0 | 0.1 |
| HEX | Percentage Inlet Pressure Difference | 0 | 20% |
| Tank | Length | 0 | 6 |
| Vaporiser | Length | 0 | 3.5 |
| Pipes | Fluid Velocity | 0 | 30 |
| Pipes | Pressure Change | - | 0 |
| Pipes | Liquid Hydrogen Density | 10 | - |

The main stopping criterion for the optimisation is related to the converge of the cost functions. Once the variation in the cost function value between iterations falls below $1E-4$, the optimisation is considered to be converged. The other criterion is related to the maximum number of optimisation iterations, which is set to 1000 in this work. Finally, the user input for each of the components implemented in the optimisations can be seen in the tables below. This input is mainly derived from mission requirements and material selections. It should be noted that the hydrogen side pipes in Table 3.6 have two values, with the first being for the $GH_2$ SP system and the second for the $LH_2$ SP and $LH_2$ Pump systems respectively. This was done to have the total pipe length and fittings the same, although the hydrogen changes phases in the vaporise for the latter architectures.

Table 3.3: SOFC user defined parameters [5].

| SOFC User Input | | |
|---|---|---|
| **Parameter** | **Value** | **Unit** |
| Maximum Hydrogen Mass Flowrate | 43.4 | $g/s$ |
| Inlet Temperature | 1073 | $K$ |
| Outlet Temperature | 1273 | $K$ |
| Operational Pressure | 5 | $bar$ |
| Fuel Utilisation | 0.8 | - |
| Air Utilisation | 0.2 | - |

Table 3.4: Compressor and Turbine exchanger user defined parameters.

| Compressor and Turbine User Input | | |
|---|---|---|
| **Parameter** | **Value** | **Unit** |
| Compressor Isentropic Efficiency | 0.9 | - |
| Turbine Isentropic Efficiency | 0.92 | - |
| Pressure at Turbine Outlet | 101325 | $Pa$ |

Table 3.5: Tank user defined parameters [12, 13].

| Tank User Input | | |
|---|---|---|
| **Parameter** | **Value** | **Unit** |
| Boil-off Mass Flowrate at Standstill | 5 | $g/s$ |
| Total Hydrogen Mass Stored | 528 | $kg$ |
| Storage Pressure (Pump-fed System) | 3 | $bar$ |
| Inner Vessel Material | Aluminium | - |
| Outer Vessel Material | Aluminium | - |
| Aluminium Density | 2780 | $kg/m^3$ |
| Aluminium Allowable Stress | 68.9 | $MPa$ |
| Aluminium E-Modulus | 72.4 | $GPa$ |
| Aluminium Poisson's Ratio | 0.33 | - |
| Aluminium Thermal Conductivity | 170 | $Wm^{-1}K^{-1}$ |
| Aluminium Emissivity | 0.075 | - |
| Insulation Type | Polysterene | - |
| Insulation Density | 32 | $kg/m^3$ |
| Insulation Thermal Conductivity | 0.022 | $Wm^{-1}K^{-1}$ |
| Excess Volume for Gaseous H2 | 7.2% | - |
| Critical Condition Fill Level | 0.8 | - |

Table 3.6: Pipe user defined parameters [5, 12].

| Pipe User Input | | |
|---|---|---|
| **Parameter** | **Value** | **Unit** |
| Pipe Material | Stainless Steel | - |
| Stainless Steel Density | 7920 | $kg/m^33$ |
| Stainless Steel Allowable Stress | 129.2 | $MPa$ |
| Stainless Steel E-Modulus | 72.4 | $GPa$ |
| Stainless Steel Poisson's Ratio | 0.33 | - |
| Stainless Steel Thermal Conductivity | 170 | $Wm^{-1}K^{-1}$ |
| Stainless Steel Emissivity | 0.35 | - |
| Insulation Type | Polysterene | - |
| Insulation Density | 32 | $kg/m3$ |
| Insulation Thermal Conductivity | 0.022 | $Wm^{-1}K^{-1}$ |
| H2 Pipe 1 Length | 6.24 / 4 | $m$ |
| H2 Pipe 2 Length | - / 2.24 | $m$ |
| Air Pipe 1 Length | 1 | $m$ |
| Air Pipe 2 Length | 1 | $m$ |
| Air Pipe 3 Length | 1 | $m$ |
| H2 Pipe 1 Height Change | -1/ 0 | $m$ |
| H2 Pipe 2 Height Change | - / -1 | $m$ |
| Air Pipe 1 Height Change | 0 | $m$ |
| Air Pipe 2 Height Change | 0 | $m$ |
| Air Pipe 3 Height Change | 0 | $m$ |
| H2 Pipe 1 k-Factor List | [0.2,0.2] / [0.2] | - |
| H2 Pipe 2 k-Factor List | - / [0.2] | - |
| Air Pipe 1 k-Factor List | [0.2] | - |
| Air Pipe 2 k-Factor List | [0.2] | - |
| Air Pipe 3 k-Factor List | [0.2] | - |

Table 3.7: Vaporiser user defined parameters [12].

| Vaporiser User Input | | |
|---|---|---|
| **Parameter** | **Value** | **Unit** |
| Total Hydrogen Mass Stored | 30 | $kg$ |
| Inner Vessel Material | Aluminium | - |
| Outer Vessel Material | Aluminium | - |
| Aluminium Density | 2780 | $kg/m^3 3$ |
| Aluminium Allowable Stress | 68.9 | $MPa$ |
| Aluminium E-Modulus | 72.4 | $GPa$ |
| Aluminium Poisson's Ratio | 0.33 | - |
| Aluminium Thermal Conductivity | 170 | $Wm^{-1}K^{-1}$ |
| Aluminium Emissivity | 0.075 | - |
| Excess Volume for Gaseous H2 | 30% | - |
| Critical Condition Fill Level | 0.5 | - |

Table 3.8: Hydrogen and Air Heat exchanger user defined parameters [29].

| Heat Exchanger User Input | | |
|---|---|---|
| **Parameter** | **Value** | **Unit** |
| Heat Exchanger Material | Inconel 625 | - |
| Inconel 625 Density | 8510 | $kg/m^3$ |
| Inconel 625 Thermal Conductivity | 18 | $Wm^{-1}K^{-1}$ |
| Plate Thickness | 0.5 | $mm$ |
| Plate Channel Height | 2 | $mm$ |
| Fin Thickness | 0.051 | $mm$ |
| Fin Height | 1.29 | $mm$ |
| Fin Pitch | 1.29 | $mm$ |
| Fin Length | 2.54 | $mm$ |
| Fin Hydraulic Diameter | 1.22 | $mm$ |

Table 3.9: Pump user defined parameters [41].

| Pump User Input | | |
|---|---|---|
| **Parameter** | **Value** | **Unit** |
| Number of Pistons | 3 | - |
| Pump Material | Inconel 718 | - |
| Density | 8193 | $kg/m^3$ |
| E-modulus | 215.8 | $GPa$ |
| Poisson's Ratio | 0.25 | - |
| Fatigue Stress | 275 | $MPa$ |
| Yield Stress | 1.3 | $GPa$ |
| Max Radial Strain | 0.01 | - |

# 4

# Results and Discussions

The results related to the optimisations performed on the architectures are presented in this chapter. First, the results of the baseline optimisations defined in Section 3.3 are discussed in Section 4.1. In this section, all the trends and results of the optimisation are presented for the architecture utilising gaseous extraction with self pressurisation. Then, the main changes of interest resulting from the addition of the new components or different extraction method are presented for the remaining architectures. A comparison of the summarised optimisation outcomes of the converged systems is performed in Section 4.2, followed by a preliminary mission analysis of the architecture utilising gaseous hydrogen extraction with self-pressurisation in Section 4.3. Subsequently, the most impactful optimisation parameters are derived via a sensitivity analysis in Section 4.4. The verification of the model implementation and the study on the number of pipe segments were performed in Section 4.5 and Section 4.6 respectively. Finally, the additional optimisations performed with a new initialisation point and a different SOFC inlet pressure are portrayed in Section 4.7.

## 4.1. Baseline Optimisations

The minimisation of two different objective functions was performed on each of the architectures. These are the minimisation of the system mass cost function and the power-mass cost function as defined in Section 3.3.2. The results of these optimisations are detailed for each architecture in Section 4.1.1, Section 4.1.2, and Section 4.1.3.

### 4.1.1. Gaseous Extraction with Self-Pressurisation

#### Mass Optimisation

The convergence of the objective function and the system mass for the gaseous hydrogen extraction with self-pressurisation ($GH_2$ SP) architecture are presented in Figure 4.1a and Figure 4.1b respectively. The final mass composition of the architecture can be seen in Figure 4.2 and Figure 4.3. The shape of the mass plot follows from the fact that the optimiser first tries to satisfy the constraints, since it starts outside the allowable design space, then manages to reduce the mass inside the design space. Once the variation in the cost function satisfies the convergence criteria, the optimisation is concluded.

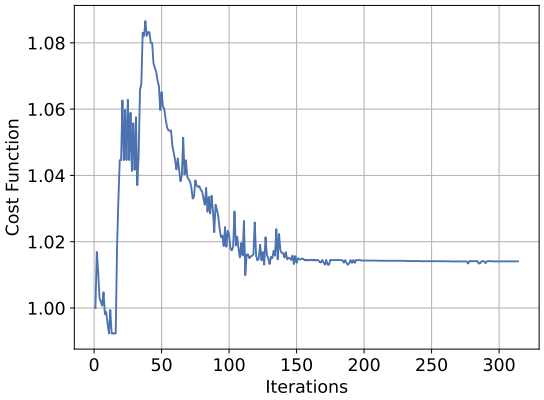


(a) Convergence of the cost function over the course of the optimisation.

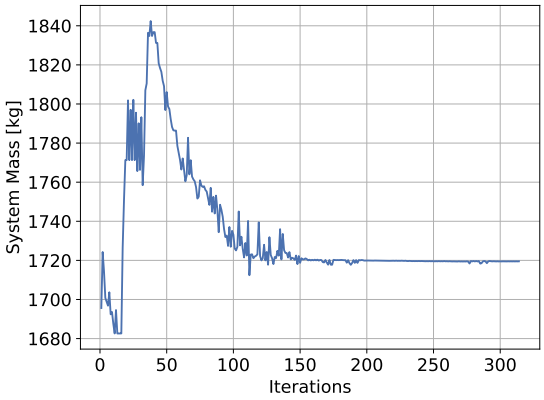


(b) Convergence of system mass plotted over the course of the optimisation.

Figure 4.1: $GH_2$ SP architecture mass optimisation convergence plots

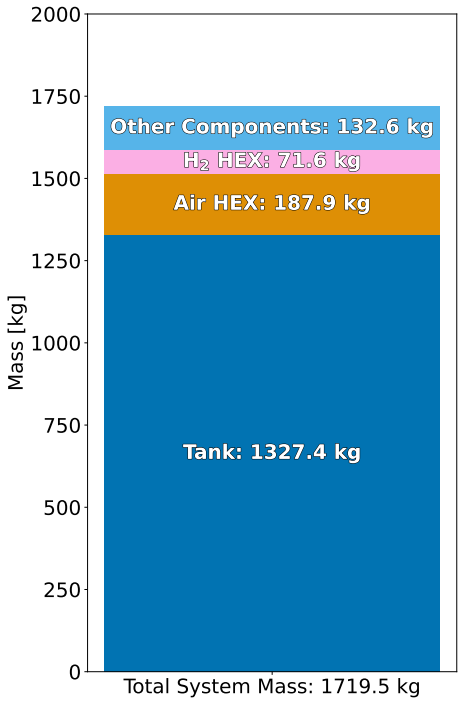


Figure 4.2: Mass optimisation: Mass composition of the complete $GH_2$ SP architecture.

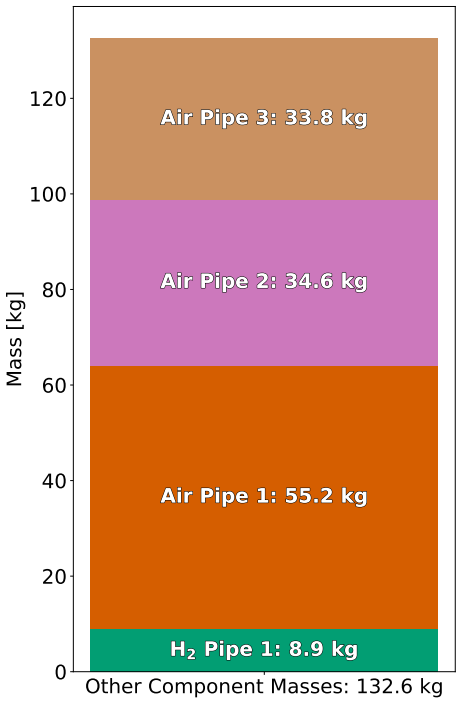


Figure 4.3: Mass optimisation: Mass composition of the remaining components of the $GH_2$ SP architecture.

As observed the tank is the largest component of the architecture, which can be justified from the fact that it contains the hydrogen mass required for the mission. This is followed by the air and hydrogen heat exchangers respectively and then the pipes. The air side pipes are significantly heavier than the hydrogen side pipes due to the much larger mass flow rate passing through them and the velocity constraints imposed by the structural requirements.

The variation in the overall system mass is mostly attributed to the change in the mass of the tanks and the heat exchangers, where the former is presented in Figure 4.4a. While the mass of the tank largely depends on the amount of hydrogen stored inside, its proportions also have an effect. It can be seen in Figure 4.4b, that the shape of the inner radius variations has a close resemblance to that of the tank mass, converging to a smaller radius and longer length than the initial guess given to the optimiser. The length of the tank is directly related to the radius given a constant hydrogen mass as described in Section 2.2.1. This correlation between

the mass and the dimensions arises from the methodology used to calculate the thickness for each layer of the structure. Particularly, for the outer shell of the tank, the wall thickness is different for the hemispherical and cylindrical part of the tank, leading to different mass compositions depending on the tank sizing parameters. Figure 4.4b shows that the optimiser is able to find an optimum ratio between the length and the radius of the tank for the given mass of hydrogen stored.

The tank pressure also has an effect its mass, as a higher pressure leads to thicker walls. This is especially clear at the beginning of the optimisation where the effect of the pressure variations can be seen in the tank mass, where the plots in Figure 4.4c and Figure 4.4a have their oscillate similarly. The plots of the tank pressure and the power required to maintain the tank pressure at a desired critical condition are presented in Figure 4.4c and Figure 4.4d. As the shape of the plots is the same but inverted, it can be derived that the power required to heat the tank varies inversely with the pressure, where a higher pressure leads to a slight decrease in the power required. The reason for this behaviour can be attributed to the vaporisation of hydrogen significantly influencing the tank power requirement, and the latent heat of vaporisation decreasing slightly with the increasing pressure, leading to less power needed. Overall, the difference between the maximum and minimum power in the plots is very small (order of 30 W) due to the fact that the tank insulation is sized to limit the heat entering the tank from the environment based on a desired boil-off rate.

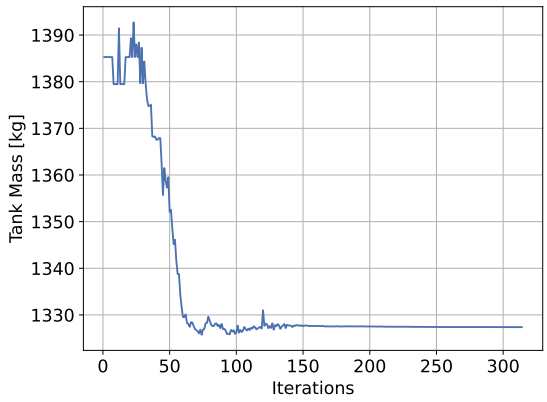


(a) Variation in the mass of the tank.

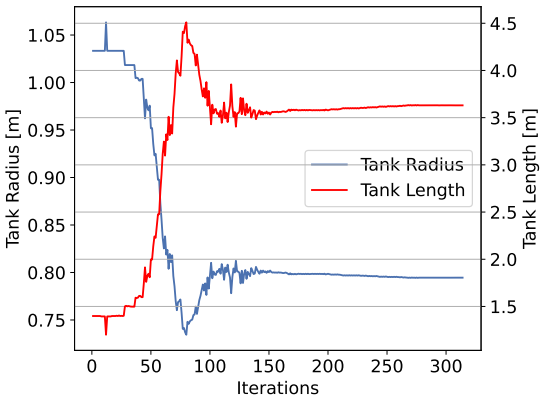


(b) Variation in the total tank dimensions.

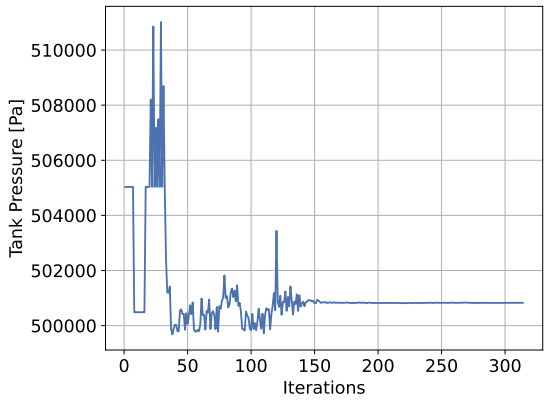


(c) Variation in the tank pressure.

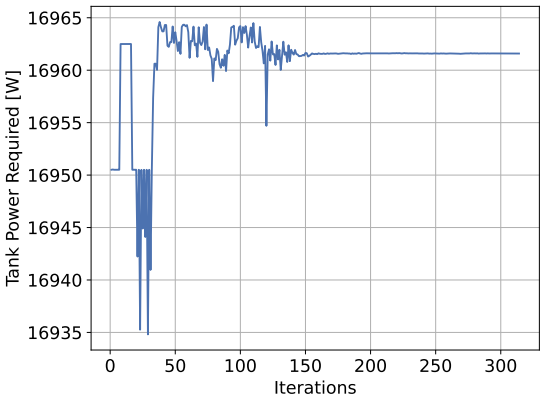


(d) Variation in the tank power required.

Figure 4.4: $GH_2$ SP architecture mass optimisation: Tank convergence plots

The variation in the required pressure is a direct consequence of the change in the hydrogen pipe radius and mass. A smaller pipe radius and mass, lead to increased pressure losses through them. This means that the storage pressure needs to be increased to compromise for it, and in turn the mass of the tank is increased. This correlation can be seen when investigating the optimisation propagation for the tank pressure, pipe mass and radius, and pressure drop in Figure 4.4c, Figure 4.5a, and Figure 4.5b. The optimiser finds a

compromise between the mass of the hydrogen side pipe and the mass of the tank.

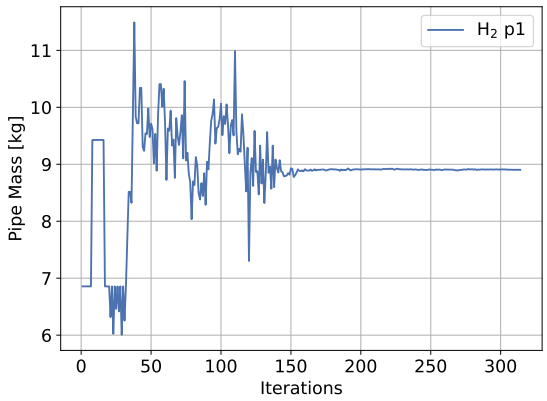


(a) Variation in the hydrogen pipe mass.

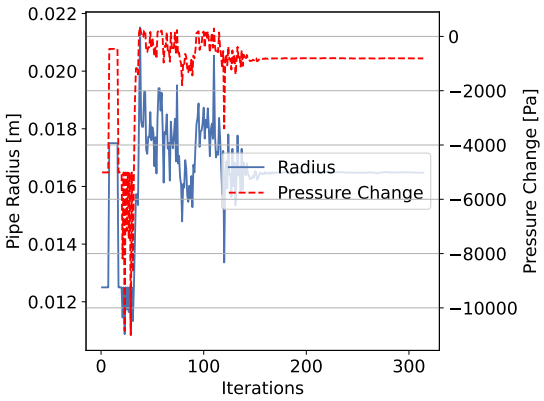


(b) Variation in the radius and pressure change of the hydrogen side pipe.

Figure 4.5: $GH_2$ SP architecture mass optimisation: Hydrogen side pipe convergence plots

On the air side, the optimisation of the first pipe connecting atmosphere inlet to the compressor is limited by the fluid velocity in the pipes (seen in Figure 4.6a), while the other two pipes reduce in mass over the entire optimisation. It can be seen that for some of the radius variations in Figure 4.6d, the jump in mass in Figure 4.6b is a larger than for the others. This stems from the method used to select the thickness of the pipeline from the ASME pipe schedules presented in Table A.1.

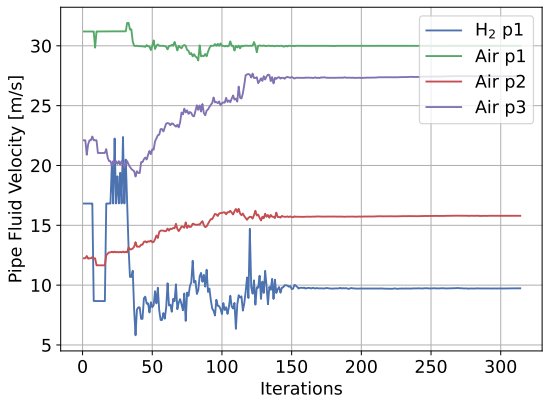


(a) Variation in the maximum fluid velocity in the pipes.

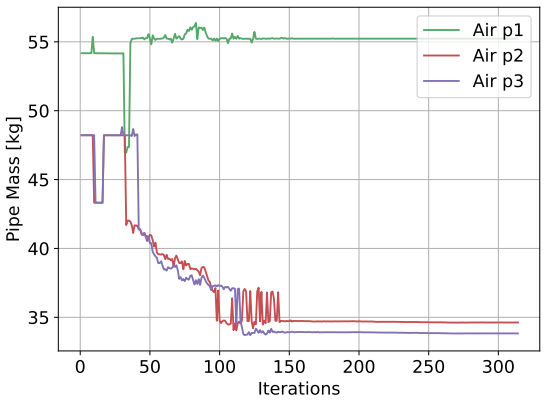


(b) Variation in the mass of the air side pipes.

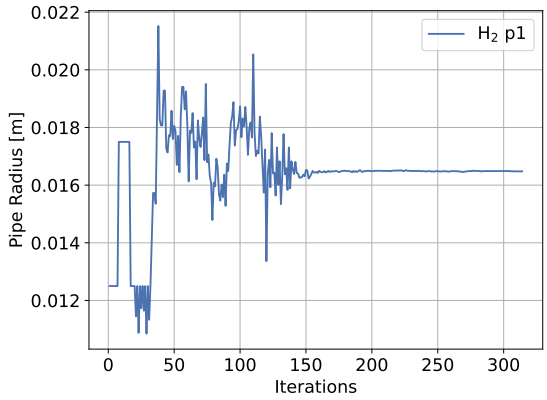


(c) Variation in the radius of the hydrogen side pipes.

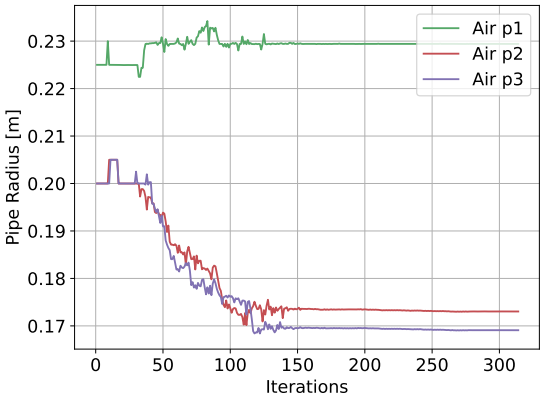


(d) Variation in the radius of the air side pipes.

Figure 4.6: $GH_2$ SP architecture mass optimisation: Hydrogen and air side pipe convergence plots

Next, the change in the masses of the heat exchangers is investigated, which was increased over the course of the optimisation by over 20 kg as seen in Figure 4.7a. This is due to the fact that the initialisation point for the heat exchanger led to it being undersized. By using the method described in Section 2.2.5, the initial heat transfer rate through the hydrogen heat exchanger was determined to be around 23 kW less than what was required for heating up the fluid. Subsequently, the heat exchanger was increased in size throughout the convergence. The optimiser does not approach the limits of the fluid velocity or the hot fluid pressure drop ratio constraints as the optimisations proceed. The resulting variation in the non-dimensionalised lengths of the cold side and hot side and the stack height for the hydrogen heat exchanger over the course of the optimisation are presented in Figure 4.7e.

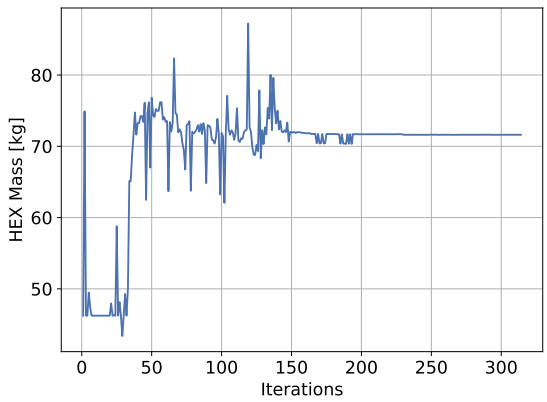


(a) Variation in the mass of the hydrogen heat exchanger.

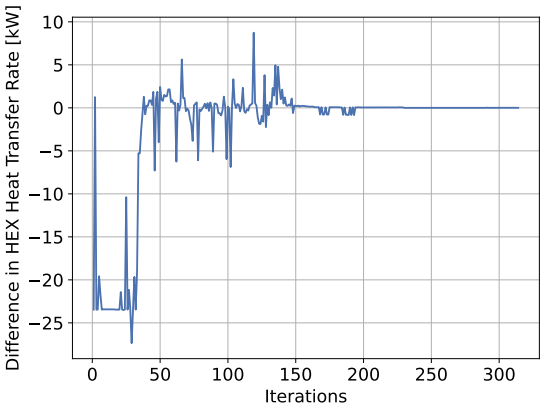


(b) Variation in the difference in the hydrogen heat exchanger heat transfer rate and fluid required heat transfer rate.

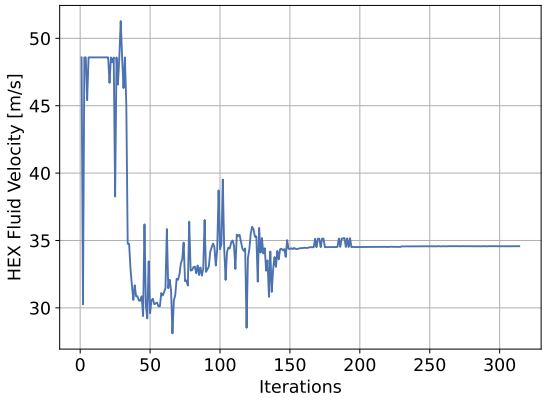


(c) Variation in the fluid velocity in the hydrogen heat exchanger.

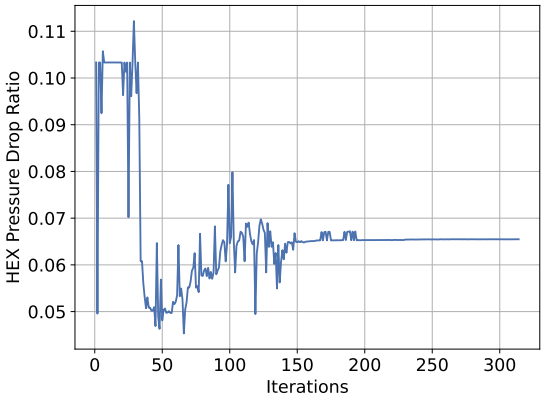


(d) Variation in the hydrogen heat exchanger hot fluid pressure drop ratio.

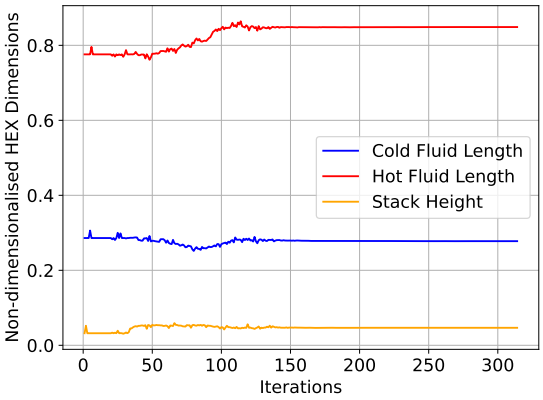


(e) Variation in the Hydrogen heat exchanger non-dimensionalised lengths.

Figure 4.7: $GH_2$ SP architecture mass optimisation: Hydrogen heat exchanger convergence plots

Similarly to the hydrogen heat exchanger, the air heat exchanger initially was not able to transfer the necessary heat between the hot and cold fluids. The difference at the beginning of the optimisation was over 250 kW as can be seen in Figure 4.8b. Subsequently, the heat exchanger needed to be increased in size which led to a larger mass as in Figure 4.8a. During the optimisation, the hot fluid pressure drop and heat exchanger fluid velocity constraints plotted in Figure 4.8c and Figure 4.8d initially restricted the design, leading to the variation in the non-dimensionalised lengths seen in Figure 4.8f.

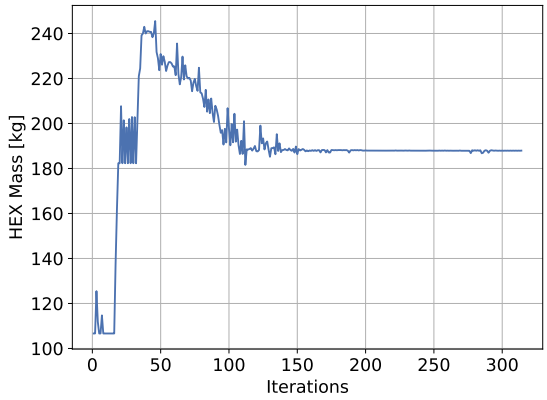


(a) Variation in the mass of the air heat exchanger.

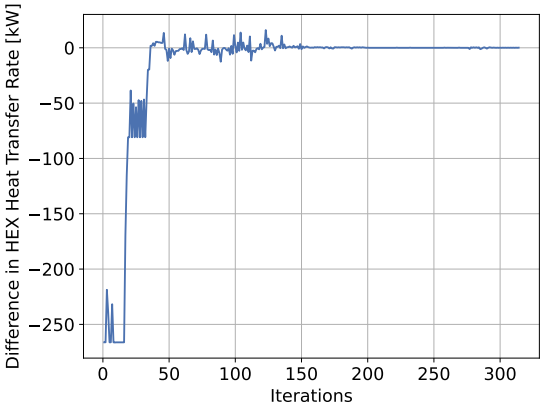


(b) Variation in the difference in the air heat exchanger heat transfer rate and fluid required heat transfer rate.

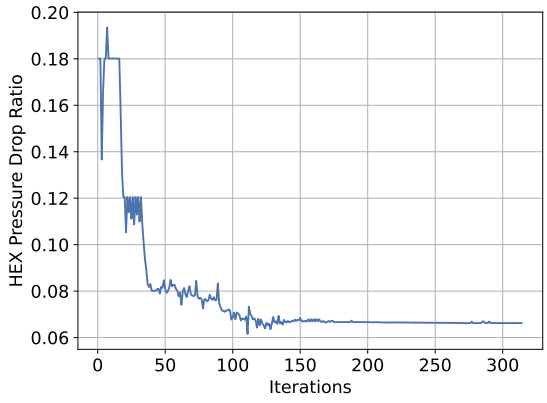


(c) Variation in the air heat exchanger hot fluid pressure drop ratio.

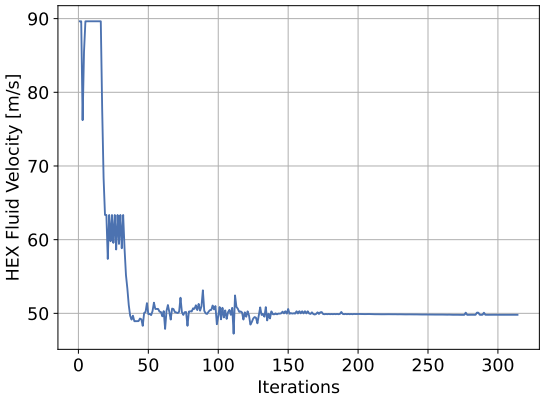


(d) Variation in the hot fluid velocity in the air heat exchanger.

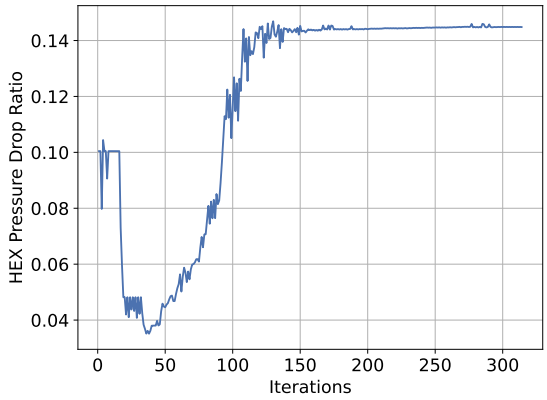


(e) Variation in the air heat exchanger cold fluid pressure drop ratio.

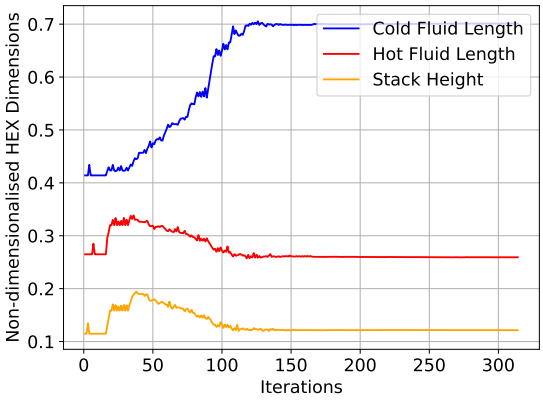


(f) Variation in the air heat exchanger non-dimensionalised lengths.

Figure 4.8: $GH_2$ SP architecture mass optimisation: Air heat exchanger convergence plots

Finally, the propagation of the turbine power recovered and the compressor power required during the optimisation are plotted in Figure 4.9a and Figure 4.9b. The turbine power recovered increases over the course of the optimisation due to the reduction in the pressure losses between the SOFC and the turbine, which are the losses of the air side heat exchanger hot fluid and the third air pipe. In particular, the turbine power recovered clearly varies inversely with the air side heat exchanger hot fluid pressure drop shown as in

Figure 4.8c. Similarly, the compressor power required is related to the pressure drops in the air side pipes and the cold fluid pressure drop in the air side heat exchanger, with the latter having a clear correlation as seen in Figure 4.8e.

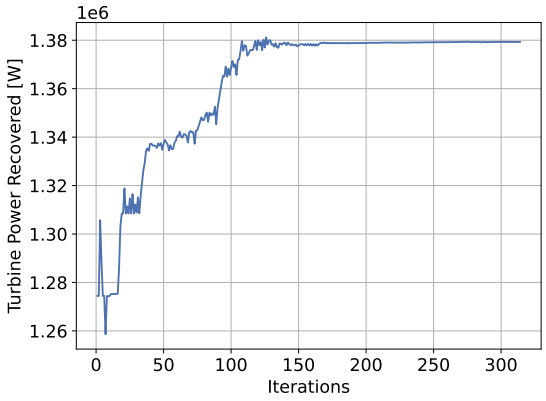


(a) Variation in the turbine power recovery.

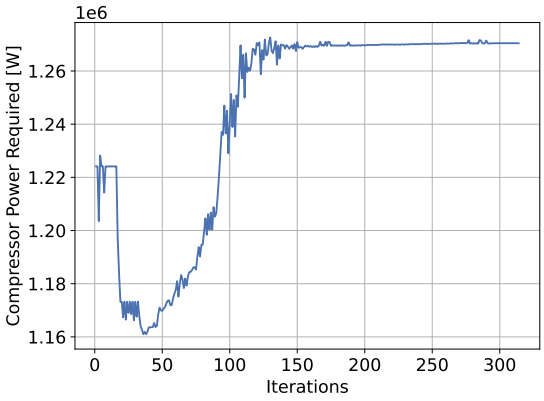


(b) Variation in the compressor required power.

Figure 4.9: $GH_2$ SP architecture mass optimisation: Turbine and compressor convergence plots

### MASS AND POWER OPTIMISATION

Next, the minimisation of the mass and power cost function for this architecture was performed, while keeping the same initialisation point. Figure 4.10a illustrates the convergence of the cost function and its individual terms (as described in Equation 3.3), while the convergence of the mass and net power recovery values can be seen in Figure 4.10b and Figure 4.10c respectively. The results for the system mass variation are comparable to the mass optimisation, albeit converging to a higher value, while the net power recovered increases throughout the entire optimisation. The system compositions are presented in Figure 4.11 and Figure 4.12. When compared to the system composition resulting from the previous optimisation in Figure 4.2 and Figure 4.3, the increase in system mass is mainly attributable to increase in the mass of the air side heat exchanger and pipes.

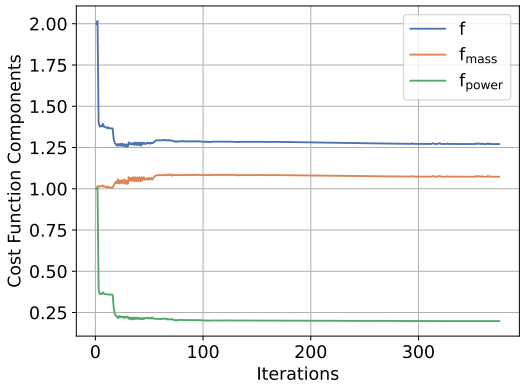


(a) Convergence of the cost function.

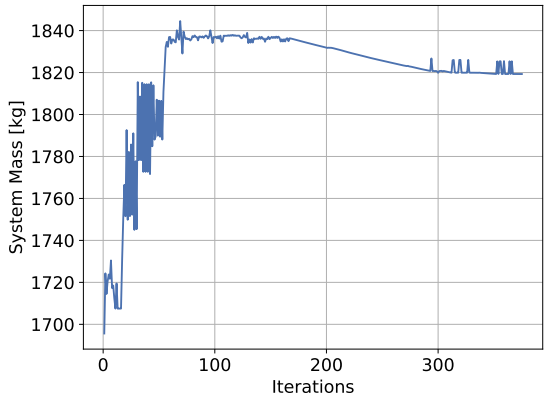


(b) Convergence of the system mass.

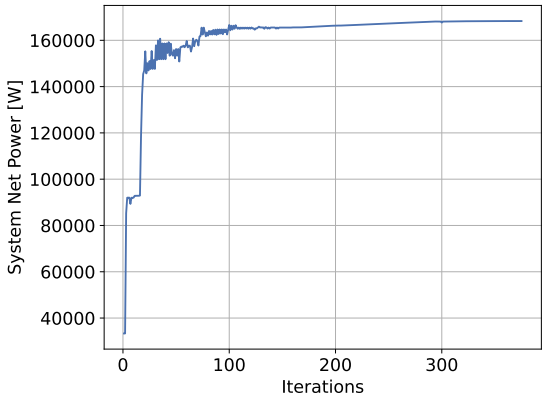


(c) Convergence of the system net power.

Figure 4.10: $GH_2$ SP architecture mass and power optimisation: Optimisation Convergence plots

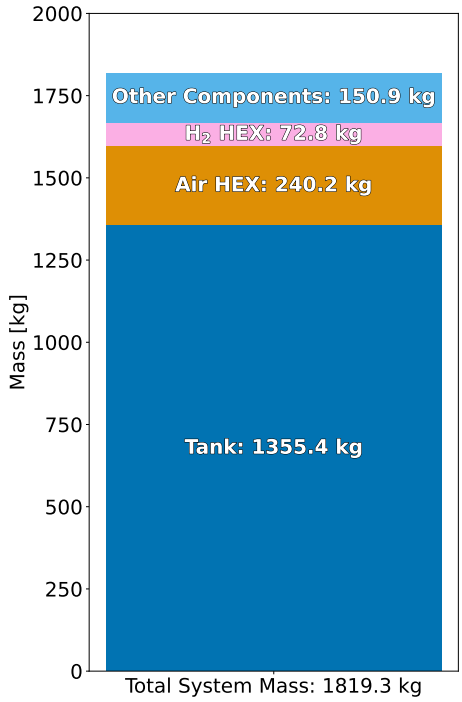


Figure 4.11: Mass and power optimisation: Mass composition of the complete $GH_2$ SP architecture.

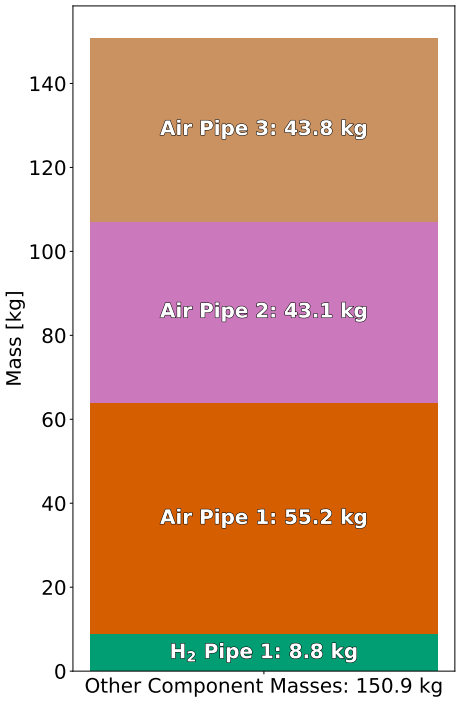


Figure 4.12: Mass and power optimisation: Mass composition of the remaining components of the $GH_2$ SP architecture.

The variation in the air side heat exchanger mass is displayed in Figure 4.13a, where it can be seen that it converges to a larger mass compared to the mass optimisation. This is due to the fact that the optimiser attempts to minimise the pressure drop over the heat exchanger, which leads to an increase in the net power recovered by reducing the pressure ratio required by the compressor and increasing the maximum expansion possible by the turbine. The pressure drop ratio of the cold and hot fluid over the heat exchanger are shown in Figure 4.13b and Figure 4.13c.

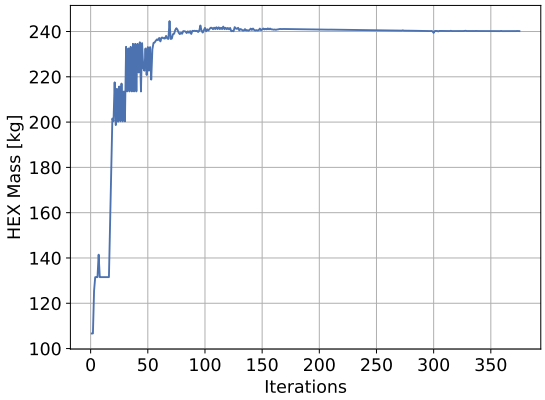


(a) Variation in the mass of the air side heat exchanger.

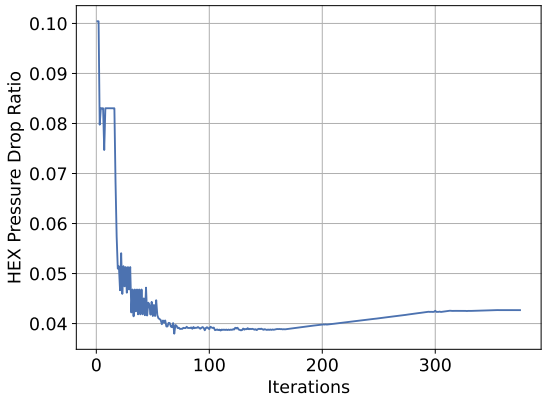


(b) Variation in the cold fluid pressure drop over the air side heat exchanger.

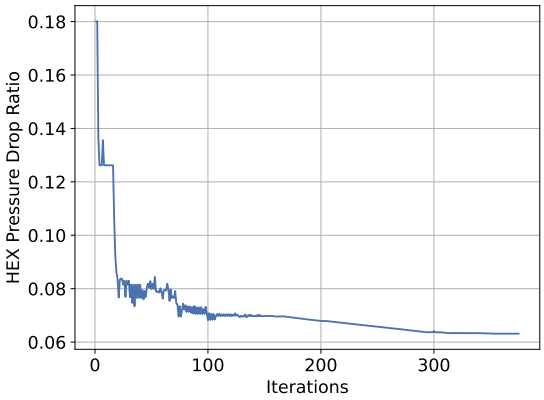


(c) Variation in the hot fluid pressure drop over the air side heat exchanger.

Figure 4.13: $GH_2$ SP architecture mass and power optimisation: Air heat exchanger convergence plots

Similarly, the converged mass and radius of the air side pipes is larger than for the ones resulted from the mass optimisation, since a larger radius leads to a reduction in the pressure drop, which again leads to a higher net power recovery. The plots of the mass and radius variations for the air side pipes are shown in Figure 4.14a and Figure 4.14b.

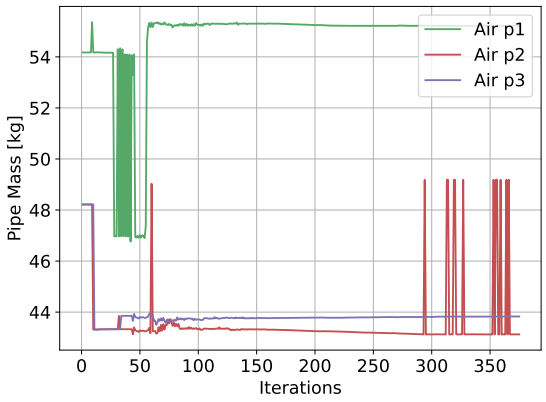


(a) Variation in the mass of the air side pipes.

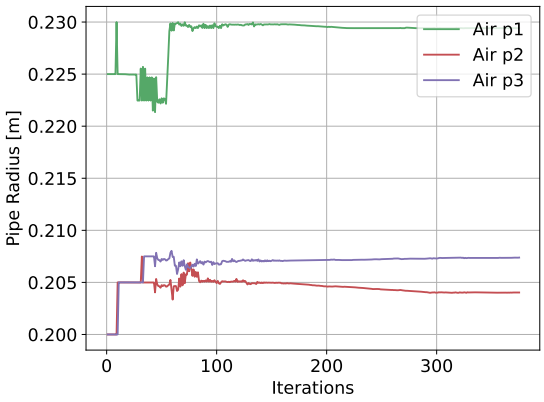


(b) Variation of the radius of the air side pipes.

Figure 4.14: $GH_2$ SP architecture mass and power optimisation: Air side pipes convergence plots

Subsequently, the power recovered by the turbine and the power required by the compressor vary as presented in Figure 4.15a and Figure 4.15b. The final part of the net power objective is the parasitic power of the system, which for this architecture only includes the power required by the tank, displayed in Figure 4.15c. The tank power does not reduce over the optimisation, as it depends on the boil off mass flow rate requirement which sizes the insulation.

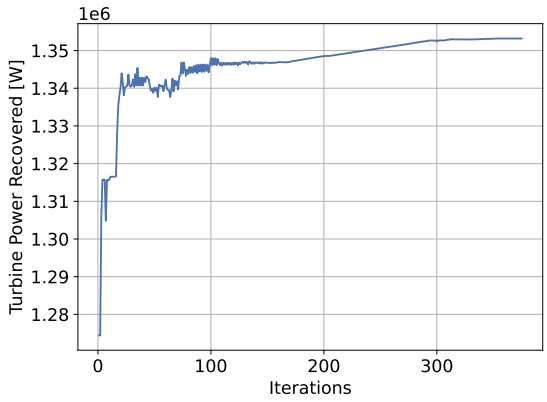


(a) Variation of the power recovered by the turbine.

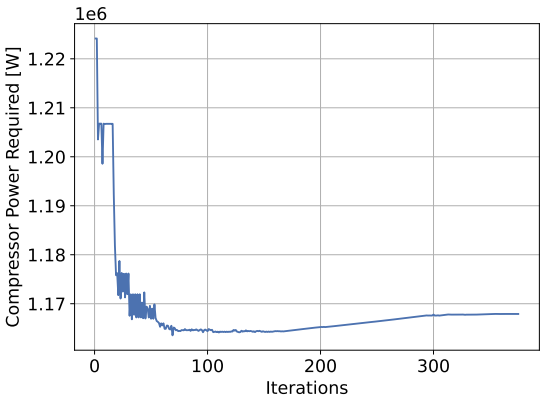


(b) Variation of the power required by the compressor.

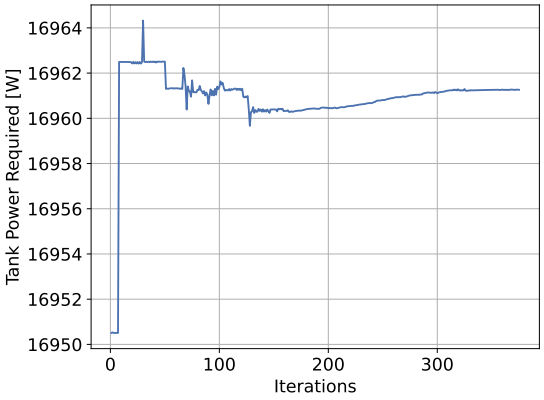


(c) Variation of the power required by the tank.

Figure 4.15: $GH_2$ SP architecture mass and power optimisation: Power convergence plots

### 4.1.2. LIQUID EXTRACTION WITH SELF-PRESSURISATION

#### MASS OPTIMISATION

The mass minimisation of the architecture utilising liquid extraction with self-pressurisation is detailed in this section. The convergence plots for the objective function in Figure 4.16a and the system mass in Figure 4.16b show that the optimisation exhibits similar behaviour as for the previous architecture. The final system mass compositions are seen in Figure 4.17 and Figure 4.18.

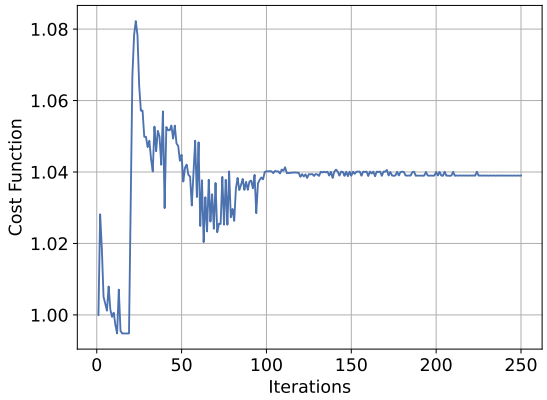


(a) Convergence of the cost function.

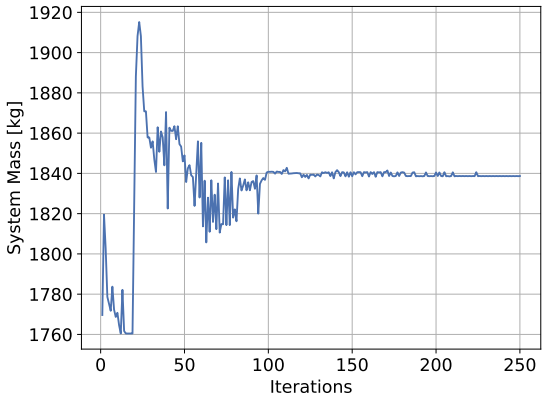


(b) Convergence of system mass.

Figure 4.16: $LH_2$ SP architecture mass optimisation: Optimisation convergence plots

The main difference between the liquid and gaseous extraction architecture masses is the addition of the vaporiser component to evaporate the liquid hydrogen. The implementation of the vaporiser allows for the reduction in the power required to maintain the pressure and desired mass flow rates through the delivery system. This results from a smaller mass of hydrogen being stored in the vaporiser, along with the lack of insulation for the vaporiser. Therefore, the total parasitic power of the system reduces, as shown in Table 4.1, at the expense of the an increase in mass in the system compositions.

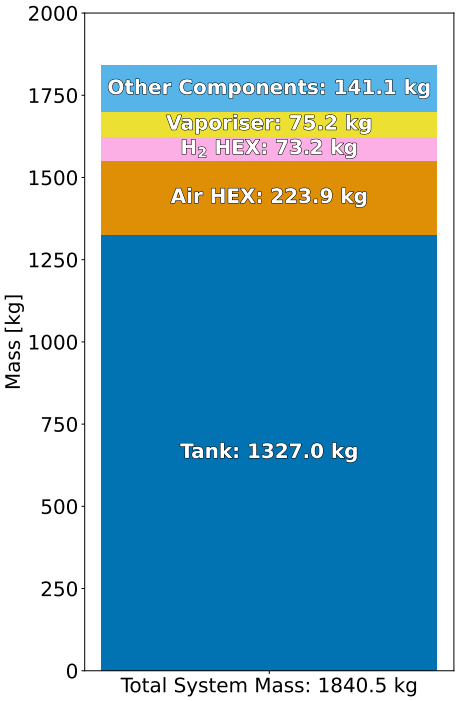


Figure 4.17: Mass optimisation: Mass composition of the complete $LH_2$ SP architecture.

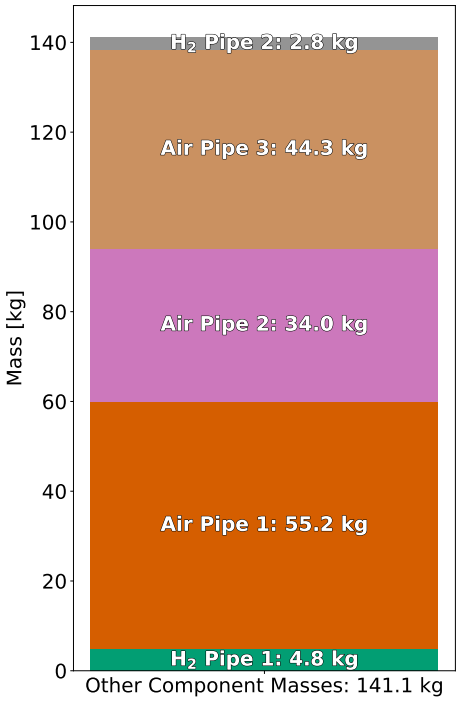


Figure 4.18: Mass optimisation: Mass composition of the remaining components of the $LH_2$ SP architecture.

The variation of the vaporiser mass with the optimisation iterations follows the same behaviour as the tank, since the method used to calculate the wall thicknesses is the same, and therefore an optimum radius can be found. The vaporiser convergence plots are portrayed in Figure 4.19

Table 4.1: Total parasitic power comparison between gaseous and liquid extraction architectures using self-pressurisation for the mass optimisation.

| | Gaseous Extraction SP | Liquid Extraction SP |
|---|---|---|
| **Tank Power [W]** | 16961.6 | 2402.6 |
| **Vaporiser Power [W]** | - | 6608.0 |
| **Total Parasitic Power [W]** | 16961.6 | 9010.5 |

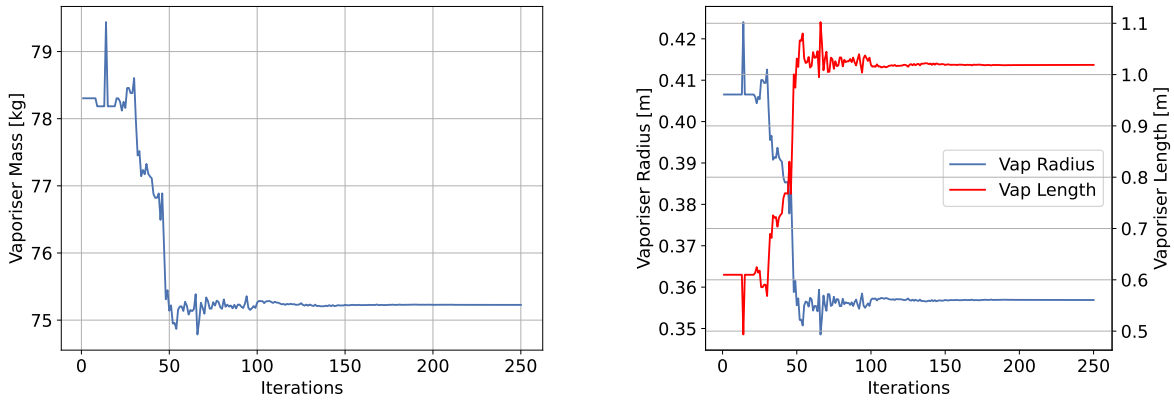


(a) Variation of the vaporiser mass.

(b) Variation of the vaporiser dimensions.

Figure 4.19: $LH_2$ SP architecture mass optimisation: Vaporiser convergence plots

Due to the addition of the vaporiser, the number of pipes on the hydrogen side increased, with the first pipe transporting liquid hydrogen from the tank to the vaporiser, and the second transporting gaseous hydrogen from the vaporiser to the heat exchanger. It is ensured that the sum of the pipe lengths in the liquid extraction architectures is the same as the length of the pipe in the gaseous extraction one. The mass and radius variation of these pipes in Figure 4.20 follows the same principle as for the previous supply architecture, with the optimiser attempting to find a compromise between the mass reduction and the pressure drops over the pipes. Although the liquid hydrogen pipe (pipe 1) has a smaller radius than the gaseous hydrogen pipe (pipe 2), the total pipe mass is larger for the former due to the large insulation thickness required to maintain the liquid phase.

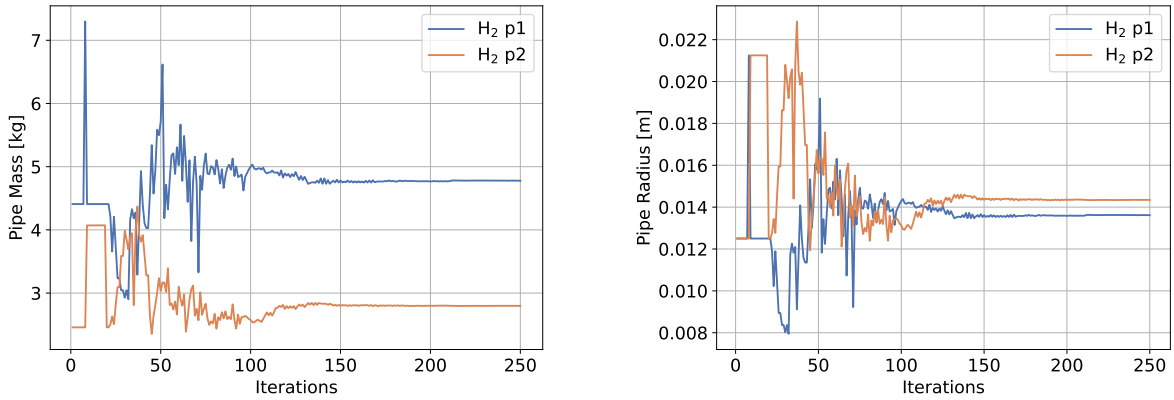


(a) Variation of the mass of the hydrogen pipes.

(b) Variation of the radius of the hydrogen pipes.

Figure 4.20: $LH_2$ SP architecture mass optimisation: Hydrogen pipe convergence plots

The remaining trends observed in the mass optimisation of this architecture are similar to those for the mass optimisation of the previous architecture.

### MASS AND POWER OPTIMISATION

When optimising for mass and power, the behaviour of the optimisation again trends towards finding a compromise between minimising the mass of the system and the pressure losses through the system. The convergence of the cost function (from Equation 3.3) and its individual terms is presented in Figure 4.21a. The variation of the total system mass and net power recovery are shown in Figure 4.21b and Figure 4.21c.

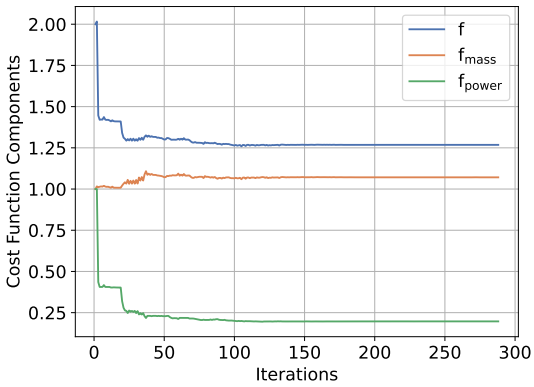


(a) Convergence of the cost function.

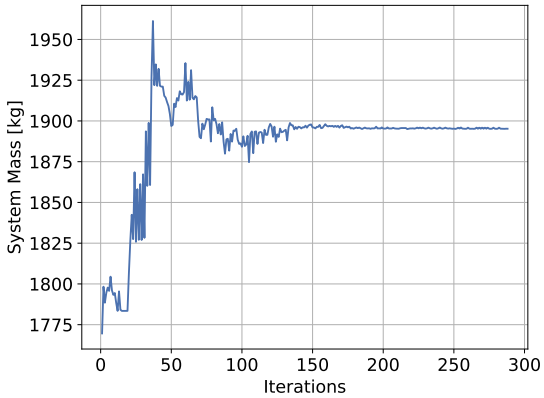


(b) Convergence of system mass.

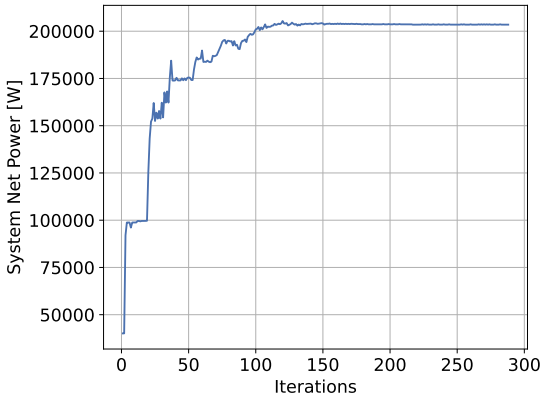


(c) Convergence of system net power recovery.

Figure 4.21: $LH_2$ SP architecture mass and power optimisation: Optimisation convergence plots

The main additional trend that is observed is related to the parasitic power required by the vaporiser. Since the vaporiser does not have insulation, the amount of heat entering the environment varies with the vaporiser dimensions, leading to a different parasitic heating required to vaporise the hydrogen and maintain its operational pressure. The change in the vaporiser dimensions and the resulting heating power required are plotted in Figure 4.22a and Figure 4.22b respectively.

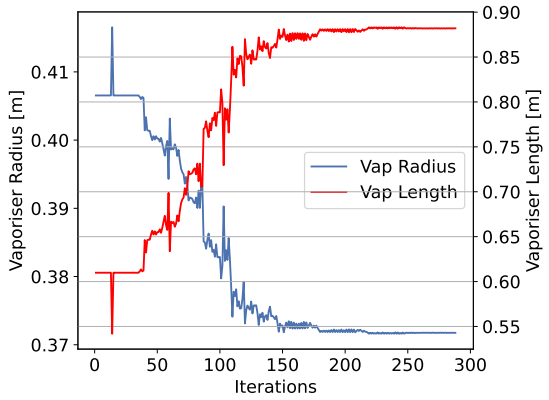


(a) Variation in the vaporiser dimensions.

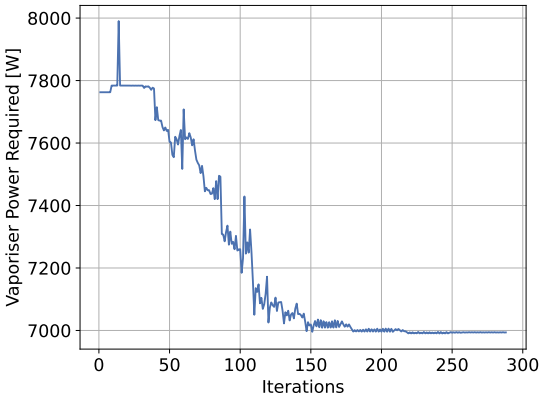


(b) Variation in the power required by the vaporiser.

Figure 4.22: $LH_2$ SP architecture mass and power optimisation: Vaporiser convergence plots

Figure 4.23 and Figure 4.24 contain the final mass compositions resulting from the mass and power optimisation. As for the previous architecture, the converged system mass is larger than the one resulting from the mass optimisation.

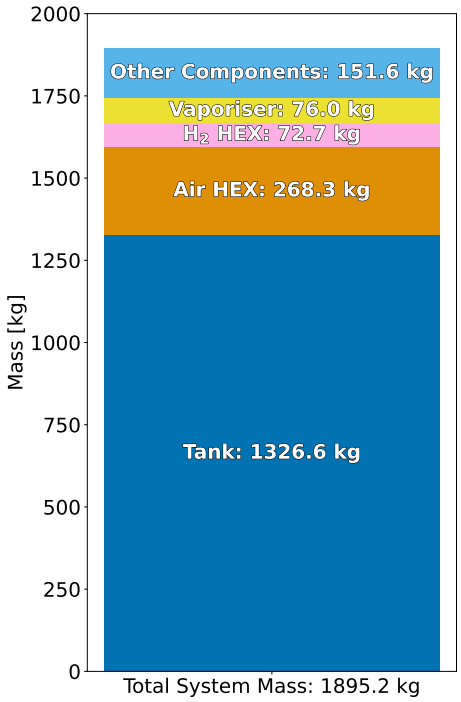


Figure 4.23: Mass and power optimisation: Mass composition of the complete $LH_2$ SP architecture.

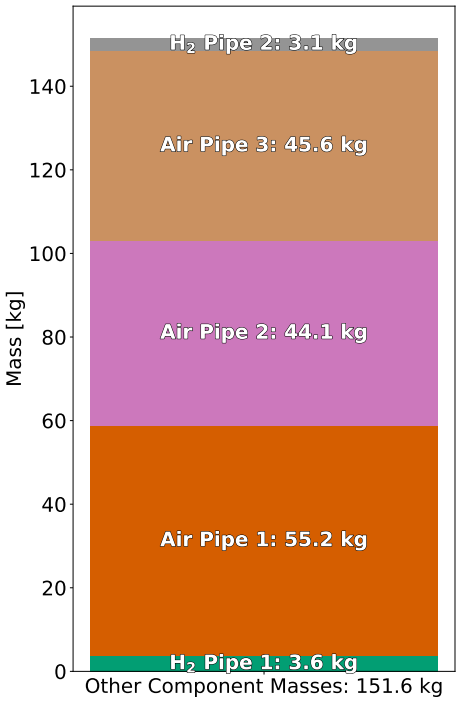


Figure 4.24: Mass and power optimisation: Mass composition of the remaining components of the $LH_2$ SP architecture.

### 4.1.3. LIQUID EXTRACTION WITH PUMPS

#### MASS OPTIMISATION

The final architecture analysed utilises liquid hydrogen extraction with a piston pump. The main benefit of this system is that it allows for lowering in the storage tank pressure compared to the self-pressurisation architectures, in this case to 3 *bar*. This leads to a large reduction in the mass of the tank as well as the power required to maintain the pressure in it. The parasitic power of the pump architecture can be seen compared to the previous architectures in Table 4.2.

Table 4.2: Total parasitic power comparison between all architectures after optimising for mass.

| | Gaseous Extraction SP | Liquid Extraction SP | Liquid Extraction Pump |
|---|---|---|---|
| **Tank Power [W]** | 16961.6 | 2402.6 | 307.8 |
| **Vaporiser Power [W]** | - | 6608.0 | 7458.7 |
| **Pump Power [W]** | - | - | 225.5 |
| **Total Parasitic Power [W]** | 16961.6 | 9010.6 | 7992.0 |

Similar to the other architectures, the size of all components is minimised leading to an increase in the system pressure drops, and resulting in a larger pump pressure rise required, as seen in Figure 4.25a. Subsequently, its mass increased throughout the optimisation as can be seen in Figure 4.25b and Figure 4.25c. Additionally, the variation of the pump optimisation parameters are presented in Figure 4.25d and Figure 4.25e. The plots show that the pressure rise through the pump has the largest effect on its power and mass, which means that it is affected by the design of the remaining system and the resulting system pressure losses.

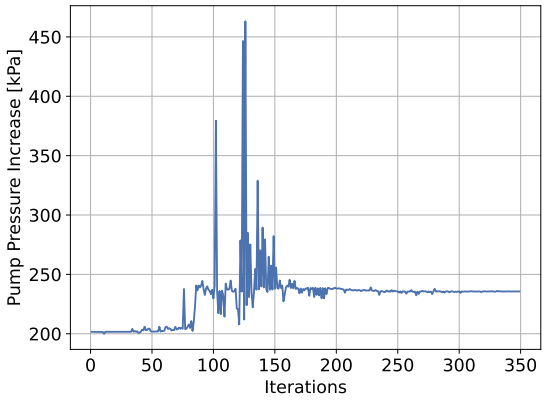


(a) Variation in the pressure increase required by the pump.

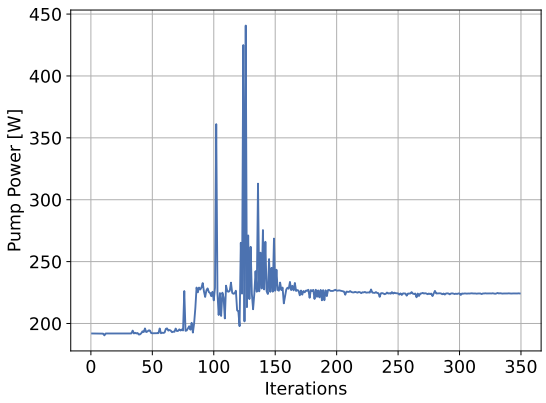


(b) Pump power variation.

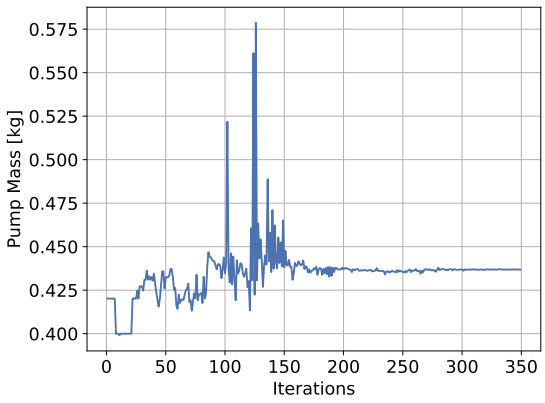


(c) Pump mass variation

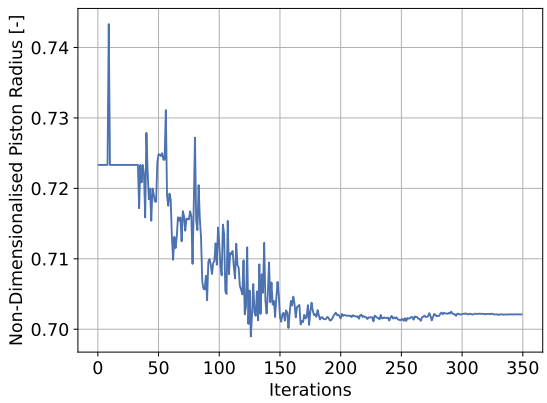


(d) Non-dimensionalised pump radius variation.

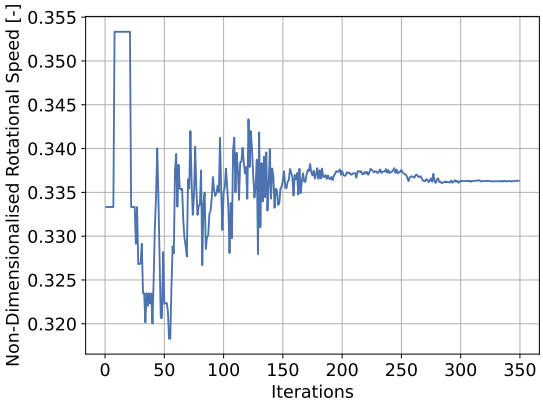


(e) Non-dimensionalised pump rotational speed variation.

Figure 4.25: $LH_2$ Pump architecture mass optimisation: Pump convergence plots

The final mass compositions of this system are shown in Figure 4.26 and Figure 4.27. When compared to the previous architectures, it is visible that the optimised mass of the tank is around 200 *kg* lighter, which is also the main reason for the large reduction in system mass.

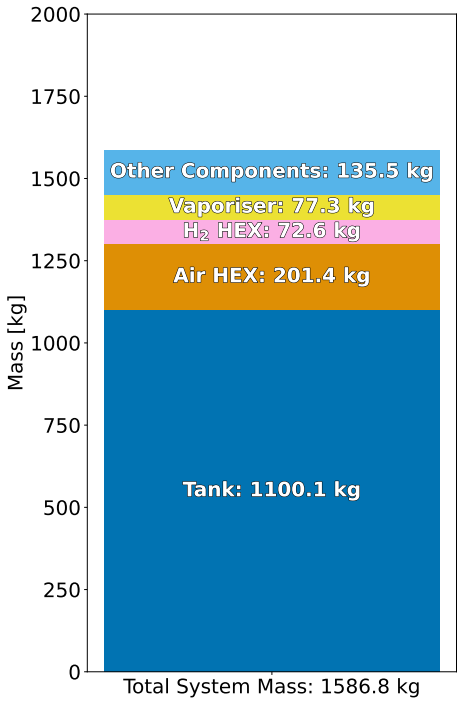


Figure 4.26: Mass optimisation: Mass composition of the complete $LH_2$ Pump architecture.

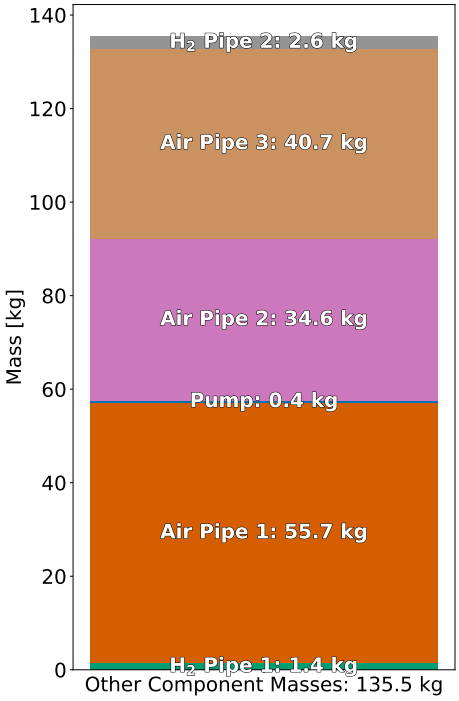


Figure 4.27: Mass optimisation: Mass composition of the remaining components of the $LH_2$ Pump architecture.

### MASS AND POWER OPTIMISATION

The optimisation convergence plots when for mass and power via the cost function in Equation 3.3 are presented in Figure 4.28. The converged pressure drop in the system is reduced when compared to the mass optimisation, leading to a decrease in the pressure rise and power required by the pump shown in Figure 4.29a and Figure 4.29b. The trends of the optimisation parameters are similar to the mass optimisation, where the radius of the pistons is reduced, while this time the rotational speed increases. The latter has a clear inverse effect on the pump mass. This is due to the fact that a higher pump rotational speed means that for the same mass flow rate, a smaller cylinder volume is required, leading to a shorter piston and cylinder for the same radius. This is also true for the mass optimisation, however, it is not as visible in the plots due as the pump remains near the initialisation value. The final composition of the architecture after performing the mass and power optimisation can be seen in Figure 4.30 and Figure 4.31.

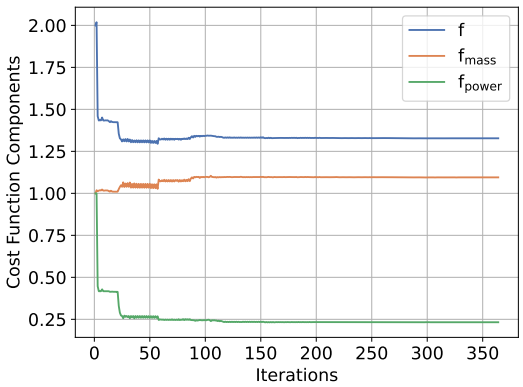


(a) Convergence of the cost function.

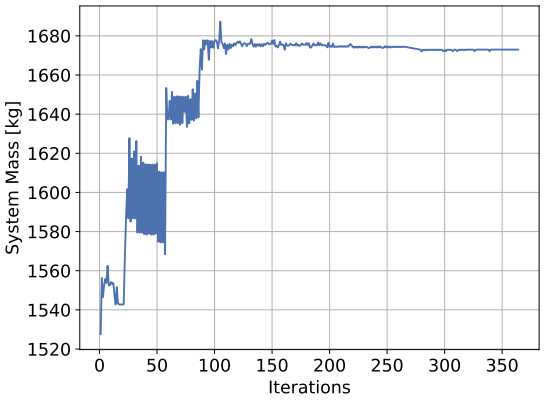


(b) Convergence of system mass.

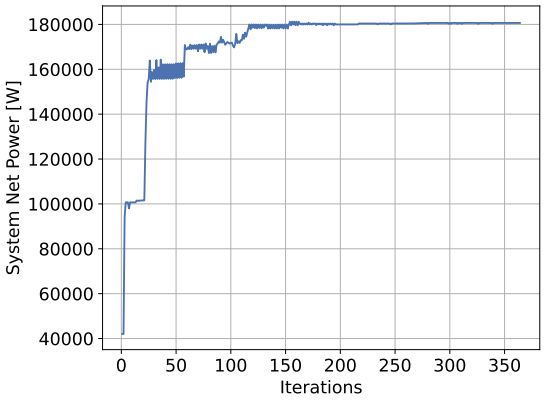


(c) Convergence of system net power recovery.

Figure 4.28: $LH_2$ Pump architecture mass and power optimisation: Optimisation convergence plots

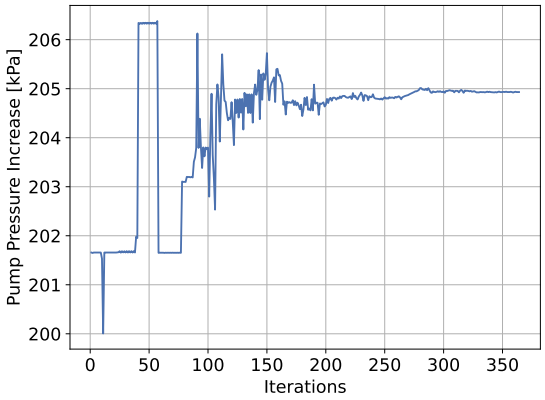


(a) Variation in the pressure increase required by the pump throughout the optimisations.

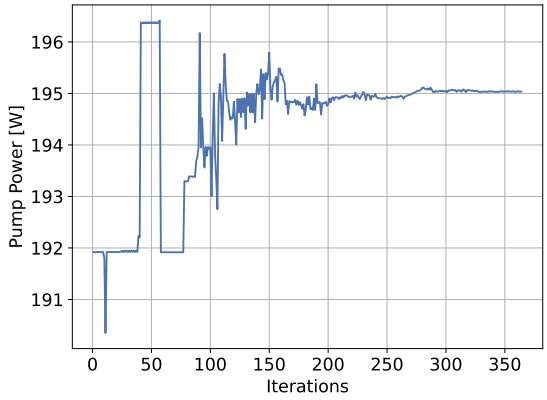


(b) Pump power variation.

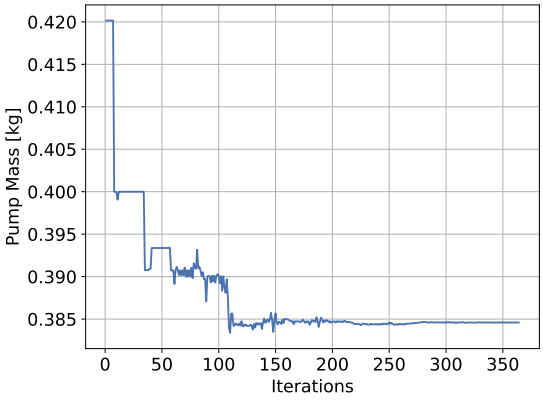


(c) Pump mass variation

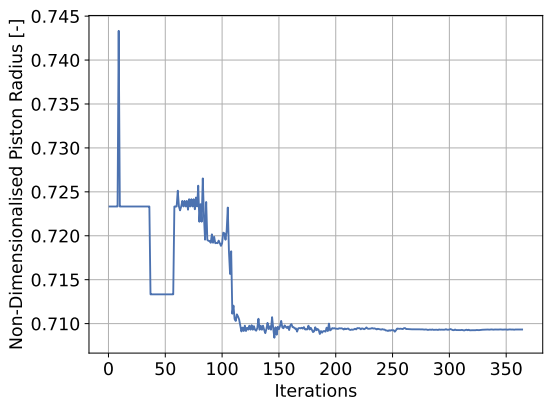


(d) Non-dimensionalised pump radius variation.

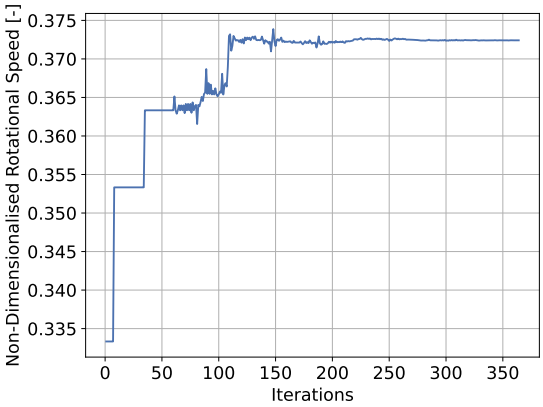


(e) Non-dimensionalised pump rotational speed variation.

Figure 4.29: $LH_2$ SP architecture mass and power optimisation: Pump convergence plots

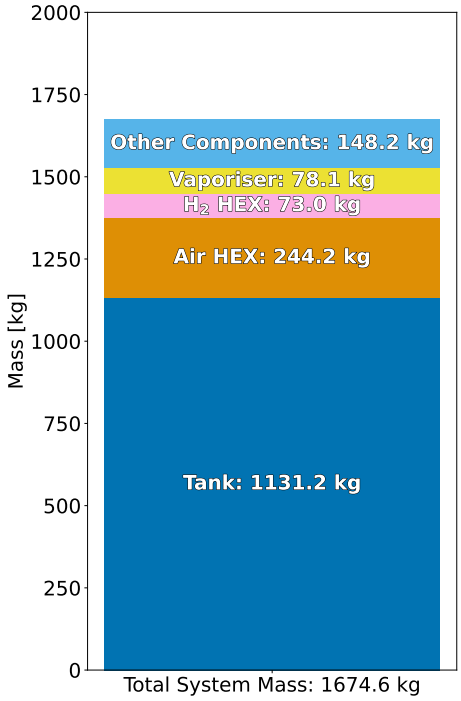


Figure 4.30: Mass and power optimisation: Mass composition of the complete $LH_2$ Pump architecture.

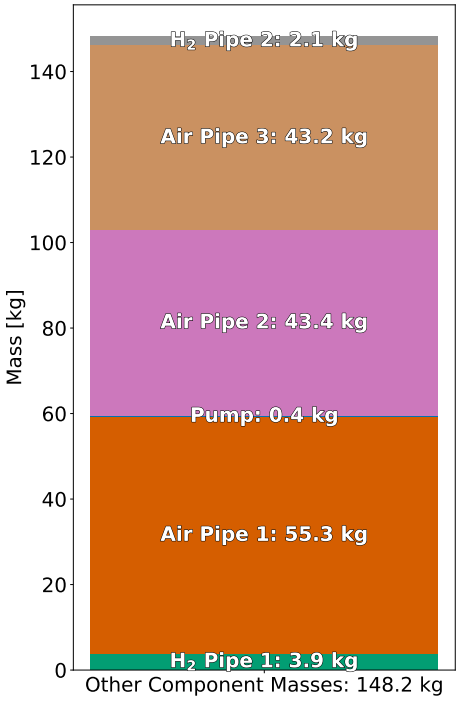


Figure 4.31: Mass and power optimisation: Mass composition of the remaining components of the $LH_2$ Pump architecture.

## 4.2. COMPARISON OF ARCHITECTURES

Two main aspects are examined when comparing the different architectures in this work. These are the mass of the system and the net power recovered by the system defined in Equation 3.2. In order to more easily compare the latter between architectures, a power recovery effectiveness $\zeta$ is defined in Equation 4.1 as the ratio of the net power recovered by the system $P_{net}$ and the Solid Oxide Fuel Cell power lost $P_{loss}$ to the fluid. The latter is estimated given the increase in fluid temperatures over the SOFC $\Delta T_{SOFC}$ and the inlet fluid conditions (mass flow rate $\dot{m}$ and specific heat capacity $c_p$) using Equation 4.2. This power is a function of the SOFC design parameters, which do not change between the optimisations.

$$\zeta = \frac{P_{net}}{P_{loss}} \tag{4.1}$$

$$P_{loss} = \dot{m}_{an,in} c_{p,H2} \Delta T_{SOFC} + \dot{m}_{cat,in} c_{p,air} \Delta T_{SOFC} \tag{4.2}$$

A collective representation of the system masses for each architecture and optimisation objective is presented in Figure 4.32, with the initialisation point included as a reference. The system mass values for each architecture are all larger than at the starting point due to the behaviour of the results described for the individual optimisations in Section 4.1. Additionally, the system mass is larger when optimising for mass and power than when only optimising for mass. The final optimisation results show that with regards to system mass, the best solution is found for the pump-fed architecture, followed by the self-pressurisation architectures, with the heaviest being the liquid hydrogen extraction.

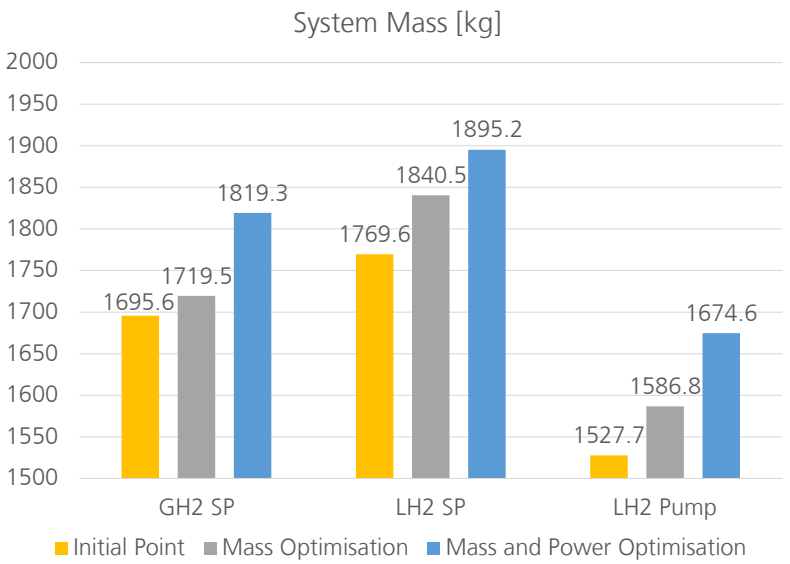


Figure 4.32: Comparison of architecture system masses.

Figure 4.33 illustrates the power recovery effectiveness of each architecture, including the initialisation point. The values are extremely low at the initialisation point due to the large pressure losses in the undersized heat exchangers. Additionally, since the turbine and compressor power values are identical between all optimisations at the initialisation point, the difference between the effectiveness values is simply due to the addition of the unoptimised additional components (i.e. vaporiser and pump). When optimising for mass, the effectiveness increases due to the reduction in pressure losses in the heat exchangers. Optimising for mass and power leads to additional reductions in pressure losses, leading to even greater values for the effectiveness. The solutions found by the optimiser show that the best architecture with respect to the power recovery is the one utilising liquid hydrogen extraction with self-pressurisation, followed by the pump-fed architecture.

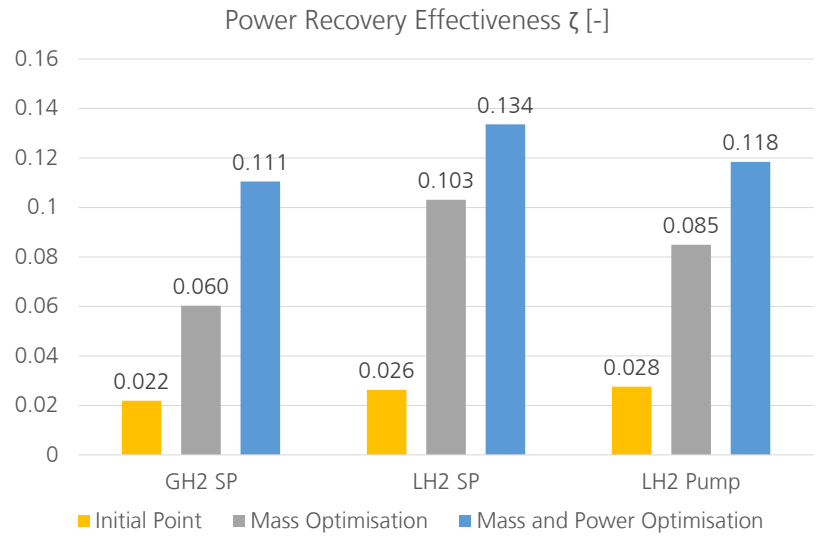


Figure 4.33: Comparison of architecture power recovery effectiveness.

Table 4.3: Power values for the mass and power optimisation of all architectures.

| **Components** | **$GH_2$ SP** | **$LH_2$ SP** | **$LH_2$ Pump** |
|---|---|---|---|
| Turbine Power Recovered [kW] | 1353.2 | 1378.5 | 1354.0 |
| Compressor Power Required [kW] | 1167.9 | 1165.6 | 1165.5 |
| Tank Power [kW] | 17.0 | 2.4 | 0.3 |
| Vaporiser Power [kW] | - | 7.0 | 7.6 |
| Pump Power [kW] | - | - | 0.2 |
| **Parasitic Power [kW]** | 17.0 | 9.4 | 8.1 |
| **Net Power Recovered [kW]** | 168.3 | 203.5 | 180.4 |

The outcome of this work led to the pump-fed liquid hydrogen extraction architecture being chosen as the most appropriate for the given mission requirements and desired objective functions. The main benefit is the much lower mass of the architecture on the propulsion system level. Additionally, the iterative "snowball effect" on the aircraft level needs to be considered, as larger propulsion system masses lead to more lift and power that needs to be provided by the aircraft, increasing the mass of the aircraft components as well as the fuel mass required, which again increases the mass of the supply architecture. Therefore, maintaining a low mass on the propulsion system level is of great importance when considering the overall aircraft design. Table 4.2 shows that the parasitic power of the pump-fed architecture is the lowest, which also leads to lower additional fuel mass required. A study on the effect the parasitic power throughout the mission is performed in Section 4.3.

There are two main takeaways that can be derived from these results regarding the optimisation itself. The first is that the initialisation point for the optimisation has a large effect on the final outcome of optimisation, in particular due to the fact that the optimiser utilises local simplex algorithm. This is especially true when considering the mass and power optimisations, as the initial guess for the heat exchanger sizing led to large reductions in the cost function early in the optimisations. A significant reason for this is that the initialisation was determined using results of individual component sizings that were performed at earlier stages in the $H_2$EAT project for different mission requirements, with the main one being a larger SOFC inlet pressure of 8 bar. This meant that the components were allowed to be smaller, as the fluids were more dense. However, for the lower inlet pressure used at this phase of the project, the pressure losses would then be higher. This correlation has also been shown experimentally by Luyben et al. [42] for the gas flow through a pipeline. Therefore the overall behaviour of the optimisations needs to be investigated for different initialisations and also for a different system pressure to ensure that the trends in the optimisations follow the same physical reasoning. Additional optimisation analyses implementing a change in the initialisation point and system pressure are presented in Section 4.7.

The second takeaway is that the optimisation algorithm also has an impact on the results. From the individual results shown in Table 4.2, it can be seen that the pump-fed architecture requires the lowest amount of parasitic power. However, Figure 4.33 shows that the optimiser finds better net power recovery values for the architecture utilising liquid hydrogen extraction with self-pressurisation. This is due to the fact that the net power recovery takes into account the turbine and compressor power values, which have a larger order of magnitude when compared to the parasitic power values. When comparing the two liquid extraction architectures optimised for mass and power, whose main power values can be seen in Table 4.3, the magnitude of the difference in turbine power recovered between architectures is over 19 times the magnitude of the parasitic power difference. The values at the beginning of the optimisation for the turbine and compressor powers is exactly the same for both. This is due to the optimiser converging differently for both architectures in that regard, most likely due to the addition of optimisation parameters for the pump-fed architecture, although both optimisations had the same convergence criteria for the cost function.

## 4.3. PRELIMINARY MISSION ANALYSIS

In this section, a preliminary mission analysis was performed for the gaseous extraction architecture with self-pressurisation to examine the effect of the tank operation on the system itself. This architecture was chosen due to its simplicity with regards to control and simulation when compared to the others. In particular, the implementation of the vaporiser in the liquid extraction architectures creates complexity in the opera-

tion of the system, as it introduces a multi-dimensional problem that must take into account the fill level and pressure in the vaporiser as well as in the tank to minimise the parasitic power of the system.

On the other hand, the simulation of the gaseous extraction architecture is much simpler. Given the results from the system sizing and the SOFC mass flow requirements over the course of the mission, the pressure losses in the system can be computed for each mission phase and in turn the tank pressure. Subsequently, the method described in Section 2.2.2 can be used to compute the power required to maintain the tank pressure for each phase.

The mission consists of a take-off, cruise, and descent phase, and also takes into account an emergency diversion climb and descent phase. It also details a short time duration for changing the pressure in the tank between phases while keeping the mass flow rate constant at the value of the preceding phase. The altitude variation throughout the mission and the average extraction and vaporisation mass flow rates ($\dot{m}_g$ and $\dot{m}_{lg}$) calculated for each phase of the mission are given and presented in Figure 4.34 and Figure 4.35 respectively. The tank pressure required at the different mission phases is displayed in Figure 4.36, where the shape of the pressure graph is similar to that of the gaseous extraction mass flow rate. Additionally, the resulting variation in the masses of the individual hydrogen phases, liquid $m_{LH_2}$ and gaseous $m_{GH_2}$, and total hydrogen mass $m_{H_2}$ can also be computed as in Figure 4.37

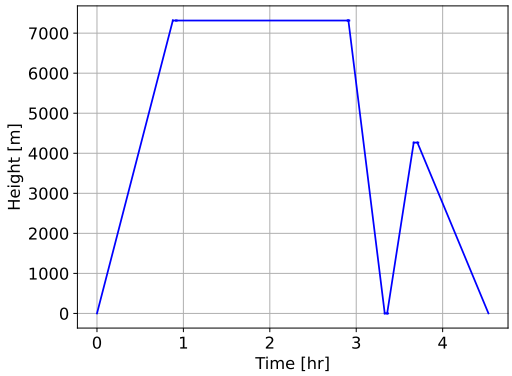


Figure 4.34: Altitude variation throughout the mission.

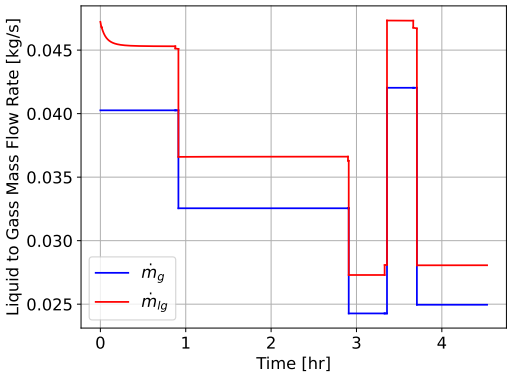


Figure 4.35: Average extraction and vaporisation mass flow rates for each mission phase.

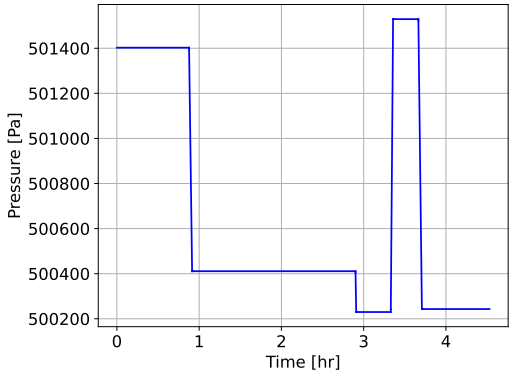


Figure 4.36: Tank pressure variation throughout the mission.

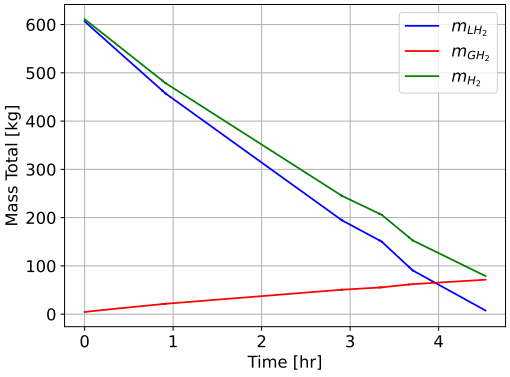


Figure 4.37: Variations in the mass of the individual hydrogen phases and the total hydrogen throughout the mission.

After extracting the aforementioned results, the parasitic heating power $Q_H$ can be calculated. It plays a significant role on the system sizing as it imposes an additional energy requirement. This power is plotted for each mission phase alongside the environmental heat transfer rate $Q_{env}$ in Figure 4.38. The latter is almost constant but varies slightly with the altitude. The parasitic power of the tank follows exactly the shape of the

vaporisation mass flow rate $\dot{m}_{lg}$ in Figure 4.35. The tank pressure is a function of the mass of hydrogen in the tank and the average density of the tank. Reducing the mass of hydrogen in the tank reduces the pressure, while reducing the average density increases it. As the liquid volume in the tank is reducing throughout the mission, the gaseous volume increases to fill the remaining space, which can only maintain the desired pressure if the vaporisation mass flow rate slightly exceeds the gaseous extraction rate. This leads to the difference in mass flow rates seen in the figure. The initial curve in both the vaporisation flow rate and heating plots is due to the low initial gaseous hydrogen volume (7.2% of the tank volume). The small steps in both plots between the main phases is due to the different power demand when the pressure in the tank is varied (lower when the pressure is reduced and vice versa).

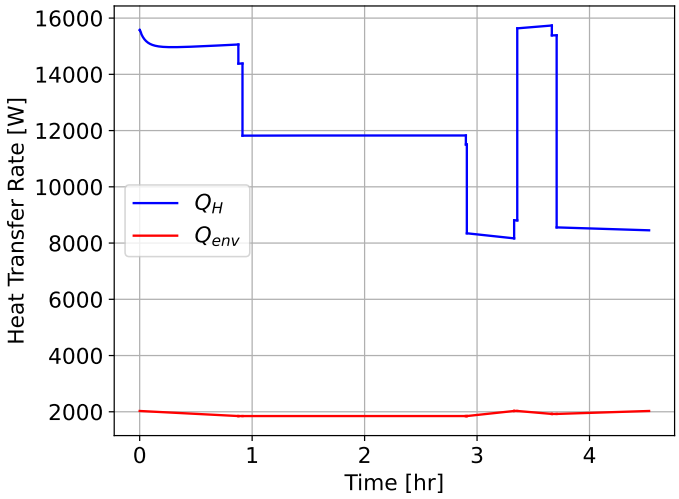


Figure 4.38: Heat transfer rate from heater and environment to tank throughout the mission.

By calculating the area under the heat transfer rate plot, the total parasitic energy required to operate the tank and maintain its pressure through the mission can be computed. For this preliminary analysis of the gaseous extraction architecture, the total parasitic energy needed is equal to 192.6 $MJ$ or 53.5 $kWh$, which could be stored in an additional battery on the aircraft. Lithium-ion batteries have gravimetric energy densities ranging from $150-250$ $Wh/kg$ and volumetric energy densities between $220-350$ $kWh/m^3$ [43]. Taking average values of 200 $Wh/kg$ and 285 $kWh/m^3$ for the gravimetric and volumetric energy densities respectively, this leads to a battery with a mass of 267.5 $kg$ and a volume of 0.19 $m^3$. When comparing this to the system mass composition of the gaseous extraction architecture shown in Figure 4.11 and Figure 4.12, this would make the battery the heaviest component excluding the tank. The total system mass would increase by 14.7% from 1819.3 $kg$ to 2086.6 $kg$. Considering that the net power recovered for the architecture is around 10 times that required by the tank as shown in Table 4.3, the power could actually be compensated by the turbine. This means that the battery mass could be reduced in reality, however it would still be required as an intermediate energy storage.

The parasitic power could also be provided by the SOFC, where it is sized to provide more power, leading to a slightly larger mass flow rate required, and therefore more hydrogen stored in the tank. However, in order to properly analyse this method, the sizing of the system needs to performed iteratively with the sizing of the SOFC in order to converge to an exact value for the total mass flow rate.

At this stage of the project, the SOFC-based system is sized to fulfil the propulsive power requirements for the concept aircraft. However, in reality, there is an additional power requirement for the auxiliary systems in the aircraft such as power for the onboard systems and actuation. Additionally, as aircraft transition towards increasing electrification, this auxiliary power requirement can become quite sizeable. For example, the Airbus A380 and Boeing 787 require around 900 $kW$ and 1.5 $MW$ of power for on-board electrical systems respectively [44]. Fioriti et al. [45] estimate a power requirement of 101 $kW$ for the essential systems of a hybrid/all-electric regional aircraft concept. This includes the ice protection, air conditioning, flight control, and landing gear systems [45]. This power is typically provided by auxiliary power units in traditional aircraft,

but can be implemented in the coupled design for fuel cell based propulsion systems in order to minimise the additional fuel or battery mass required.

## 4.4. SENSITIVITY ANALYSIS ON OPTIMISATION PARAMETERS

The derivation of the most impactful optimisation parameters with regards to designing a system to achieve a desired objective is an important outcome from the optimisation, as it can provide insight to the user on which components require more attention in the individual design phases and need to be simulated with higher fidelity models. For example, in the preliminary design phase, this can have an impact on the trade-off between different component concepts, as the implementation of more complex types of components could become viable if the effect on the system becomes large enough. A simple way to obtain this derivation is by performing a sensitivity study on the final values of the optimisation parameters, and in particular, by calculating the slope of the optimisation objective function with respect to a small variation in each parameter with a forward-difference approximation [46]. This method is easily implementable using the RCE COBYLA optimiser, as the first set of iterations are used to calculate this derivative for each parameter.

The main concern with this method, is that a suitable step size for the variation has to be selected. The convergence of the optimisations described in the report results in a local minimum. Reducing the step size reduces the truncation error of the forward-difference approximation, while too small step sizes could lead to the slope calculation being dominated by numerical instabilities [46]. Therefore the computations are performed for a set of step sizes to determine a range where the change in slope is minimal for the non-dimensionalised optimisation parameters.

This sensitivity analysis was performed on the converged optimisation results of the pump-fed liquid hydrogen extraction architecture for both objectives, with the slopes for the mass objective with respect to the variation in the parameters presented in Figure 4.39, and those for the mass and power objective in Figure 4.40.

For the sensitivity derivatives of the mass objective, the values with respect to almost all parameters are constant for all the step sizes. The main exception is the variation in the objective slope with respect to the inner radius of air pipe 2, where the value exponentially increases as the step size decreases, until a step size of 0.005, after which it reduces significantly. The latter can also be seen for the values related to the both heat exchanger stack heights. The magnitude of the derivatives and order with respect to each optimisation parameter are determined to vary minimally for step sizes ranging between 0.0125 and 0.025, and therefore a step size of 0.01625 was taken for determining which optimisation parameters have the largest impact on the objective function. At this step size, the absolute value of the sensitivity derivative was used to determine the "impact" of each parameter. Those values are presented in Table 4.4, where as expected from the optimisation plots, the most impactful parameters are those related to the geometry of the air and hydrogen heat exchangers. The sensitivity derivative magnitude for the tank and vaporiser are quite low for although they take up a large portion of the system mass composition, which could be due to the fact that they are sized based on a hydrogen mass requirement. The least impactful parameters are those related to the insulation, as they have a small effect on the mass of the system. From the pump parameters, the rotational speed has a larger effect due to its effect on the pump cylinder volume, while the piston radius has a negligible impact on the system mass.

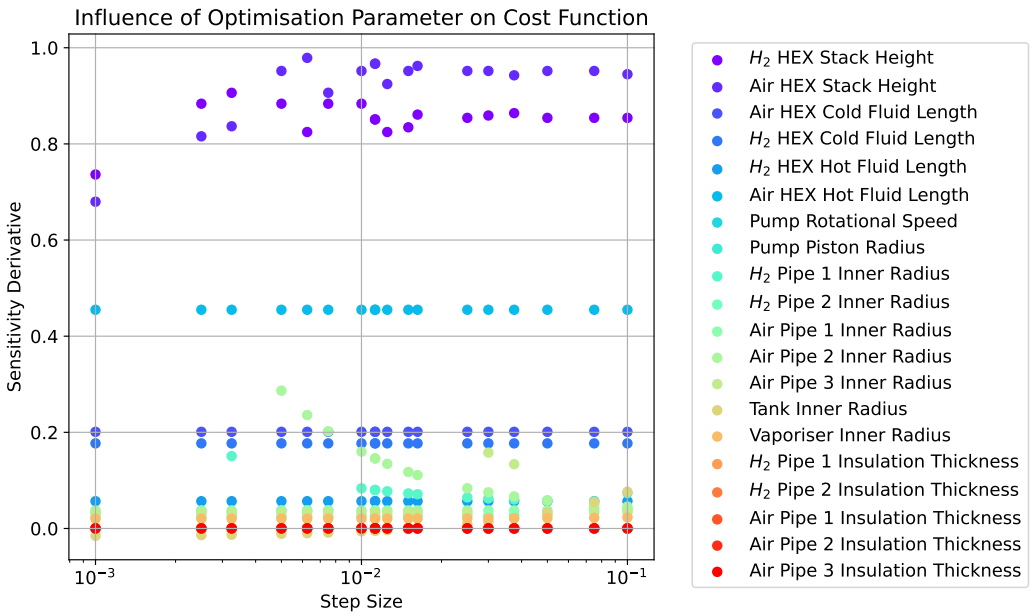


Figure 4.39: Results of forward-difference slope approximation for the mass optimisation.

Table 4.4: Value of the sensitivity derivative in order of most impactful parameters for the mass optimisation.

| **Optimisation Parameter** | **Value of Sensitivity Derivative** |
|---|---|
| Air HEX Stack Height | 0.9622 |
| $H_2$ HEX Stack Height | 0.8609 |
| Air HEX Hot Fluid Length | 0.4550 |
| Air HEX Cold Fluid Length | 0.2010 |
| $H_2$ HEX Cold Fluid Length | 0.1771 |
| Air Pipe 2 Inner Radius | 0.1110 |
| $H_2$ Pipe 1 Inner Radius | 0.0714 |
| $H_2$ HEX Hot Fluid Length | 0.0567 |
| Air Pipe 1 Inner Radius | 0.0375 |
| Air Pipe 3 Inner Radius | 0.0329 |
| $H_2$ Pipe 2 Inner Radius | 0.0261 |
| Vaporiser Inner Radius | 0.0206 |
| Pump Rotational Speed | -6.4E-4 |
| Tank Inner Radius | 4.7E-4 |
| Air Pipe 1 Insulation Thickness | 3.0E-4 |
| Air Pipe 3 Insulation Thickness | 2.5E-4 |
| Air Pipe 2 Insulation Thickness | 2.3E-4 |
| $H_2$ Pipe 2 Insulation Thickness | 2.0E-5 |
| $H_2$ Pipe 1 Insulation Thickness | 1.8E-5 |
| Pump Piston Radius | 1.3E-14 |

Figure 4.40 shows the results of the forward-difference sensitivity derivative calculation for the mass and power optimisation. The values are extremely consistent for all step sizes, except for the stack heights of both heat exchangers at the extremes. A step size of 0.0075 was taken for determining the sensitivity derivatives, leading to the values found in Table 4.5. Again, the heat exchanger stack heights have the largest impact, however, parameters that influence on the pressure losses and parasitic power were found to have a larger value for the derivative when compared to the mass optimisation. For example, the inner radius of air pipe 3 has a larger impact, as it directly affects the power recovered by the turbine. A large increase was found in the derivative magnitude with respect to the tank inner radius, when compared to the mass optimisation, stem-

ming from the fact that the objective function converged locally at a larger tank mass. This outcome shows that the parameters can also have a smaller impact on the objective function value the closer they are to their individual optimum.

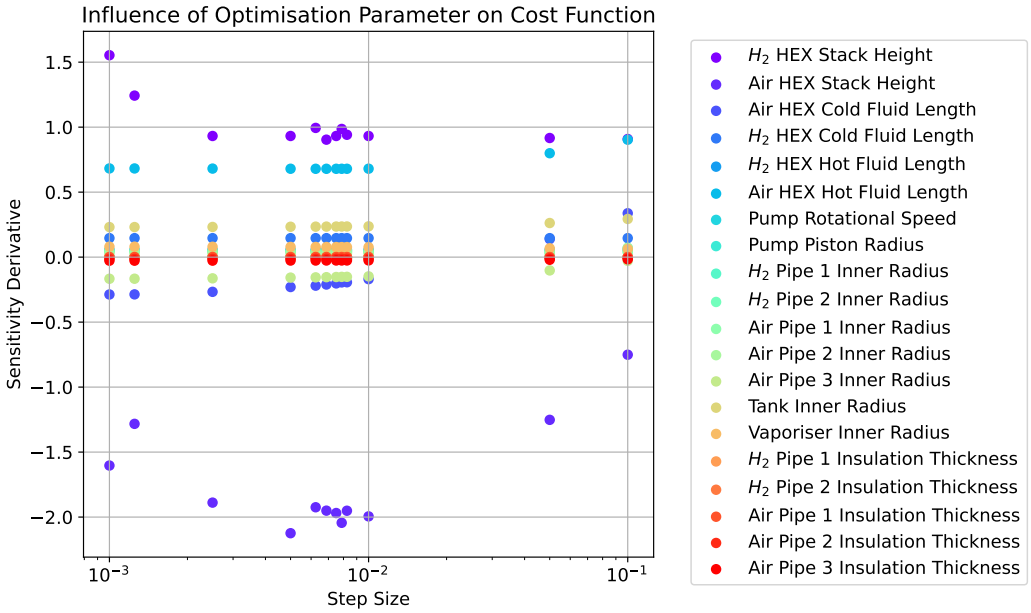


Figure 4.40: Results of forward-difference slope approximation for the mass and power optimisation.

Table 4.5: Value of the sensitivity derivative in order of most impactful parameters for the mass and power optimisation.

| **Optimisation Parameter** | **Value of Sensitivity Derivative** |
|---|---|
| Air HEX Stack Height | -1.9505 |
| $H_2$ HEX Stack Height | 0.9038 |
| Air HEX Hot Fluid Length | 0.6796 |
| Tank Inner Radius | 0.2349 |
| Air HEX Cold Fluid Length | -0.2108 |
| Air Pipe 3 Inner Radius | -0.1543 |
| $H_2$ HEX Cold Fluid Length | 0.1460 |
| Vaporiser Inner Radius | 0.0779 |
| $H_2$ HEX Hot Fluid Length | 0.0561 |
| $H_2$ Pipe 1 Inner Radius | 0.0492 |
| Air Pipe 1 Inner Radius | 0.0420 |
| $H_2$ Pipe 2 Inner Radius | 0.0408 |
| Air Pipe 2 Inner Radius | 0.0280 |
| Air Pipe 3 Insulation Thickness | -0.0260 |
| Air Pipe 2 Insulation Thickness | -0.0126 |
| Pump Rotational Speed | -5.0E-4 |
| Air Pipe 1 Insulation Thickness | 2.1E-4 |
| $H_2$ Pipe 2 Insulation Thickness | 2.7E-5 |
| $H_2$ Pipe 1 Insulation Thickness | 2.5E-5 |
| Pump Piston Radius | 1.5E-14 |

## 4.5. VERIFICATION AND VALIDATION

The verification and validation of the component model implementation needs to be performed to ensure that their sizing and the behaviour of the fluids through them is accurate. Verification deals with ensuring

that the methodology produces the expected behaviour given the reference methodology, while validation ensures that the results of the model regarding the sizing and the fluid behaviour matches experimental results or the results of other well-validated software. Due to the novelty of the propulsion system architecture, the verification and validation of a complete model is not possible, however it was performed to different extents for the individual models constructed in this work.

The calculations related to the sizing of the inner and outer vessel of the tank, along with the calculated pipe thicknesses, are verified against examples provided in Barron [12] for a liquid oxygen system. Similarly, the insulation computations are verified against the results of Colozza [13]. However, it should be noted that Colozza does not take into account the thermal conductivity of the inner vessel and does not have an outer vessel in his tank model. The verification of the heat exchanger models was performed by Bhapkar et al. [29] by comparing to results presented by Shah [30].

The verification of the pump model was performed as follows. The modelling of the flow fluctuations was verified against the results from Singh et al. [47], and in particular the percent peak fluctuations above and below the mean flow line, as it is constant and independent of piston dimensions and pump speeds. The comparison of the results is shown in Table 4.6. For the calculation of the pump cylinder thickness, the method was verified against examples in the Advanced Mechanics of Materials and Elasticity book [27].

Table 4.6: Fluctuations above and below the mean for the devised pump model for L/r = 6 obtained compared to the results from Singh et al. [47].

| **Number of Pistons** | **Percent Above Mean** | | | **Percent Below Mean** | | |
|---|---|---|---|---|---|---|
| | **Calculated** | **Literature** | **Percentage Difference** | **Calculated** | **Literature** | **Percentage Difference** |
| 3 | 6.2 | 6 | 3.3% | 16.9 | 17 | -0.6% |
| 4 | 11.1 | 11 | 0.9% | 21.5 | 22 | -2.3% |
| 5 | 1.9 | 2 | -5.0% | 5.2 | 5 | 4.0% |
| 6 | 4.7 | 5 | -6.0% | 9.3 | 9 | 3.3% |

The models of the temperature and pressure changes in the pipe are compared to the work done by Kuczyński et al. [23], where a model for long-distance hydrogen transmission was presented. The results from the verification process are presented for the temperature and pressure change models in Figure 4.41 and Figure 4.42 respectively. It can be seen that the results of the model created in this work closely match the results of Kuczyński et al. [23] for a mass flow rate of 1 $kg/s$ and a pipe diameter of 0.15 $m$. The maximum percentage difference between the results can be seen in Table 4.7. While there is still a difference between the results, this could be due to some unknown input to the model provided by Kuczyński et al. [23]. For example, the pipe roughness was not given and estimated to be 0.04 $mm$ to achieve the closest results, which is within the range of welded steel pipes. Additionally, for the temperature change computations, the effect of the insulation and pipe types and thicknesses could only be obtained from a single heat transfer coefficient value, which was defined for different interior diameters. Finally, some of the difference can be accounted for by the fact that the authors use some approximations and empirical correlations to compute properties of the fluid, such as the friction coefficient, compressibility, and specific heat, while the values in this work are obtained from the PyFluids python package which match the results in the standardised NIST tables [48]. The pressure drop change model was also verified against the examples presented in the Gas Pipeline Hydraulics Book [17], where the difference in results was within 0.2% between the methods.

Table 4.7: Pressure and Temperature Verification Results

| | **Pressure Change** | **Temperature Change** |
|---|---|---|
| **Maximum Percentage Difference** | 4.1% | 8.6% |

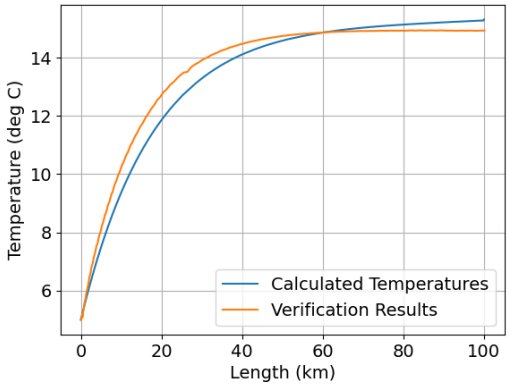


Figure 4.41: Verification of model of the temperature change in the pipes.

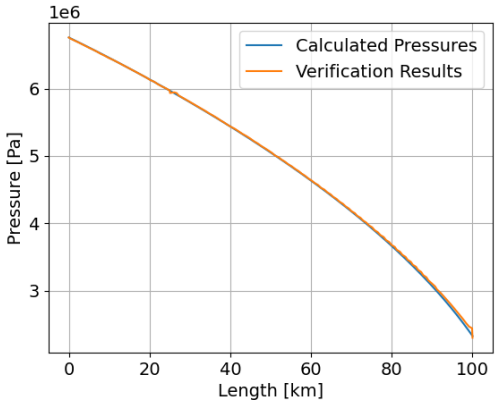


Figure 4.42: Verification of model of the pressure change in the pipes.

Finally, the pressure control model was verified against the BOILFAST software created by Al Ghafri et al., which itself was validated by comparing to experimental data related to the self-pressurisation of liquid hydrogen storage tanks produced by NASA [14]. For the verification, the tank produced for the gaseous hydrogen architecture with self-pressurisation was utilised. The dimensions of the tank, heat transfer rate from the environment, and the initial properties of the hydrogen stored can all be defined in BOILFAST. Additionally, the heat transfer coefficient between the gaseous and liquid hydrogen is set to be extremely high to match the assumption taken in this report (all heat is instantly transferred from the vapour to liquid phase). Then for the initial pressure, and given that no mass flow rate is leaving the tank, the increase in pressure over a set duration can be computed with both models and is compared in Figure 4.43a. It is derived that the maximum difference in the pressure in the tank computed by both models is 0.2%. The mass flow rate from liquid to gaseous hydrogen shown in Figure 4.43b also matches the one obtained using BOILFAST with a slight difference as it approaches the venting condition, after which it is constant and equal to the verification results. This leads to the liquid and gaseous hydrogen mass variations seen in Figure 4.43c andFigure 4.43d respectively, with a 1.4% difference in the mass at the venting point. On the other hand, after venting starts to occur, the masses begin to diverge more, due to the difference in the mass flow rates seen in Figure 4.43e. The difference is accounted for by the method used to compute the state of the gaseous hydrogen. In the model created in this work, the properties are determined given a change in the density and pressure of the gaseous hydrogen based on the mass flow rates of the fluid. On the other hand, for the BOILFAST model, the properties are solved iteratively by estimating an initial vapour temperature and solving the mass balances given the heat transfer coefficient and heat transfer rate from the environment [14]. This leads to different values for the fluid properties, such as the gaseous temperature seen in Figure 4.43f, where the maximum difference is within 5.5% at the point when venting occurs. The maximum percentage difference between the venting mass flow rate of the two models is also determined to be less than 10%. Therefore, the results of the model are considered to be accurate up until the venting point.

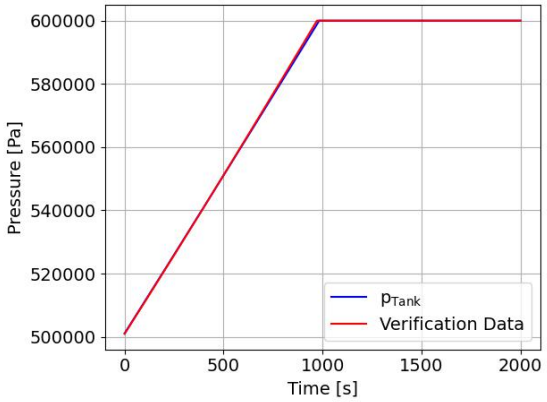


(a) Pressure change in the tank.

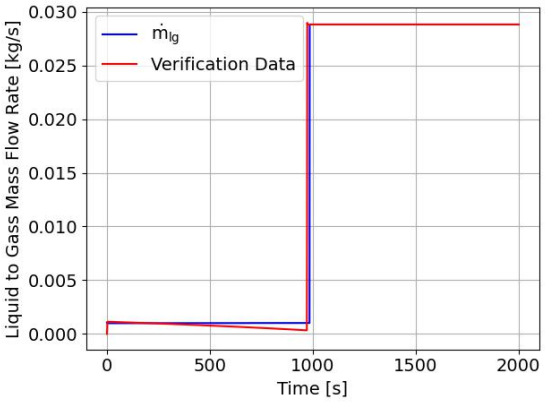


(b) Mass flow rate from liquid to gaseous phase.

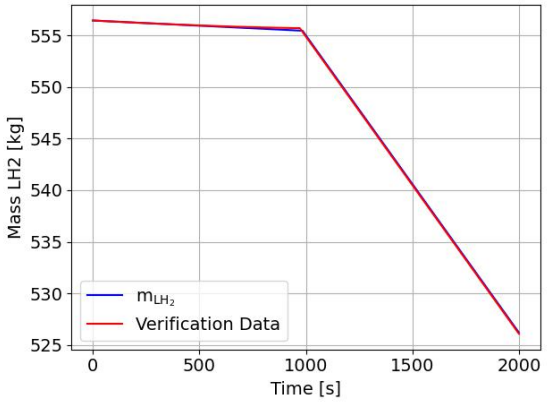


(c) Liquid hydrogen mass in the tank.

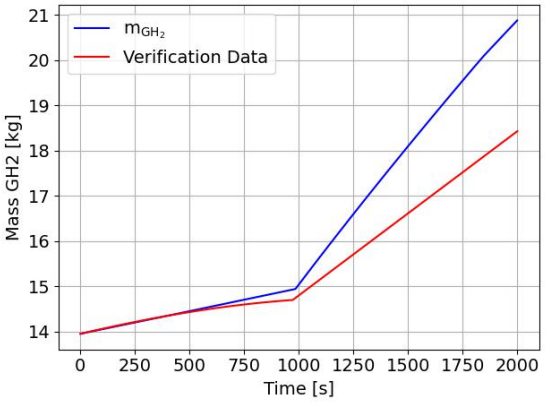


(d) Gaseous hydrogen mass in the tank.

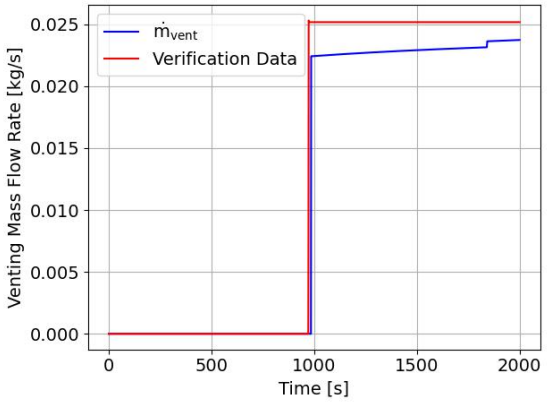


(e) Venting mass flow rate.

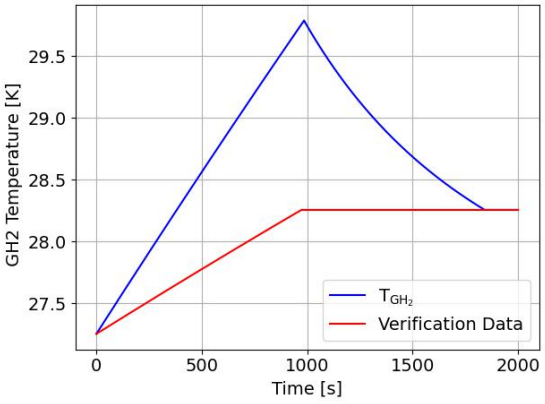


(f) Mass flow rate from liquid to gaseous phase.

Figure 4.43: Verification of the self-pressurisation model results against BOILFAST [14].

## 4.6. STUDY ON THE NUMBER OF PIPE SEGMENTS

In this section, a short study on the effect of the number of pipe segments taken for the pressure and temperature change computations is performed. The pipe parameters in Table 4.8 are taken for the study.

This pipe is investigated for both phases of hydrogen. with an inlet pressure of 5 bar. The inlet temperatures for the liquid and gaseous hydrogen are taken to be 20 K and 100 K respectively, and the mass flow rate analysed is set to 50 g/s for both. The following list of segment numbers was analysed: 1, 5, 10, 50, 100, 200, 500, and 1000.

Table 4.8: Table of pipe parameters taken for segment number studies.

| Parameter | Value | Unit |
|---|---|---|
| Pipe Length | 10 | m |
| Pipe Radius | 0.0102 | m |
| Insulation Thickness | 7.8 | mm |
| Allowable Stress | 129.2 | MPa |
| Pipe Material Density | 7920 | kg/m3 |
| Insulation Density | 32 | kg/m3 |
| Pipe Thermal Conductivity | 3.3 | W/mK |
| Insulation Thermal Conductivity | 0.022 | W/mK |
| Pipe Roughness | 0.1 | mm |
| Pipe Emissivity | 0.33 | - |

For the liquid hydrogen analysis, the change in temperature and pressure over the pipe length are plotted against the number of segments in Figure 4.44a and Figure 4.44b. It can be seen that as the number of segments increases, the solution converges towards the same number. The absolute percentage difference of the values with respect to the value at 1000 segments is plotted for each computation in Figure 4.44c. The study determines that from 10 segments onwards, the percentage difference for both computations lies under 0.5% when compared to the computations at 1000 segments. However, the runtime required for the computations increases exponentially with number of segments as seen in Figure 4.44d, with the computation at 10 segments taking around 40 milliseconds while the computation at 1000 segments taking over 2 seconds. Since the optimisations described in Section 3.3 can have hundreds of iterations, with multiple pipe components implemented, the number of segments was chosen to be 10 as a good compromise between computational time and result accuracy. It should be noted that this is for a pipe length of 10 m, which is around the largest order of magnitude utilised in the hydrogen supply architectures. For different pipe length orders of magnitude, a similar study can be performed to select a number of segments.

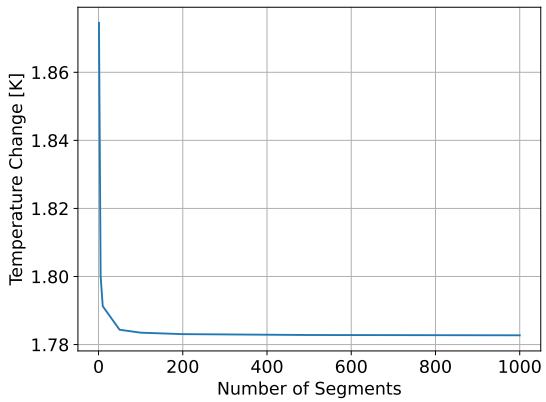


(a) Liquid hydrogen temperature variation.

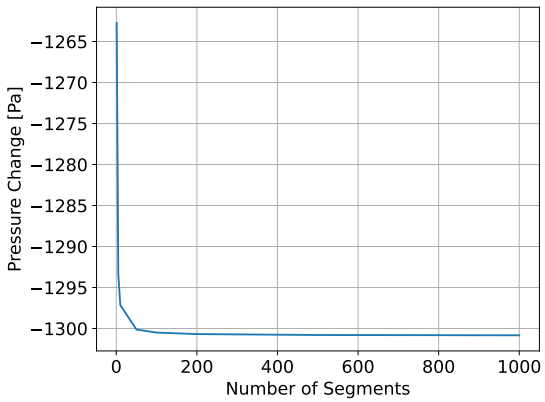


(b) Liquid hydrogen pressure variation.

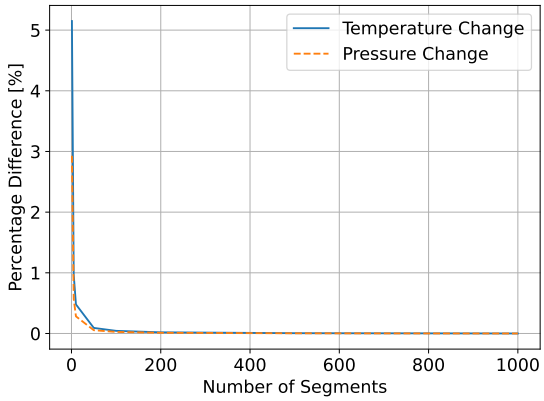


(c) Percentage difference with respect to value at 1000 segments.

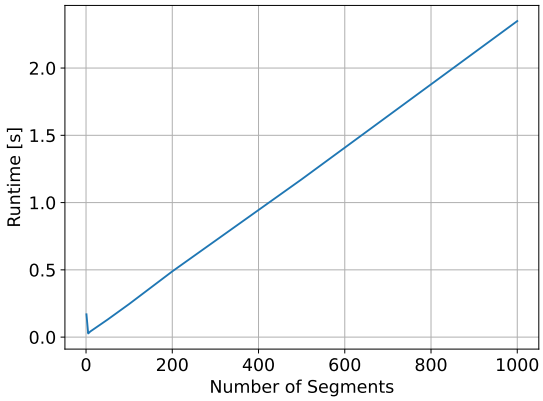


(d) Runtime variation.

Figure 4.44: Study of liquid hydrogen pipe computations plotted against number of segments

This same analysis was performed for gaseous hydrogen, where the results of the temperature and pressure change can be seen in Figure 4.45a and Figure 4.45b respectively, and the percentage difference plot in Figure 4.45c. For this study, the percentage difference is less than 0.1% for computations with more than 10 segments, while the runtime is around the same as for the liquid hydrogen analysis. Therefore, the number of segments was again chosen to be 10.

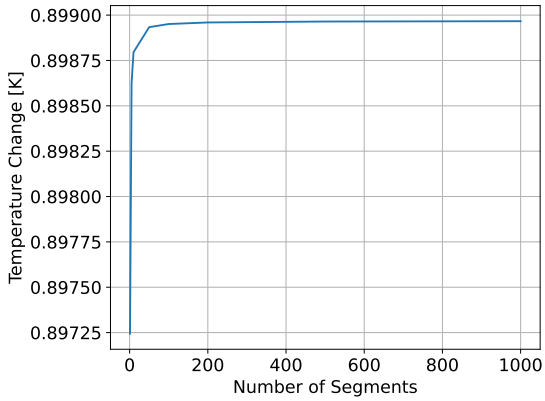


(a) Gaseous hydrogen temperature change variation.

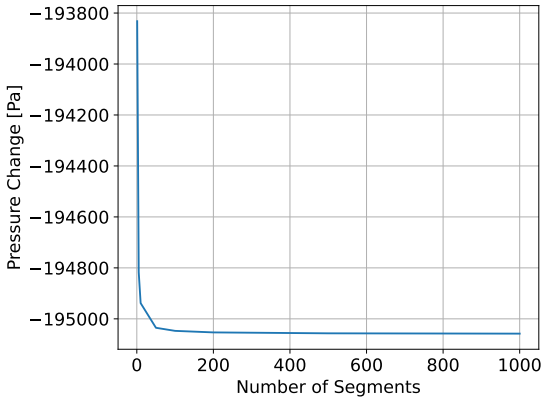


(b) Gaseous hydrogen pressure change variation.

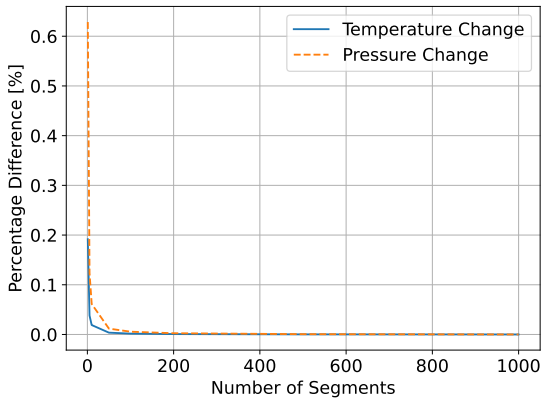


(c) Percentage difference with respect to value at 1000 segments.

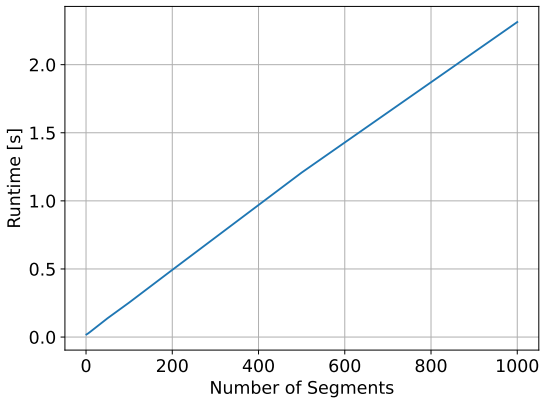


(d) Runtime variation.

Figure 4.45: Study of gaseous hydrogen pipe computations plotted against number of segments

## 4.7. ADDITIONAL OPTIMISATION ANALYSES

As discussed in Section 4.2, due to the nature of the optimiser, the initialisation point can have a sizeable impact on the final result obtained. In this section, two additional analyses are performed to ensure that the trends of the optimisation follows the same physical behaviour observed in Section 4.1. In particular, the effect on the sizing of both heat exchangers is examined, as they were determined to have the largest impact on the system in Section 4.4. The first additional analysis discussed in Section 4.7.1 uses the initialisation point shown in Table 4.9, where, with help from colleagues at the DLR, the new point was chosen such that the heat exchangers would be oversized compared to the requirements for the SOFC inlet. Additional variations in the initialisation include slightly different tank and vaporiser initial radii. The second additional analysis presented in Section 4.7.2 implements a larger SOFC inlet pressure of 8 *bar* compared to the previous inlet pressure of 5 *bar*. The original initialisation point is used for the second analysis.

Table 4.9: Table of optimisation parameters for the new intialisation point

| Optimisation Parameter | Range | Starting Value | Maximum Value | Architectures* |
|---|---|---|---|---|
| Tank Inner Radius | (0.1, 1) | 0.8 | 1.5 m | All |
| Stack Height Hydrogen HEX | (0.02,1) | 0.169 | 5 m | All |
| Stack Height Air HEX | (0.02,1) | 0.3 | 5 m | All |
| Cold Side Length Hydrogen HEX | (0.0833,1) | 0.2 | 0.6 m | All |
| Cold Side Length Air HEX | (0.1,1) | 0.5 | 0.6 m | All |
| Hot Side Length Hydrogen HEX | (0.05,1) | 0.4 | 1 m | All |
| Hot Side Length Air HEX | (0.05,1) | 0.5 | 1 m | All |
| Pipe 1 Radius | (0.02,1) | 0.05 | 0.25 m | All |
| Pipe 1 Insulation Thickness | (0.01,1) | 0.8 | 0.01 m | All |
| Pipe 2 Radius | (0.04,1) | 0.05 | 0.25 m | 2, 3 |
| Pipe 2 Insulation Thickness | (0.01,1) | 0.3 | 0.01 m | 2, 3 |
| Pipe 3 Radius | (0.02,1) | 0.9 | 0.25 m | All |
| Pipe 3 Insulation Thickness | (0.01,1) | 0.3 | 0.01 m | All |
| Pipe 4 Radius | (0.02,1) | 0.8 | 0.25 m | All |
| Pipe 4 Insulation Thickness | (0.01,1) | 0.3 | 0.01 m | All |
| Pipe 5 Radius | (0.01,1) | 0.8 | 0.25 m | All |
| Pipe 5 Insulation Thickness | (0.01,1) | 0.3 | 0.01 m | All |
| Vaporiser Inner Radius | (0.01,1) | 0.9 | 0.5 m | 2, 3 |
| Pump Rotational Speed | (0.01,1) | 0.33 | 60 rad/s | 3 |
| Piston Inner Radius | (0.01,1) | 0.723 | 0.3 m | 3 |

* The self-pressurisation architecture with gaseous and liquid hydrogen extraction are numbered 1 and 2 respectively, and the pump-fed architecture with liquid hydrogen extraction is numbered 3.

### 4.7.1. VARIATION OF THE OPTIMISATION INITIALISATION

A detailed description of the results is performed for the pump-fed liquid hydrogen extraction architecture, as it contains all components and the behaviour is similar between them.

#### Mass Optimisation

The convergence of the cost function and the system mass for the mass optimisation of the architecture are presented in Figure 4.46a and Figure 4.46b respectively. As opposed to the cost function convergence of the previous initialisation shown in Figure 4.1a, the function converges to a value below the initial one.

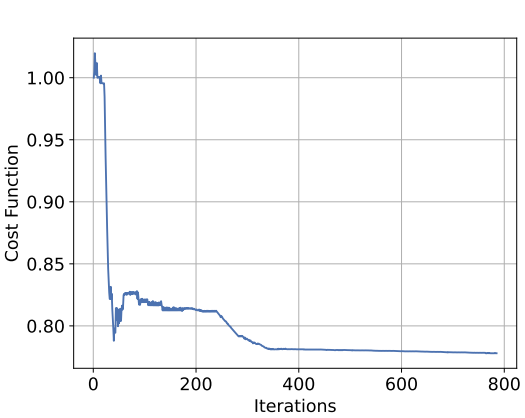


(a) Convergence of the cost function.

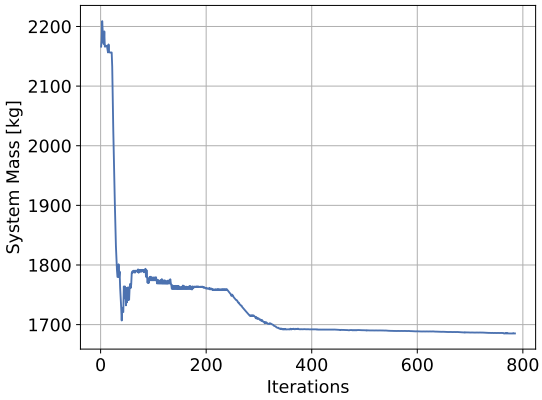


(b) Convergence of the system mass.

Figure 4.46: $LH_2$ Pump architecture mass optimisation: Optimisaton convergence plots for the new intialisation point.

The main reason is due to the fact that the starting point for both heat exchangers causes them to be oversized, which means that the heat transfer rate through the heat exchanger to the cold fluid is higher than what is required to condition it. This can be seen in Figure 4.47a and Figure 4.47b, where the heat exchanger is initially oversized by around 6 $kW$, which allows for a reduction in its mass throughout the optimisation. While the heat exchanger is now sized for the same heat transfer rate as the converged baseline optimisations, the final mass in this analysis is larger. This is due to the fact that a different combination of heat exchanger dimensions led to the same performance achieved, with slightly different masses. The variation in the non-dimensionalised hydrogen heat exchanger dimensions for the new and previous initialisation point are presented in Figure 4.47c and Figure 4.47d respectively. It can be seen that although they both achieve the required heat transfer rate, the converged sizing of the new initialisation point does so at a higher stack height and smaller lengths for the cold and hot fluid sides, while the opposite is true for the previous initialisation point, which results in different masses for both. The pressure drops for the hot and cold fluids through the heat exchanger are displayed in Figure 4.47e and Figure 4.47f respectively, where it is evident that the values do not exceed the maximum constraint.

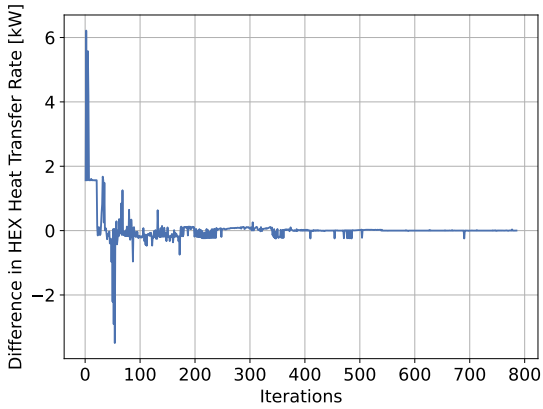


(a) Variation in the difference in the hydrogen heat exchanger heat transfer rate and fluid required heat transfer rate.

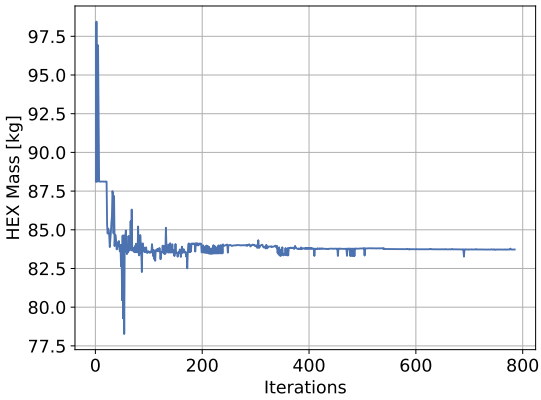


(b) Variation in the hydrogen heat exchanger mass.

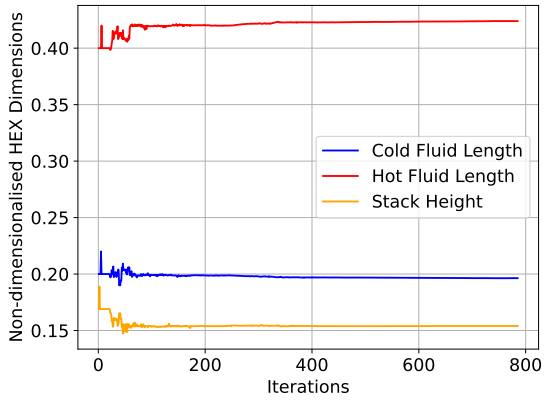


(c) Variation in the non-dimensionalised hydrogen heat exchanger geometry parameters.

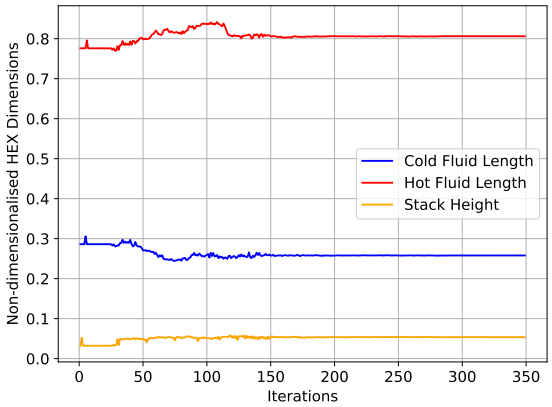


(d) Variation in the non-dimensionalised hydrogen heat exchanger geometry parameters for the previous initialisation point.

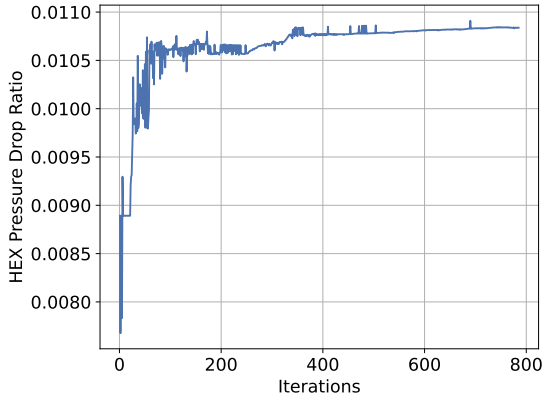


(e) Variation in the hydrogen heat exchanger hot fluid pressure drop.

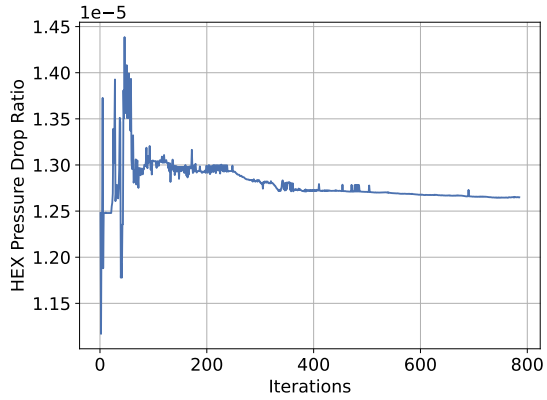


(f) Variation in the hydrogen heat exchanger cold fluid pressure drop.

Figure 4.47: $LH_2$ Pump architecture mass optimisation: Hydrogen heat exchanger convergence plots for the new initialisation point

The same effect is visible in the air heat exchanger plots presented in Figure 4.48a and Figure 4.48b. The air heat exchanger was greatly oversized by around 250 *kW*, which allowed for a large reduction in its mass. The difference in the air heat exchanger mass between the two initialisations is again due to a different combination of dimensions that achieve the same heat transfer rate requirements. The variations in the non-dimensionalised dimensions throughout the optimisation for the new and previous initialisation are displayed in Figure 4.48c and Figure 4.48d respectively, and the change in pressure drops of the hot and cold fluid through the air heat exchanger in Figure 4.48e and Figure 4.48f. At the beginning of the optimisation, the air side heat exchanger was exceeding the maximum pressure drop constraint for the hot fluid, which is why the sizing took longer to converge than for the hydrogen heat exchanger.

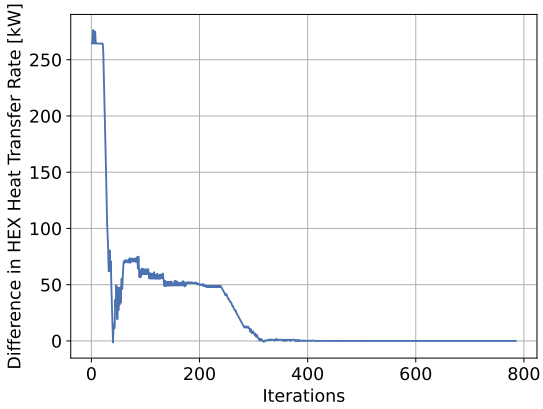


(a) Variation in the difference in the air heat exchanger heat transfer rate and fluid required heat transfer rate.

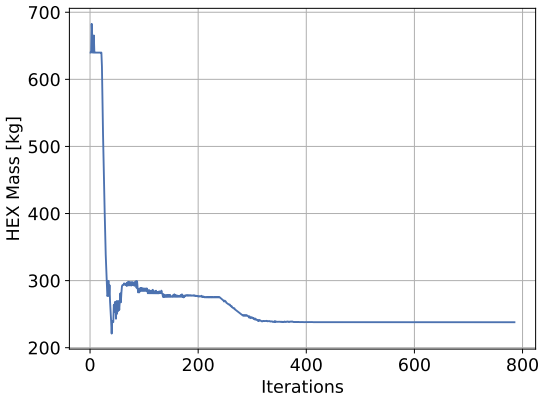


(b) Variation in the air heat exchanger mass.

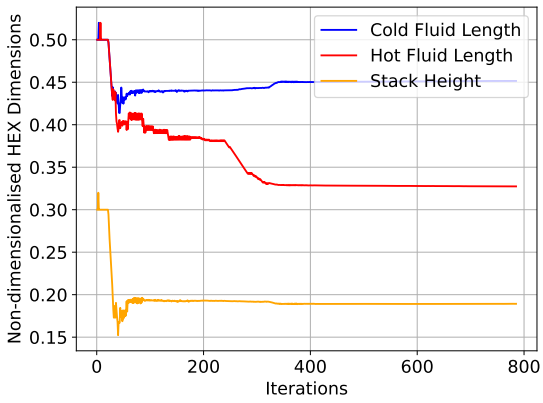


(c) Variation in the non-dimensionalised air heat exchanger geometry parameters.

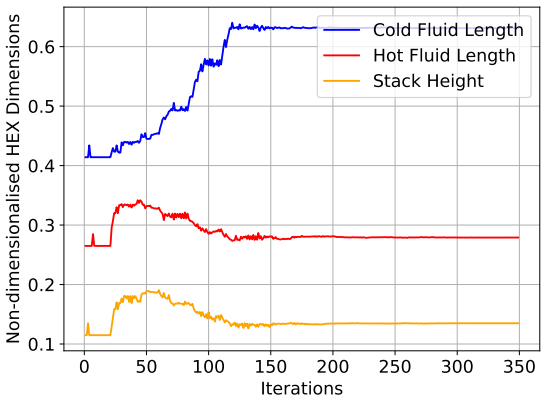


(d) Variation in the non-dimensionalised air heat exchanger geometry parameters for the previous initialisation point.

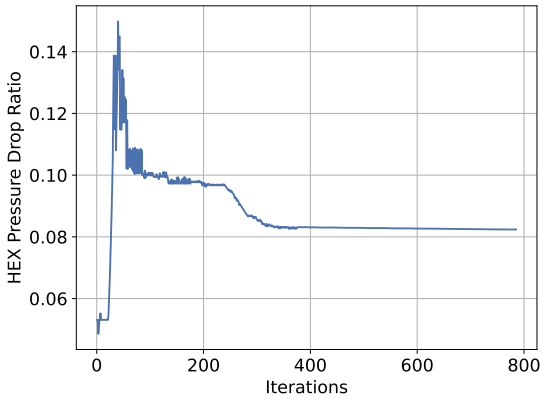


(e) Variation in the air heat exchanger hot fluid pressure drop.

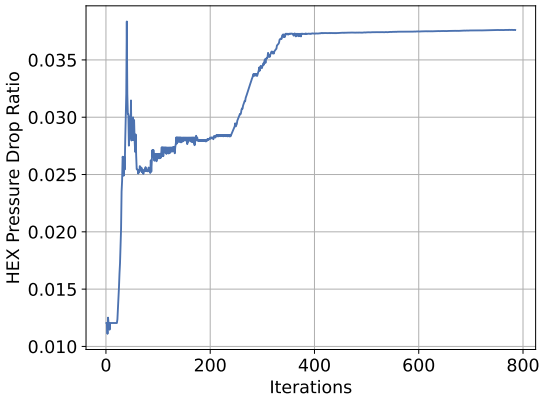


(f) Variation in the air heat exchanger cold fluid pressure drop.

Figure 4.48: $LH_2$ Pump architecture mass optimisation: Air heat exchanger convergence plots for the new initialisation point

The trend in the tank mass variation is similar for both initialisation points, as the mass decreases with increasing tank radius. However, since the initial tank radius is larger in this initialisation, the optimiser converges before the minimum tank mass. This can be seen in Figure 4.49a and Figure 4.49b. Similar trends are observed for the vaporiser mass and dimensions in Figure 4.50a and Figure 4.50b.

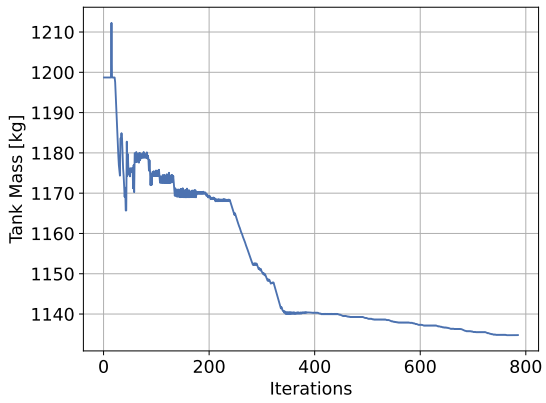


(a) Variation in the mass of the tank.

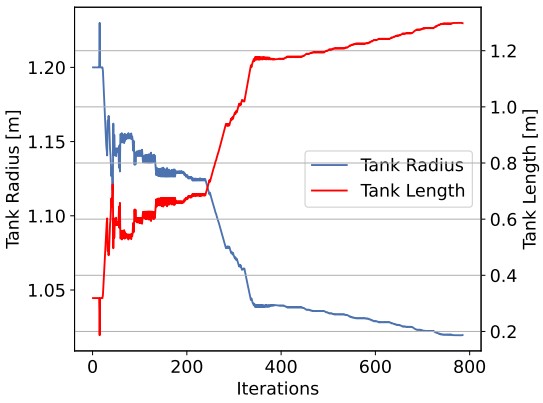


(b) Variation in the tank dimensions.

Figure 4.49: $LH_2$ Pump architecture mass optimisation: Tank convergence plots for the new initialisation point

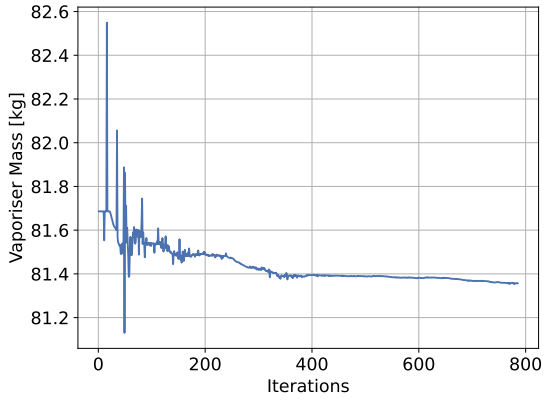


(a) Variation in the mass of the vaporiser.

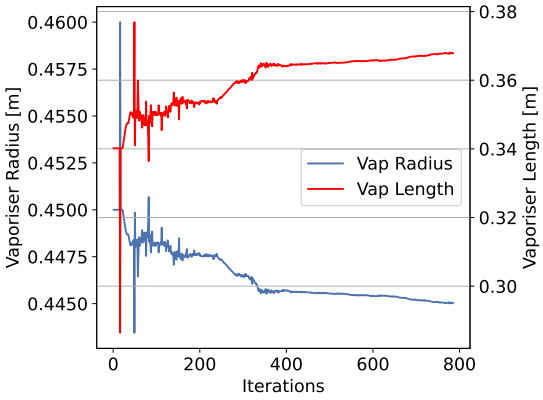


(b) Variation in the vaporiser dimensions.

Figure 4.50: $LH_2$ Pump architecture mass optimisation: Vaporiser convergence plots for the new initialisation point

The final mass compositions for this optimisation run are presented in Figure 4.51 and Figure 4.52. The results show that although the behaviour of the optimisation follows the same principles, the initialisation point still led to a larger overall converged system mass.

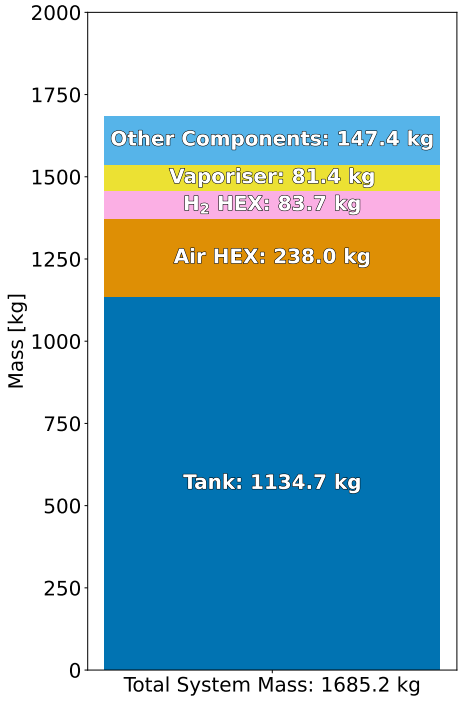


Figure 4.51: Mass optimisation: Mass composition of the complete $LH_2$ Pump architecture for the new initialisation point.

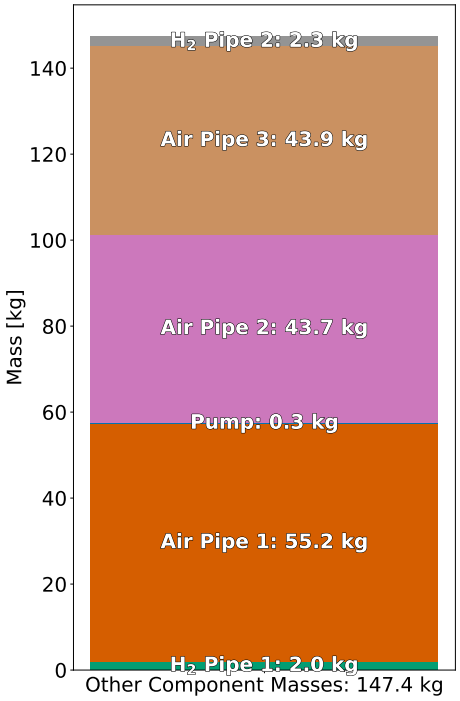


Figure 4.52: Mass optimisation: Mass composition of the remaining components of the $LH_2$ Pump architecture for the new initialisation point.

### Mass and Power Optimisation

For the mass and power optimisation, the optimiser again tries to reduce the pressure losses in the system as for the previous initialisation point in order to maximise the net power recovery. This is especially visible for the air side heat exchanger, where the pressure drops of the hot and cold fluid are presented in Figure 4.53a and Figure 4.53b, and both converge to lower values than for the mass optimisation. The corresponding changes in the turbine power recovered and compressor power required are shown in Figure 4.54a and Figure 4.54b.

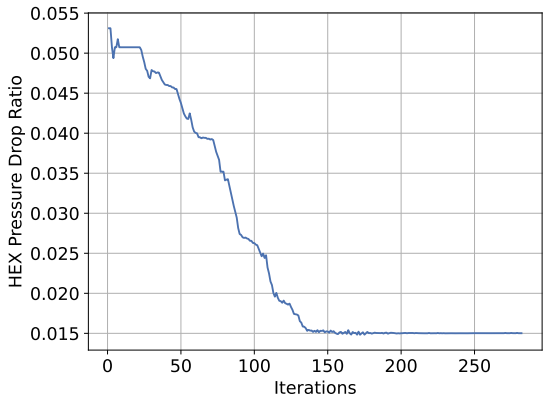


(a) Variation in the air heat exchanger hot fluid pressure drop.

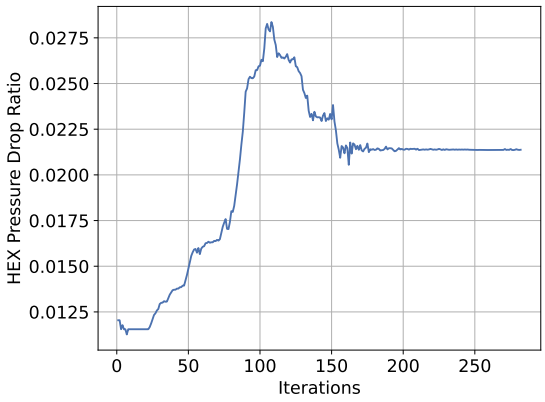


(b) Variation in the air heat exchanger cold fluid pressure drop.

Figure 4.53: $LH_2$ Pump architecture mass and power optimisation: Air heat exchanger convergence plots for the new initialisation point

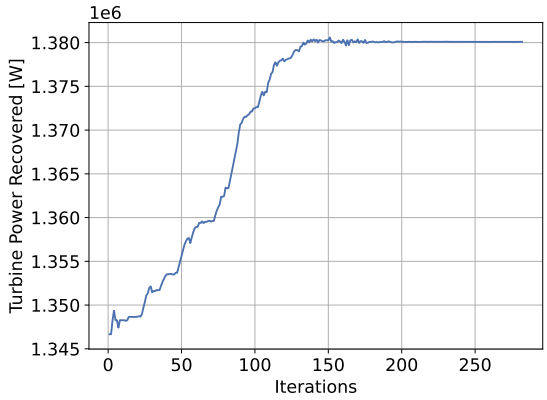


(a) Variation in the turbine power recovered.

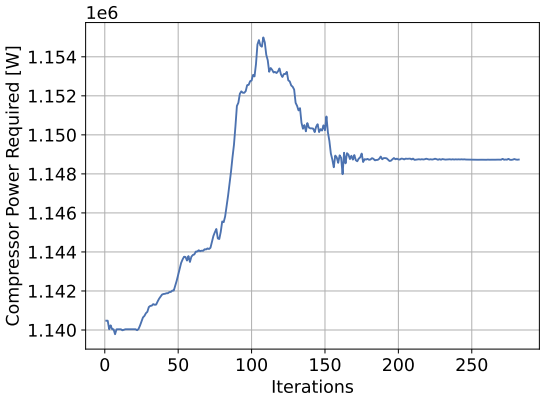


(b) Variation in the compressor power required.

Figure 4.54: $LH_2$ Pump architecture mass and power optimisation: Turbine and compressor convergence plots for the new initialisation point

The final composition for the mass and power optimisation of the pump-fed liquid hydrogen extraction architecture is presented in Figure 4.55 and Figure 4.56. Similarly to the previous initialisation point, the total system mass is larger due to the increased mass of the components related to the pressure drop in the system.

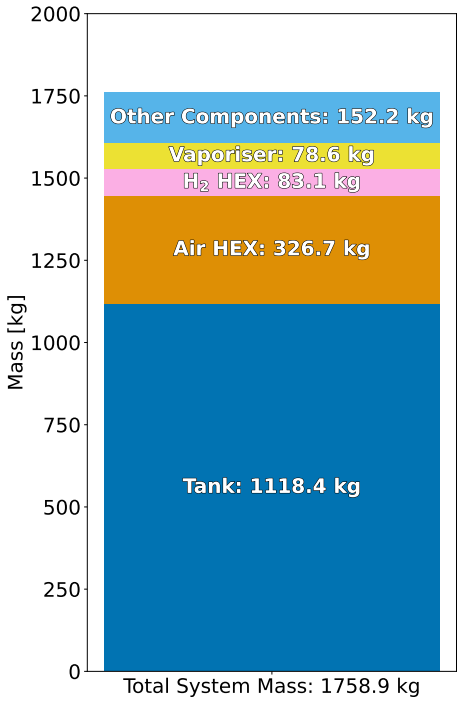


Figure 4.55: Mass and power optimisation: Mass composition of the complete $LH_2$ Pump architecture for the new initialisation point.

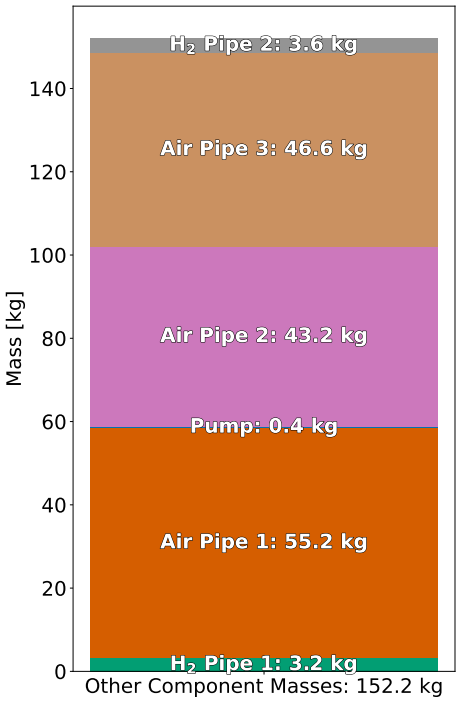


Figure 4.56: Mass and power optimisation: Mass composition of the remaining components of the $LH_2$ Pump architecture for the new initialisation point.

These optimisation were performed for all architectures and the main results related to the optimisation objectives are summarised in Figure 4.57 and Figure 4.58. One of the main differences between the two initialisation points is that the converged system masses are larger overall for the new initialisation point, due to the larger initial system mass for each architecture. Similarly, the optimiser is also able to converge to large power recovery effectiveness values. However, overall, the pattern of the results is the same as for the previous initialisation.

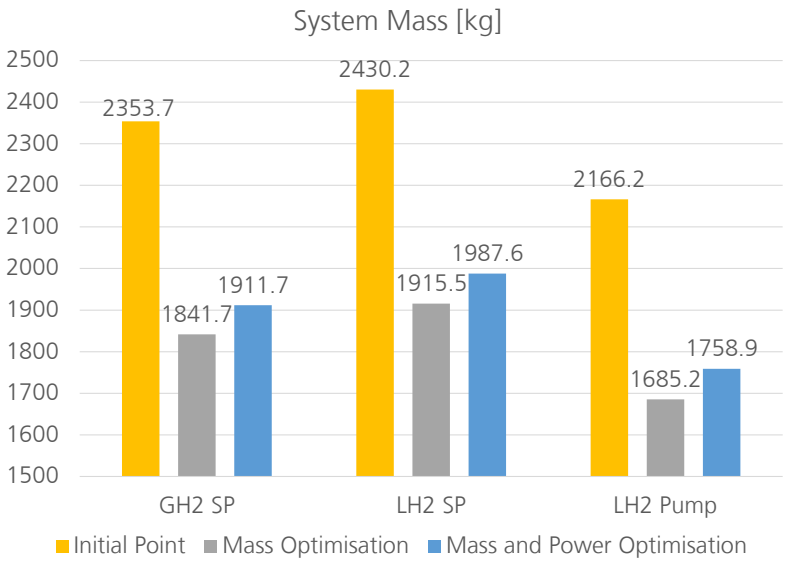


Figure 4.57: Comparison of architecture system masses for the new initialisation point.

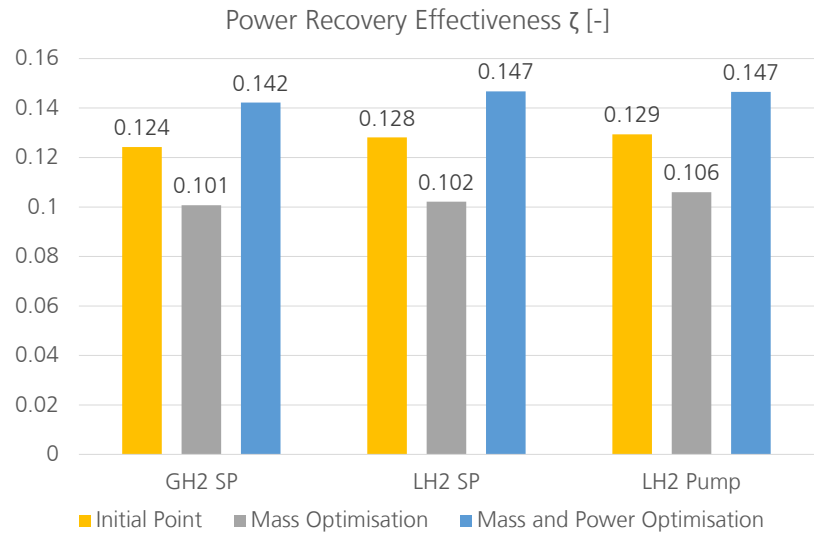


Figure 4.58: Comparison of architecture power recovery effectiveness for the new initialisation point.

### 4.7.2. VARIATION OF THE SOFC INLET PRESSURE

Next, the same analysis is performed for the first initialisation point, where the only change is increasing the SOFC inlet pressure from 5 *bar* to 8 *bar*. The main effects from increasing the pressure are examined via the results of the mass and power optimisation of both liquid extraction architectures.

**Liquid Hydrogen Extraction with Self-Pressurisation**

The convergence of the cost function for the mass and power optimisation of this architecture is presented in Figure 4.59a. When compared to the optimisations for the previous inlet pressure in Figure 4.21a, it can be seen that the drop in the cost function is not as large. This is in particular due to the larger initial net power recovery for the system in Figure 4.59c when compared to the baseline optimisations in Figure 4.21c.

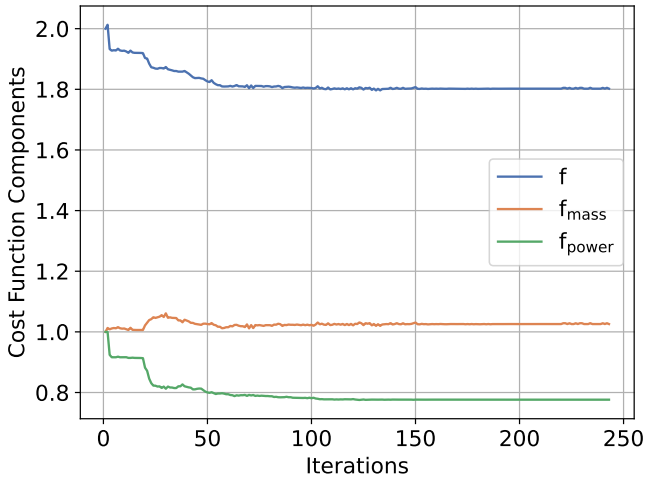


(a) Convergence of the cost function.

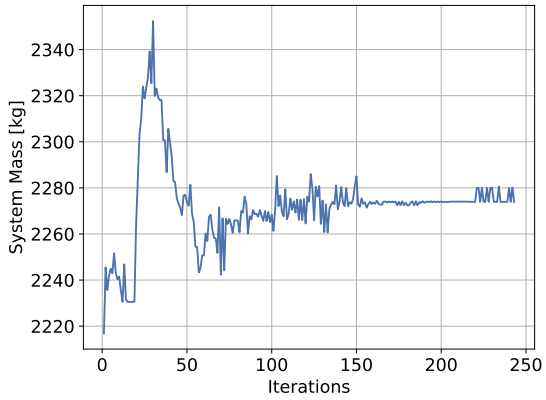


(b) Convergence of system mass.

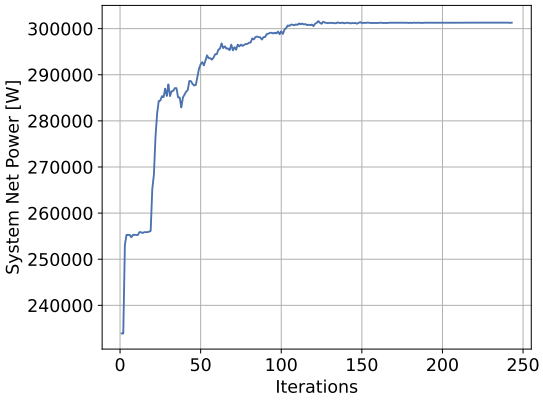


(c) Convergence of system net power recovery.

Figure 4.59: $LH_2$ SP architecture mass and power optimisation: Optimisation convergence plots for 8 *bar* SOFC inlet pressure.

The difference in the initial net power recovery is due to the comparatively lower pressure drops through the system, which is especially true for the air heat exchanger, where the values for the pressure drops of each fluid is displayed in Table 4.10. As discussed earlier, this difference in values could be attributed to the much less dense fluid passing through the same heat exchanger at the lower pressures with the same temperature, leading to larger pressure drops. The corresponding initial turbine power recovery and compressor power required for the different SOFC inlet pressure values are shown in Table 4.11.

Table 4.10: Initial pressure drop ratio values through the air heat exchanger for different SOFC inlet pressures.

| SOFC Inlet Pressure | Cold Fluid Pressure Drop Ratio | Hot Fluid Pressure Drop Ratio |
|---|---|---|
| 5 bar | 0.100 | 0.180 |
| 8 bar | 0.046 | 0.073 |

Table 4.11: Initial turbine and compressor power values for different SOFC inlet pressures.

| SOFC Inlet Pressure | Initial Turbine Power Recovered | Initial Compressor Power Required |
|---|---|---|
| 5 bar | 1.274 MW | 1.224 MW |
| 8 bar | 1.866 MW | 1.622 MW |

The final mass compositions resulting from this optimisation can be seen in Figure 4.60 and Figure 4.61. Here, the mass of the tank and vaporiser can be seen to be significantly larger than for the 5 *bar* SOFC inlet pressure in Figure 4.23 and Figure 4.24, stemming from the increased wall thickness required for the higher pressure.

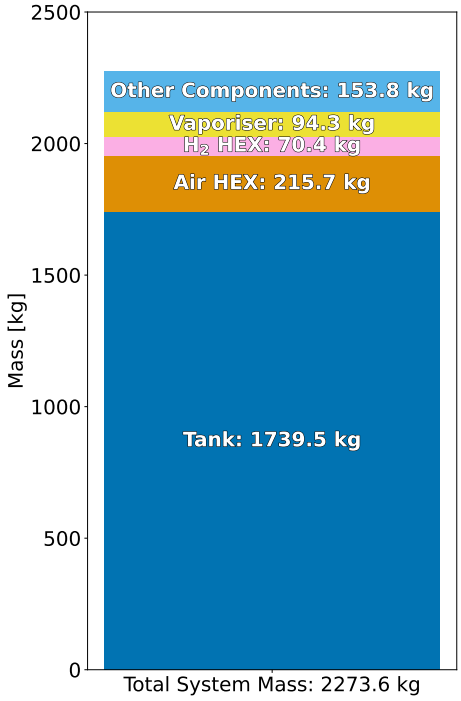


Figure 4.60: Mass and power optimisation: Mass composition of the complete $LH_2$ SP architecture for 8 *bar* SOFC inlet pressure.

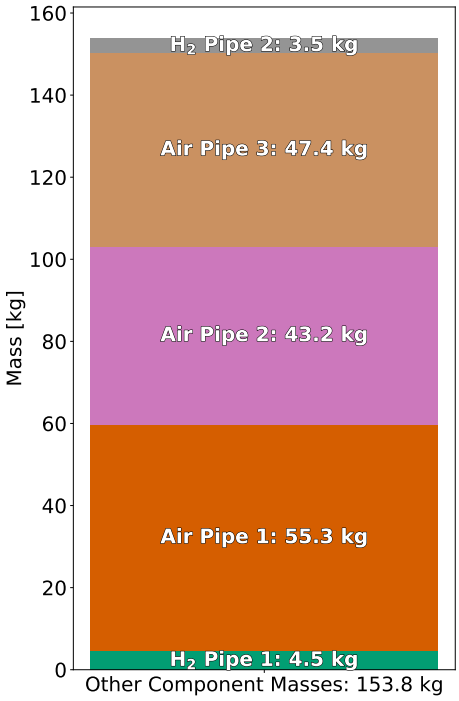


Figure 4.61: Mass and power optimisation: Mass composition of the remaining components of the $LH_2$ SP architecture for 8 *bar* SOFC inlet pressure.

**Liquid Hydrogen Extraction with Pumps**

When implementing the pump-fed architecture, with the same tank pressure defined by the user as for the baseline optimisation (3 *bar*), the pump power required increased with increasing SOFC inlet pressure in Table 4.12.

Table 4.12: Converged pump power values of mass and power optimisation for different SOFC inlet pressures.

| SOFC Inlet Pressure | Pump Power Required |
|---|---|
| 5 bar | 194.9 W |
| 8 bar | 515.7 W |

The final composition is presented in Figure 4.62 and Figure 4.63. The lower pressure in the tank allows for a much lower system mass compared to the self-pressurisation architecture. Additionally, it is determined that for a higher SOFC pressure, the pump-fed architecture total mass converges to a larger value.

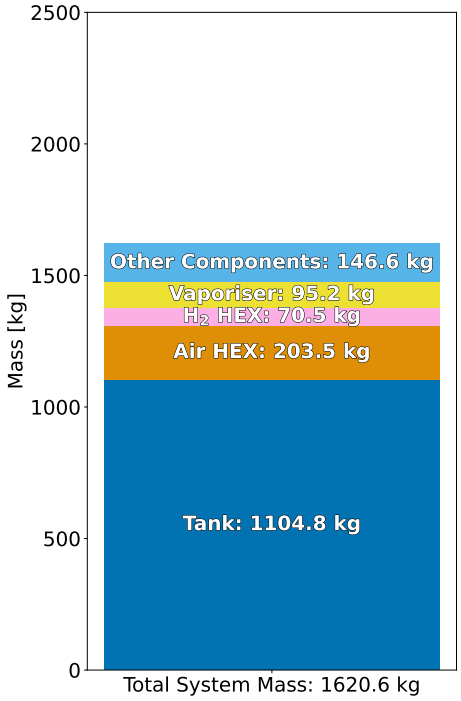


Figure 4.62: Mass and power optimisation: Mass composition of the complete $LH_2$ Pump architecture for 8 *bar* SOFC inlet pressure.

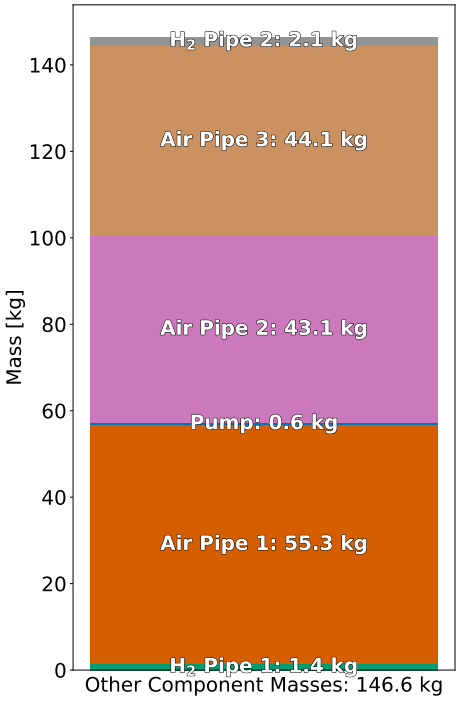


Figure 4.63: Mass and power optimisation: Mass composition of the remaining components for the $LH_2$ Pump architecture for 8 *bar* SOFC inlet pressure.

The optimisations were performed for all architectures for both objective functions, where the summarised results are presented in Figure 4.64 and Figure 4.65. Again, the results follow the same trends as for the previous analyses. It can be seen that the converged system masses in all cases are quite close to the initialisation for both objective functions, as the local optimisation algorithm starts closer to the optimal location for the heat exchanger components. The converged power recovery effectiveness of the architectures at 8 *bar* is larger than for those at 5 *bar*, due to the fact that the lower initial pressure drop through the heat exchangers, the optimiser is able to converge to even lower pressure drops and higher net power recovery values.

Table 4.13 outlines the power values for each of the components in the system, where one can observe that different values are obtained than for the optimisations at the lower SOFC inlet pressures in Table 4.3. As explained in Section 2.2.2, the power computation of the pressurised vessels is a function of multiple variables including the mass flow rates in and out of the tank and the enthalpies of the fluids. For a saturated fluid, the latent heat of vaporisation reduces with increasing pressure could be a reason for the power reduction of the components where gaseous hydrogen is extracted such as the vaporiser. Overall, the total parasitic power follows the same trend as for the optimisations at the lower pressure.

Table 4.13: Power values for the mass and power optimisations for 8 *bar* SOFC inlet pressure.

| **Components** | **$GH_2$ SP** | **$LH_2$ SP** | **$LH_2$ Pump** |
|---|---|---|---|
| Turbine Power Recovered [kW] | 1896.5 | 1898.8 | 1896.8 |
| Compressor Power Required [kW] | 1587.7 | 1588.6 | 1591.1 |
| Tank Power [kW] | 15.9 | 5.5 | 0.3 |
| Vaporiser Power [kW] | - | 3.0 | 3.1 |
| Pump Power [kW] | - | - | 0.5 |
| **Parasitic Power [kW]** | 15.9 | 8.5 | 3.9 |
| **Net Power Recovered [kW]** | 292.9 | 301.7 | 301.7 |

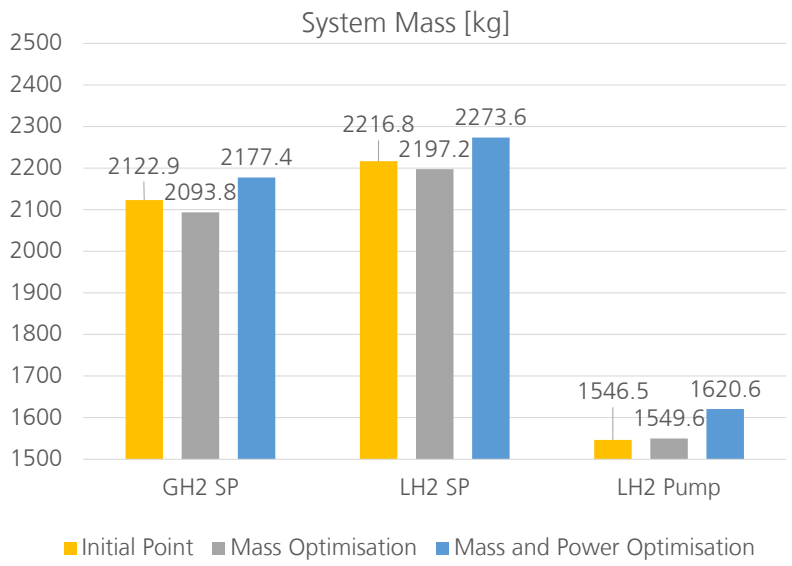


Figure 4.64: Comparison of architecture system masses for the 8 *bar* SOFC inlet pressure.

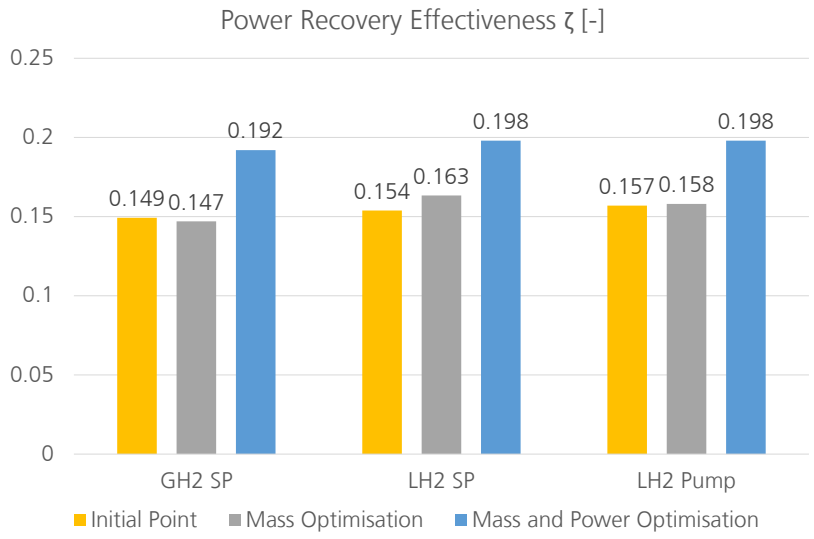


Figure 4.65: Comparison of architecture power recovery effectiveness for the 8 *bar* SOFC inlet pressure.

# 5

# Conclusions and Outlook

## 5.1. Conclusions from the Results

The thesis set out to develop a framework for the design, optimisation, and assessment of hydrogen fuel cell supply architectures. This framework was applied in the $H_2$EAT project at the DLR Institute of Electrified Aero Engines, which involved the conceptual design of a Solid Oxide Fuel Cell (SOFC) powered regional aircraft [5]. The following three different systems were defined for this application. Two of them utilised the tank self-pressurisation as the driving force behind the hydrogen flow in the system, with the one extracting gaseous hydrogen from the tank and the other extracting the liquid hydrogen. The final architecture employed liquid hydrogen extraction using piston pumps.

Analytical models were utilised for sizing of each component and modelling the hydrogen and air flow through them. These components included cryogenic storage tanks, vaporisers, pipes, heat exchangers, pumps, turbines and compressors. These models were then implemented in an optimisation loop using the built-in optimiser tool in the DLR open-source, workflow-driven integration environment RCE [35]. The complete architectures were optimised for two different optimisation objectives. The first objective was to minimise the total system mass, and the second combined the minimisation of the system mass with maximising the net power recovered of the system. The initialisation point for the optimisations was obtained from individual component sizings performed at earlier stages in the project or via expert interviews with DLR colleagues.

The results show that choice of objective function greatly impacts the final converged system. When optimising for mass, the optimiser minimises the mass of all components in the air side of the system. On the hydrogen side, for the self-pressurisation architectures, a compromise between the mass of the tank and the mass of the remaining components is found. This stems from the fact than reducing the size of the remaining components increases the pressure drop through them, and with it the storage pressure required to achieve the desired SOFC inlet conditions. A larger storage pressure requires a greater tank thickness and leads to a larger mass. For the pump-fed systems, the same effect is observed to a lesser extent, as the change in output pressure required by the pump does not have that large of an effect on the mass. This is due to the relatively low volumetric flow rates and pressure rise needed. When optimising for mass and power, the convergence tends to reduce the pressure drops in the air side in order to maximise the power recovered by the turbine and minimise that required by the compressor. The final converged system mass is larger than that for the mass optimisation. However, massive benefits in the net power recovered by the system are achieved.

The main impact from the different architecture layouts is related to the parasitic power of the system, which includes the additional power required to maintain the storage pressure in the tank and vaporiser as well as the pump power. The implementation of a vaporiser in the liquid extraction architectures reduces the tank power as the greatest proportion is related to the heat required to evaporate the liquid hydrogen. Additionally, the vaporiser power is less due to the lower total mass stored inside, leading to a total reduction in the parasitic power. Similarly, the implementation of the pump allows for the storage of the tank at a lower pressure, which reduces the mass of the tank and the power required to maintain this pressure. There is an

overall reduction in the parasitic power despite the additional pump power.

It was concluded that the pump-fed liquid extraction architecture is the most applicable for SOFC powered aircraft based on the preliminary analysis performed in this work, due to its low system mass and parasitic power, and its higher converged net power recovered. A sensitivity analysis was performed on the final optimised parameter values to determine which has the largest impact on the converged system. This was done using a forward-difference approximation of the objective slope with respect to a suitable step size in the parameter values. The sensitivity analysis determined that the heat exchanger geometrical parameters have the largest impact on both objective functions. This follows from the optimisation trends, as the heat exchangers comprise a large percentage of the overall system mass and have a sizeable effect on the pressure losses in the system, which can impact the mass of other components like the tank and pipes. The analysis also shows that components related to the pressure drop, such as the pipes, become more important when optimising for mass and power than just for mass.

A preliminary mission analysis focusing on the tank operation was performed for the gaseous extraction architecture. This architecture was chosen due to its low complexity when compared to the liquid extraction ones, where a detailed simulation and control of the fill levels, mass flow rates, and pressures in the vaporiser are required to ensure the optimal operation. The analysis showed that the mission operation requires a large amount of additional energy is required to maintain the required pressures in the tank. If this energy is stored in lithium-ion batteries, it would correspond to a 14.7% increase in the system mass. In reality, some of the power could be provided by recovering waste energy from the turbine. However, since the analysis does not consider the additional amount of energy required to operate the on-board aircraft systems, some additional mass would be required. This mass could also be provided by storing additional fuel in the in the tank and maintaining a larger mass flow rate, which would lead to a heavier system. Both increases in mass have a "snowball" effect on the aircraft and propulsion system design, where an iterative design process would be required. However, this is beyond the scope of the thesis.

Finally, it was examined that the initialisation point of the optimisation has a noticeable effect on the optimisation outcome. This arises from the optimisation algorithm implemented being a local simplex-based method. The initial heat exchanger dimensions provided were obtained from an earlier stage of the project which assumed a different operational pressure, which led to the initial heating provided to fluid being not sufficient and to an increase in the heat exchanger sizes and, in turn, the system mass. Therefore, two additional optimisation analyses were performed. The first used a different initialisation point that oversized the heat exchangers, tank, and vaporiser to observe the convergence of the system from a larger initial system mass. The second implemented the operational pressure from the previous phase of the project. Both analyses showed that the additional optimisations followed the same physical trends as the baseline optimisations. Furthermore, the pump-fed architecture was again determined to be the most applicable for both optimisations.

The methodology implemented in this work is successful in achieving the defined research objective. It is most applicable for performing a preliminary analysis of a desired hydrogen fuel cell supply architecture for a given mission and a preliminary aircraft and SOFC design. It can also be used to identify the aspects and components of the system have the most impact and therefore demand a detailed examination in the earlier stages of the project. The main prerequisite to the utilisation of this framework is a clear definition of objective functions and constraints for the system based on the mission requirements. While not explored in this thesis, the framework could be integrated in a greater design loop for the entire propulsion system or aircraft due to the general nature of the implementation. Additionally, as the component model implementations are modular, higher fidelity models can replace lower fidelity models at any stage in the system to ensure more accurate results.

## 5.2. LIMITATIONS OF THE FRAMEWORK

The study performed in this thesis is not without limitations. The most important limitation is with regards to the optimisation algorithm implemented. This algorithm was chosen due to its quick convergence speeds and high efficiencies, which allowed for the quick analysis of multiple architectures with multiple cost functions at different initialisation points. However, due to the nature of the algorithm, the optimiser converges to

local minima and the final architecture resulting from the optimisations can not be assumed to be the ideal architecture. The results from this optimisation should be used to understand the relations between the different components of the systems and how their sizing affect each other.

In order to maintain a reasonable computational effort, low fidelity analytical models were used for the modelling of the different components. While this provides a robust baseline for preliminary system analyses, this does not allow for a detailed analysis of complex interactions in the system. The assumption of homogeneous hydrogen phases in the tank and vaporiser simplify the computations regarding the insulation and power requirements. However, the stratification of hydrogen would have noticeable effects on those computations and on the outlet fluid conditions. Additionally, the complex fluid interactions within the pipe related to temperature and pressure change and interactions with the walls were greatly simplified.

The pump modelling was also greatly simplified due to the lack of available material regarding the sizing and simulation of piston pumps for cryogenic conditions. The mass of the pump only assumed criteria concerning the pressure difference, however, additional mass is likely required considering the cryogenic conditions which could be related to insulation required to keep the liquid phase or embrittlement of the pump material. Additionally, the occurrence of cavitation in the pump is likely due to the low boiling point of hydrogen which could lead to further wear of the pump. Therefore, while the pump system was established to be the most applicable in these analyses, further research is required to determine its feasibility.

The self-pressurisation model implemented in this work was based on the work of well-validated BOIL-FAST model of Al Ghafri et al. [14]. However, additional factors related to the mass flow of hydrogen in and out of the tank were added to the base energy balance equations of the original model, which can have an important effect on the pressure and power computations. These additions could not be verified against their model. Additionally, the verification process implemented the assumption of all heat transferred to the gaseous phase from the environment is passed along to the liquid phase [13]. This assumption greatly simplifies the model and aids in quickly producing preliminary power requirements for the tank and vaporiser. However, the implementation of tank stratification is required for further detailed analysis of the tank self-pressurisation and power requirements.

## 5.3. RECOMMENDATIONS FOR FUTURE WORK

Despite the limitations of the work in the thesis, the findings open a wide variety of avenues for further research that can build upon the framework developed in this work. A few of the possibilities are explored below. The main recommendation that can be implemented to expand directly on the work performed is related to the utilisation of different optimisation algorithms and investigating their effect on the final converged solution. In particular the utilisation of global optimisation algorithms could be used to provide an improved initialisation point for a local optimisation. This combination ensures that the converged solution will be as close as possible to the global optimum. However, this is much more computationally intensive than just using local algorithms.

The analysis of other test cases can also be of great value, especially when considering different mass flow rate requirements. This could be done for smaller aircraft such as for business jets, or for long-range aircraft. However for this to be performed, a preliminary analysis of the missions should be performed in addition to an individual sizing for the components.

The implementation of high fidelity fluid simulations can provide detailed insight into its behaviour in different components of the system. Modelling the stratification of hydrogen in the tank and vaporiser is of great importance when simulating the heat transfer inside the tank and with the environment, and can lead to more accurate values for the tank power and pressure computations. The analysis of fluid flow within the pipes using Computational Fluid Dynamics (CFD) simulations can also provide more accurate information on its temperature and pressure changes and the possible impact of two-phase flow. Similarly, high fidelity CFD simulations can be used to more accurately model the heat transfer and pressure drops in the heat exchanger. These high fidelity models and the lower fidelity analytical models used in this work can also be validated in the future by performing small-scale lab experiments.

The coupled sizing of the fuel cell supply architecture with the electric propulsion system can be also be performed. The framework so far only takes into account the fuel and air utilisation parameters to model the inefficiencies of the fuel cell. Combining this with the sizing of the electric propulsion system components and taking into account their inefficiencies will reflect on the sizing of the fuel cell supply architecture components. The next step would then be determining the effect of the two systems on the aircraft level and generating an iterative design process for the system and aircraft sizings. Future research can also be performed in the field of the control and operations of both systems, for example by simulating the response times of both systems to throttle input and maintaining the required pressure levels in more complex fuel cell supply architectures.

Finally, it is recommended to investigate the feasibility of cryogenic piston pumps for aviation applications, as the impact of the cryogenic conditions could have undesired effects on regarding their operation and maintenance. This requires high fidelity modelling of the pumps with regards to sizing, cavitation, and their effect on heating up the liquid hydrogen in the tank.

# BIBLIOGRAPHY


[1] V. Grewe, A. Gangoli Rao, T. Grönstedt, C. Xisto, F. Linke, J. Melkert, J. Middel, B. Ohlenforst, S. Blakey, S. Christie, S. Matthes, and K. Dahlmann, *Evaluating the climate impact of aviation emission scenarios towards the paris agreement including covid-19 effects,* Nature communications **12**, 3841 (2021).

[2] D. S. Lee, D. W. Fahey, A. Skowron, M. R. Allen, U. Burkhardt, Q. Chen, S. J. Doherty, S. Freeman, P. M. Forster, J. Fuglestvedt, A. Gettelman, R. R. de León, L. L. Lim, M. T. Lund, R. J. Millar, B. Owen, J. E. Penner, G. Pitari, M. J. Prather, R. Sausen, and L. J. Wilcox, *The contribution of global aviation to anthropogenic climate forcing for 2000 to 2018,* Atmospheric environment (Oxford, England : 1994) **244**, 117834 (2021).

[3] European Commission, Directorate-General for Mobility, Transport, Directorate-General for Research, and Innovation, *Flightpath 2050 : Europe's vision for aviation : maintaining global leadership and serving society's needs* (Publications Office, 2011).

[4] B. J. Brelje and J. R. Martins, *Electric, hybrid, and turboelectric fixed-wing aircraft: A review of concepts, models, and design approaches,* Progress in Aerospace Sciences **104**, 1 (2019).

[5] S. Kazula, M. Staggat, S. de Graaf, T. Geyer, A. Link, D. Keller, J. Ramm, and M. Pick, *Can sofc-systems power electric regional aircraft in 2050? - the dlr-project h2eat,* (In Press).

[6] G. Onorato, *Fuel tank integration for hydrogen airliners,* (2021).

[7] G. Vonhoff, *Conceptual Design of Hydrogen Fuel Cell Aircraft: Flying on hydrogen for a more sustainable future,* (2021).

[8] M. G. Millis, R. T. Tornabene, J. M. Jurns, M. D. Guynn, T. M. Tomsik, and T. J. V. Overbeke, *Hydrogen fuel system design trades for high-altitude long-endurance remotely- operated aircraft,* (2009).

[9] R. O'Hayre, S.-W. Cha, W. Colella, and F. B. Prinz, *Fuel Cell Fundamentals* (John Wiley & Sons, 2016).

[10] S. Kazula, S. de Graaf, and L. Enghardt, *Review of fuel cell technologies and evaluation of their potential and challenges for electrified propulsion systems in commercial aviation,* Journal of the Global Power and Propulsion Society **7**, 43 (2023).

[11] J. Larminie and A. Dicks, *Fuel cell systems explained*, 2nd ed. (J. Wiley, Chichester, West Sussex, 2003).

[12] R. F. Barron, *Cryogenic Systems* (Oxford University Press, 1985).

[13] A. J. Colozza, A. Corporation, and B. Park, *Hydrogen storage for aircraft applications overview,* (2002).

[14] S. Z. S. Al Ghafri, A. Swanger, V. Jusko, A. Siahvashi, F. Perez, M. L. Johns, and E. F. May, *Modelling of liquid hydrogen boil-off,* **15**, 1149 (2022), number: 3 Publisher: Multidisciplinary Digital Publishing Institute.

[15] ASME B36.10M-2015, *Welded and Seamless Wrought Steel Pipes*, Standard (The American Society of Mechanical Engineers, New York, USA, 2015).

[16] N. J. Aavik, *Theoretical analysis of pipe flow during liquid hydrogen bunkering,* (2022).

[17] E. S. Menon, *Gas Pipeline Hydraulics*, 0th ed. (CRC Press, 2005).

[18] P. M. Coelho and C. Pinho, *Considerations about equations for steady state flow in natural gas pipelines,* Journal of the Brazilian Society of Mechanical Sciences and Engineering **29**, 262 (2007).

[19] H. Kudela, *Hydraulic losses in pipes,* Wroclas University of Science and (2012).

[20] S. Moran, *Bridging the Gap Between Theory and Practice,* Back to Basics (2016).

[21] D. W. Green and M. Z. Southard, eds., *Perry's chemical engineers' handbook*, ninth edition, 85th anniversary edition ed. (McGraw Hill Education, New York, 2019).

[22] E. Rothuizen, B. Elmegaard, and M. Rokni, *Dynamic simulation of the effect of vehicle-side pressure loss of hydrogen fueling process,* International Journal of Hydrogen Energy **45**, 9025 (2020).

[23] S. Kuczyński, M. Łaciak, A. Olijnyk, A. Szurlej, and T. Włodek, *Thermodynamic and Technical Issues of Hydrogen and Methane-Hydrogen Mixtures Pipeline Transmission,* Energies **12**, 569 (2019).

[24] R. Rayner, *Centrifugal pump nomenclature, characteristics and components,* in *Pump Users Handbook* (Elsevier, 1995) pp. 39–110.

[25] J. F. Gülich, *Centrifugal Pumps* (Springer International Publishing, Cham, 2020).

[26] J. E. Miller, *The reciprocating pump: Theory, design, and use*, 2nd ed. (Krieger Pub. Co, Malabar Fla., 1995).

[27] A. C. Ugural and S. K. Fenster, *Advanced mechanics of materials and elasticity*, 5th ed. (Prentice Hall, Upper Saddle River NJ, 2011).

[28] V. Bahrs, M. Staggat, and L. Enghardt, *Analytical model for electric machine sizing in electrified aviation,* (2021).

[29] S. Bhapkar and S. Kazula, *Development of a predictive model for the preliminary design of heat exchangers in electric aviation,* in *DEUTSCHER LUFT- UND RAUMFAHRTKONGRESS 2023* (2023).

[30] R. K. Shah and D. P. Sekulic, *Fundamentals of Heat Exchanger Design* (John Wiley & Sons, 2003) google-Books-ID: beSXNAZblWQC.

[31] X. Zhang, H. Keramati, M. Arie, F. Singer, R. Tiwari, A. Shooshtari, and M. Ohadi, *Recent developments in high temperature heat exchangers: A review,* Frontiers in Heat and Mass Transfer **11** (2018), 10.5098/hmt.11.18.

[32] S. Kakac, H. Liu, and A. Pramuanjaroenkij, *HEAT EXCHANGERS: Selection, rating, and thermal design, fourth edition* (CRC Press, [Place of publication not identified], 2020).

[33] J. van Buijtenen, W. Visser, and A. Rao, *Aero engine technology, ae4-238,* (2021).

[34] I. H. Bell, J. Wronski, S. Quoilin, and V. Lemort, *Pure and pseudo-pure fluid thermophysical property evaluation and the open-source thermophysical property library coolprop,* Industrial & Engineering Chemistry Research **53**, 2498 (2014), http://pubs.acs.org/doi/pdf/10.1021/ie4033999 .

[35] B. Boden, J. Flink, N. Först, R. Mischke, K. Schaffert, A. Weinert, A. Wohlan, and A. Schreiber, *Rce: An integration environment for engineering and science,* SoftwareX **15**, 100759 (2021).

[36] A. B. Lambe and J. R. R. A. Martins, *Extensions to the design structure matrix for the description of multidisciplinary design, analysis, and optimization processes,* Structural and Multidisciplinary Optimization **46**, 273 (2012).

[37] B. Adams, W. Bohnhoff, K. Dalbey, M. Ebeida, J. Eddy, M. Eldred, R. Hooper, P. Hough, K. Hu, J. Jakeman, M. Khalil, K. Maupin, J. Monschke, E. Ridgway, A. Rushdi, D. Seidl, J. Stephens, and J. Winokur, *Dakota, a multilevel parallel object-oriented framework for design optimization, parameter estimation, uncertainty quantification, and sensitivity analysis: Version 6.13 user's manual,* (2020).

[38] M. Frings, B. Berkels, M. Behr, and S. Elgeti, *Comparison of optimization algorithms for the slow shot phase in hpdc,* (Author(s), 2018) p. 110005.

[39] A. Tröltzsch, M. Siggel, A. Kopp, and T. Schwanekamp, *Multidisciplinary analysis of the dlr spaceliner concept by different optimization techniques,* in *5th European Conference on Computational Mechanics*, edited by E. Onate, J. Oliver, and A. Huerta (International Center for Numerical Methods in Engineering, 2014).

[40] F. Madani Sani, S. Huizinga, K. A. Esaklul, and S. Nesic, *Review of the api rp 14e erosional velocity equation: Origin, applications, misuses, limitations and alternatives,* Wear **426-427**, 620 (2019).

[41] SPECIAL METALS, *Inconel alloy 718,* (2007).

[42] W. L. Luyben and K. Tuzla, *Gas pressure-drop experiment,* Chemical Engineering Education **44**, 183 (2010).

[43] A. Chen and P. K. Sen, *Advancement in battery technology: A state-of-the-art review,* in *2016 IEEE Industry Applications Society Annual Meeting* (2016) pp. 1–10.

[44] F. Adamčík and M. Schrotter, *Changes of on-board power systems of modern aircraft in the context of wider electrification,* Advances in Military Technology **14**, 71 (2019).

[45] M. Fioriti, F. Di Fede, S. Corpino, P. Iodice, G. Cerino, *et al.*, *On-board system architectures for hybrid/all-electric regional aircraft,* in *32nd Congress of the International Council of the Aeronautical Sciences, ICAS 2021* (International Council of the Aeronautical Sciences, 2021) p. 32.

[46] D. A. Tortorelli and P. Michaleris, *Design sensitivity analysis: Overview and review,* Inverse Problems in Engineering **1**, 71 (1994).

[47] P. J. Singh, N. K. Madavan, *et al.*, *Complete analysis and simulation of reciprocating pumps including system piping,* in *Proceedings of the 4th International Pump Users Symposium* (Turbomachinery Laboratories, Department of Mechanical Engineering, Texas A&M . . . , 1987).

[48] P. Linstrom, *Nist chemistry webbook, nist standard reference database 69,* (1997).

# A

# ASME Pipe Thicknesses

Table A.1 contains the ASME standard thicknesses for stainless steel pipes [15].

Table A.1: Standard thicknesses for different pipe schedules based on ASME Code B36.10M [15]

| N.D. (In.) | O.D. (In.) | 5 | 10 | 20 | 30 | 40 | STD | 60 | 80 | XH | 100 | 120 | 140 | 160 | XXH |
|---|---|---|---|---|---|---|---|---|---|---|---|---|---|---|---|
| 0.125 | 0.405 | 0.035 | 0.049 | | | 0.068 | 0.068 | | 0.095 | 0.095 | | | | | |
| 0.25 | 0.54 | 0.049 | 0.065 | | | 0.088 | 0.088 | | 0.119 | 0.119 | | | | | |
| 0.375 | 0.675 | 0.049 | 0.065 | | | 0.091 | 0.091 | | 0.126 | 0.126 | | | | | |
| 0.5 | 0.84 | 0.065 | 0.083 | | | 0.109 | 0.109 | | 0.147 | 0.147 | | | | 0.188 | 0.294 |
| 0.75 | 1.05 | 0.065 | 0.083 | | | 0.113 | 0.113 | | 0.154 | 0.154 | | | | 0.219 | 0.308 |
| 1 | 1.315 | 0.065 | 0.109 | | | 0.133 | 0.133 | | 0.179 | 0.179 | | | | 0.25 | 0.358 |
| 1.25 | 1.66 | 0.065 | 0.109 | | | 0.14 | 0.14 | | 0.191 | 0.191 | | | | 0.25 | 0.382 |
| 1.5 | 1.9 | 0.065 | 0.109 | | | 0.145 | 0.145 | | 0.2 | 0.2 | | | | 0.281 | 0.4 |
| 2 | 2.375 | 0.065 | 0.109 | | | 0.154 | 0.154 | | 0.218 | 0.218 | | | | 0.344 | 0.436 |
| 2.5 | 2.875 | 0.083 | 0.12 | | | 0.203 | 0.203 | | 0.276 | 0.276 | | | | 0.375 | 0.552 |
| 3 | 3.5 | 0.083 | 0.12 | | | 0.216 | 0.216 | | 0.3 | 0.3 | | | | 0.438 | 0.6 |
| 3.5 | 4 | 0.083 | 0.12 | | | 0.226 | 0.226 | | 0.318 | 0.318 | | | | | 0.636 |
| 4 | 4.5 | 0.083 | 0.12 | | | 0.237 | 0.237 | 0.281 | 0.337 | 0.337 | | 0.438 | | 0.531 | 0.674 |
| 4.5 | 5 | 0.109 | | | | | 0.247 | | | 0.355 | | | | | 0.71 |
| 5 | 5.563 | 0.109 | 0.134 | | | 0.258 | 0.258 | | 0.375 | 0.375 | | 0.5 | | 0.625 | 0.75 |
| 6 | 6.625 | 0.109 | 0.134 | | | 0.28 | 0.28 | | 0.432 | 0.432 | | 0.562 | | 0.719 | 0.864 |
| 7 | 7.625 | 0.109 | | | | | 0.301 | | | 0.5 | | | | | 0.875 |
| 8 | 8.625 | 0.109 | 0.148 | 0.25 | 0.277 | 0.322 | 0.322 | 0.406 | 0.5 | 0.5 | 0.594 | 0.719 | 0.812 | 0.906 | 0.875 |
| 9 | 9.625 | 0.134 | | | | | 0.342 | | | 0.5 | | | | | |
| 10 | 10.75 | 0.134 | 0.165 | 0.25 | 0.307 | 0.365 | 0.365 | 0.5 | 0.594 | 0.5 | 0.719 | 0.844 | 1 | 1.125 | |
| 11 | 11.75 | 0.156 | | | | | 0.375 | | | 0.5 | | | | | |
| 12 | 12.75 | 0.156 | 0.18 | 0.25 | 0.33 | 0.406 | 0.375 | 0.562 | 0.688 | 0.5 | 0.844 | 1 | 1.125 | 1.312 | |
| 14 | 14 | 0.156 | 0.25 | 0.312 | 0.375 | 0.438 | 0.375 | 0.594 | 0.75 | 0.5 | 0.938 | 1.094 | 1.25 | 1.406 | |
| 16 | 16 | 0.165 | 0.25 | 0.312 | 0.375 | 0.5 | 0.375 | 0.656 | 0.844 | 0.5 | 1.031 | 1.219 | 1.437 | 1.594 | |
| 18 | 18 | 0.165 | 0.25 | 0.312 | 0.438 | 0.562 | 0.375 | 0.75 | 0.938 | 0.5 | 1.156 | 1.375 | 1.562 | 1.781 | |
| 20 | 20 | 0.188 | 0.25 | 0.375 | 0.5 | 0.594 | 0.375 | 0.812 | 1.031 | 0.5 | 1.28 | 1.5 | 1.75 | 1.968 | |
| 22 | 22 | 0.188 | 0.25 | 0.375 | 0.5 | | 0.375 | 0.875 | 1.125 | 0.5 | 1.375 | 1.625 | 1.875 | 2.125 | |
| 24 | 24 | 0.218 | 0.25 | 0.375 | 0.562 | 0.688 | 0.375 | 0.969 | 1.219 | 0.5 | 1.531 | 1.812 | 2.062 | 2.344 | |
| 26 | 26 | 0.25 | 0.312 | 0.5 | | | 0.375 | | | 0.5 | | | | | |

# B

# Baseline Optimisation Plots

The remaining results from all the baseline optimisations not presented in the main text are available in this chapter.

## B.1. Gaseous Extraction with Self-Pressurisation

### B.1.1. Mass and Power Optimisation

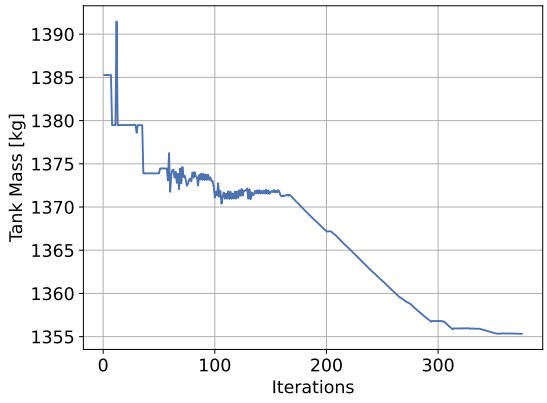


(a) Variation in the mass of the tank.

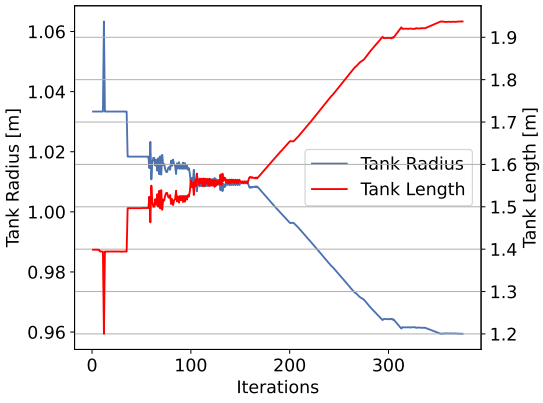


(b) Variation in the total tank dimensions.

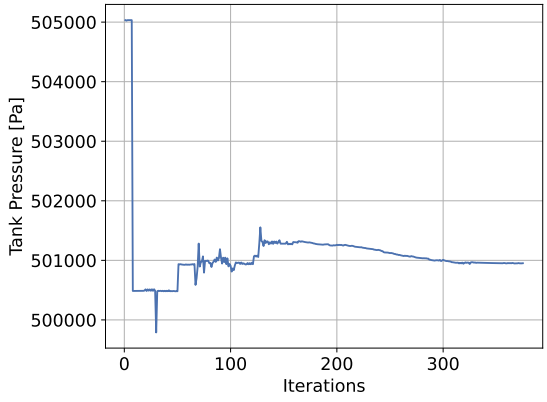


(c) Variation in the tank pressure.

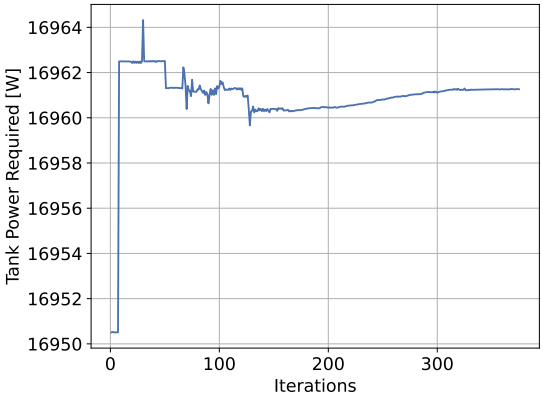


(d) Variation in the tank power required.

Figure B.1: $GH_2$ SP architecture mass and power optimisation: Tank convergence plots

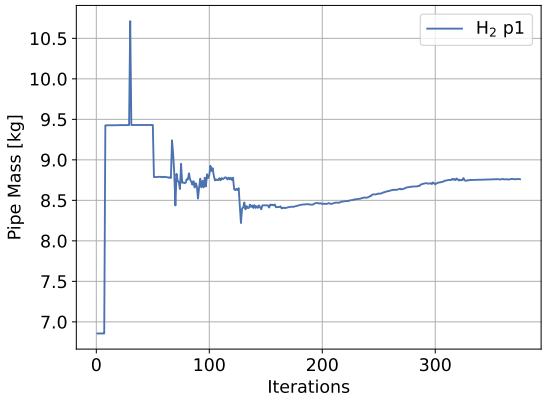


(a) Variation in the hydrogen pipe mass.

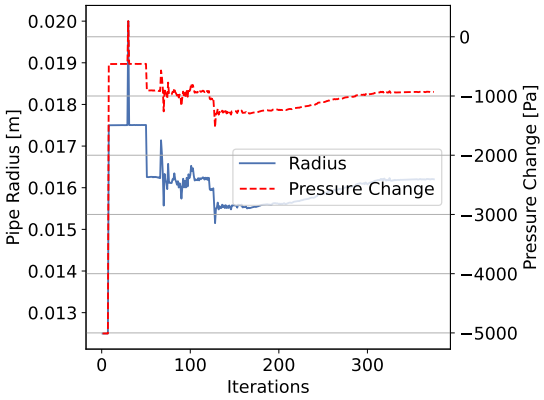


(b) Variation in the radius and pressure change of the hydrogen side pipe.

Figure B.2: $GH_2$ SP architecture mass optimisation: Hydrogen side pipe convergence plots

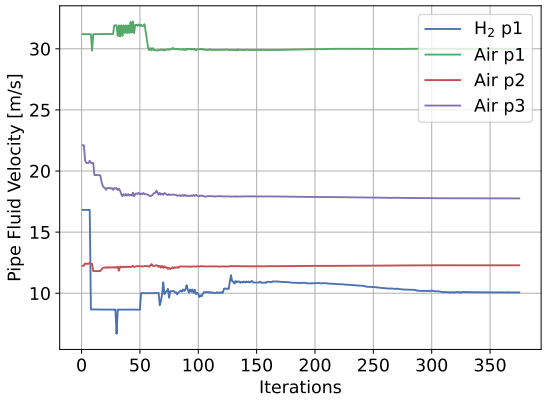


(a) Variation in the maximum fluid velocity in the pipes.

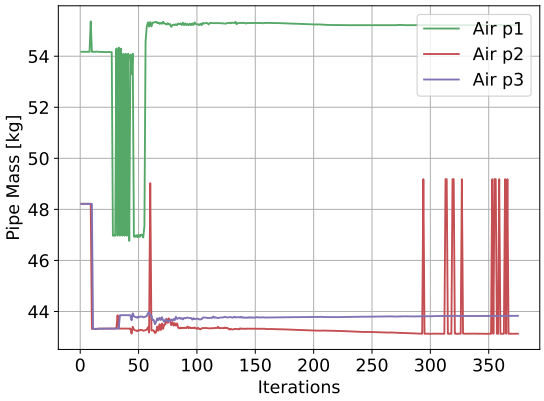


(b) Variation in the mass of the air side pipes.

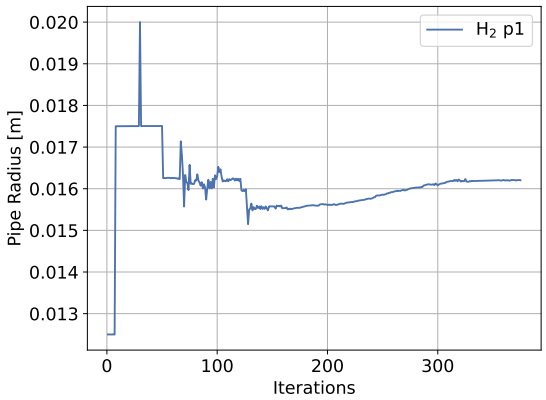


(c) Variation in the radius of the hydrogen side pipes.

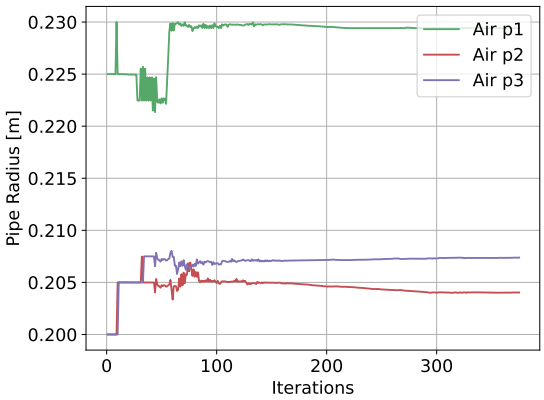


(d) Variation in the radius of the air side pipes.

Figure B.3: $GH_2$ SP architecture mass and power optimisation: Hydrogen and air side pipe convergence plots

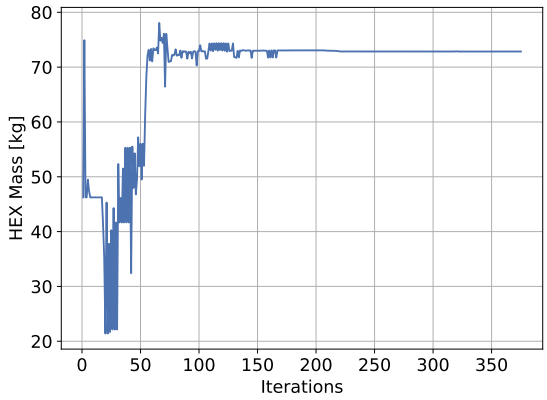


(a) Variation in the mass of the hydrogen heat exchanger.

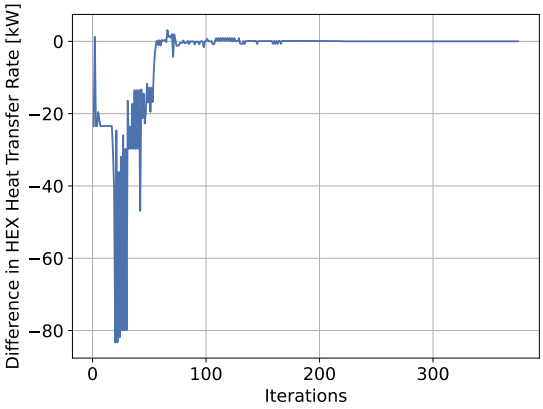


(b) Variation in the difference in the hydrogen heat exchanger heat transfer rate and fluid required heat transfer rate.

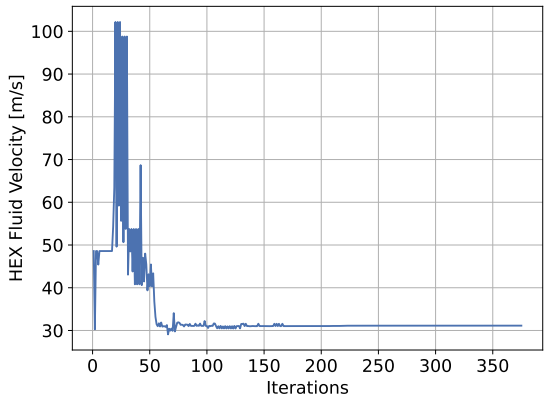


(c) Variation in the fluid velocity in the hydrogen heat exchanger.

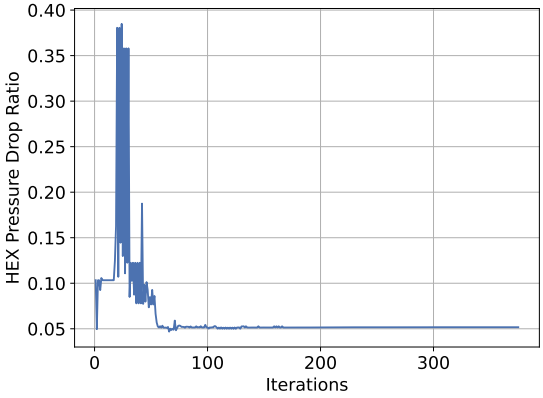


(d) Variation in the hydrogen heat exchanger hot fluid pressure drop ratio.

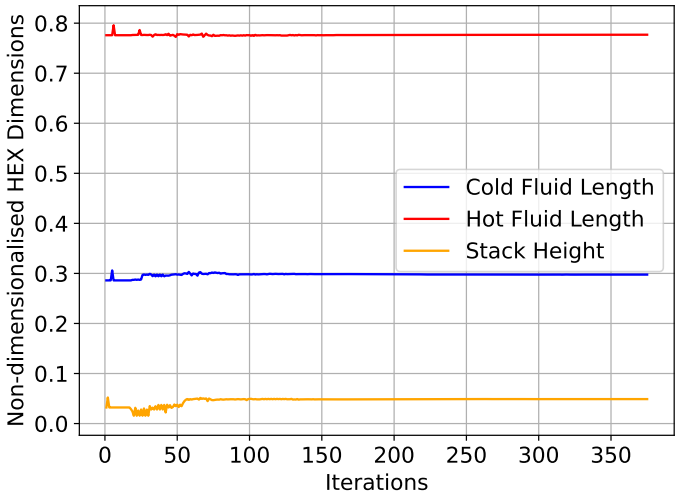


(e) Variation in the Hydrogen heat exchanger non-dimensionalised lengths.

Figure B.4: $GH_2$ SP architecture mass and power optimisation: Hydrogen heat exchanger convergence plots

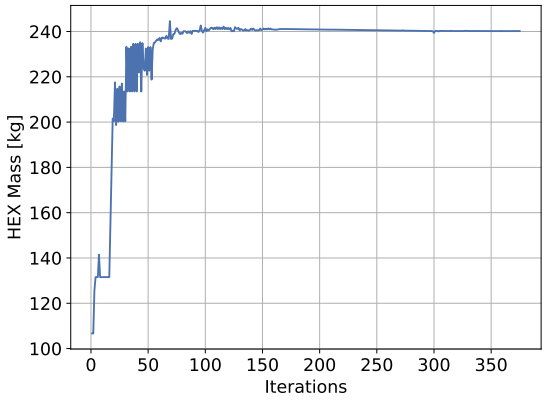


(a) Variation in the mass of the air heat exchanger.

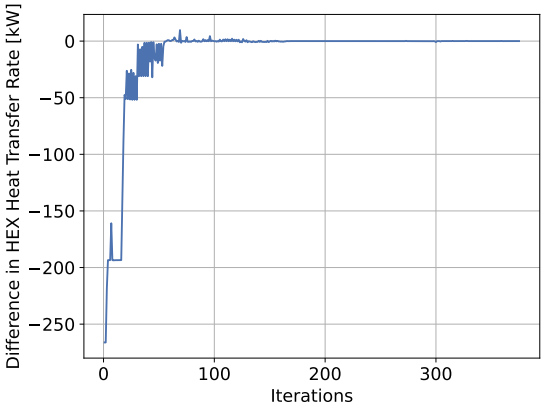


(b) Variation in the difference in the air heat exchanger heat transfer rate and fluid required heat transfer rate.

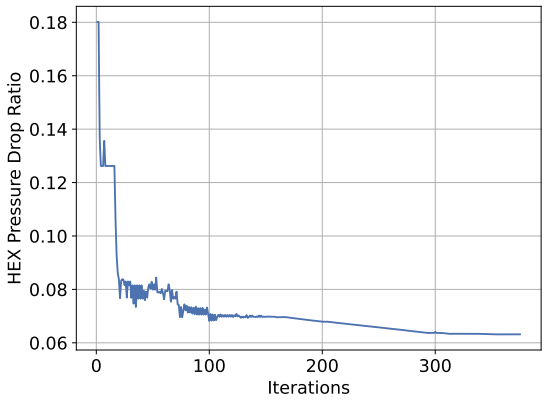


(c) Variation in the air heat exchanger hot fluid pressure drop ratio.

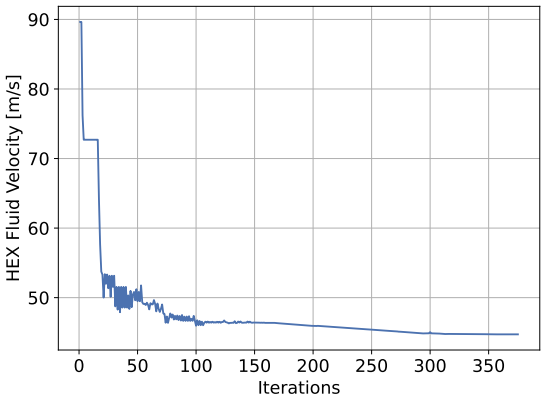


(d) Variation in the hot fluid velocity in the air heat exchanger.

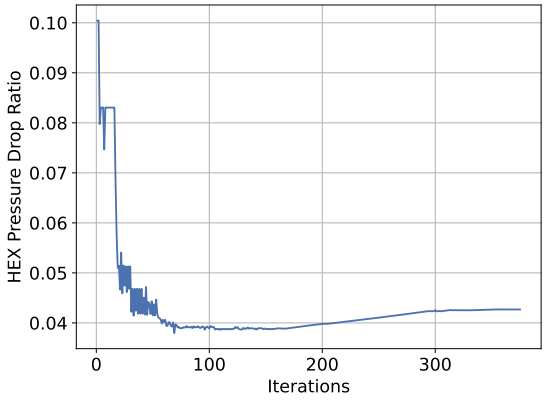


(e) Variation in the air heat exchanger cold fluid pressure drop ratio.

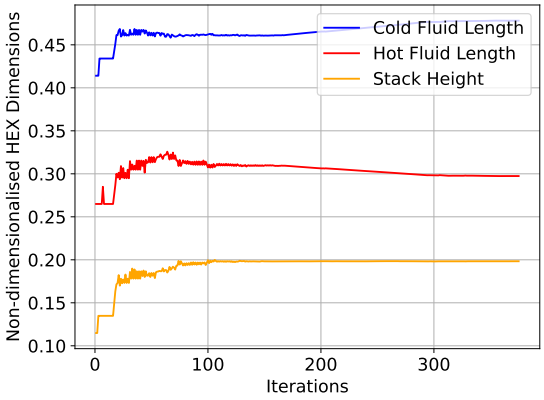


(f) Variation in the air heat exchanger non-dimensionalised lengths.

Figure B.5: $LH_2$ SP architecture mass and power optimisation: Air heat exchanger convergence plots

# B.2. LIQUID EXTRACTION WITH SELF-PRESSURISATION

## B.2.1. MASS OPTIMISATION

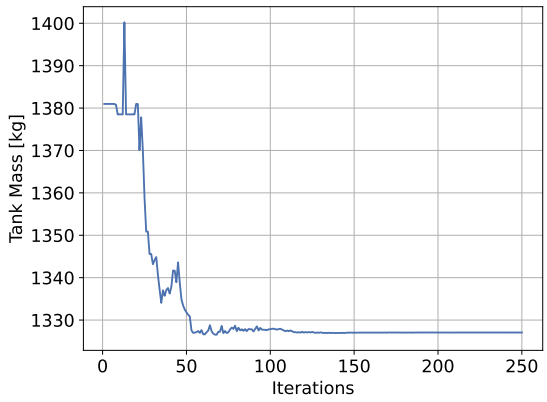


(a) Variation in the mass of the tank.

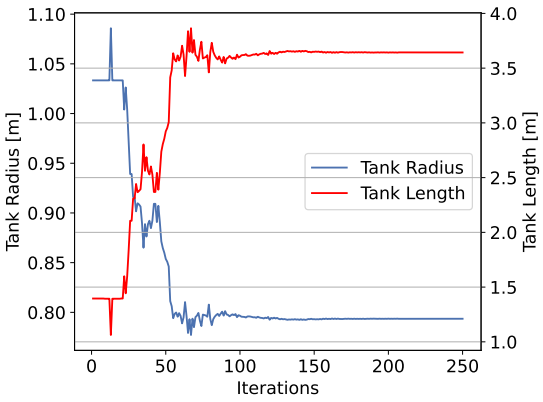


(b) Variation in the total tank dimensions.

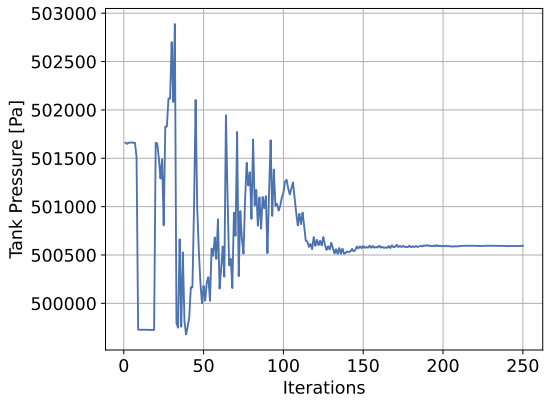


(c) Variation in the tank pressure.

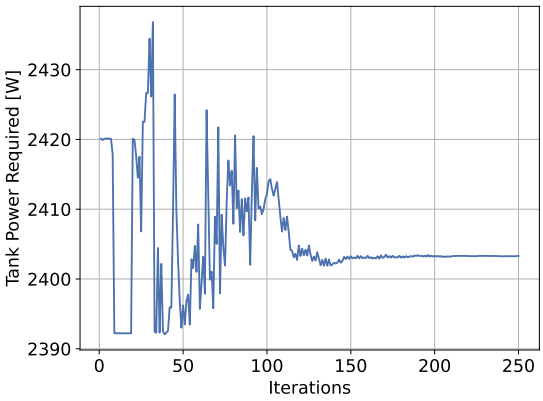


(d) Variation in the tank power required.

Figure B.6: $LH_2$ SP architecture mass and power optimisation: Tank convergence plots

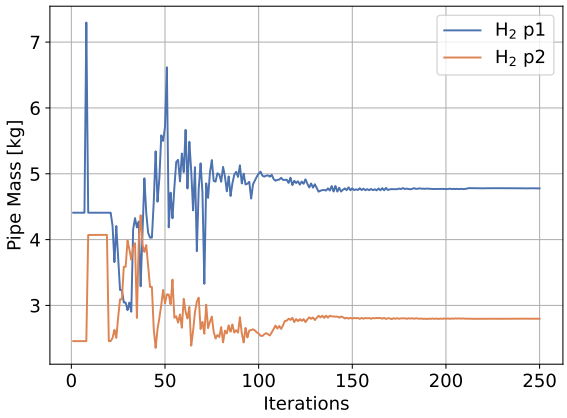


(a) Variation in the hydrogen pipe mass.

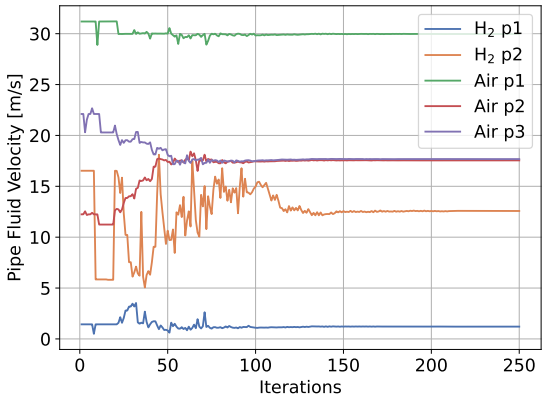


(b) Variation in the maximum fluid velocity in the pipes.

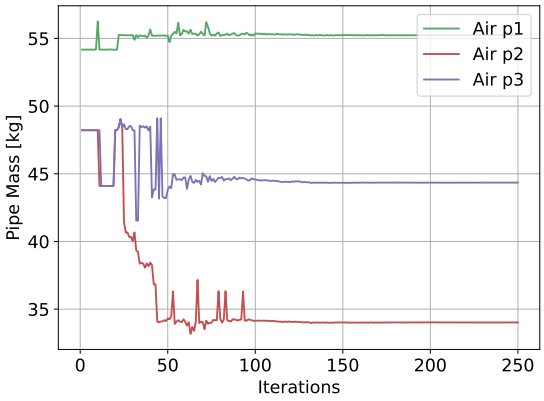


(c) Variation in the mass of the air side pipes.

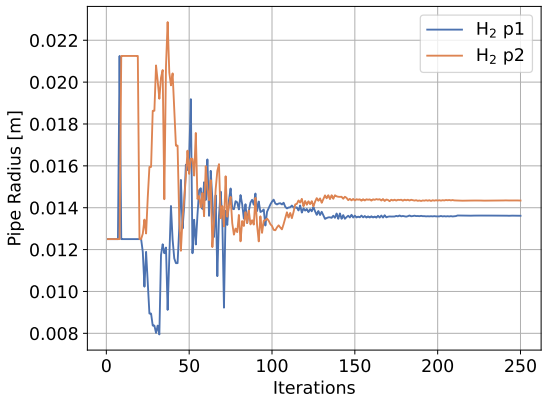


(d) Variation in the radius of the hydrogen side pipes.

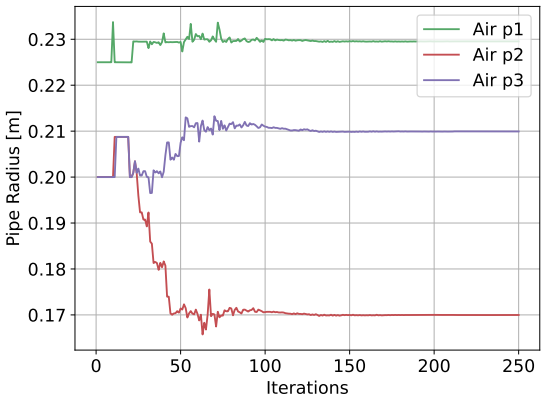


(e) Variation in the radius of the air side pipes.

Figure B.7: $LH_2$ SP architecture mass and power optimisation: Hydrogen and air side pipe convergence plots

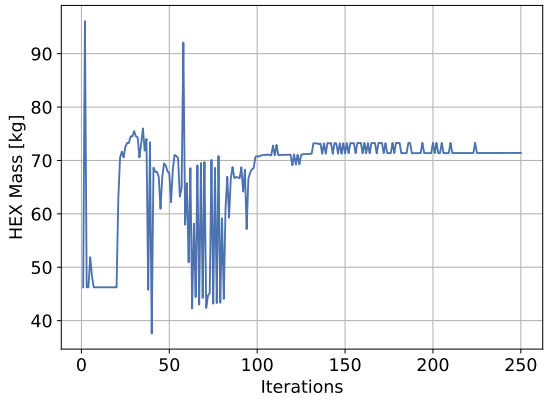


(a) Variation in the mass of the hydrogen heat exchanger.

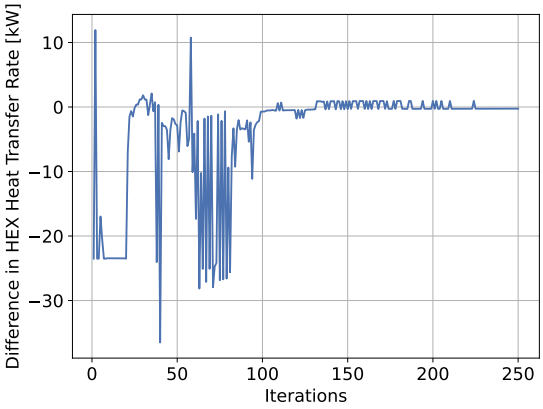


(b) Variation in the difference in the hydrogen heat exchanger heat transfer rate and fluid required heat transfer rate.

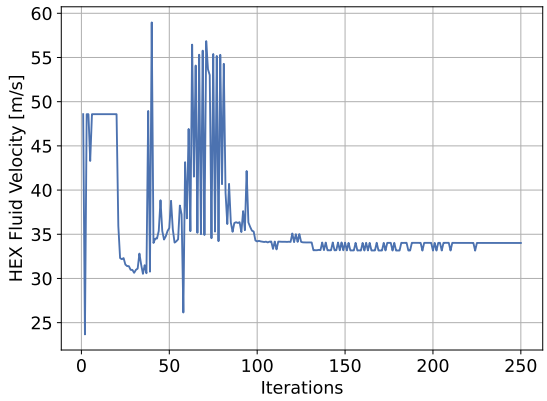


(c) Variation in the fluid velocity in the hydrogen heat exchanger.

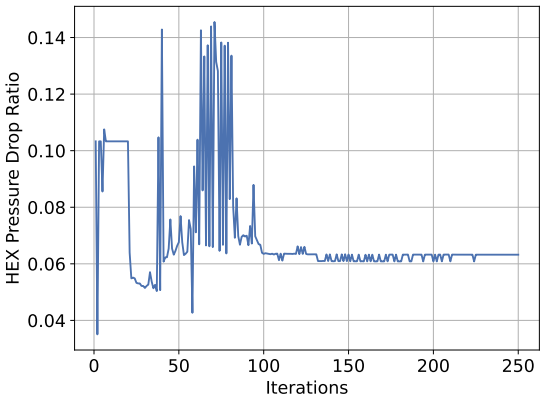


(d) Variation in the hydrogen heat exchanger hot fluid pressure drop ratio.

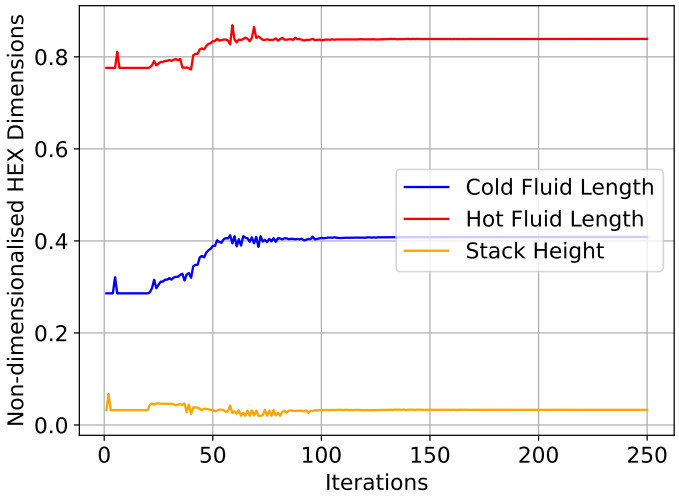


(e) Variation in the Hydrogen heat exchanger non-dimensionalised lengths.

Figure B.8: $LH_2$ SP architecture mass and power optimisation: Hydrogen heat exchanger convergence plots

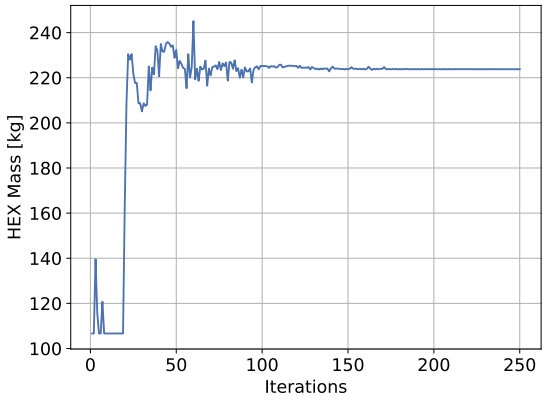


(a) Variation in the mass of the air heat exchanger.

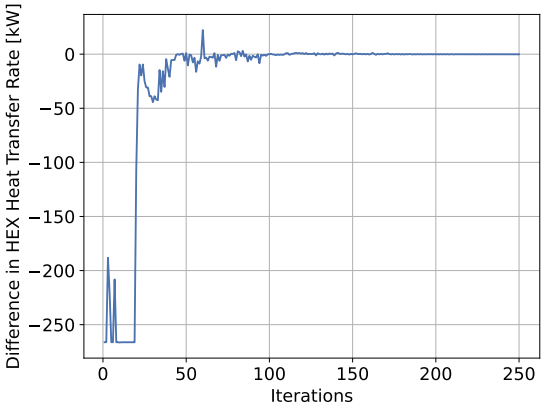


(b) Variation in the difference in the air heat exchanger heat transfer rate and fluid required heat transfer rate.

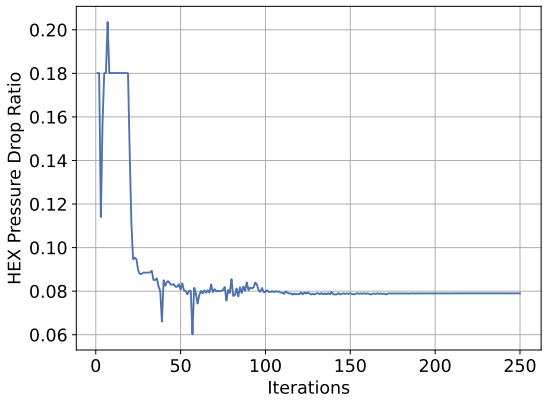


(c) Variation in the air heat exchanger hot fluid pressure drop ratio.

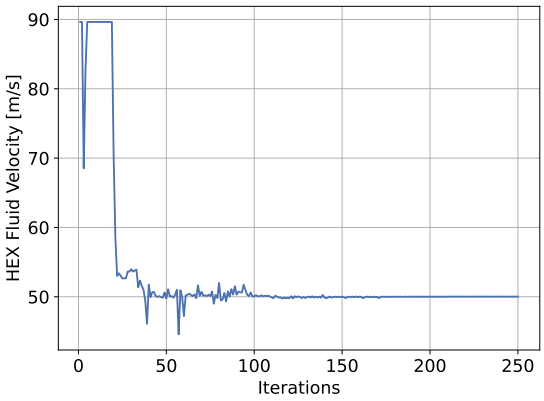


(d) Variation in the hot fluid velocity in the air heat exchanger.

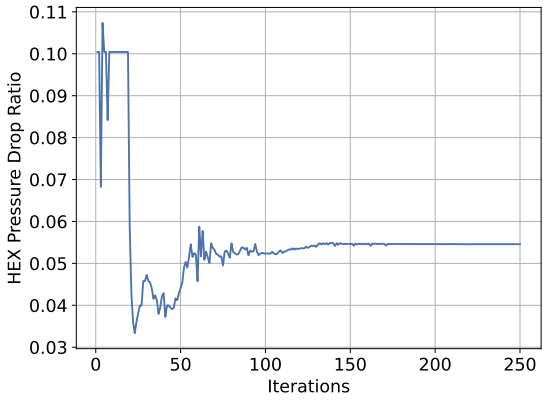


(e) Variation in the air heat exchanger cold fluid pressure drop ratio.

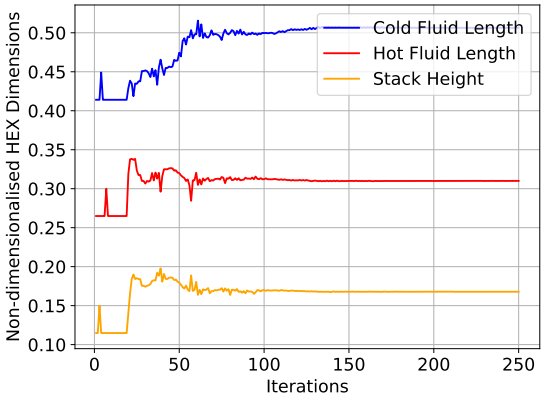


(f) Variation in the air heat exchanger non-dimensionalised lengths.

Figure B.9: $LH_2$ SP architecture mass and power optimisation: Air heat exchanger convergence plots

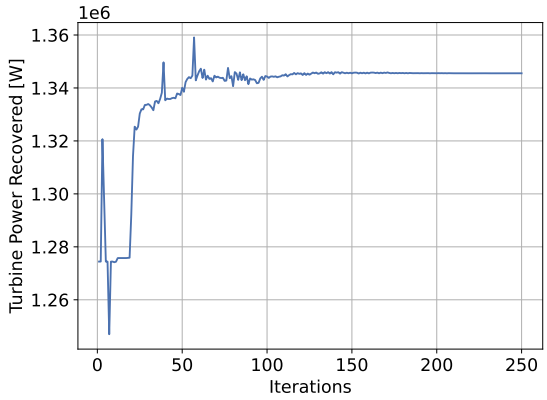


(a) Variation of the power recovered by the turbine.

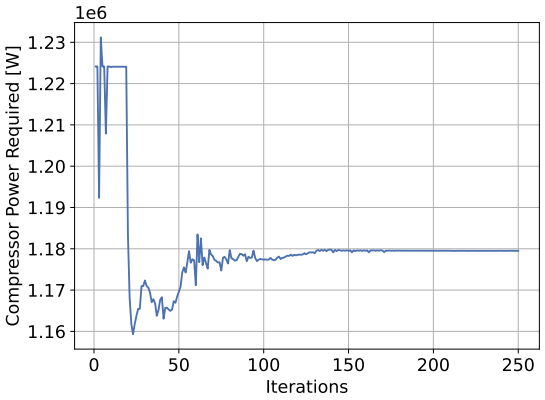


(b) Variation of the power required by the compressor.

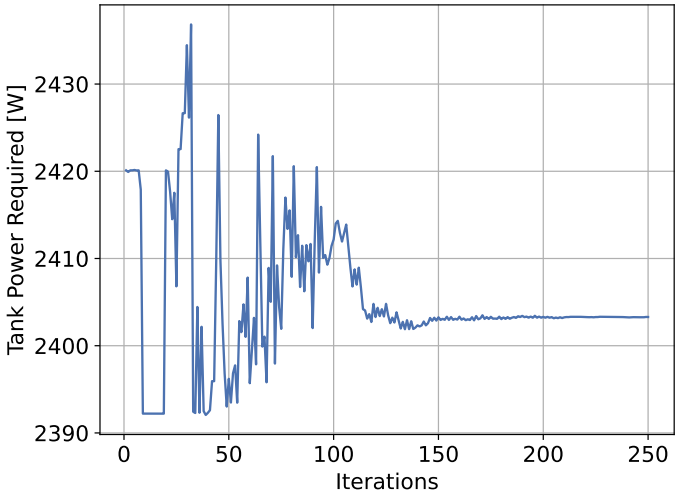


(c) Variation of the power required by the tank.

Figure B.10: $LH_2$ SP architecture mass and power optimisation: Power convergence plots

### B.2.2. MASS AND POWER OPTIMISATION

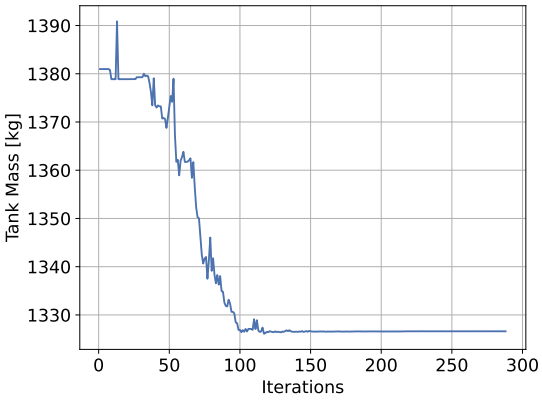


(a) Variation in the mass of the tank.

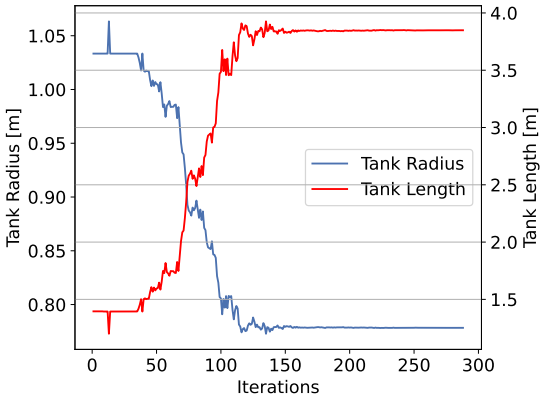


(b) Variation in the total tank dimensions.

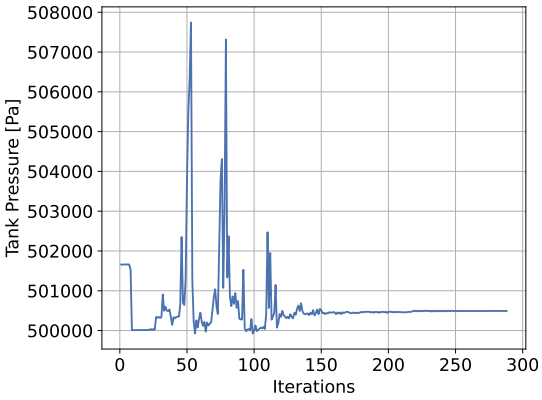


(c) Variation in the tank pressure.

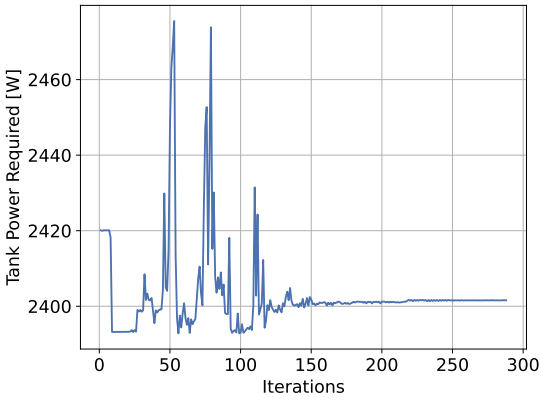


(d) Variation in the tank power required.

Figure B.11: $LH_2$ SP architecture mass and power optimisation: Tank convergence plots

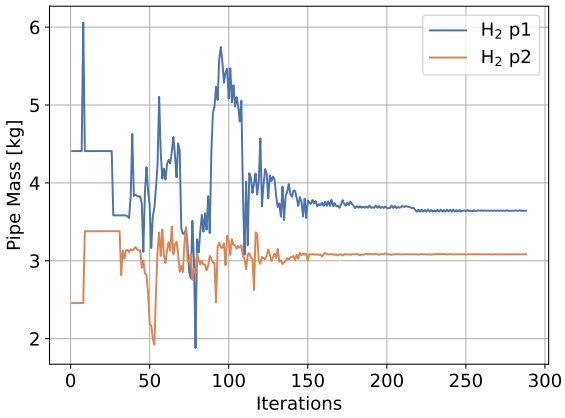


(a) Variation in the hydrogen pipe mass.

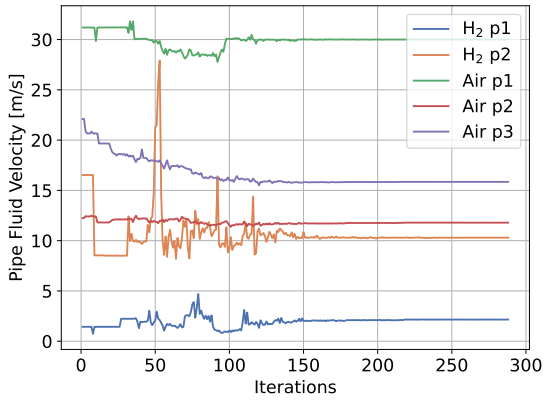


(b) Variation in the maximum fluid velocity in the pipes.

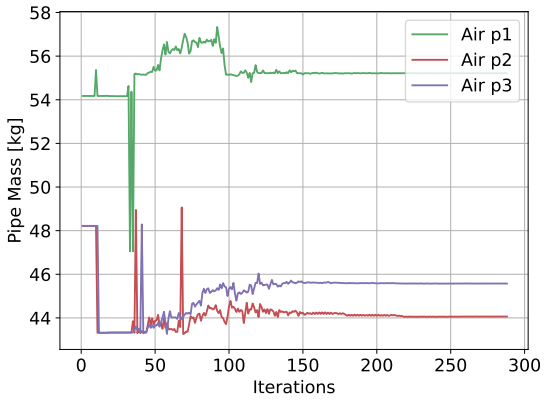


(c) Variation in the mass of the air side pipes.

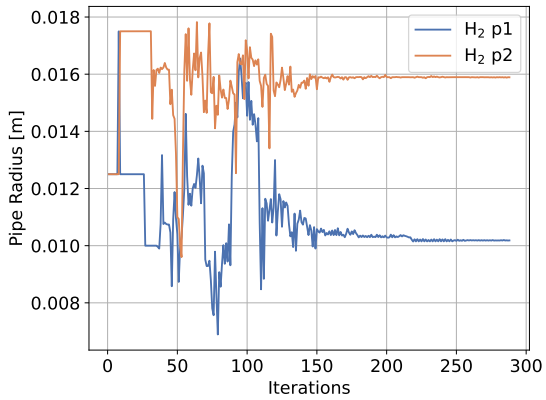


(d) Variation in the radius of the hydrogen side pipes.

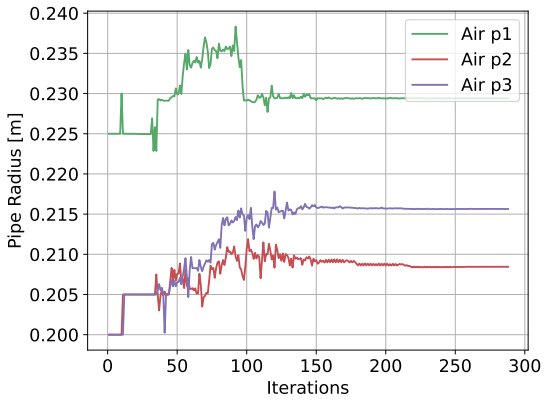


(e) Variation in the radius of the air side pipes.

Figure B.12: $LH_2$ SP architecture mass and power optimisation: Hydrogen and air side pipe convergence plots

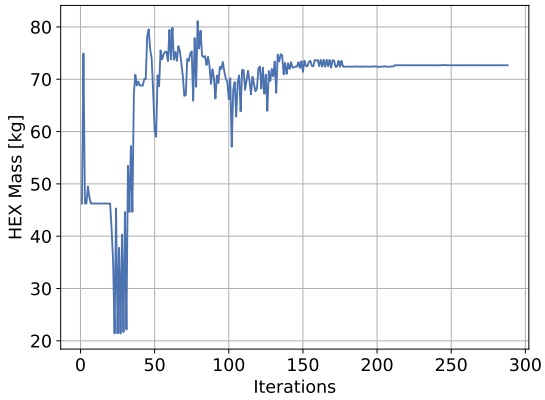


(a) Variation in the mass of the hydrogen heat exchanger.

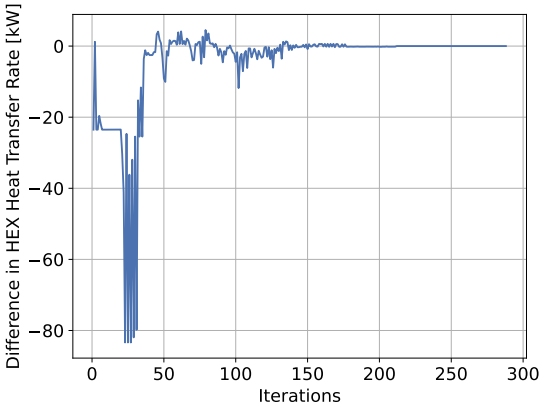


(b) Variation in the difference in the hydrogen heat exchanger heat transfer rate and fluid required heat transfer rate.

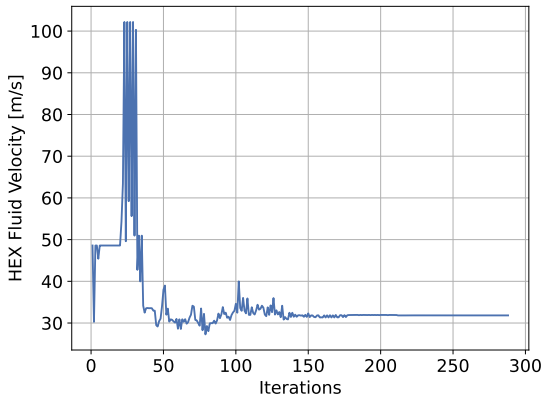


(c) Variation in the fluid velocity in the hydrogen heat exchanger.

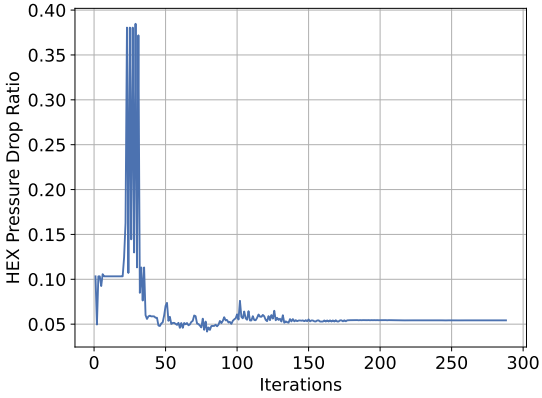


(d) Variation in the hydrogen heat exchanger hot fluid pressure drop ratio.

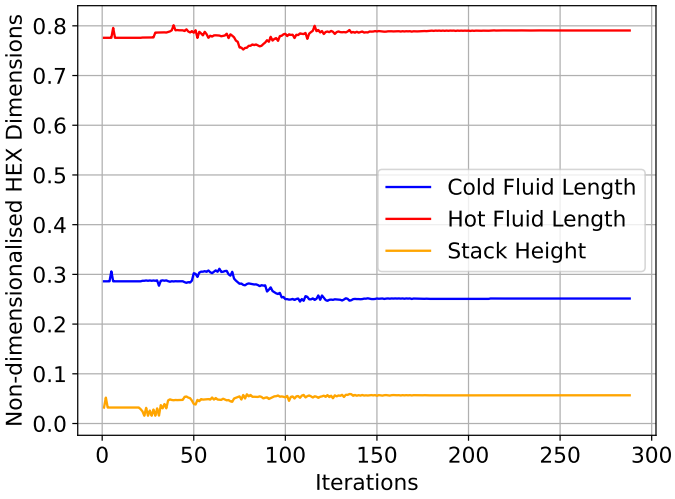


(e) Variation in the Hydrogen heat exchanger non-dimensionalised lengths.

Figure B.13: $LH_2$ SP architecture mass and power optimisation: Hydrogen heat exchanger convergence plots

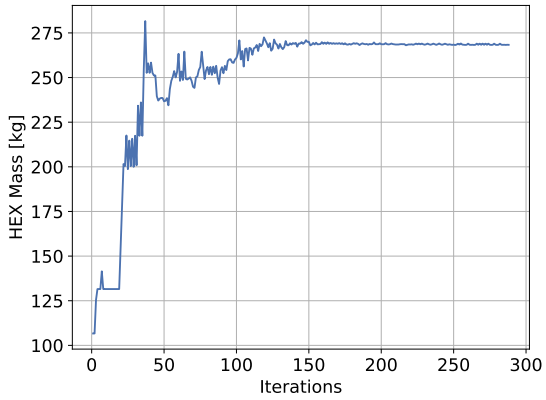


(a) Variation in the mass of the air heat exchanger.

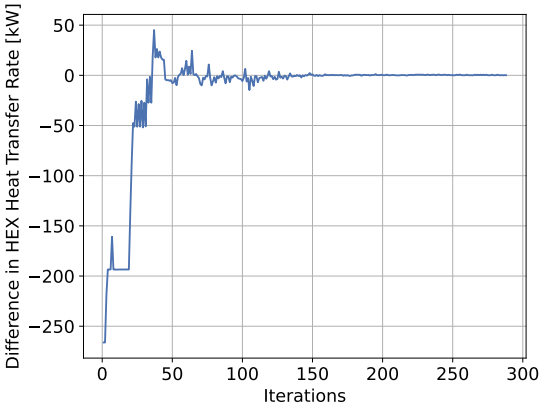


(b) Variation in the difference in the air heat exchanger heat transfer rate and fluid required heat transfer rate.

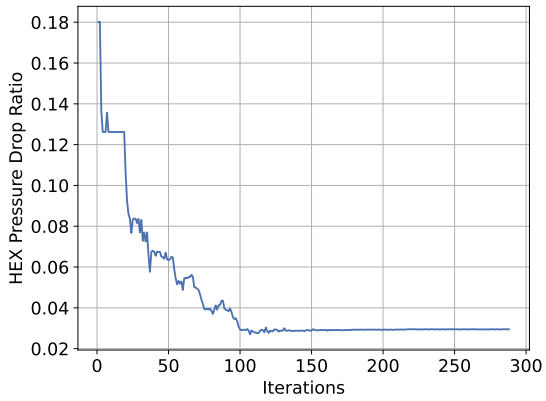


(c) Variation in the air heat exchanger hot fluid pressure drop ratio.

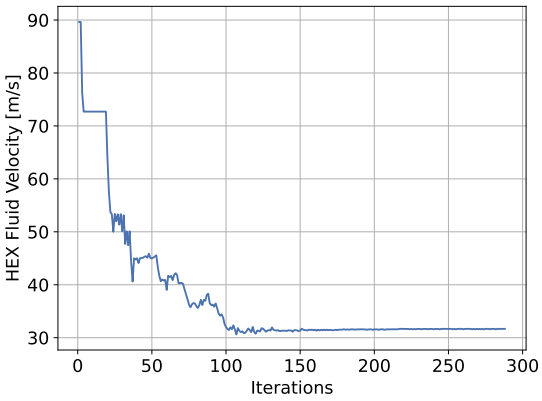


(d) Variation in the hot fluid velocity in the air heat exchanger.

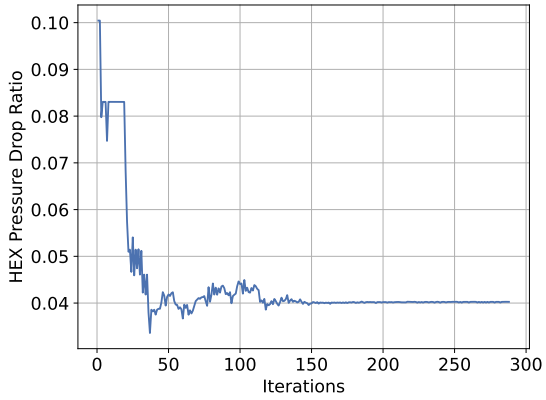


(e) Variation in the air heat exchanger cold fluid pressure drop ratio.

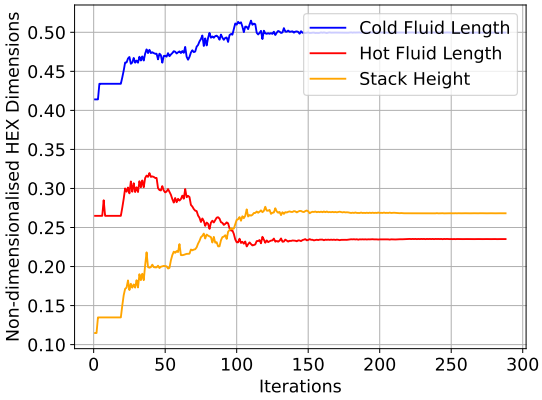


(f) Variation in the air heat exchanger non-dimensionalised lengths.

Figure B.14: $LH_2$ SP architecture mass and power optimisation: Air heat exchanger convergence plots

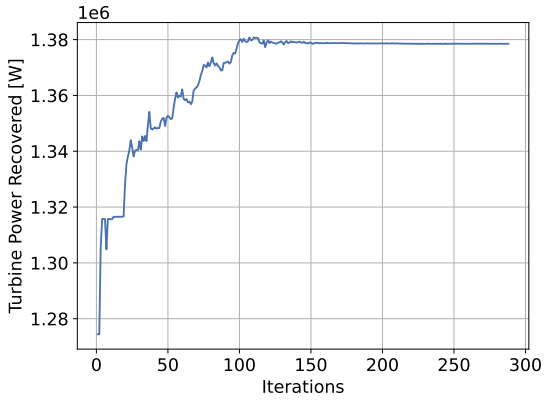


(a) Variation of the power recovered by the turbine.

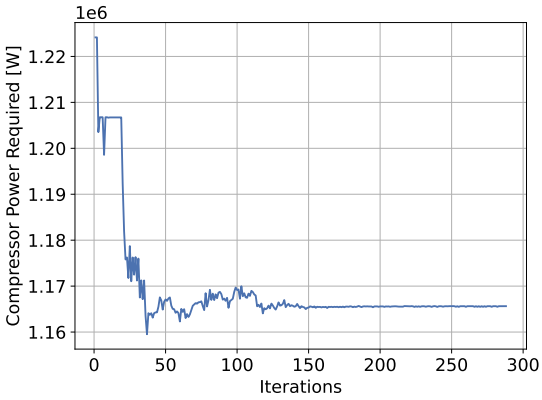


(b) Variation of the power required by the compressor.

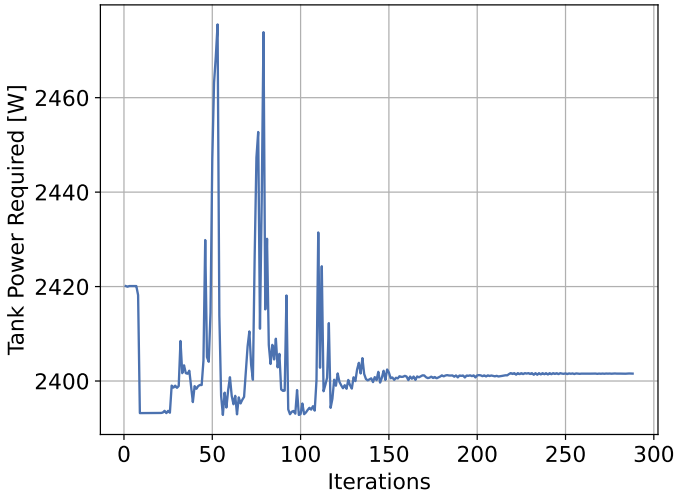


(c) Variation of the power required by the tank.

Figure B.15: $LH_2$ SP architecture mass and power optimisation: Power convergence plots

## B.3. LIQUID EXTRACTION WITH PUMPS

### B.3.1. MASS OPTIMISATION

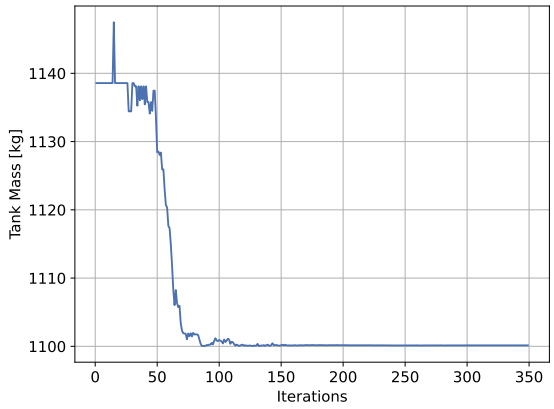


(a) Variation in the mass of the tank.

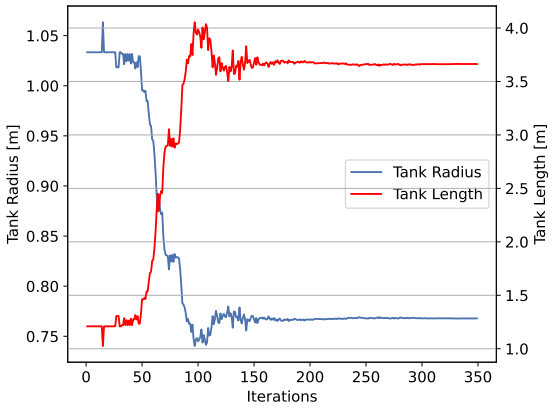


(b) Variation in the total tank dimensions.

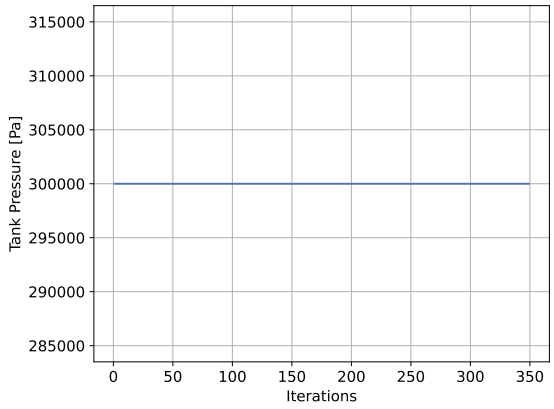


(c) Variation in the tank pressure.

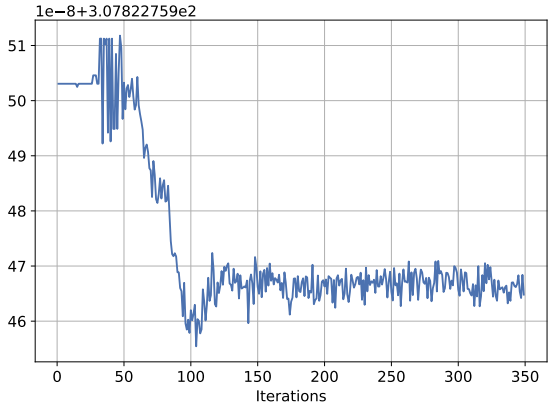


(d) Variation in the tank power required.

Figure B.16: $LH_2$ Pump architecture mass and power optimisation: Tank convergence plots

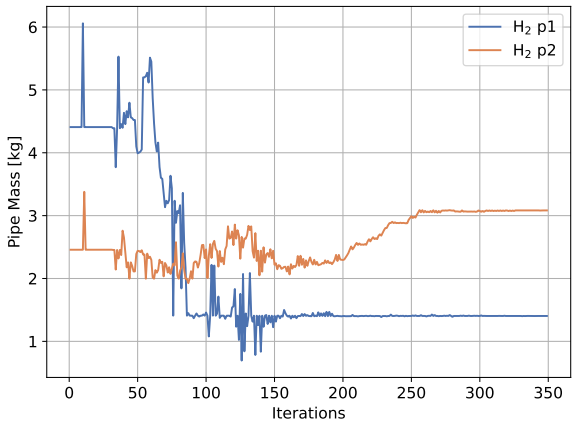


(a) Variation in the hydrogen pipe mass.

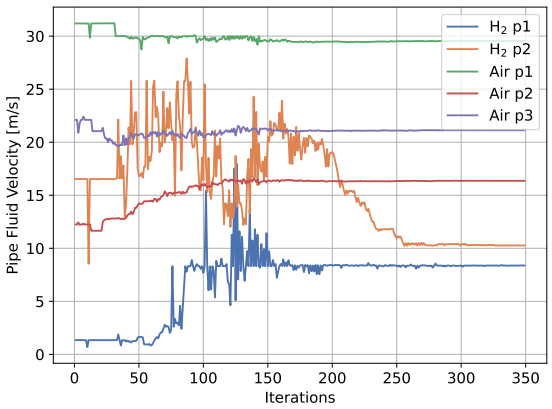


(b) Variation in the maximum fluid velocity in the pipes.

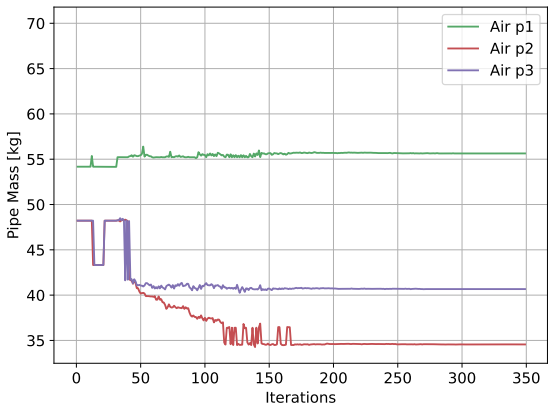


(c) Variation in the mass of the air side pipes.

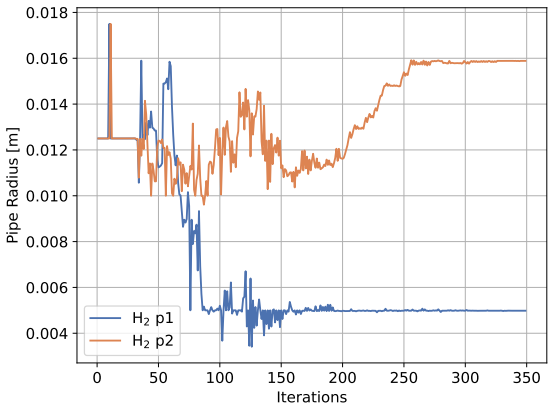


(d) Variation in the radius of the hydrogen side pipes.

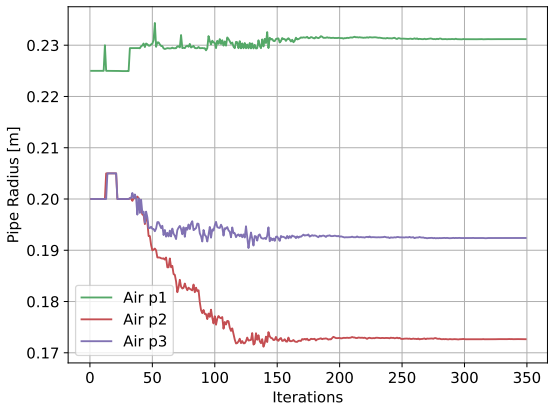


(e) Variation in the radius of the air side pipes.

Figure B.17: $LH_2$ Pump architecture mass and power optimisation: Hydrogen and air side pipe convergence plots

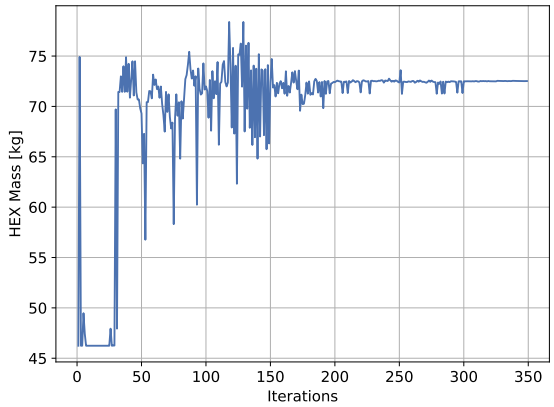


(a) Variation in the mass of the hydrogen heat exchanger.

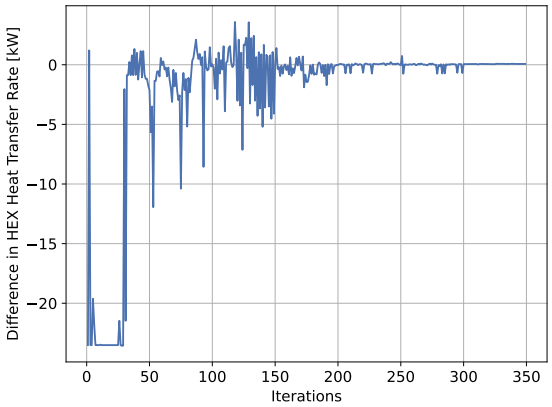


(b) Variation in the difference in the hydrogen heat exchanger heat transfer rate and fluid required heat transfer rate.

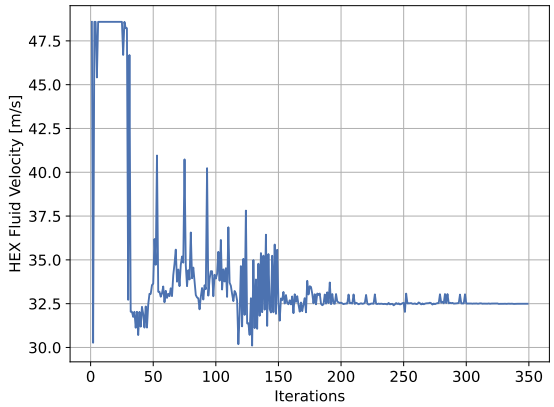


(c) Variation in the fluid velocity in the hydrogen heat exchanger.

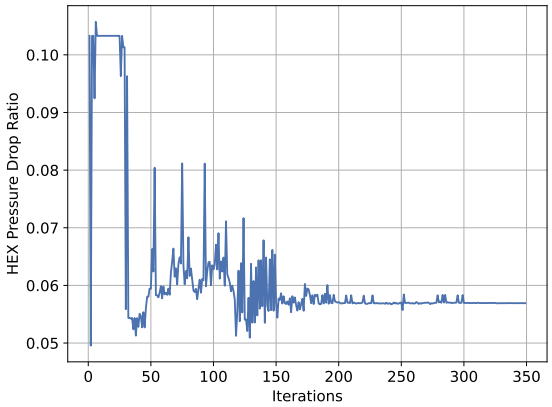


(d) Variation in the hydrogen heat exchanger hot fluid pressure drop ratio.

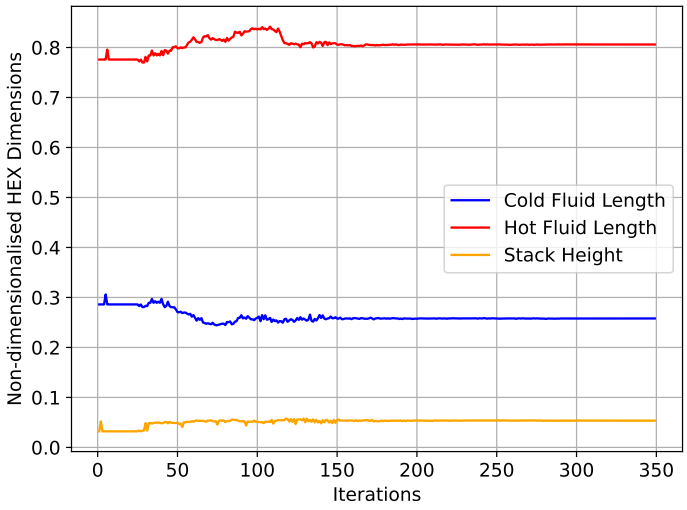


(e) Variation in the Hydrogen heat exchanger non-dimensionalised lengths.

Figure B.18: $LH_2$ Pump architecture mass and power optimisation: Hydrogen heat exchanger convergence plots

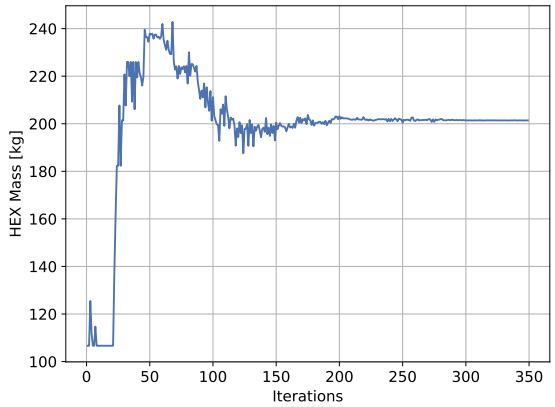


(a) Variation in the mass of the air heat exchanger.

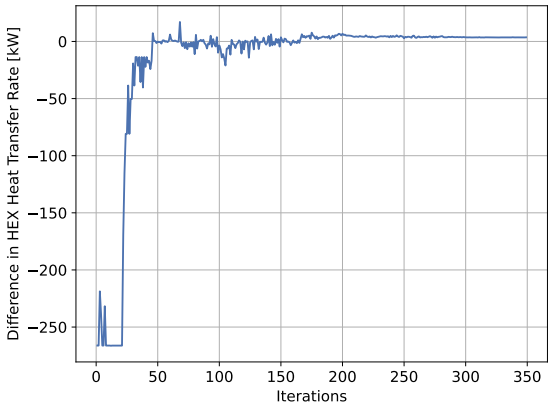


(b) Variation in the difference in the air heat exchanger heat transfer rate and fluid required heat transfer rate.

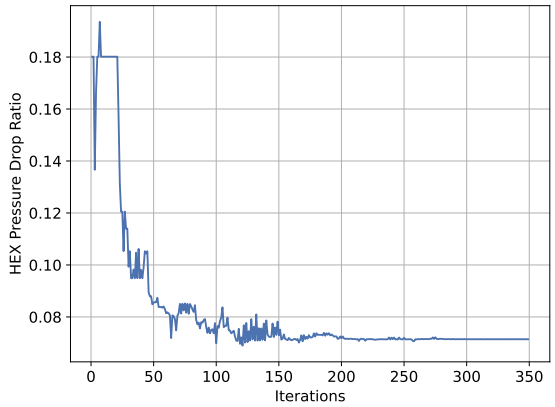


(c) Variation in the air heat exchanger hot fluid pressure drop ratio.

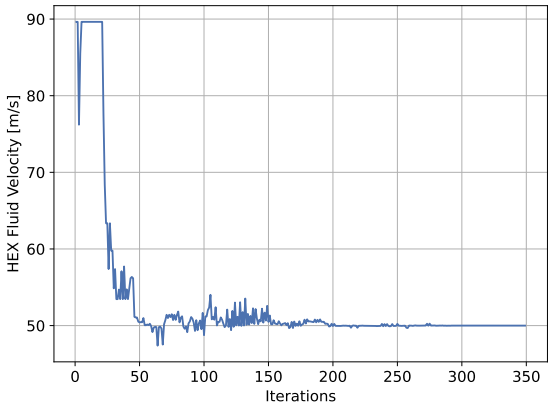


(d) Variation in the hot fluid velocity in the air heat exchanger.

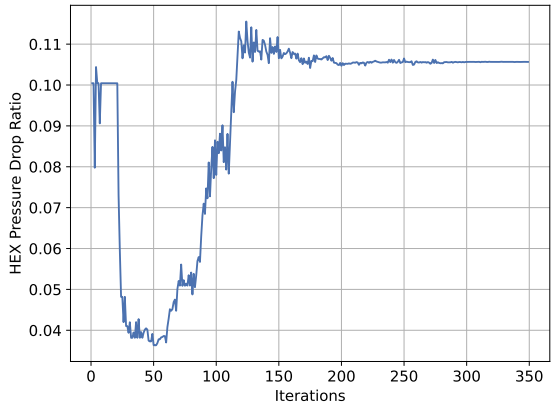


(e) Variation in the air heat exchanger cold fluid pressure drop ratio.

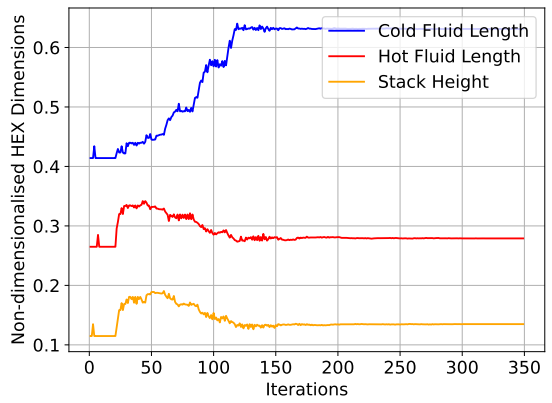


(f) Variation in the air heat exchanger non-dimensionalised lengths.

Figure B.19: $LH_2$ Pump architecture mass and power optimisation: Air heat exchanger convergence plots

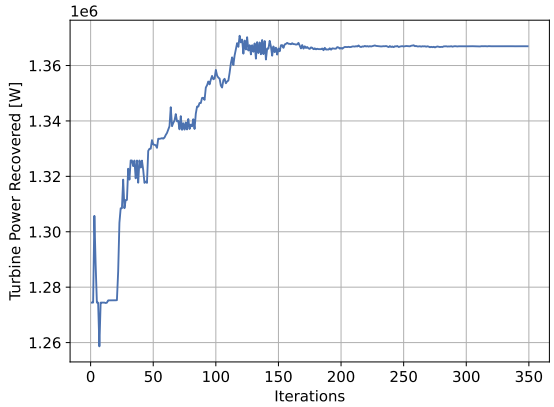


(a) Variation of the power recovered by the turbine.

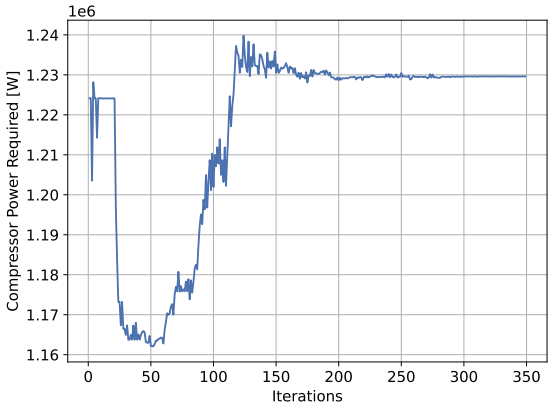


(b) Variation of the power required by the compressor.

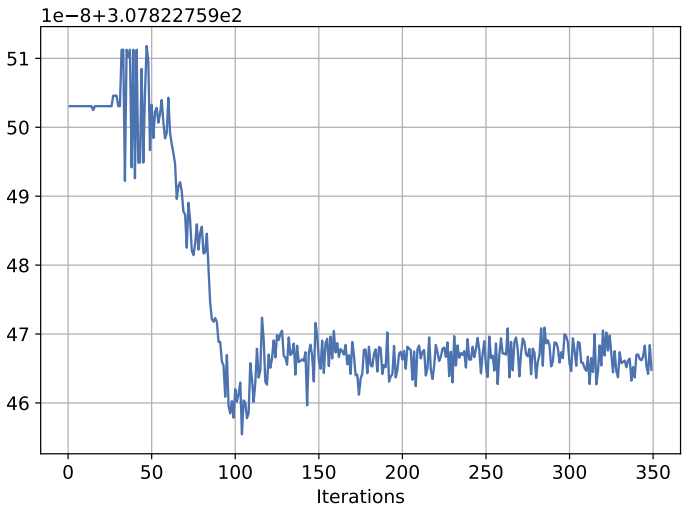


(c) Variation of the power required by the tank.

Figure B.20: $LH_2$ Pump architecture mass and power optimisation: Power convergence plots

### B.3.2. MASS AND POWER OPTIMISATION

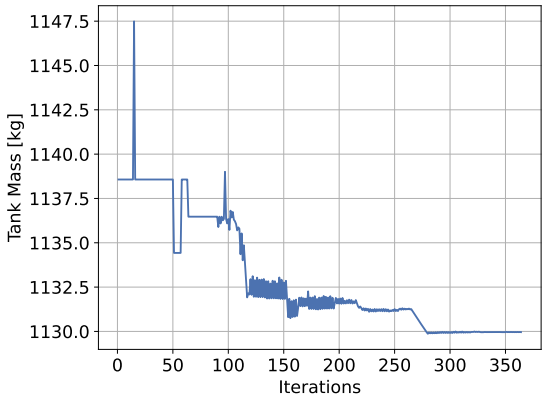


(a) Variation in the mass of the tank.

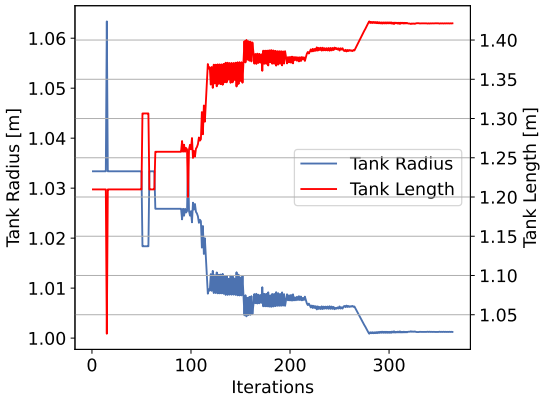


(b) Variation in the total tank dimensions.

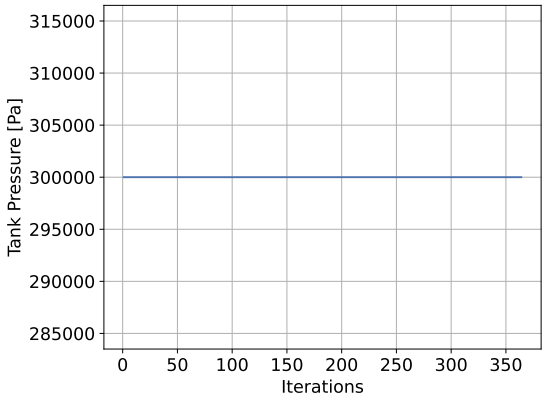


(c) Variation in the tank pressure.

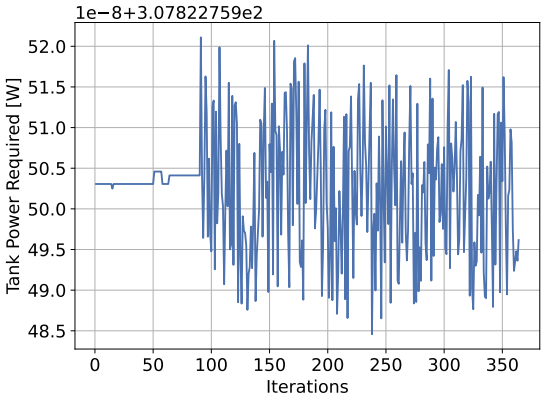


(d) Variation in the tank power required.

Figure B.21: $LH_2$ Pump architecture mass and power optimisation: Tank convergence plots

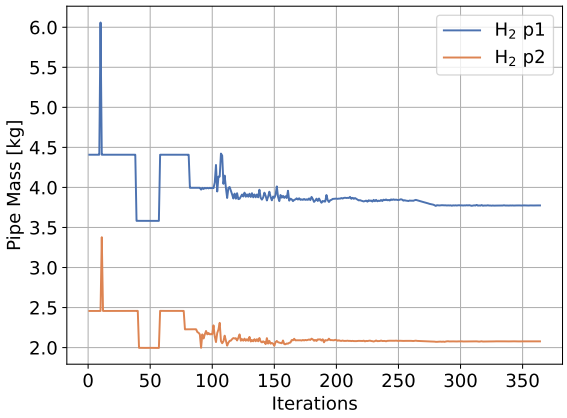


(a) Variation in the hydrogen pipe mass.

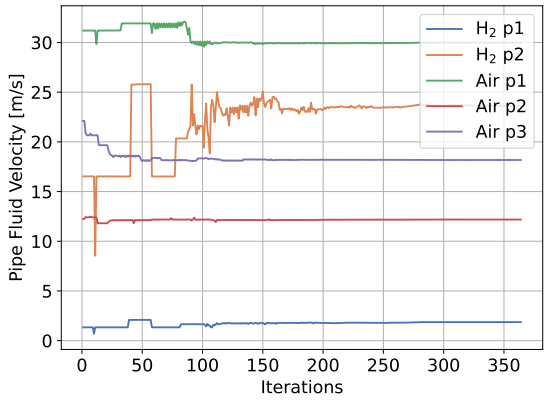


(b) Variation in the maximum fluid velocity in the pipes.

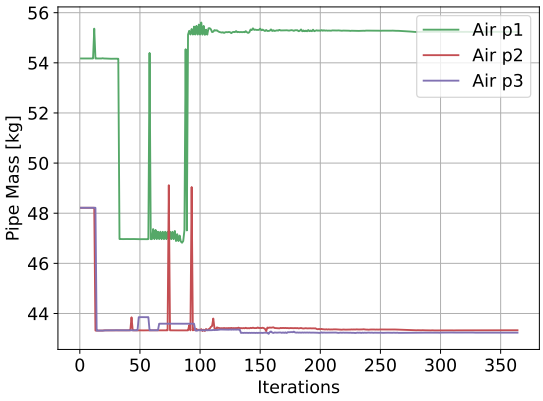


(c) Variation in the mass of the air side pipes.

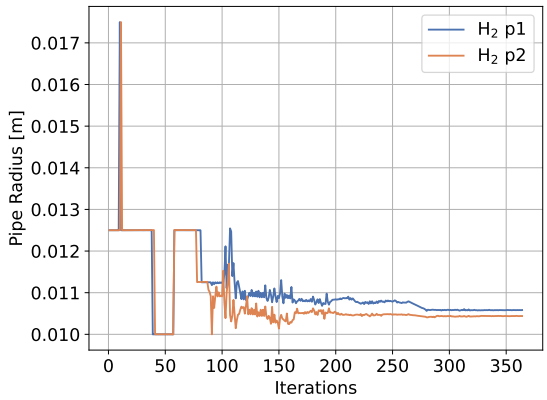


(d) Variation in the radius of the hydrogen side pipes.

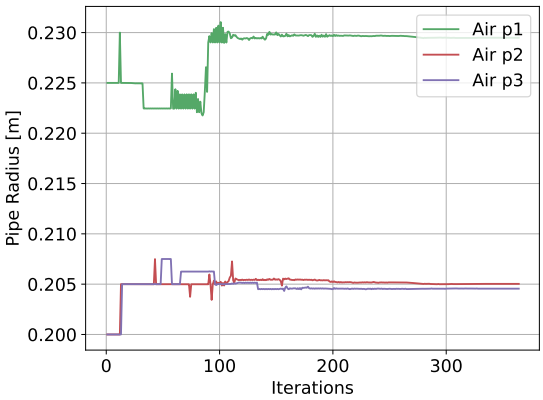


(e) Variation in the radius of the air side pipes.

Figure B.22: $LH_2$ Pump architecture mass and power optimisation: Hydrogen and air side pipe convergence plots

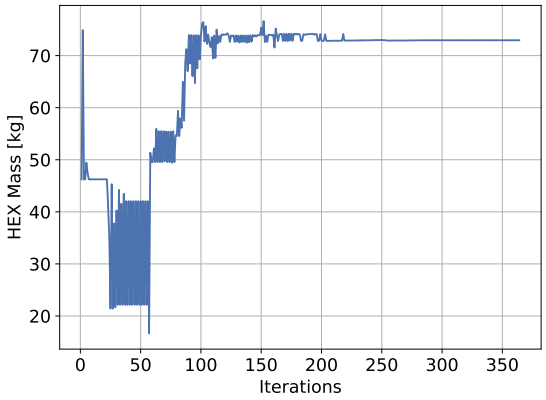


(a) Variation in the mass of the hydrogen heat exchanger.

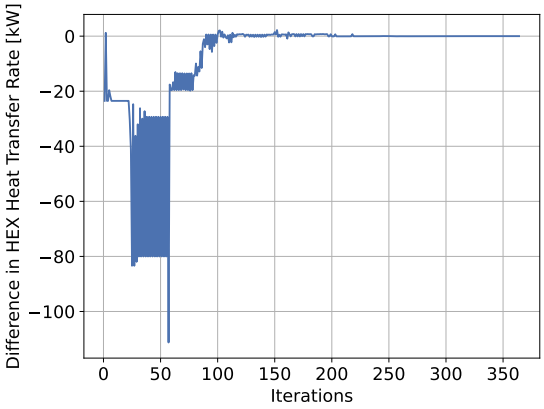


(b) Variation in the difference in the hydrogen heat exchanger heat transfer rate and fluid required heat transfer rate.

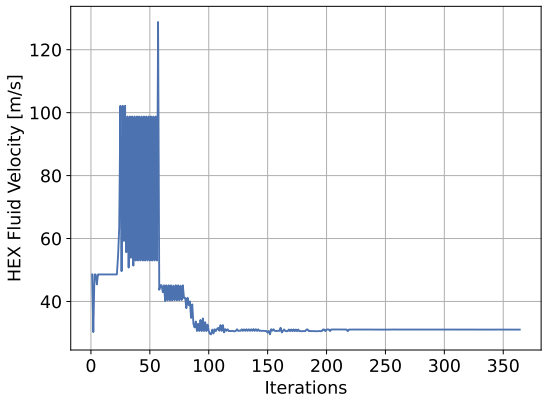


(c) Variation in the fluid velocity in the hydrogen heat exchanger.

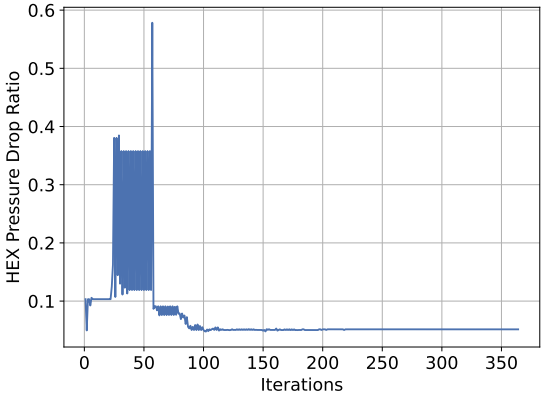


(d) Variation in the hydrogen heat exchanger hot fluid pressure drop ratio.

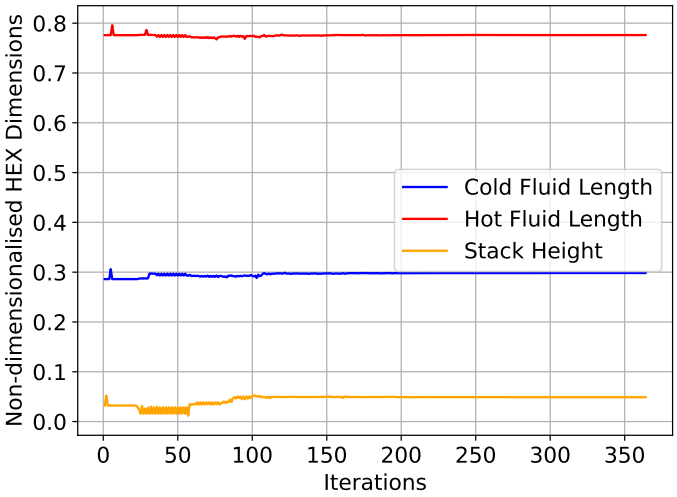


(e) Variation in the Hydrogen heat exchanger non-dimensionalised lengths.

Figure B.23: $LH_2$ Pump architecture mass and power optimisation: Hydrogen heat exchanger convergence plots

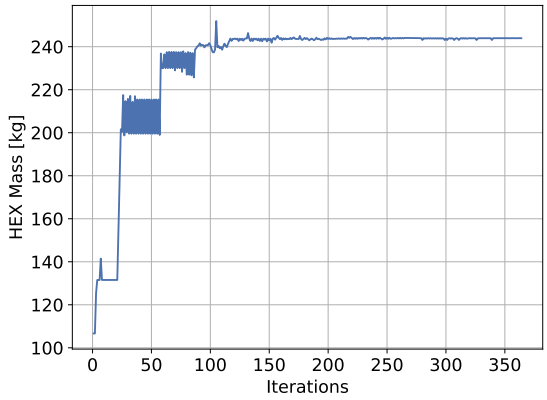


(a) Variation in the mass of the air heat exchanger.

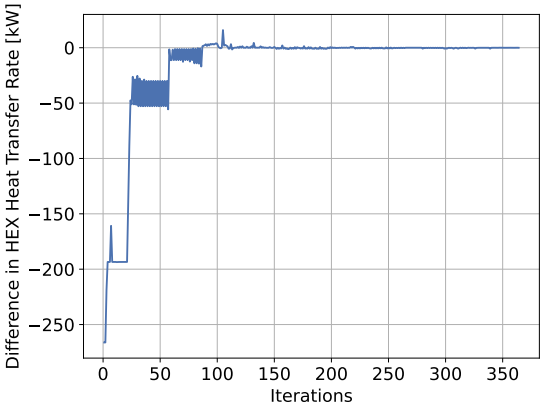


(b) Variation in the difference in the air heat exchanger heat transfer rate and fluid required heat transfer rate.

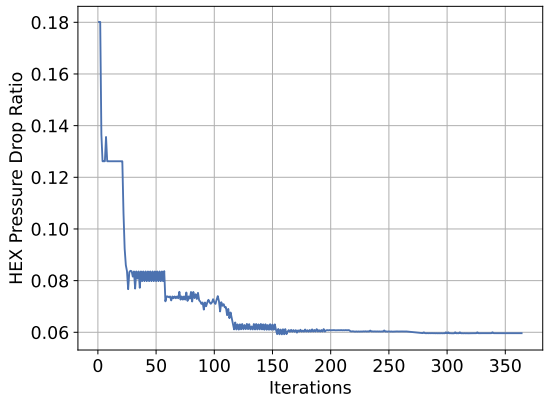


(c) Variation in the air heat exchanger hot fluid pressure drop ratio.

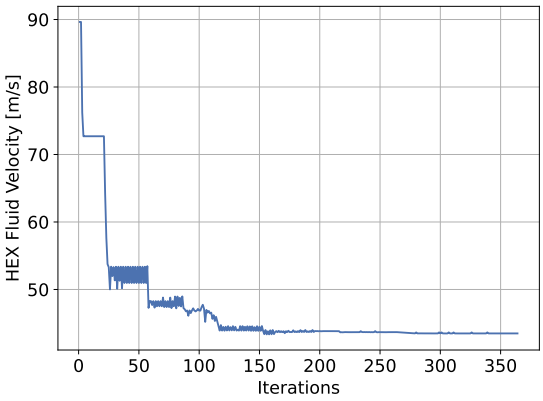


(d) Variation in the hot fluid velocity in the air heat exchanger.

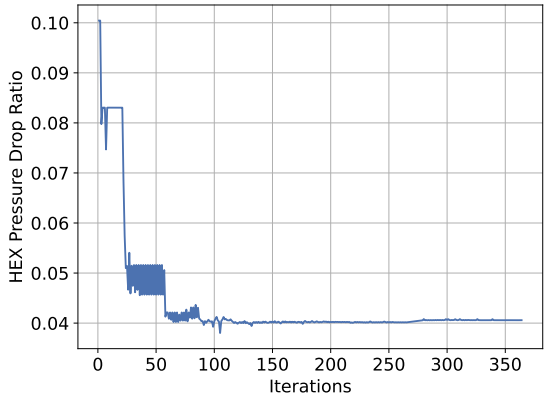


(e) Variation in the air heat exchanger cold fluid pressure drop ratio.

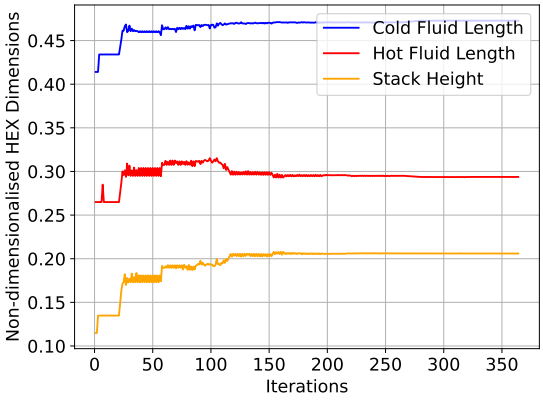


(f) Variation in the air heat exchanger non-dimensionalised lengths.

Figure B.24: $LH_2$ Pump architecture mass and power optimisation: Air heat exchanger convergence plots

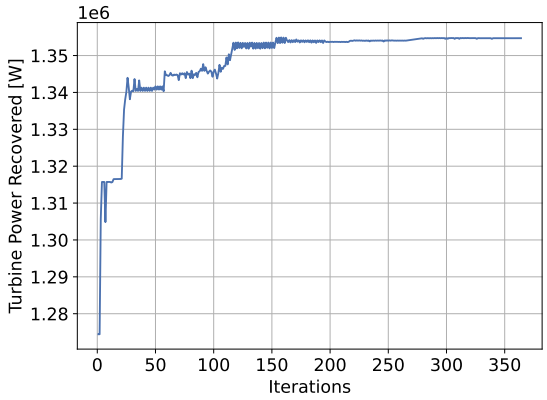


(a) Variation of the power recovered by the turbine.

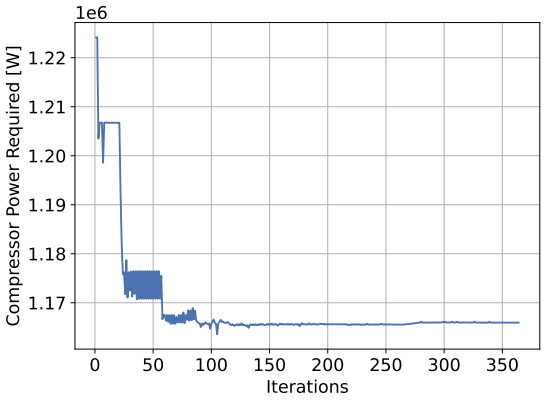


(b) Variation of the power required by the compressor.

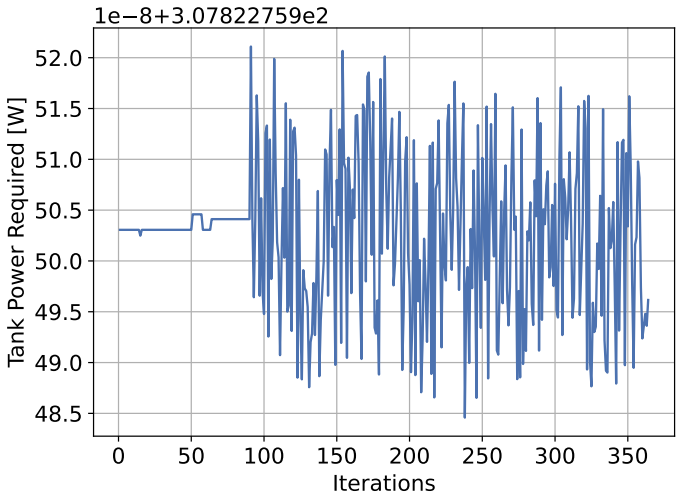


(c) Variation of the power required by the tank.

Figure B.25: $LH_2$ Pump architecture mass and power optimisation: Power convergence plots